UNIVERSITY OF SOUTHAMPTON

A Numerical Investigation of the Effects of the Spanwise Length on the Three-Dimensional Wake of a Circular Cylinder

by
David François Lionel Labbé

A thesis submitted for the degree of
Doctor of Philosophy

Fluid-Structure Interaction Research Group
School of Engineering Sciences
Faculty of Engineering, Science and Mathematics

July 2004

To my family and my friends,

Acknowledgements

First and foremost, I would like to thank my supervisor, Professor Philip A. Wilson, for giving me the opportunity to study for this PhD and to participate to an exchange program with the Federal University of Rio de Janeiro in Brazil. His constant support throughout the course of the study and his encouragement during the difficult moments have most certainly been the driving force of my work.

I would also like to thank Professor Carlos A. Levi da Conceiçao of the Federal University of Rio de Janeiro for his incredible welcome in Brazil, his friendship, trust and invaluable contribution to this work. He introduced me to the world of vortex-induced vibration and provided me with all the tools and knowledge to progress in that field. Without his help, I would not have appreciated my stay in Rio as much, and most likely, I would not have known that there could be so many good restaurants in one place.

My sincere thanks goes to all the people of the Ocean Engineering department of the Federal University of Rio de Janeiro who went out of their way to make me feel welcome, in particular my friends Eduardo, Johnny, Henrique, and Osvaldo and all the staff members, Lucimar, Glace, Nilda. They made my stay in Rio de Janeiro a truly unique experience.

This work could not have been possible without the constant love and support of my family, in particular, my mother, my father, Mike and Sylvie. Their encouragements at all time provided me with all the motivation to make it a reality.

Finally, I would like to thank my partner Flavia for her love, support and understanding throughout the good, the bad and the ugly moments. Her kindness and help in dealing with every day life matters enabled me to concentrate fully on my work and her presence on my side made it all worthwhile.

A great thanks to all the many other people not mentioned here who also contributed in various ways to this work and to my life during this period.

Abstract

The numerical prediction of vortex induced vibrations has been the focus of numerous investigations to date using tools such as computational fluid dynamics. In particular, the flow around a circular cylinder has raised much attention as it is present in critical engineering problems such as marine cables or risers. Limitations due to the computational cost imposed by the solution of a large number of equations have resulted in the study of mostly two-dimensional flows with only a few exceptions. The discrepancies found between experimental data and two-dimensional numerical simulations suggested that three-dimensional instabilities occurred in the wake of the cylinder that affect substantially the characteristics of the flow. The few three-dimensional numerical solutions available in the literature confirmed such a hypothesis.

In the present investigation the effect of the spanwise extension of the solution domain on the three-dimensional wake of a circular cylinder is investigated for various Reynolds numbers between 40 and 1000. By assessing the minimum spanwise extension required to predict accurately the flow around a circular cylinder, the infinitely long cylinder is reduced to a finite length cylinder, thus making numerical solution an effective way of investigating flows around circular cylinders.

Based on the projection method, and using the finite volume discretisation, a method is presented to solve the incompressible form of the Navier-Stokes equations. A parallel algorithm is used to distribute the computations onto several cluster nodes, thus enabling large domain to be solved.

Results are presented for three different spanwise extensions, namely $\pi/2D$, πD and $2\pi D$. The analysis of the force coefficients obtained for the various Reynolds numbers together with a visualisation of the three-dimensionalities in the wake of the cylinder allowed for a comparison between the effects of the three spanwise extensions. Furthermore, by showing the different modes of vortex shedding present in the wake and by analysing the streamwise components of the vorticity, it was possible to estimate the spanwise wavelengths at the various Reynolds and to demonstrate that a finite spanwise extension is sufficient to accurately predict the flow past an infinitely long circular cylinder.

Contents

List of Figures

List of Tables

Nomenclature

Variables and Parameters

U_∞	Flow velocity in the far field
D	Cylinder diameter
ν	Kinematic viscosity
μ	Dynamic viscosity
ρ	Density
Re	Reynolds number
S_t	Strouhal number
x_i	Cartesian coordinate in the i direction
ξ_i	Curvilinear coordinate in the i direction
J	Jacobian of the coordinate transformation
S_i^j	Grid cell metric
u_i	Velocity component in the i direction
p	Pressure
q	Pseudo pressure
t	Time
ω_i	Vorticity component in the i direction
U^i	Contravariant component of velocity in the i direction
U_r^i	Contravariant component of relative velocity in the i direction
$\tau_i j$	Reynolds stress tensor
S_{ij}	Rate of strain tensor
$\mathbf{F}$	Force vector
$\mathcal{L}$	Laplacian
$\mathcal{C}$	Convective term of the discretised momentum equation
$\mathcal{D}$	Diffusive term of the discretised momentum equation
m, c, k	Mass, damping and spring stiffness
m^*, ζ, U^*	Mass, damping and velocity ratios
f_n	Natural frequency

f_s	Vortex Shedding frequency
S_g	Skop-Griffin parameter

Superscripts

$*$	Non dimensional
n	Time level

Subscripts

e, w, n, s, t, b	East, west, north, south, top and bottom cell face
E, W, N, S, T, B	East, west, north, south, top and bottom neighbouring cell centre
GC	Ghost cell
DC	Domain cell

Acronyms

CFD	Computational Fluid Dynamics
VIV	Vortex-Induced Vibrations
TFI	Transfinite Interpolation
LSA	Lineal Spring Analogy
FDM	Finite Difference Method
FVM	Finite Volume Method
FEM	Finite Element Method
BEM	Boundary Element Method
PM	Particle Method
DNS	Direct Numerical Simulation
LES	Large Eddy Simulation
$RANS$	Reynolds Averaged Navier-Stokes
RSE	Reynolds Stress Equations
SF	Structure Function
SSF	Selective Structure Function

ILU	Lower Upper Factorisation
ILU	Incomplete Lower Upper Factorisation
SOR	Successive Over-Relaxation
CG	Conjugate Gradient
CGS	Conjugate Gradient Squared
$CGSTAB$	Conjugate Gradient Stabilised
$GMRES$	Generalised Minimal Residual
CPU	Central Processing Unit
RAM	Random Access Memory
MPI	Message Passing Interface
$SPMD$	Single Program Multiple Data
$BSNR$	Blocking Send, Non-blocking Receive
$NSBR$	Non-blocking Send, Blocking Receive

Chapter 1

Introduction

1.1 Vortex Induced Vibrations

Vortex-induced vibration (VIV) or flow-induced vibration (FIV) as it is sometimes referred to, has been the subject of intensive research for many years. Historically, the first experiments were carried out by Strouhal in 1878 on Aeolian tones. Strouhal found that the pitch of the Aeolian tone was not dependent on the tension, length or material, but rather on the flow speed and diameter only. By reproducing the aeolian tone using resonating wires, he observed that a synchronisation phenomenon occurred when the frequency of eddy shedding is locked onto the natural frequency of the wire (Zdravkovitch [99]). In the following paragraphs, a general introduction to vortex-induced vibration will be given followed by a brief review of the research carried out.

In practical applications such as in the wind or offshore engineering where slender bodies with low structural damping are exposed to unsteady fluid forces, consideration has to be given to the influence of the vortex shedding. It is well known that vortex induced vibration can occur when the frequency of the vortex shedding coincides with a structural frequency (Bearman [4]). Furthermore, the maximum amplitude of response is influenced by both the damping and the magnitude of the mass ratio. One of the major differences between flexible structures in the air and in the water is that in the later case, the mass ratio is much smaller leading to greater fluid/structure interaction. Such greater interaction results in larger vortex-induced vibration amplitudes as well as a broader range of flow over which the amplitude of the oscillations are significant and the possible excitation of not only the transverse but also the in-line oscillations. This becomes critical in the case of marine risers. As the oil field development activities moved into deeper waters and areas of stronger ocean currents, the importance of vortex-induced vibrations becomes critical at the system design stages (Cook *et al.* [19]) as it can result in serious fatigue failure or interference and clashing.

Prediction of VIV around cylindrical structures has thus become the centre of many research projects over the years. As most of the interesting fluid dynamic phenomena are present (Dalton [21]) such as boundary layer and boundary layer separation, laminar and turbulent flow, shear layer and shear layer roll up, vortices and vortex shedding, and unsteady lift and drag, the task of capturing or predicting all of these represents a major challenge. In an attempt to categorise the VIV research, whether it is for the offshore engineering or other, one could consider various stand points (Huse [40]):

- the kind of **structure** targeted (rigid or flexible pipes installed horizontally or vertically).
- the kind of **phenomenon** of interest (in-line or transverse deformation, bending moment, fatigue ...)
- the kind of **natural environment condition** considered (current, wave, forced oscillation)
- the kind of **top or bottom condition** of the riser (fixed, spring support, rotation free..)
- the kind of **section configuration** (circular or rectangular cylinder, arbitrary cross section)
- the kind of **flow condition** (uniform or oscillatory, regular or irregular ...)
- the kind of **flow parameters** (Reynolds number, Keulegan-Carpenter number, reduced velocity...)

These aspects, although still under intense investigations are however well documented in the literature. Davis *et al.* [22] compared rigid and flexible cylinders and observed significant difference between the VIV responses although the two structures achieved similar Reynolds number, mass ratio and damping ratio. Miliou *et al.* [60] simulated the effect of flow around curved riser pipes for various velocity profiles and flow directions and presented results for the fluid dynamic loading and wake structure behind the pipes. Maeda [56] presented in his review of the research on VIV in Japan various work carried out on the influence of wave forces acting on circular cylinders, behaviour of long flexible pipes and the effect of transverse hydrodynamic forces on towed vibrating cylinders. Yamamoto *et al.* [96] carried out numerical analysis of the VIV response of flexible risers. Bearman *et al.* [5] studied the in-line response of large scale models while Anagnostopoulos *et al* [3] analysed the phenomenon numerically. Fujana *et al.* [30] showed the similarities between the dynamic behaviour of flexible cantilevers and elastically mounted rigid cylinders. Vandiver [85] showed the important role of flow parameters in VIV response of risers. Other works involve the study of multiple risers. Huse [40] raised the increasingly concerning issue of collisions or clashing of risers for future deep sea floating production unit. Caly *et al.* [13] presented a detailed experimental study of the flow past a pair of cylinders inside by side configuration. Mahir *et al.* [57] [58] conducted experiments on a pair of side by side cylinders, comparing the lock-in phenomenon for the single cylinder and for the pair of cylinders and focusing on the wake patterns and velocity spectra due to the forced oscillations. Laneville *et al.* [47] studied the mechanical and fluid coupling between two circular cylinders focusing on the relative response between the cylinder. Zhou *et al.* [105] presented an experimental investigation of a the wake interaction for a two and a three side-by-side cylinders configuration.

1.2 Aims and Objectives

1.2.1 Aims

The aim of the present research is to investigate the wake behind a circular cylinder and determine the influence of the spanwise extension of the solution domain onto the three-dimensional solution of the flow past a circular cylinder. Furthermore, the research aims at determining the minimum spanwise extension required to obtain accurate prediction of the flow past the cylinder.

1.2.2 Objectives

To achieve this aim, several objectives have to be fulfilled that can be summarised in three parts, namely the *tool development*, its *validation* and the *application*.

The vortex-induced vibrations of marine risers is becoming critical as offshore exploration moves into deeper water where stronger ocean currents occur. Furthermore, since the viscous effects in such flows is of significant importance, they must be accounted for in the prediction of the flow. To numerically predict vortex-induced vibration, it is thus necessary to solve the Navier-Stokes equations. In the context of the present research, as no commercial CFD software was available, it was deemed necessary to develop a solver. Developing a solver is by far not a trivial task as it involves not only the coding of a complex algorithm but also the validation of the code. It is thus equally important to present the requirements for the solver as well as the validation of the algorithm.

Tool Development

It is not intended to present here in detail the algorithm used in the solver but rather the various features or capabilities it should possesses. Furthermore, in the interest of future developments outside the scope of the current research whose focus is on the flows past a fixed circular cylinder, the possibility of investigating oscillating cylinders must be taken into account in the method development.

The development of a three-dimensional Navier-Stokes solver for incompressible flows should thus include:

- **curvilinear multi-blocks** grid handling to tackle complex geometries.
- an adequate algorithm for the **pressure solver** to close the system of equation by means of the projection method with a second order accuracy.
- a suitable **turbulence model** such as a Large Eddy Simulation model.
- a fluid/structure interaction method including a **force model**, a **structural model** for rigid bodies subject to spring and damping forces, a **moving grid** capability to tackle the oscillating objects.
- a **message passing model** for parallel computation to handle large meshes.

Tool Validation

Before being able to carry out the application part, it is necessary to establish a set of validation tests. Such a validation consists of carrying out a number of benchmark tests and comparing the results obtained with the code with those published in the literature. As the majority of results available are for two-dimensional problems, the validation process will focus on two-dimensional tests only.

Although the Reynolds numbers for practical applications can range from 10^5 to 10^6 (Vandiver [85]), the transition from two- to three-dimensional flows occurs at a much lower Reynolds number between 150 and 300 (Roshko [72]). Furthermore, as the Reynolds is increased from 300 to 1000, turbulence starts occurring as the disorder in the fine scale three-dimensionalities increases. Two-dimensional simulations will thus be carried out for flows around a circular cylinder at Reynolds number varying from 40 to 1000 and compared with the various results available in the literature. Particular attention will be paid to the Strouhal-Reynolds relationship in the two-dimensional regime.

An oscillating cylinder case will also be undertaken in the two-dimensional case only to assess the capabilities of the method to tackle the flow past a circular cylinder undergoing VIV.

Three-Dimensional Flow Around Circular Cylinders

From the two-dimensional results obtained as part of the validation of the method, three-dimensional numerical solutions will be carried out by increasing the spanwise extension of the domain. Various Reynolds numbers in the transition regime and in the fully three-dimensional regime will be examined focusing on quantities such as the force coefficients and the Strouhal number.

The visualisation of the three-dimensional features in the wake of the cylinder in the considered range of Reynolds numbers will allow for the different modes of vortex shedding to be examined. Particular attention will be paid to the transition between the two- and three-dimensional wake.

Such a systematic study will allow for the assessment of the influence of the spanwise extension of the domain on the solution. It will then be possible to determine, if such is the case, the minimum spanwise extension required to capture accurately the three-dimensional flows around the cylinder.

1.3 Format

Having defined the aim and the objectives to be achieved, it is now possible to present in more details the format that will be adopted for this report. The following paragraphs will provide a brief description of the chapters to follow.

In chapter 2, a review of the current status of the numerical prediction of VIV will be carried out leading to a number of key questions that remain unanswered.

In chapter 3 the numerical methods currently available will be investigated, focusing on various aspects such as modelling and discretisation, turbulence models, moving grids and parallel computation. The discussion aims at defining the method to be employed in the present work.

Chapters 4 and 5 focus on the method developed in the context of this research. Firstly the mathematical model will be introduced focusing on the governing equations for incompressible flows, the force description, the structural motion equation, and finally the moving grid model. The numerical method will then be presented, detailing the finite volume discretisation, the boundary conditions treatment and the methods for the forces computation and moving grid method. Throughout the chapter, a discussion of the implication of a parallel implementation will be carried out when relevant.

Chapter 6 will present the validation of the method and its numerical implementation through a comparison with benchmark test cases for circular cylinder found in the literature.

Chapter 7 will deal with the application of the method to the problem of interest, namely the assessment of the three-dimensionality of the flow around a circular cylinder. The results for solution domains with different spanwise extension will be presented together with a visualisation of the wake behind the cylinder and a discussion on the key issues.

Finally, chapter 8 will draw conclusions from the present investigation and extend the discussion to possible future areas of investigation to be conducted on the subject.

Chapter 2

Towards the Three-Dimensional Numerical Prediction of Vortex Induced Vibration of circular Cylinder

2.1 Overview of Numerical Prediction of Vortex Induced Vibration

Prediction of VIV response has traditionally been carried out using either an empirical or a numerical approach.

Empirical models have been traditionally based on data from oscillatory test with short cylinder sections and are almost exclusively based on the assumption that VIV will appear as a response at discrete frequency (Larsen [49]). Stochastic models (Vandiver [85]) have been used as well as discrete frequency models.

The VIV response of a body can be interpreted as the combination of an excitation and a response to that excitation. Both the excitation force and the response of the body to that excitation constitute the complete fluid-structure interaction. A full numerical prediction of the VIV response would encompass both aspects. However, owing to the complexity of the phenomenon and the computation limitations, the numerical prediction of VIV response has so far been focused on one of the two aspects only, i.e. the excitation or the response. Some recent models combine both numerical models for response through finite element computations and empirical data for excitation (Larsen *et al.* [50]).

The determination of the response to a prescribed excitation, i.e. the structural deformation due to the excitation, is generally carried out numerically using methods based on the finite element approaches.

The determination of the excitation, i.e. the determination of the behaviour of the fluid around the body, is generally carried out by means of computational fluid dynamic (CFD) methods. Such methods include discrete vortex methods and methods based on the complete solution of the Navier-Stokes equations (Maeda [56]).

Discrete shed vortex methods are based on the idea raised by Chorin [17] that vortex blobs can be generated on the boundary of a body to satisfy the no-slip condition. These blobs are then convected and diffused according to the vorticity transport equation. One of the major advantages of such a method is the relative simplicity of its implementation. Also, being a grid-free method, the computational elements are automatically concentrated in the regions of most interest. However, such a method presents several shortcomings. Two of the most critical are the inaccurate representation of the velocity field near the boundaries of the body and the exponentially increasing computational cost as the number of elements grows with time. Several extensions to the method led to the development of better approaches. The Vortex-in-Cell technique (VIC) first introduced by Christiansen [18] improves the solution of the pressure by introducing a grid around the body and thus gives a better representation of the velocity field near the body. Furthermore, it substantially reduces the computational cost. Other methods retain the field grid free formulation and improved the solution by using boundary integral methods to solve the pressure and a vortex sheet algorithm to improve the boundary layer solution and thus the representation of the flow near the body (Yeung *et al.* [98]).

Methods based on the solution of the Navier-Stokes equations have been the most popular methods to numerically predict the VIV response around circular cylinders. Such methods consist of solving for a set of primitive variables on a mesh defined in a domain around the body. For such a solution to produce results of interests, the mesh used must be such that it allows the capture of all phenomenon occurring in the flow. This dependency upon the mesh size and quality implies that the accurate solution of the Navier-Stokes equations is a computationally costly method. Intense investigations into the generation of grids have been carried out to produce better quality meshes using less elements. Methods using adaptive meshes have also been developed where the mesh evolves by addition, subtraction or motion of the mesh elements while the solution of the flow is being carried out. A comprehensive collection of work on numerical grid generation and adaption can be found in Thompson *et al.* [82] . Also, investigations into the discretisation methods (finite difference, finite volumes or finite elements) used to solve the Navier-Stokes equations led to more accurate solutions by means of higher order representations of the terms of the equations.

2.2 Three-Dimensional Numerical Prediction

To assess the progress and validity of numerical simulations, it is necessary to consider the experimental research on the subject. The study of the flow around circular cylinders has been the centre of many investigations for over a 100 years and it is now common knowledge that the flow around cylinders can be characterised essentially by two parameters, namely the Reynolds number $Re = UD/\nu$ and the Strouhal number $St = fD/U$ where U is the far stream velocity, D is the cylinder diameter, ν is the kinematic viscosity of the flow and f is the frequency of the shedding of vortices from the cylinder.

Recent progress in the measurement techniques has allowed for considerable developments to be made. In the early 1980's, Bouard *et al* [8] used flow visualisation techniques to study the early development of the wake behind a circular cylinder for Reynolds numbers ranging from 40 to 10^4 giving an insight into the nature of the vortex shedding behind the circular cylinder.

The first definition of the flow regimes around a circular cylinder was given by Roshko [72] who established a Reynolds-Strouhal numbers relationship as shown in figure 2.1. His measurements of the velocity fluctuation, spectra and frequency allowed for the identification of a transitional region for $150 < Re < 300$ while distinct irregularities could be observed for $Re > 300$.

Williamson [90] provided further evidence of the transition from two-dimensional to three-dimensional flows in the Strouhal-Reynolds number relationship. He also identified two stages in the transition to three-dimensional flows characterised by two discontinuities in the Strouhal-Reynolds number relationship, the first one at $Re = 178$ and the second for Reynolds numbers between 230 and 260. He further associated those discontinuities with a mode change in the shedding of vortices in the cylinder wake (Williamson [92]). The first mode, named mode A is characterised by the inception of streamwise vortex loops. The primary vortices roll up and deform in a wavy pattern along their length during process of shedding to result in the local spanwise formation of vortex loops. The second mode, namely mode B, associated with the second discontinuity, is characterised by the formation of finer-scale streamwise vortex pairs.

Reviewing the numerical simulations of vortex shedding, he also noted the very good agreement found between three-dimensional direct numerical simulation and experimental results and how the numerical solution were capable of capturing the two mode changes (Thompson *et al.* [83]). He further commented that the discontinuities observed in the Strouhal-Reynolds number relationship were not achieved with two-dimensional numerical solutions as can be shown in figure 2.2.

He further described the flow regimes around a circular cylinder in function of the Reynolds number as follows:

$Re < 49$	Laminar steady regime
$49 < Re < 140 - 194$	Laminar vortex shedding
$194 < Re < 260$	3-D wake transition regime
$260 < Re < 1000$	Increasing disorder in the fine scale three-dimensionalities
$1000 < Re < 200000$	Shear layer transition regime
$200000 < Re < 400000$	Asymmetric reattachment regime
$400000 < Re < 800000$	Symmetric reattachment regime
$Re > 800000$	Boundary layer transition regime

Williamson [91] also reported the importance of the end conditions of the cylinder in an experimental set-up and how oblique or parallel modes of vortex shedding in the spanwise direction could be produced in the wake of a cylinder. He also stated that end conditions could be responsible for the different critical Reynolds numbers found in the literature at which transition to three-dimensional wake occur. One can thus be expected that for Reynolds number between 140 and 200, three-dimensional features will start appearing in the wake of the cylinder, and transition to three-dimensional wake will start occurring.

In their study of three-dimensional vortex structures in a cylinder wake, Wu *et al* [95] used digital particle image velocimetry (DPIV) to measure the instantaneous velocity field in the vertical plane in the near wake of a cylinder at $Re = 525$. The measured velocity field was then used to compute accurately the vorticity field. No visual evidence of the presence of the two transitional modes presented by Williamson were found, but the importance of vortex stretching was shown. An interesting comment raised by Wu *et al* in the observation of the results is the remarkable regularity of the vortices in the streamwise and spanwise directions although some variability appeared due to the distortion of the vortex sheet.

Numerical simulations of VIV excitation of circular cylinders using the solution of the Navier-Stokes equations have been the focus of numerous work in the literature but essentially restricted to the two-dimensional simulations owing to the limitation of the computational resources. Several aspects of the fluid-structure interactions are examined in these works among which the computation of the forces acting on the cylinder, the shedding of vortex from the cylinder and the

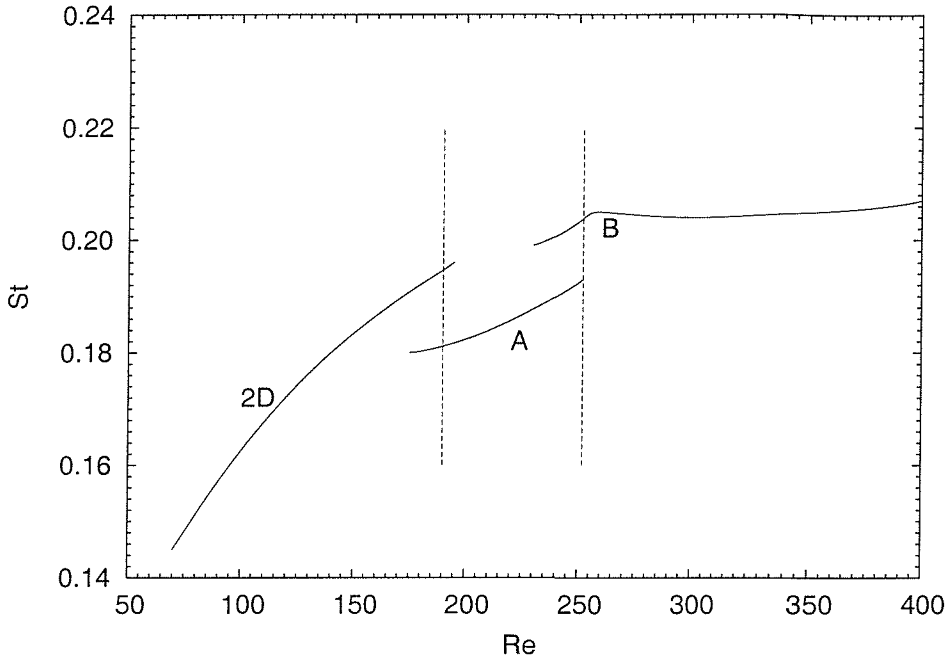

Figure 2.1: Strouhal-Reynolds number relationship

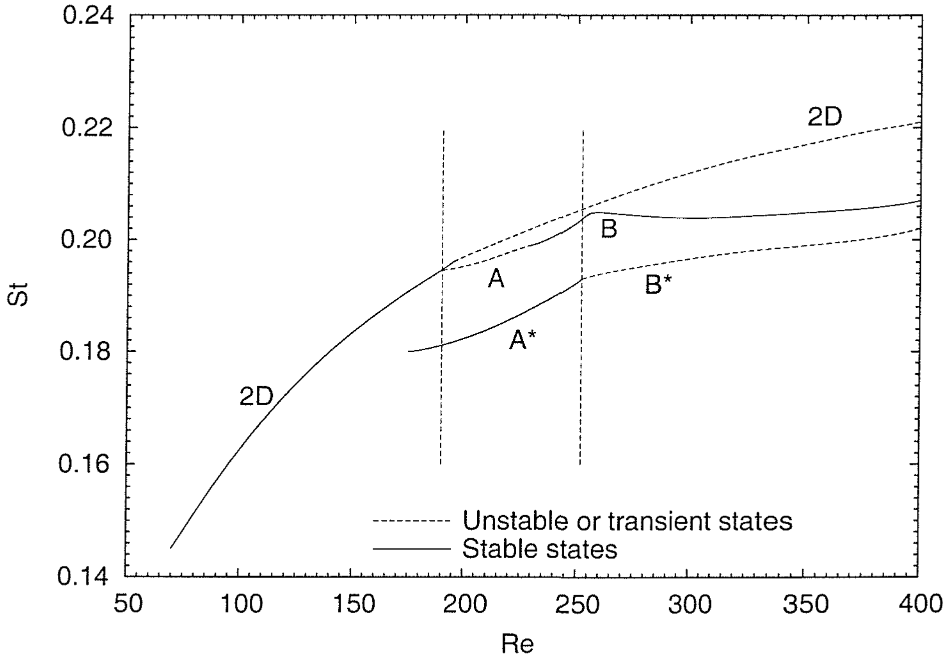

Figure 2.2: Strouhal-Reynolds number relationship (from Williamson [92])

wake of the cylinder.

For example, Cheer [15] simulated flows around a two dimensional circular cylinder at Reynolds numbers between 3000 and 10^4 and examined the formation of primary and secondary vortex structure behind an impulsively started circular cylinder.

As the computational resources improved over the years, different flow conditions became the focus of researchers. Yeung *et al* [98] used a modified random vortex method to study the accelerated flow past a fixed cylinder and compared the results with a cylinder accelerating in a static flow, showing that the two kinematically identical flows were producing identical results when the uniform velocity was attained. They also presented a simulation of an oscillating flow past a fixed cylinder and results for an oscillating cylinder in a uniform flow.

But as the Reynolds numbers of interest for practical flow problems can range from 10^5 to 10^6 (Vandiver [85]), researchers focused their numerical investigations on higher Reynolds numbers and started encountering discrepancies between their two-dimensional numerical results and the experimental data.

Kalro *et al* [42] studied the flows around a three-dimensional circular cylinder in a uniform flow and found that the results obtained for the Reynolds number 300 compared well with the two-dimensional results. Since three-dimensional effects appear for Reynolds number of about 190, this indicates that for $Re = 300$, little three-dimensional features are present. On the other hand, the results they obtained for $Re = 800$ were clearly different from the two-dimensional ones, indicating that the three-dimensional features were much stronger. They concluded that, as the boundary layer is thiner at higher Reynolds number, the velocity gradients in the near cylinder region are much larger, thus implying the release of stronger vortices. It follows that the amplitude of the force coefficients in two-dimensional simulations is larger at $Re = 800$ than at $Re = 300$. However, this is not seen in the three-dimensional computations since the vortices are significantly distorted and posses components besides that in the spanwise directions.

Zhang *et al.* [101] studied the flow around three-dimensional cylinders at $Re = 100$ and $Re = 200$ and confirmed the two-dimensional nature of the flow for the $Re = 100$ case. However, their results for the $Re = 200$ case clearly show the presence of distinct three-dimensional features and emphasised that the flow in the wake was becoming three-dimensional before it even becomes turbulent. Furthermore, their studies stressed the importance of the proper representation of the flow in the wake as it has a noticeable effect on the force coefficients and the Strouhal number. Zhang also commented that as two-dimensional computations were still cheaper than three-dimensional solutions, if a cautious estimate of the effect of the lack of three-dimensional features could be established, two-dimensional simulations could still provide a qualitative understanding of the flow.

Breuer [10] further details the differences between the two-dimensional and three-dimensional computations by showing, at $Re = 3900$, the striking differences in the time-averaged streamlines patterns characterised by the absence, in two-dimensional results, of a recirculation zone behind the cylinder clearly showing in the three-dimensional results. He noted that the two-dimensional field was more asymmetrical than the three-dimensional one as the vortices shed from the cylinder moved downstream along an axis which is inclined with reference to the symmetry line. As a consequence, the drag coefficient and the base pressure coefficient were much too high in two-dimensional computations. He thus concluded that, even for nearly two-dimensional flow problems, two-dimensional computations were useless as three-dimensional structures strongly influenced the near wake flow.

In a later publication on the influence of subgrid-scale models for large-eddy simulations around circular cylinders in three-dimensions, Breuer [11] noted that the flow around the circular cylinder was not only a function of the Reynolds number, but also, among other factors, it was a function of the cylinder's aspect ratio. He thus stressed that the difference between numerical and experimental results were apparent and that the most relevant factor to evaluate numerical simulations was the spanwise extension of the integration domain often limited due to computational resources.

So far, mostly fixed cylinder cases have been considered, but practical engineering problems generally involve the oscillation of such a cylinder whether in a free or forced mode. The occurrence of the two free and forced oscillation mode can be explained in the context of a marine riser. When a marine riser is excited at one elevation due to the shedding of vortices, it oscillates at another elevation while exposed to the current at this elevation (Lu *et al.* [55]). The oscillations of the cylinder give rise to another commonly used characteristic parameter, namely the Keulegan-Carpenter number $KC = U/fD$ where the frequency f describes the oscillation frequency. A parameter taking both the Reynolds number and the Keulegan-Carpenter number into account can be found in the literature: $\beta = Re/KC$.

Anagnostopoulos [2] reported in his study of the response of a vortex-excited cylinder in a uniform flow that the numerical solution failed to predict the high amplitude and low beat oscillations above the lock-in region observed experimentally. He also stressed that the mesh refinement and the formula to compute the vorticity on the solid wall boundary significantly influenced the accuracy of the results. Such a comment underlines the importance of the representation of the flow in the near cylinder region for the computation of the forces acting on the cylinder.

Lu *et al* [55] examined the vortex switching phenomenon around a circular cylinder in an oscillating flow and found that as the frequency of excitation increased, the initially formed concentration of vorticity moved closer to the cylinder until a limiting position was reached and then switched abruptly to the opposite side of the cylinder. They presented results for both oscillating and non-oscillating flow around a cylinder for Reynolds numbers of 185, 500 and 1000. While the non-oscillating values of the mean drag coefficient and the Strouhal number for $Re = 185$ compare rather well with experimental data, they are overpredicted for the higher Reynolds number. This confirms the findings of Williamson [92] that at Reynolds above 200, the Strouhal number obtained through numerical solution is overpredicted (see figure 2.2).

Sun *et al* [80] presented two-dimensional simulation results for oscillating flows around a circular cylinder at $\beta = 1035$ and $0.4 < KC < 4.0$. The small KC results showed good agreement with experimental data while simulations at $KC > 2$ demonstrated that two-dimensional numerical solutions were inadequate to describe an established three-dimensional flow.

Lu *et al* [54] compared the three-dimensional numerical solution of an oscillating flow past a circular cylinder for various KC with the experimental results from Sarpkaya [73]. Good agreement with the experimental data was found for the mean drag coefficient.

It is interesting to note that, for $\beta = 1035$, Sarpkaya identifies three regimes of the oscillating flow, namely a transition to three-dimensional flow at $KC = 1.1$, a turbulent regime at $KC = 1.5$ and a separation at $KC = 1.9$. As $\beta = 1035$ and $KC = 1.1$ correspond to a Reynolds number of 1138, this suggests that the transition to a three-dimensional flow occurs at a much higher Re than for the fixed cylinder case (Re 190). A possible explanation can be found in [104] where Zhou *et al* studied the numerical solutions of a two-dimensional uniform flow past an elastic cylinder and commented that the structural vibration normally enhance the spanwise correlation of the wake, thus promoting the two-dimensionality in the wake. Their two-dimensional simulation exhibited differences with the experimental data suggesting the presence of three-dimensional features in the wake. As a two-dimensional solution assumes a perfect spanwise correlation, the overpredicted lift coefficient and thus vibration amplitude can be explained. They also noted that the streamwise oscillations had a substantial effect on the transverse vibrations and their characteristics.

2.3 Summary

From the above review of the literature on the flow around circular cylinder, several conclusions can be drawn and questions raised.

It is clear that two-dimensional numerical solutions are inadequate to describe practical flow problems as they result in an erroneous representation of the wake of the cylinder and cannot reproduce the three-dimensional features occurring above *Re* 190. Using two-dimensional numerical predictions is thus inadequate for practical engineering problems as they can lead to inaccurate force prediction.

Also, it has been found that three-dimensional simulations were in good agreement with experimental results. However, such simulations are highly dependent on the spanwise extension of the domain considered. Furthermore, to accurately predict the flow past the circular cylinder, particular attention has to be paid to the representation of the flow field in the near vicinity of the cylinder and in its wake.

An interesting issue concerns the aspect of the wake of the cylinder at low Reynolds number. As it has been reported that the vortex pattern was remarkably regular in the spanwise directions and moreover that a spanwise periodicity of the flow occurs in the wake, one may wonder, if such a periodicity exists, what is its spanwise extension and how is it affected by the different flow regimes?

As far as oscillating cylinders are concerns, it seems that the transition to the three-dimensional regime occurs at higher Reynolds numbers. Furthermore, the vibrations of the cylinder tend to promote the two-dimensionality of the flow. One could think that if the wake of the cylinder was displaying some periodicity in the spanwise direction, the transverse and streamwise vibrations could influence the extent of that periodicity. If such is the case, how is the periodicity affected by the vibrations?

If a periodicity really occurs in the spanwise direction, the problem of an infinitely long cylinder in a flow would be reduced to that of a flow past a finite length cylinder, therefore reducing the computational cost substantially.

Chapter 3

Numerical Methods - Background

3.1 Flow Solver

Since most engineering flows satisfy the Navier-Stokes equations, it is natural that over the years much effort has been spent on their solution. In the following section, a brief presentation of the numerical methods for the solution to the Navier-Stokes equations will be given.

The interest of the current work being on incompressible flows, the incompressible form of the equations will be considered and the methods for their solution discussed. Furthermore, since three-dimensional flows are at the focus of this research, the primitive variable form will be adopted.

A general discussion on the numerical solution will follow focusing on both the spatial and temporal discretisation of the equations. For such purposes, the finite volume method will be briefly presented and explicit and implicit temporal schemes discussed.

3.1.1 Incompressible Navier-Stokes Equations

All fluids are compressible to a greater or lesser degree. By assuming the density as a constant, the incompressibility condition represent an idealisation of the physical behaviour of fluids for certain flow conditions.

The compressible Navier-Stokes equations can be derived by applying the conservation laws to the extensive properties such as the momentum of a given control mass. However, in a fluid, it is generally more convenient to use a control volume rather than a control mass.

The incompressible Navier-Stokes equations can then be derived from the compressible form by simply treating the density as a constant, thus giving:

Continuity (Mass conservation):

$$\frac{\partial u_i}{\partial x_i} = 0 \tag{3.1}$$

Momentum (Momentum conservation):

$$\frac{\partial u_i}{\partial t} + \frac{\partial (u_i u_j)}{\partial x_j} = -\frac{1}{\rho}\frac{\partial p}{\partial x_i} + \nu \frac{\partial}{\partial x_j}\left(\frac{\partial u_i}{\partial x_j} + \frac{\partial u_j}{\partial x_i}\right) \tag{3.2}$$

Although the above set of equation seems sufficient to solve the primitive variables u_i and p, one can notice the absence of a time derivative for the pressure. This is due to the fact that, for incompressible flows, the pressure waves are propagated at infinite speed. Furthermore, this results in the decoupling of the continuity equation from the momentum equations.

The incompressibility condition thus makes the enforcement of the continuity constraint particularly difficult. Over the years numerous methods to solve the incompressible Navier-Stokes equations have been derived but they generally fall in one of two categories, namely the coupled approaches and the pressure correction approaches (Tannehill *et al.* [81]).

Coupled Approaches: Artificial Compressibility Methods

The coupled approach is one of the earliest techniques employed to solve the incompressible Navier-Stokes equations. The equations are solved treating the dependent variables as simultaneous unknowns. Since there are one less equation than the number of unknowns, an artificial time derivative of the pressure is introduced. This is known as the artificial compressibility method.

The continuity equation (3.1) is thus replaced by:

$$\frac{1}{\beta}\frac{\partial p}{\partial \tilde{t}} + \frac{\partial u_i}{\partial x_i} = 0 \tag{3.3}$$

Where $\tilde{t}$ is a pseudo time and β is the incompressibility factor.

The value taken by β is somewhat dependent on the problem tackled but values in the range $0.1 - 10.0$ (Tannehill *et al.* [81]) seem to be suitable for most problems.

Upon convergence of the steady state solution, the pseudo time term vanishes.

In the case of time-dependent solutions, the solution of a steady-state intermediary step must be reached before advancing the physical time. This constitutes one of the major drawback of this method as the sub-iterations required for time-dependent solution can substantially add to the overall computational cost of the solution (Kiris *et al.* [45]).

Pressure Correction Methods

An alternative to the use of artificial compressibility methods consists of using a pressure correction method.

In such methods, the momentum equations are solved in an uncoupled fashion using an available estimate of the pressure. The velocity components are thus solved without using the continuity constraint. A Poisson equation for the pressure or pressure change is generally used to alter the velocity field so as to satisfy the continuity equation.

There exist a number of pressure correction methods among which the most widely used are the projection (fractional step) methods. The projection methods were first introduced by Chorin [16]. One of the characteristics of the original formulation resides in the omission of the pressure gradients from the momentum equations.

$$\frac{\partial u_i^*}{\partial t} + \frac{\partial \left(u_i^* u_j^*\right)}{\partial x_j} = \nu \frac{\partial}{\partial x_j} \left(\frac{\partial u_i^*}{\partial x_j} + \frac{\partial u_j^*}{\partial x_i} \right) \tag{3.4}$$

The momentum equations are solved in a first step to obtain a temporary velocity field u_i^*. The velocity are then corrected by accounting for the pressure gradient and the continuity constraint.

By considering that:

$$\frac{u_i^{n+1} - u_i^{*n}}{\Delta t} + \nabla p^{n+1} = 0 \tag{3.5}$$

And taking the divergence of the momentum equation and applying the continuity equation, the following Poisson equation can be obtained:

$$\nabla^2 p^{n+1} = \frac{\nabla \cdot u_i^{*n}}{\Delta t} \tag{3.6}$$

The final velocity field is then obtained by projecting the provisional velocity field on a divergence-free space using the pressure gradient.

From equation (3.5):

$$u_i^{n+1} = u_i^{*n} - \Delta t \nabla p^{n+1} \tag{3.7}$$

Several variants of this method have been derived and used successfully over the years. Kiris *et al.* [45] include the pressure gradients into the momentum equations, using previously calculated values for the pressure. Such scheme allows for higher order solution in time. However, Guermond *et al.* [34] showed that different interpolation order for the pressure and velocity led to improved convergence rate and stability of the solution. Equal interpolation order for both pressure and velocity often led to numerical instabilities in the solutions, characterised by severe node to node oscillations. Using lower order for the pressure than for the velocity avoided those numerical oscillations.

Other pressure correction methods include the Semi-Implicit Method for Pressure Linked Equation (SIMPLE) family of methods. These methods are based on a prediction-correction cycle. The velocities are first calculated using a guessed pressure field. The velocities are then corrected to satisfy the continuity constraint. The main difference between this type of method and the projection method resides in the formulation of the pressure and velocity corrections. The pressure corrections are related to the velocity corrections through approximate forms of the momentum equations. Furthermore, only the pressure corrections are solved for using a Poisson equation. Such methods have been widely used but present the inconvenience of overestimating the pressure corrections to be applied, thus slowing down the convergence process. Very often, an under-relaxation factor is used to attenuate the pressure prediction.

3.1.2 Spatial Discretisation: the Finite Volume Method

The selection of a mathematical model constitutes the first part of a numerical method. The next step involves the choice of a suitable discretisation method, i.e. the method to approximate the differential equations. Many approaches have been used but the mainstream ones are the finite difference (FD), the finite volume (FV) and the finite element (FE) methods.

Selecting a discretisation method is somehow a matter of taste. In the context of the present research, the finite volume method was chosen as it is one of the most straight forward method to understand and implement, and it can deal with complex geometries. The finite volume method has been widely employed and is now textbook material. Detailed description of the method can be found for example in Ferziger *et al.* [29], Versteeg *et al.* [87] or Tannehill *et al.* [81]. In the next few paragraph, only a brief presentation of the method will be given.

The finite volume discretisation method uses the integral form of the conservation equations. The solution domain is decomposed into a set of contiguous control volumes (CV) of arbitrary shapes, and the equations are applied to each CV.

Continuity:

$$\int_S \mathbf{u} \cdot \mathbf{n} \mathrm{d}S = 0 \tag{3.8}$$

Momentum:

$$\frac{\partial}{\partial t} \int_V u_i \mathrm{d}V + \int_S u_i \mathbf{u} \cdot \mathbf{n} \mathrm{d}S = -\frac{1}{\rho} \int_S p \mathbf{i}_\mathrm{i} \cdot \mathbf{n} \mathrm{d}S + \int_S \left(\nu \left(\frac{\partial u_i}{\partial x_j} + \frac{\partial u_j}{\partial x_i} \right) \mathbf{i}_\mathrm{i} \right) \cdot \mathbf{n} \mathrm{d}S \tag{3.9}$$

Where V is the volume enclosed by the CV and S the surface bounding it.

The decomposition of the domain is usually carried out adopting either a structured or an unstructured strategy. In the structured decomposition, the domain is simply divided into quadrilateral (in 2D) or hexahedral (3D) elements with a straight forward connectivity. In the unstructured approach, the elements can be of a completely arbitrary shape usually triangular (2D) or tetrahedral (3D), thus facilitating the representation of complex geometries. In contrast with the structured decomposition, the unstructured grids do not possess a simple connectivity, thus making the implementation of an unstructured scheme a rather complex task. In both cases, to account for the complex geometries present in the solution domain, it is preferable to adopt boundary fitted grids. Such grids can be generated by mapping the physical space (x, y, z) into a computational space (ξ, η, ζ). The major advantage of such a boundary fitted grid is that the grid lines follow the boundary, thus enabling a straight forward implementation of the boundary conditions.

Usually, the variable values are calculated at the centre of each CV, although some schemes use the cell vertices. Interpolation is then used to compute the face variables in terms of the cell-centred values. By using suitable expressions for the surface and volume integrals, one can thus obtain an algebraic equation for each CV where the cell-centred variable is expressed in terms of the neighbouring CVs value.

Approximation of the surface integrals is usually carried out by considering the sum of the integrals over the faces of the CV. If ϕ is component of a vector in the normal direction to the CV face (e.g. $u_i \mathbf{u} \cdot \mathbf{n}$, $p\mathbf{i}_\mathrm{i} \cdot \mathbf{n}$, ...) , then:

$$\int_S \phi \mathrm{d}S = \sum_i \int_{S_i} \phi \mathrm{d}S \tag{3.10}$$

Thus, in the 2D case, for a quadrilateral CV as illustrated in figure 3.1:

$$\int_S \phi \mathrm{d}S = \int_{S_e} \phi \mathrm{d}S + \int_{S_w} \phi \mathrm{d}S + \int_{S_n} \phi \mathrm{d}S + \int_{S_s} \phi \mathrm{d}S \tag{3.11}$$

The integral can then be approximated by the product of the integrand at the face centre and the face area, giving:

$$\int_S \phi \mathrm{d}S \approx \phi_e S_e + \phi_w S_w + \phi_n S_n + \phi_s S_s \tag{3.12}$$

Since the face values are not readily available, they have to be interpolated from the cell-centred values. Linear interpolation is usually employed for that matter as it gives a second order accuracy. Other schemes giving the same order of accuracy may be used such as the upwind scheme where the value taken is that of the CV upstream of the considered CV, or Quadratic Upwind Interpolation for Convective Kinematics (QUICK) that makes use of a parabola fit.

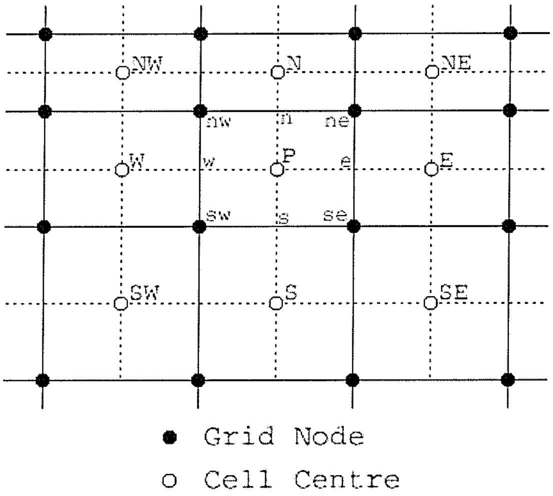

Figure 3.1: Typical Control Volume and its neighbours

Volume integrals are usually approximated by the product of the cell-centred value with the CV volume:

$$\int_V \phi \mathrm{d}V \approx \phi \Delta V \tag{3.13}$$

For CVs lying on the boundaries of the domain, special care must be taken to derive the face values as no information is available on the other side of the boundary. The boundary conditions are usually enforced by either prescribing the values or the gradient at the boundary. This results either in a explicit face value or in a face value that can be computed using the interior value and the prescribed gradient.

Summing all the approximation, an algebraic equation is obtained for each CV where the variable value for that CV is expressed in terms of the neighbouring variable values. Gathering all the equation results in a system of linear algebraic equations:

$$A\phi = Q \tag{3.14}$$

where A is the coefficient matrix, ϕ the vector of variable values at the centre of the CVs and Q the vector composed of all the terms not containing unknown variable values.

To solve such a system of equations, although direct methods such as the Gaussian elimination could be used, it is generally found that iterative methods are more efficient. The Successive Over-Relaxation method (SOR), the Conjugate Gradient (CG) and its variants (CGS, CGSTAB, GMRES) and the incomplete LU decomposition (ILU) are some of the most commonly used methods.

3.1.3 Temporal Discretisation

Since most practical problems are time-dependent, one must take into account a fourth coordinate direction: time. This implies that the time derivative present in the Navier-Stokes equations must also be discretised. Several methods can be found in the literature to carry out such a discretisation.

Considering that the equations can be reduced to the following:

$$\frac{\partial \phi}{\partial t} = f\left(\phi, t\right) \tag{3.15}$$

where f represent the components other than the time derivative one.

Then if one knows an initial condition ϕ_0, the above equation can be solved through time by advancing in time steps.

Integrating between two instants t_n and t_{n+1}, the following can be obtained:

$$\int_{t_n}^{t_{n+1}} \frac{\partial \phi}{\partial t} \mathrm{d}t = \int_{t_n}^{t_{n+1}} f\left(\phi, t\right) \mathrm{d}t \tag{3.16}$$

By using an adequate approximation, the integrals can be evaluated. The most commonly found approximation methods are the so-called Euler explicit and Euler implicit methods.

The Euler explicit method simply consists of evaluating the right hand side integral using the initial value of the integrand. Thus:

$$\phi^{n+1} = \phi^n + f\left(\phi^n, t_n\right)\Delta t \tag{3.17}$$

On the other hand, the Euler implicit method makes use of the final value of the integrand, leading to:

$$\phi^{n+1} = \phi^n + f\left(\phi^{n+1}, t_{n+1}\right)\Delta t \tag{3.18}$$

Also, by using a simple average between the initial and final values, the so-called trapezoid rule method can be define:

$$\phi^{n+1} = \phi^n + \frac{1}{2}\left[f\left(\phi^n, t_n\right) + f\left(\phi^{n+1}, t_{n+1}\right)\right]\Delta t \tag{3.19}$$

It is interesting to note that appart from the first method, all the others require the value of ϕ at a time other than t_n. These methods belong to the implicit method class. If the time step Δt is small enough, both classes of methods will produce good solutions (Ferziger *et al.* [29]). However, if Δt is larger, explicit method become unstable as smaller time scales cannot be captured.

Other methods can be used for the approximation of the time derivative such as the multipoint methods. One of the most commonly known method is the Adams-Bashford method where a Lagrangian polynomial is fitted to the derivatives at different points in time. The second order accurate version of such a method is given by:

$$\phi^{n+1} = \phi^n + \frac{\Delta t}{2}\left[3f\left(t_n, \phi^n\right) - f\left(t_{n-1}, \phi^{n-1}\right)\right] \tag{3.20}$$

The multipoint approach presents the advantage of being rather simple to implement. However, one has to be carefull when considering the initial conditions as no information is available for a previous time step. A simple explicit scheme such as the Euler one may be employed in the first few steps to account for this matter.

The choice of an explicit or an implicit method is dependent upon the problem to be tackled and is also usually a trade-off between stability, accuracy and computational cost of the solution.

Explicit methods have the major disadvantage of presenting severe constraints on the time step to be employed, particularly when using very refined grids. However, they are very simple to implement and require very few calculation.

In implicit methods, the time steps can be much larger. Thus the desired solution can be obtained in fewer steps. Although implicit methods require much more computation per time step, this can result in an overall shorter computational time. However, owing to the much larger computation per time step, the truncation error due to computer limitation can be much larger than for explicit methods. This implies that implicit methods can lead to less accurate solution than explicit methods. However, in the case of a time-independent solution where the steady state is the desired result the resultant difference is negligible.

3.1.4 Errors, Stability and Convergence

As can be seen from the previous discussion, numerical solutions are only approximate solutions. Several approximations are applied that introduce three types of errors (Ferziger *et al.* [29]):

- Modeling errors
- Discretisation errors
- Iterative errors also referred to as truncation or round-off errors

The modeling errors are related to our inability to fully represent the flow through mathematical equations. The discretisation errors come from the approximation of the differential equation. The iterative or truncation errors are due to the computational representation of numbers. The latter are also called round-off errors.

If we define $\mathcal{R}$ as the real flow, $\mathcal{A}$, the analytical solution of the model equation, $\mathcal{D}$, the exact solution of the discretised equation and $\mathcal{N}$, the numerical solution of the discretised equation, then the various errors can be described as follows:

$$\begin{aligned} \text{Modeling error:} \quad & \epsilon_{\mathcal{M}} = \mathcal{R} - \mathcal{A} \\ \text{Discretisation error:} \quad & \epsilon_{\mathcal{D}} = \mathcal{A} - \mathcal{D} \\ \text{Iterative error:} \quad & \epsilon_{\mathcal{I}} = \mathcal{D} - \mathcal{N} \end{aligned} \tag{3.21}$$

These errors can be used to assess the properties of a particular method. The stability criterion previously mentioned relates to the iterative or truncation error. In fact, a method will be stable if $\epsilon_{\mathcal{I}}$ tends to zero or at best stays constant as the iteration progress. If this error grows, then the solution is unstable.

Also, the method will be convergent if $\epsilon_{\mathcal{D}}$reduces to zero as the grid spacing and time step are decreased.

However, convergence often refers to the error reduction in the iterative solution ($\epsilon_{\mathcal{I}}$). It is thus important to differentiate the convergence of the numerical solution to the exact solution and the iterative convergence. In the latter case, the iterative error is used as a criterion to stop the computation. Assessing the convergence to the exact solution is not a trivial case and is usually achieved by performing grid dependency tests. The solution is carried out on grids, the refinement of which is progressively increased, until the solution is not improved by further refinement.

3.2 Turbulence Modelling

The choices for a method to solve a problem using CFD techniques are often bound to the computational capabilities. It becomes all too obvious when looking at turbulence modelling. In the following section, the major turbulence modelling techniques will be discussed. A brief outline of the methods will be presented followed by a discussion to assess their suitability for the present investigations not only in terms of results produced but also in terms of computational efficiency and adequacy

Most of practical engineering flows are turbulent and thus possess various properties such as the highly unsteady nature, the three-dimensionality, the important vorticity, the diffusive behaviour or the fluctuation on a broad range of lengths and time scales of the flow (Ferziger *et al.* [29]). It is generally accepted that the most common fluids encountered in engineering, air and water, can be described by the Navier-Stokes equations. Furthermore, these equations not only describe adequately the laminar flows, but also the turbulent flows. Although the numerical solution of laminar flows does not present any real difficulty, the computation of turbulent flows on the other hand can be a real challenge. This is essentially due to the non-linearities in the Navier-Stokes equations, giving rise to a broad range of spatial and temporal turbulent scales, the larger scales being related for the major part to the turbulent diffusion, and the smaller scales, related to the turbulent dissipation (Deng *et al.* [35]). A simulation which is to produce meaningful results has to cover suitably both the diffusive and dissipative effects.

A complete solution of all the scales using the so-called Direct Numerical Simulation (DNS) would satisfy the requirements. Such a solution, however, requires a number of grid points highly dependent upon the Reynolds number and thus is currently restricted to simple flows at low Reynolds numbers. A more suitable solution consists of simulating the larger scales while modelling the smaller ones. One such method, known as the Large Eddy Simulation (LES), reduces the Reynolds number restrictions of the DNS by directly simulating the large scales and modelling the small scale by means of subgrid models. A further simplification of the problem of resolving turbulent flows consists of modelling the entire flow by suitably averaging both the mean and turbulent motions. Such a procedure, known as the Reynolds averaging, consists of the solution of the so-called Reynolds-Averaged Navier-Stokes (RANS) equations for the mean motions coupled with a closure scheme to model the turbulent Reynolds stresses (Deng *et al.* [32]). This procedure has been and is still widely used in engineering problems.

3.2.1 Reynolds-Averaged Navier-Stokes Equations

The formulation of the RANS equations and the closure schemes have been presented in textbooks by various authors such as Hirsch [38], Ferziger *et al.* [29], Deng *et al.* [32], Versteeg *et al.* [87] or Deschamps [25] among others and will only be outlined here.

The Reynolds averaging procedure consists of the decomposition of any flow variable into a time averaged value and a fluctuation about that value:

$$\phi\left(\mathrm{x},t\right)=\overline{\phi}\left(\mathrm{x}\right)+\phi'\left(\mathrm{x},t\right) \tag{3.22}$$

Where:

$$\overline{\phi}\left(\mathrm{x}\right)=\lim_{T\to\infty}\frac{1}{T}\int_{0}^{T}\phi\left(\mathrm{x},t\right)\mathrm{d}t \tag{3.23}$$

With t, the time, and T the averaging interval.

In the case where the flow is unsteady, a separation of the time scales must be assumed, i.e. the averaging time interval T must be at most equal to the time scale for the mean flow t. This results in a constraint on the time step used to resolve the time-dependent flow. In practice, this is rarely achieved.

Applying the above decomposition to the continuity and momentum equations in the case of incompressible flows, gives, in tensor notation:

$$\frac{\partial\overline{u_i}}{\partial x_i}=0 \tag{3.24}$$

$$\frac{\partial\overline{u_i}}{\partial t}+\frac{\partial\left(\overline{u_i}\,\overline{u_j}\right)}{\partial x_j}=-\frac{1}{\rho}\frac{\partial\overline{p}}{\partial x_i}+\frac{\mu}{\rho}\frac{\partial}{\partial x_j}\left(\frac{\partial\overline{u_i}}{\partial x_j}+\frac{\partial\overline{u_j}}{\partial x_i}\right)-\frac{\partial\left(\tau_{ij}\right)}{\partial x_j} \tag{3.25}$$

Where τ_{ij}, the Reynolds stress tensor, is:

$$\tau_{ij}=\overline{u_i'u_j'} \tag{3.26}$$

Since the fluctuations are unknown, the Reynolds stress tensor τ_{ij} cannot be found explicitely. The above system of equations is thus not closed. Various closure schemes have been developed and used over the years, including simple zero-equation or one-equation systems, or more complex models such as the Reynolds Stress Equations (RSE), or two-equations models like the $k - \epsilon$ or the $k - \omega$ models (Wilcox [89], Zheng *et al.* [103, 102]).

3.2.2 Large Eddy Simulation Models

The RANS models as seen above, model all scales of turbulence, and thus make it unlikely for such models to represent all turbulent flows due to the complexity of turbulence. Furthermore, the time averaging procedure imposes a restriction on the time step used to resolve all the time scale of the flow. In turbulent flows, the transport of the conserved properties is essentially provided by the large scale motions, the small scale motions being far less effective. It appears thus obvious that a method that simulates the large eddies more accurately than the small ones would provide more sensible results. By filtering out the small scale motions, LES simulates exactly the large scales while modelling at the so-called subgrid scales. As was shown by Murakami *et al* [64], although LES calculations are more CPU intensive, they presented better agreement with experimental results than RANS models such as RSE or $k - \epsilon$ models.

The filtering process of the Navier-Stokes equations appears somewhat similar to that in the averaging procedure of the RANS. The major difference resides in the fact that in the LES method, the filtering procedure is of a spatial nature rather than a temporal one. The decomposition of the flow variables separates the filtered part, i.e. the part corresponding to the large scale motions, and the subgrid part accounting for the smaller scale motions.

$$\phi\left(\mathrm{x}, t\right) = \overline{\phi}\left(\mathrm{x}, t\right) + \phi'\left(\mathrm{x}, t\right) \tag{3.27}$$

Where:

$$\overline{\phi}\left(\mathrm{x}, t\right) = \oint_D \left[\prod G\left(\mathrm{x}, \mathrm{x}'\right)\right] \phi\left(\mathrm{x}', t\right) \mathrm{d}\mathrm{x}' \tag{3.28}$$

Where D is the domain and G the filter kernel. The most common definition of the filter kernel is the volume filter:

$$G_j\left(x_j - x_j'\right) = \begin{cases} 1/\Delta_j & \text{if } \left|x_j - x_j'\right| \leq \Delta_j/2 \\ 0 & \text{otherwise} \end{cases} \tag{3.29}$$

Where Δ_j is the control volume spacing in the j^{th} direction
Giving:

Page 28
missing

Assuming that the SGS turbulence is locally in a state of equilibrium between production and dissipation, Smagorinsky [76] derived the following expression for the eddy viscosity:

$$\nu_t = C_S^2 \Delta \left|\overline{S}\right| \qquad \text{with} \qquad \left|\overline{S}\right| = \sqrt{2\overline{S}_{kl}\,\overline{S}_{kl}} \tag{3.38}$$

Where Δ is the filter width, usually taken as an average of the local mesh sizes, and C_S is a non-dimensional constant commonly called Smagorinsky constant. Theoretically, the Smagorinsky constant is equal to about 0.17, but in practice, the optimum values for C_S range from 0.07 to 0.24 depending on the flow considered (Deng *et al.* [35]).

The inability to represent the variety of phenomena present in turbulent flows with a single universal constant led Germano *et al* [33] to develop a dynamic subgrid scale model where the Smagorinsky constant C_S is calculated dynamically. Such a procedure, modified by Lilly [52], has been presented in the literature whether in cartesian or in curvilinear form (Jordan *et al.* [41], Yang *et al.* [97]). Other variants of the dynamic subgrid-scale model have been developed such as the Dynamic Mixed Model (Péneau *et al.* [67]) but its validity still has to be shown.

Another approach to modelling the subgrid-scales, based on statistical turbulence, is the structure function model developed by Métais and Lesieur [59]. In this method, the eddy-viscosity is evaluated as follows:

$$\nu_t\left(\vec{x}, \Delta, t\right) = 0.063\Delta\sqrt{\overline{F}_2\left(\vec{x}, \Delta, t\right)} \tag{3.39}$$

Where Δ is the mean mesh size, and $\overline{F}_2$ is the second order structure function of the resolved velocity field for a radius Δ:

$$\overline{F}_2\left(\vec{x}, \Delta, t\right) = \left\langle \left\|\overline{u}\left(\mathrm{x}+\mathrm{r}, t\right) - \overline{u}\left(\mathrm{x}, t\right)\right\|^2 \right\rangle_{\|\vec{r}\|=\Delta} \tag{3.40}$$

A further development of the structure function model is the selective structure function model that switches off the eddy viscosity when the flow is not sufficiently three-dimensional. The three-dimensionality of the flow is assessed from the angle β between the local vorticity vector and the average vorticity vector evaluated over the neighboring points. The formulation of the eddy-viscosity is thus as follows:

$$\nu_t\left(\vec{x}, \Delta, t\right) = 0.098\gamma\Delta\sqrt{\overline{F}_2\left(\vec{x}, \Delta, t\right)} \tag{3.41}$$

Where γ is the selective parameter. Lesieur and Métais recommended a threshold value of 20^o for the angle β. Rather than using an abrupt on-off switch, a smoothly varying function is often used such as:

$$\gamma = \begin{cases} 0 & \text{for } \beta < 20^o \\ e^{-(d\beta/3)^2} & \text{for } 20^o \geq \beta \geq 10^o \text{ and } \mathrm{d}\beta = |\beta - 20| \\ 1 & \text{for } \beta > 20^o \end{cases} \tag{3.42}$$

Suksangpanomrung *et al* [79] compared the structure function model, the selective structure function model and the Smagorinsky eddy viscosity model for the case of separated flow over a bluff rectangle plate for Reynolds number of 50,000. In the case of the selective structure function model, both the mean flow and turbulence statistic obtained were in good agreement with experimental data. The Smagorinsky model yielded a mean reattachment length in good agreement with the experiments but the turbulence statistics and the dynamics of the flow were deficient. Both the Smagorinsky model and the structure function models delayed the break-up and three-dimensionalisation of the separated shear layer.

In the particular case of flow past a cylinder, whether two or three dimensional, numerous investigations using LES have been carried out. Lu et al [54] used a Smagorinsky Eddy viscosity model and showed the good agreement between LES and experimental results for such flow problems. Dalton [21] further emphasised the validity of LES for flow past cylinder by showing the very accurate predictions of drag, lift and inertia coefficients at Reynolds number of the order of 10^4. Jordan *et al* [41] investigated the formation and transport of Strouhal vortices in the near wake of circular cylinder and concluded that LES gave accurate prediction of the base pressure coefficient directly behind the cylinder, thus adequately simulating the fundamental Strouhal vortices characteristics. Murakami *et al* [64] showed how the lock-in phenomena was well reproduced by three-dimensional LES computations while two-dimensional computations could not produce accurate results. However, Bouris *et al* [9] showed that two-dimensional LES computations should not be dismissed for quasi two-dimensional flows, the only requirements being satisfactory grid refinements. Breuer [10] investigated the impact of three dimensionality for LES computations and the discretisation schemes, comparing various subgrid-scale models for the flow past circular cylinder. High Reynolds numbers simulation around circular cylinder were carried out by Breuer [11], that showed that grid refinement did not automatically lead to improved results for all quantities. He also reached the conclusion that although the dynamic subgrid-scale model gave very satisfying results, its superiority over Smagorinsky's eddy viscosity model could not be proven.

3.3 Force and Structural Motion Description

In the recent years, as the methods to solve fluid dynamic problems matured, the complexity of problems tackled has increased. One of the most interesting aspects *which is the subject of numerous studies is that of the coupled fluid-structure interaction where the motion of one or more objects in the flow is taken into account. Such motions of objects imply the determination of both the forces acting on the objects and the resulting displacements. In the following section, a brief presentation of the method used to determine the fluid forces acting on an object will be given followed by a description of the structural model used to calculate the motion.*

3.3.1 Force Description

By definition, the force acting on a body can be expressed as follow:

$$\mathbf{F} = \mathbf{F_p} + \mathbf{F_v} = -\int_S (p\mathrm{n} + \mathbf{\Sigma} \cdot \mathbf{n})\,\mathrm{d}S \tag{3.43}$$

Where $\mathbf{F_p}$ and $\mathbf{F_v}$ are the contributions of the pressure force and the viscous force respectively, p is the pressure, $\mathbf{\Sigma}$ the viscous stress tensor, and S is the surface of the body.

Another form of the above equation making use of the vorticity ω is:

$$\mathbf{F} = \mathbf{F_p} + \mathbf{F_v} = -\int_S (p\mathrm{n} + \mu\mathrm{n} \times \omega)\,\mathrm{d}S \tag{3.44}$$

Both formulations are widely used. Given the velocity field, the contribution of the viscous force can be determined in a straight forward manner. The accuracy will only depend on the resolution of the mesh in the proximity of the object. On the other hand, the pressure not being a local variable, i.e. the pressure at a point depends on the velocity and vorticity in the whole domain, the determination of the contribution of the pressure force can be difficult.

To overcome the difficulties associated with the determination of the contribution of the pressure force, alternative approaches such as the vorticity impulse have been sought, eliminating the pressure information. The major inconvenience of this method is that the vorticity in the near and far wake contribute equally to the hydrodynamic force (Protas *et al.* [70]). Using a control volume approach as a starting point, Noca *et al* [65] modified the approach by considering the momentum balance in a finite control volume surrounding the body. However, although the method seems advantageous as it does not require any pressure or shear stress information, the results do not differ significantly with those obtained using the classical pressure-shear stress formulation.

3.3.2 Structural Motion Description

Having obtained the hydrodynamic force acting on the object, the resultant motion of the object must be determined. In the case of the flow around a circular cylinder, as for most objects, it is generally assumed that the system is equivalent to a mass-spring-damping system. The equation of dynamic equilibrium for such a system can be expressed as:

$$m\frac{\partial^2 \mathbf{x}}{\partial t^2} + c\frac{\partial \mathbf{x}}{\partial t} + k\mathbf{x} = \mathbf{F} \tag{3.45}$$

Where m is the mass of the cylinder, c is the damping coefficient, k is the spring stiffness, $\mathbf{F}$ is the fluid force acting on the cylinder and $\mathbf{x}$ the resultant displacement of the cylinder.

Using the following non-dimensional parameter:

$$\mathbf{x}^* = \frac{\mathbf{x}}{D}\ ;\ t^* = \frac{tU_\infty}{D}\ ;\ \zeta = \frac{c}{2\sqrt{km}}\ ;\ U^* = \frac{U_\infty}{f_n D}\ ;\ \mathbf{C_F} = \frac{2\mathbf{F}}{\rho U_\infty^2 D}\ ;\ m^* = \frac{m}{\rho D^2}\ ; \tag{3.46}$$

Where x^* is the non-dimensional displacement, t^* is the non-dimensional time, ζ is the damping ratio, U^* is the velocity ratio also referred to as the reduced velocity, $\mathbf{C_F}$ is the force coefficient and m^* is the mass ratio
then equation (3.45) is equivalent to:

$$\frac{\partial^2 \mathbf{x}^*}{\partial t^{*2}} + \left(\frac{4\pi\zeta}{U^*}\right)\frac{\partial \mathbf{x}^*}{\partial t^*} + \left(\frac{2\pi}{U^*}\right)^2 \mathbf{x}^* = \frac{\mathbf{C_F}}{2m^*} \tag{3.47}$$

Furthermore, if one considers the frequency ratio defined by $f^* = \frac{f_n}{f_s}$ where f_n is the natural frequency of the cylinder and f_s is the vortex-shedding frequency, then equation (3.47) can be written as:

$$\frac{\partial^2 \mathbf{x}^*}{\partial t^{*2}} + \left(4\pi\zeta S_t f^*\right)\frac{\partial \mathbf{x}^*}{\partial t^*} + \left(2\pi S_t f^*\right)^2 \mathbf{x}^* = \frac{\mathbf{C_F}}{2m^*} \tag{3.48}$$

Where S_t is the Strouhal number defined by:

$$S_t = \frac{f_s D}{U_\infty} = \frac{f_s}{f_n}\frac{f_n D}{U_\infty} = \frac{U^*}{f^*} \tag{3.49}$$

The last two description of the dynamic equilibrium of the system are commonly found in the literature. Mittal *et al* [62] used a form similar to that in equation (3.48) where the non-dimensionalisation of the displacement is carried out using the cylinder radius as opposed to the diameter. The resulting equation of motion thus appears different but is strictly equivalent to the ones presented above. The only difference lies in the expression used for the various ratios such as the mass ratio or the velocity ratio that they define as the reduced natural frequency.

It was found that the flow-induced vibration of a structure is a self-limiting process and the amplitude of the vibration could be correlated with a parameter known as the Skop-Griffin parameter (Khalak *et al.* [43, 44]):

$$S_g = 2\pi^3 S_t^2 \left(m^* \zeta\right) \tag{3.50}$$

For that reason, Zhou *et al* [104] used the second formulation (equation (3.48)) as it present the advantage of a better control over the frequency ratio f^* and thus provide a simple mean to achieve a desired S_g.

For a given mass, damping and frequency ratio, and a given S_g, one can simply deduce the Strouhal number. The solution of the equation of dynamic equilibrium of the system is then carried out numerically using methods such as the Runge-Kutta method.

3.4 Moving Grid Method

Once the forces acting on an object and the resulting displacement of that object have been calculated, the motion of the computational mesh representing the solution domain must be determined. Several methods have been used for such purposes which will be reviewed in the following sections.

When attempting to solve numerically the flow around an object, much effort is put into the generation of a mesh representing the domain with a quality enabling the accurate capture of the flow phenomenon. Mesh generation has been the subject of intense investigations and has always been a computationally expensive process. It seems thus quite clear that if one was to re-generate a complete mesh when displacing an object in the solution domain, such a process would increase tremendously the overall computational cost of the solution. For such a reason, the process of deforming the mesh must not be a complete re-generation, but rather a modification of the current mesh. Also, the process must be completely independent of the method used to create the initial grid. This defines the concept of the so-called dynamic mesh.

3.4.1 Algebraic Methods

Several methods can be considered to carry out such a modification. Schulz *et al* [75] use a simple algebraic method to deform the mesh based on a distance function from the moving objects. To preserve the local quality of the mesh in the neighbourhood of the objects, the displacement of the mesh vertices surrounding an object is matched with the displacement of the object itself. The displacement of the remaining mesh vertices are then linearly reduced based on the distance away from the structure such that the domain boundaries remain unchanged. In the case of multiple structures present in the field, the contribution of the motion of each structure is taken into account by super-imposing the displacement of the vertex according to the motion of each individual structure.

$$\Delta\vec{r}_{\text{vertex}} = \sum_{i=1}^{\text{num. bodies}} (d_i)\,(\Delta\vec{r}_{\text{body}})_i \tag{3.51}$$

where $\Delta\vec{r}$ is the displacement vector and d_i is the distance function for the body i ,normalised so that it ranges from 0 on the domain boundaries to 1 on the body surface.

An illustration of the motion of a mesh vertex in the presence of two bodies is shown in figure 3.2

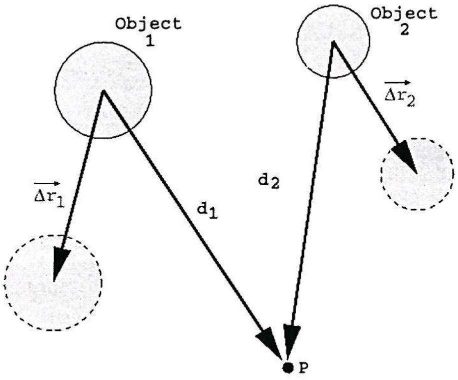

Figure 3.2: Example of tandem cylinder geometry

An attractive quality of such a method resides in the fact it preserves the quality of the grid in the immediate surrounding of the objects and provides for multiple objects configurations. Furthermore, its implementation is straight forward and the added computational cost small. However, the overall grid quality cannot be guaranteed by such a method.

3.4.2 Iterative Methods - The Linear Spring Analogy

A popular method for the creation of dynamic meshes that provides a solution for the preservation of the quality of the whole grid is the so-called lineal spring analogy (LSA) method. The edges of the mesh are assimilated with a network of lineal springs whose stiffnesses are inversely proportional to the length of the supporting edge. The system is thus in equilibrium if for all the mesh vertices:

$$\sum_{i=1}^{\text{num. edges}} k_i \Delta l_i = 0 \tag{3.52}$$

Where k_i is the stiffness of the spring supported by the i^{th} edge and Δl_i is the expansion of the spring from its resting state.

i.e.:

$$\sum_{i=1}^{\text{num. edges}} k_i (\Delta \vec{r}_{\text{vertex}} - \Delta \vec{r}_i) = 0 \tag{3.53}$$

Where $\Delta \vec{r}_{vertex}$ corresponds to the displacement of the vertex considered and $\Delta \vec{r}_i$ corresponds to the displacement of the other vertex composing the edge i.

To solve the above system of equations, iterative methods are employed such as the Jacobi or the Successive Over Relaxation (SOR) methods. An immediate consequence is that at each time step of the solution, a large number of computation must be carried out to update the mesh, thus adding substantial time to the computation of the solution. However, in the case of small displacements of the bodies present in the domain, very few iterations are required to deform the mesh.

Furthermore, a major advantage of the method lies in the preservation of the quality of the mesh. As the stiffness of the springs is inversely proportional to the length of the supporting edge, small edges found in region of high level of refinement are extremely stiff. Thus very little deformation of these regions occurs. On the other hand, regions where the mesh refinement is not so important, and thus where the mesh edges are not so small, higher deformation occur. Another advantage of the method resides in the fact that as two vertices tend to get closer, the spring supported by the edge joining these vertices gets stiffer and thus prevent them from colliding. However, in the case of larger deformations, overlapping of mesh elements may occur, thus making the method inadequate for a lot of practical engineering problems.

The major deficiency of the lineal spring analogy method is that the stiffness of the springs do not take into account the mesh elements area or angles, leading to possible crossover of mesh elements. To overcome this problem, the notion of torsional springs was introduced and is now widely used to generate dynamic meshes (Farhat *et al.* [28], Degand *et al.* [23]. Further torsional springs are attached to each vertex whose stiffnesses are functions of the length of the edges connected to the vertex and the area of the grid elements connected at the vertex.

This method, although it prevents the crossover of grid lines and preserves the overall mesh quality is however rather complex and computationally costly.

3.4.3 Hybrid Methods - Transfinite Interpolation and Lineal Spring Analogy

An alternative to the solution of a large system of equations involves the transfinite interpolation (TFI) of the grid point displacements. Such a technique, based on an algebraic method of grid generation, can be seen as a perturbation method rather than a complete re-generation. Dubuc *et al.* [27], Liu *et al.* [53] and Wong *et al.* [94] used a combined TFI and spring analogy approach on a multi-block configuration.

The process is decomposed in two major stages according to the method employed:

First, the spring analogy is applied to a high level grid formed by the corners of the blocks. If A and B are two corners forming an edge of a block, them $\Delta\vec{r}_A$ and $\Delta\vec{r}_B$ are obtained by solving the linear system of equations as described previously.

Then, the TFI of the grid point displacements is applied to the edges, faces and interior vertices of each blocks.

Considering a two-dimensional case, the edges and faces of the blocks are the same, thus if P is a vertex on the edge formed by A and B, its displacement is updated using:

$$\Delta\vec{r}_P = \left(1 - \frac{a}{c}\right) d\vec{r}_A + \left(1 - \frac{b}{c}\right) d\vec{r}_B \tag{3.54}$$

Where a, b and c are distances calculated from the initial points coordinates as $a = \left\|\vec{AP}\right\|$, $b = \left\|\vec{BP}\right\|$ and $c = \left\|\vec{AB}\right\|$.

The displacement of the interior vertices is obtained from:

$$\Delta\vec{r}(\xi,\eta) = f_1(\xi,\eta) + \phi_1^0(\eta)\left[d\vec{r}_{b1}(\xi) - f_1(\xi,0)\right] + \phi_2^0(\eta) + \left[d\vec{r}_{b3}(\xi) - f_1(\xi,1)\right] \tag{3.55}$$

Where:

$$f_1(\xi,\eta) = \psi_1^0(\xi)\, d\vec{r}_{b4}(\eta) + \psi_2^0(\xi)\, d\vec{r}_{b2}(\eta) \tag{3.56}$$

Also, $d\vec{r}_{b1}$, $d\vec{r}_{b2}$, $d\vec{r}_{b3}$ and $d\vec{r}_{b4}$ are the interpolated displacements along the four block faces.

ϕ and ψ are blending functions in the ξ and η direction respectively defined by:

$$\begin{aligned}
\phi_1^0(\eta) &= 1 - s_1(\xi) \\
\phi_2^0(\eta) &= s_3(\xi) \\
\psi_1^0(\xi) &= 1 - s_4(\eta) \\
\psi_2^0(\xi) &= s_2(\eta)
\end{aligned}$$

s_1, s_2, s_3 and s_4 are stretching functions defined simply by:

$$s_1(\xi) = \frac{\text{length from } A \text{ to } \vec{r}(\xi, 0)}{\text{length of curve from } A \text{ to } B} \tag{3.57}$$

$$s_2(\eta) = \frac{\text{length from } B \text{ to } \vec{r}(1, \eta)}{\text{length of curve from } B \text{ to } C} \tag{3.58}$$

$$s_3(\xi) = \frac{\text{length from } D \text{ to } \vec{r}(\xi, 1)}{\text{length of curve from } D \text{ to } C} \tag{3.59}$$

$$s_4(\xi) = \frac{\text{length from } A \text{ to } \vec{r}(0, \eta)}{\text{length of curve from } A \text{ to } D} \tag{3.60}$$

Finally, the coordinates of the displaced points are updates using:

$$\vec{r}(\xi, \eta) = \vec{r}_0(\xi, \eta) + d\vec{r}(\xi, \eta) \tag{3.61}$$

Figure 3.3 illustrates the mesh deformation process.

This method guarantees the matching of the displacements of the block faces of two adjacent blocks. Furthermore, the large amplitude motions that were problematic in the case of the lineal spring analogy can be studied without the risk of cross-over cells.

3.5 Parallel Computation Methods in CFD

One of the greatest limitations of numerical computations remains the available computing capabilities. The main difficulty encountered is related to both the size of the problem and its type. The size of the problem is accounted for by the memory of the computational unit (essentially Cache memory and Random Access

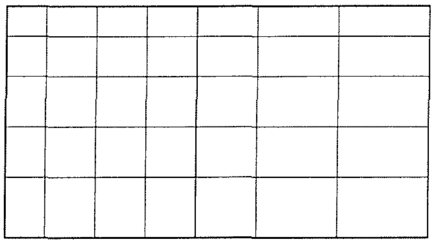

Original grid

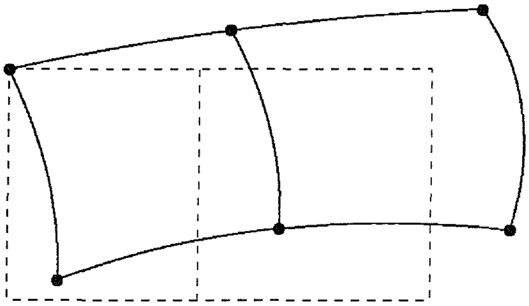

Displacement of block corners using the spring analogy method

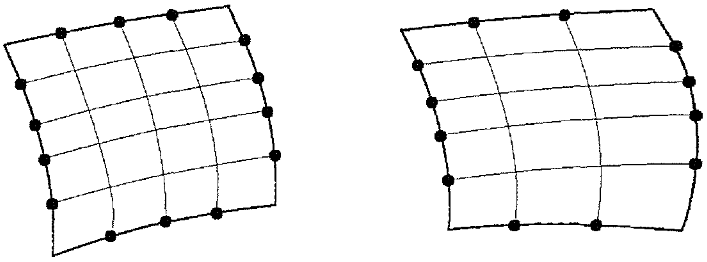

Displacement of block faces using the TFI method

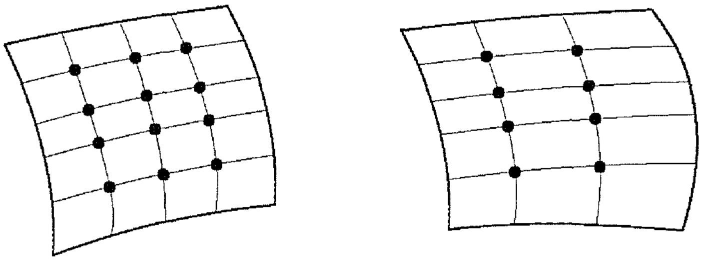

Displacement of block interior vertices using the TFI method

Figure 3.3: Combined Spring Analogy and TFI method on multi-block mesh

Memory or RAM). Depending on the type of problem tackled (transient or turbulent flows ...), the size of the problem will also have an impact on the processing time. It is thus clear that as the complexity of the problems solved increases, the amount of memory and the processing power become critical. A solution to this issue lies in what is called parallel computation.

In the following sections, the different parallel computer systems will be presented and the parallelisation strategies for the solution discussed.

3.5.1 Parallel Computer Systems

Parallel computations can be performed on three types of computer architectures:

- vector computers that make the best use of vector calculations for matrix operations,
- shared memory computers that possess a common memory area between several processors,
- and the distributed computers where each computer node possesses its own processor and local memory.

The first type of architecture presents the inconvenience to require specific algorithm adaptation and also is not scalable.

The second type possesses the great advantage of not requiring special care for the data exchange processes. However, the complexity of such machines due to the control over the access to the global memory limits their potential.

The third type, although requiring great care as far as the data exchange is concerned, offers the best compromise as its scalability allows more complex problems to be tackled.

Furthermore, the first two types of computer architectures, namely the supercomputers, are extremely costly and restricted in their availability. On the other hand, the third type of architecture can be achieved by simply networking several standard workstations into a computer cluster. With the recent slow down in the growth in processor speed, such a system can be built at a much more viable cost and present a real alternative to supercomputers.

3.5.2 Parallel Computation Strategies

Parallelising the computation on a distributed system consists of breaking up the solution process so that the complete solution is distributed among several processing units. Individual processing unit will thus treat part of the solution. Since all the parts of the solution are closely related and cannot be treated independently, the different processes must communicate during the solution procedure thus linking the various parts of the solution.

Winkelmann *et al.* [93] suggested that the parallelisation of an algorithm on a distributed system can generally be performed in three different ways: at the loop level, at the task level, i.e. functional decomposition, or at the data level, i.e. the domain over which the solution is carried out is distributed.

When performed at the loop or at the task level, i.e. task parallelism the speed of execution depends on the least efficient part of the code. It is thus necessary to minimise the non-parallel part of the code in order to achieve maximum efficiency.

An alternative way that is more suited to CFD problems and thus has been widely adopted (Garbey *et al.* [31], di-Serafino [26], Lanteri [48], Moitra *et al.* [63], Vatsa *et al.* [86], Akay *et al.* [1], Carré *et al.* [14]) is achieved by performing a domain decomposition, i.e. data parallelism. In a convenient manner, the solution domain is divided into sub-domains, each being assigned to a processing unit. If the decomposition is of a spatial nature, then it is similar to block structuring of grids. As most of the complex geometries are represented using multiple blocks, the natural partitioning of the domain can be used. To maximise efficiency, it is important that each processing unit is given the same amount of work to do so that the waiting time (time during which one or more processing unit are idle) is reduced. The load balancing is then achieved by dividing the solution domain into sub-domains of similar sizes (mesh size). Each sub-domain is assigned to one processor but more than one grid block may be handled by one processor.

The same code runs on each node of the cluster with its own set of data. This correspond to the Single Program Multiple Data (SPMD) programming paradigm. Since each processor requires data residing in other sub-domains, exchange of data between processors is required. Furthermore, since there is no mechanism for any process to directly access the memory of another, the sharing of the data between processes must take place by explicitly sending and receiving data. Specific communication tools for the data exchange process such as the Message Passing Interface libraries (MPI) provide a useful set of routines for that purpose.

Parallelism is thus achieved by combining the partitioning of the domain and the interfacing of the various processes.

3.5.3 Domain Partition and Message Passing Model

Interfacing the various sub-domains constitutes one of the most important part of the parallel process. Two distinct aspects have to be taken into consideration, one being the partitioning of the data on the various sub-domains, and the other being the communication of the information from one sub-domain to its neighbours.

Domain Partitioning

In his study on parallel solutions of compressible flows, Lanteri [48] identifies two different strategies for the partitioning of data, namely using overlapping and non-overlapping mesh partitioning.

In the overlapping mesh partitioning strategy, a layer of cells surrounding each blocks is introduced, the ghost cells, and used to store the information from neighbouring blocks. At appropriate times during the numerical solution, the information in these cells is updated. The major advantage of this method is that the communication between processes is minimal. However, according to Lanteri, such a method results in redundant floating point operations.

In the second case, i.e. the non-overlapping mesh partitioning strategy, a sub-domain will not contain any information from the neighbouring sub-domain. The information required for the computation are directly exchanged when required. This results in fewer floating point operations than for the previous method but implies a much larger communication cost.

Overlapping mesh partitioning is probably the most widely used strategy. Its implementation is straight forward and the resulting additional computation have little impact on the overall cost of the solution in comparison with the communication cost incurred by the non-overlapping mesh method.

Message Passing Model

Having discussed the partitioning strategies, one must consider the message passing model. Most implementation to date make use of the Message Passing Interface (MPI) as it is intended as a standard implementation of the message passing model of parallel computation.

The basic concept of MPI is the transfer of data between a pair of processes, one sending and the other receiving. This is generally called the point-to-point communication. Most send and receive functions provided by MPI are based on this type of communication. Other type of functions available involve collective communication whereby information is sent to or gathered from all the processes.

The default communication modes are so called "blocking" modes, i.e. both the sender and the receiver do not proceed further until the communication has completed. One inconvenience of this type of calls is that it can lead to deadlock situations where two processes try to send data to each other at the same time without any matching receiving calls.

MPI provides another type of communication mode: the non-blocking mode, allowing one process to carry on with its task although the communication has not yet completed. One process thus becomes a "communication" server, initiating the exchange while proceeding onto other tasks, and the "client" process execute the exchange when required.

Winkelmann *et al.* [93] defined two basic strategy adopted for the update of the ghost cells data:

- The Blocking Send, Non-blocking Receive (BSNR) strategy illustrated by the algorithm 3.1 where the code sets up non blocking receives for all incoming messages, then looping over all blocks, a message is sent to each neighbouring blocks.
- The Non-blocking Send, Blocking Receive (NSBR) strategy illustrated by the algorithm 3.2 where a single loop over all blocks is used and messages are sent as soon as the information is ready. Then for each neighbouring block, a blocking receive is posted.

Algorithm 3.1: Blocking Send Non-Blocking Receive Strategy

```
1. Loop over all blocks:
    • Exchange ghost cells information
2. Loop over iteration:
    • Solve the equations on the local domain
3. Loop over all blocks:
    • Exchange ghost cells information
4. Store the solution
```

In the BSNR method, since the communication and computation are separated, all communication will occur at the same time. This could result in a very slow solution in the case of a slow networking system. In contrast, the NBSR method spreads communication traffic in time. Furthermore, in the case of the NSBR method, no deadlock can occur.

Algorithm 3.2: Non-Blocking Send Blocking Receive Strategy

```
1. Loop over all blocks:
     • Send ghost cells information
2. Loop over iteration:
     (a) Receive ghost cells information (blocking)
     (b) Solve the equations on the local domain
     (c) Send ghost cells information (non-blocking)
3. Loop over all blocks:
     • Receive ghost cells information
4. Store the solution
```

3.6 Summary

The review carried out in this chapter leads to the following conclusions for the method to be used in the present research:

Mathematical Model:

- The flow will be modelled by the incompressible form of the Navier-Stokes equations. The equations will be filtered for the LES turbulence model. To enforce the continuity constraint and thus solve the incompressibility of the flow, the projection method will be used.
- To account for complex geometries, a boundary fitted coordinates (BFC) system will be adopted.
- The Force calculation will be based on the integration around the object of the pressure and shear stress contributions.
- The Structural motion will be derived from a simple mass-spring-damping system.

Numerical Method:

- The flow governing equations will be discretised using the finite volume method.
- To compute the structural displacement of the object, the Runge-Kutta method will be used.

- The mesh deformation will be carried out using a hybrid TFI / spring analogy method.

Numerical Implementation:

- The method will be parallelised to carry out the computation on a computer cluster, thus enabling the large size problem to be solved. The parallel implementation will be based on the Single Program Multiple Data (SPMD) model with a domain decomposition using overlapping blocks. The parallel interface will use the MPI message passing model.

Chapter 4

Flow Solver: The Projection Method

4.1 Mathematical Model

As previously discussed, a numerical solution is composed of several components. The first and most critical one is the mathematical formulation of the problem. For the purpose of the present work, the incompressible Navier-Stokes equations expressed in body fitted coordinates (i.e. curvilinear coordinates) and filtered for the large eddy simulation turbulence model are the most suited.

Since the filtering and coordinate transformation processes are lengthy, only the final form of the equations are presented below. The details of the derivation can be found in appendix A and B.

The flow governing equations can thus be written in a non-dimensional form as follows, using the Einstein notation:

Continuity:

$$\frac{\partial\left(J\overline{U^i}\right)}{\partial\xi_i} = 0 \tag{4.1}$$

Momentum:

$$\begin{aligned}\frac{\partial}{\partial t}\left(J\overline{u}_i^*\right) + \frac{\partial}{\partial\xi_k}\left(\overline{U_r}^{*k}\overline{u}_i^*\right) &= -J^{-1}S_i^j\frac{\partial\overline{q}}{\partial\xi_j} + \\ &+ \frac{\partial}{\partial\xi_k}\left[\left(\frac{1}{Re}+\frac{1}{Re_t}\right)\left(J^{-1}S_j^kS_j^l\frac{\partial\overline{u}_i^*}{\partial\xi_l}\right)\right]\end{aligned} \tag{4.2}$$

Where J is the Jacobian of the coordinate transformation:

$$J = \frac{D(x, y, z)}{D(\xi, \eta, \zeta)} \tag{4.3}$$

$\overline{U^j}$ is the filtered contravariant component of velocity:

$$\overline{U^j} = S_i^j \overline{u}_i \tag{4.4}$$

$\overline{U_r^j}$ is the filtered contravariant component of relative velocity:

$$\overline{U_r^j} = S_i^j \left(\overline{u}_i - \overline{u_{g}}_i \right) \tag{4.5}$$

Where $\overline{u_g}_i$ is the filtered grid velocity component, and $\overline{q}$ is the pseudo pressure defined by:

$$\overline{q} = \overline{p} - \frac{1}{3}\tau_{ll} \tag{4.6}$$

And S_j^i are the metrics of the transformation defined by:

$$S_j^i = J\frac{\partial \xi_i}{\partial x_j} \qquad \text{with } i,\ j \text{ and } k \text{ cyclic} \tag{4.7}$$

Re_t is the turbulent Reynolds number as obtained using one of the following LES models:

Smagorinsky model:

$$Re_t = \frac{U_\infty L}{C_s^2 \Delta \left|\overline{S}\right|} \tag{4.8}$$

Where $\left|\overline{S}\right| = \sqrt{2\overline{S}_{ij}\overline{S}_{ij}}$ and the rate-of-strain tensor $\overline{S}_{ij} = \frac{J}{2}\left(S_j^k \frac{\partial \overline{u}_i}{\partial \xi_k} + S_i^l \frac{\partial \overline{u}_j}{\partial \xi_l} \right)$.

Structure function model:

$$Re_t = \frac{U_\infty L}{0.063\Delta\sqrt{\overline{F}_2(\xi, \Delta t)}} \tag{4.9}$$

Where the function $\overline{F}_2$ can be obtained from:

$$\overline{F}_2 = \left\langle \left\| \mathbf{u}(\xi + \mathbf{r}) - \mathbf{u}(\xi) \right\|^2 \right\rangle_{\|\mathbf{r}| = 1} \tag{4.10}$$

Selective structure function model:

$$Re_t = \frac{U_\infty L}{0.098\gamma\Delta\sqrt{\overline{F}_2(\xi, \Delta t)}} \tag{4.11}$$

function $\overline{F}_2$ is as above and γ is a switch function that uses the tween the local vorticity vector and the average vorticity vector in the ing region:

$$\gamma = \begin{cases} 0 & \text{for } \beta < 20^o \\ e^{-(d\beta/3)^2} & \text{for } 20^o \geq \beta \geq 10^o \text{ and } d\beta = |\beta - 20| \\ 1 & \text{for } \beta > 20^o \end{cases} \tag{4.12}$$

$$\beta = \cos^{-1}\left(\frac{\omega \cdot \omega_{av}}{||\omega||\;||\omega_{av}||}\right) \tag{4.13}$$

ity components can be obtained from:

$${}_i = \frac{1}{J}\left[\frac{\partial\left(S_j^m \overline{u}_k\right)}{\partial \xi_m} - \frac{\partial\left(S_k^n \overline{u}_j\right)}{\partial \xi_n}\right] \qquad (i, j, k \;\text{ in cyclic order}) \tag{4.14}$$

he Projection Method in Finite Volume

the incompressible Navier-Stokes equations, the projection method as d originally by Chorin [16] was chosen for its simplicity and efficiency. ted before in chapter 3, the projection method consists of three steps:

momentum equations are solved ignoring the pressure terms to obtain ntermediate velocity field that does not satisfy the continuity constraint. equations resulting from the omission of the pressure terms from the nentum equations are named the Burger equations.

pressure is then solved by using the Poisson equation.

using the pressure gradient, a provisional velocity field is projected onto ivergence-free space thus resulting in a velocity field complying with the tinuity constraint.

e these three steps, the equations governing the flow need first to be dis- ısing the finite volume method. Since the full discretisation procedure is only the final representation will be formulated here. The author refers r to appendix C for a more comprehensive description and derivation of etised equations.

liscretisation presented in the following section, the control volume lay- notation adopted is illustrated for the two-dimensional case by figure the three-dimensional case, an upper (top) and lower (bottom) layers d to the computational cell. As a convention, capital letters will denote

Page 48
missing

Where $j = BW, SW, W, NW, TW, BS, B, BN, S, P, N, TS, T, TN, BE, SE, E, NE, TE$. The complete definition of the laplacian $\mathcal{L}$ can be found in appendix C.

Now, since:

$$\int_V \frac{\partial}{\partial t}\left(J\overline{u}_i^*\right) \mathrm{d}V = \frac{\partial}{\partial t}\left(J\overline{u}_i^*\right) \tag{4.17}$$

then the spatially discretised Burger equations are:

$$\frac{\partial}{\partial t}\left(J\overline{u}_i^*\right) + \mathcal{C}_i = \mathcal{D}_i \tag{4.18}$$

Integrating now between two instants t^n and $t^{n+1} = t^n + \Delta t$ gives:

$$\int_{t^n}^{t^{n+1}} \frac{\partial}{\partial t}\left(J\overline{u}_i^*\right) \mathrm{d}t + \int_{t^n}^{t^{n+1}} \mathcal{C}_i \mathrm{d}t = \int_{t^n}^{t^{n+1}} \mathcal{D}_i \mathrm{d}t \tag{4.19}$$

Using a simple Euler explicit scheme for the temporal derivative term, the Adams-Bashford scheme for the convective term and the Crank-Nicolson scheme for the diffusive term, a second order time accurate solution is obtained:

$$\int_{t^n}^{t^{n+1}} \frac{\partial}{\partial t}\left(J\overline{u}_i^*\right) \mathrm{d}t \approx \left(J\overline{u}_i^*\right)^{n+1} - \left(J\overline{u}_i^*\right)^n \tag{4.20}$$

$$\int_{t^n}^{t^{n+1}} \mathcal{C}_i \mathrm{d}t \approx \frac{\Delta t}{2}\left(3\mathcal{C}_i^n - \mathcal{C}_i^{n-1}\right) \tag{4.21}$$

$$\int_{t^n}^{t^{n+1}} \mathcal{D}_i \mathrm{d}t \approx \frac{\Delta t}{2}\left(\mathcal{D}_i^n + \mathcal{D}_i^{n+1}\right) \tag{4.22}$$

The fully discretised Burger equations are thus:

$$\left(J\overline{u}_i^*\right)^{n+1} - \left(J\overline{u}_i^*\right)^n + \frac{\Delta t}{2}\left(3\mathcal{C}_i^n - \mathcal{C}_i^{n-1}\right) = \frac{\Delta t}{2}\left(\mathcal{D}_i^n + \mathcal{D}_i^{n+1}\right) \tag{4.23}$$

Grouping now the terms at instant t^{n+1} on one side and the others on the other side gives:

$$\frac{2}{\Delta t}\left(J\overline{u}_i^*\right)^{n+1} - \mathcal{D}_i^{n+1} = \frac{2}{\Delta t}\left(J\overline{u}_i^*\right)^n - 3\mathcal{C}_i^n + \mathcal{C}_i^{n-1} + \mathcal{D}_i^n \tag{4.24}$$

i.e., using equation (4.16):

$$\sum_j \mathcal{L}_j \left(1 + \frac{2\delta_{jP}}{\Delta t}\right) \overline{u}_{i_j}^{*n+1} = \frac{2}{\Delta t}\left(J\overline{u}_i^*\right)^n - 3\mathcal{C}_i^n + \mathcal{C}_i^{n-1} + \mathcal{D}_i^n \tag{4.25}$$

Where δ_{jP} is the Kronecker delta function defined by:

$$\delta_{jP} = \begin{cases} 1 & \text{if } j = P \\ 0 & \text{otherwise} \end{cases} \tag{4.26}$$

For each control volume in the solution domain, equation (4.25) must be solved for each velocity component. The resulting system of equations for the whole domain is thus of the form:

$$A\mathbf{U_i} = \mathbf{B_i} \qquad \text{for } i = 1, 2, 3 \tag{4.27}$$

Where A is the matrix of coefficients to be applied to the velocity components as defined in equation (4.25), $\mathbf{U_i}$ is the vector of velocity component i for all the control volumes and $\mathbf{B_i}$ is the vector corresponding to the right hand side term of equation (4.25).

Following the projection method steps, the pressure field must now be solved by using the Poisson equation.

The curvilinear form of such a Poisson equation can be written as:

$$\frac{\partial}{\partial \xi_k}\left(J^{-1} S_i^k S_i^l \frac{\partial \overline{q}}{\partial \xi_l}\right) = \frac{\partial}{\partial \xi_k}\left(\overline{U}^{*m}\right) \tag{4.28}$$

In a very similar way to that used for the diffusive part of the Burger equations, the discretisation of the Poisson equation results in the following approximation:

$$\sum_j \mathcal{L}_j \overline{q}_j = [\overline{U}^*]_e - [\overline{U}^*]_w + [\overline{V}^*]_n - [\overline{V}^*]_s + [\overline{W}^*]_t - [\overline{W}^*]_b \tag{4.29}$$

As for the Burger equation, the above equation must be solved for each control volume in the domain. This results in a system of equations of the following form:

$$A\mathbf{Q} = \mathbf{B} \tag{4.30}$$

Where A is the matrix of coefficients to be applied to the pseudo pressure defined in equation (4.29), $\mathbf{Q}$ is the vector of pseudo pressure for all the control volumes and $\mathbf{B}$ is the vector corresponding to the right hand side term of equation 4.29.

Finally, the actual velocity field satisfying the continuity constraints is simply solved using the projection equation. In its curvilinear form, the latter can be written as follows:

$$\overline{u}_i = \overline{u}_i^* - J^{-1} S_i^j \frac{\partial \overline{q}}{\partial \xi_j} \tag{4.31}$$

Applying the finite volume discretisation gives:

$$\overline{u}_i = \overline{u}_i^* - (2J)^{-1}\left[S_i^1\left(\overline{q}_E - \overline{q}_W\right) + S_i^2\left(\overline{q}_N - \overline{q}_S\right) + S_i^3\left(\overline{q}_T - \overline{q}_B\right)\right] \tag{4.32}$$

The complete solution method for the projection method can thus be summarised as follows:

1. Solve equation system (4.27) to obtain the provisional velocity field.
2. Solve equation system (4.30) to obtain the pressure field.
3. Solve equation (4.32) to obtain the actual velocity field.

4.3 Boundary Conditions Implementation

From the discretisation presented previously, and taking into account that the flow is solved using the primitive variables at the cell centre, it appears quite clear that the computational cell used in solving the set of equations is composed of a single layer of cells around the current cell as illustrated in figure 4.2.

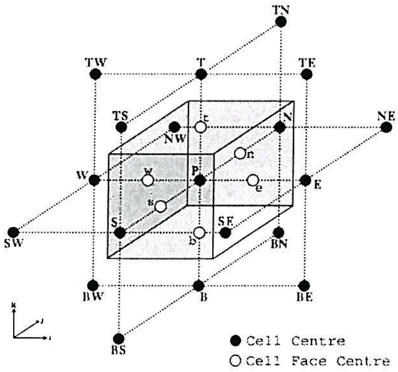

Figure 4.2: The computational cell

However, at the domain boundaries, some of the neighbouring cells are non-existent. To account for such an absence of cells, a layer of so-called "ghost cells" is introduced around the block as can be seen in figure 4.3. Such ghost cells must then be set to represent appropriately the boundary conditions.

Conveniently, these ghost cells can also be used to store information from adjacent blocks. The overlapping mesh strategy discussed in chapter 3 can thus be enforced in a straight forward manner using the ghost cells as the overlapping mesh area. Figure 4.4 illustrates the subdivision of a domain into sub-domains, and the data dependency between the sub-domains with the overlapping mesh strategy.

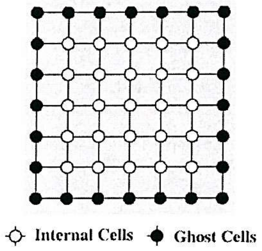

Figure 4.3: Block Cells Arrangement

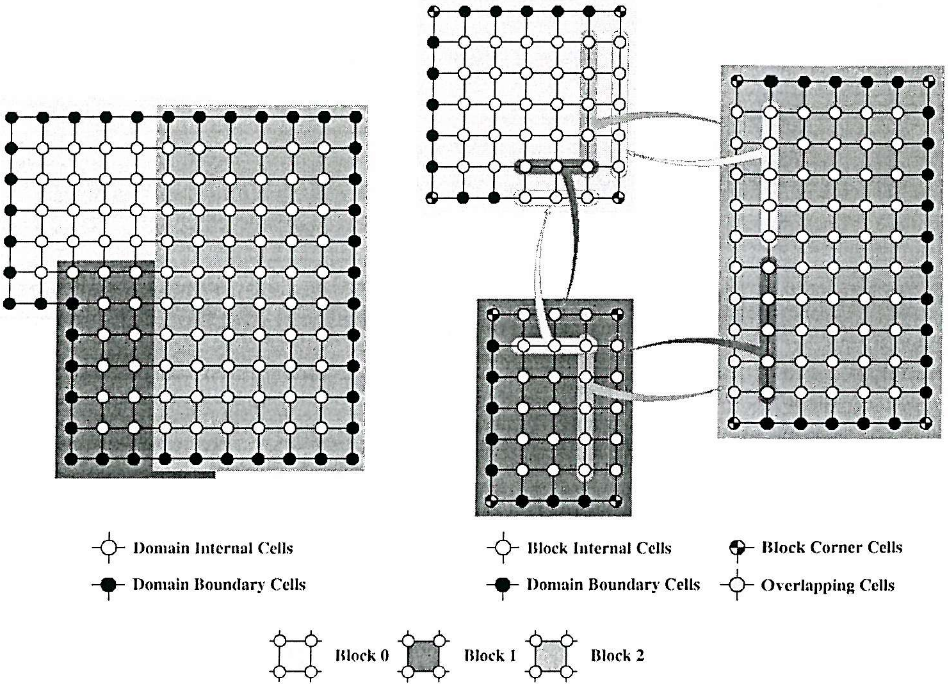

Figure 4.4: Multi-block domain decomposition and data dependency

In the following discussion, it will be assumed that the boundary cells, whether domain cells or ghost cells, are normal to the boundary.

In most cases, the boundary conditions used in the resolution of the Navier-Stokes equations are associated with the velocity, the nature of the problem usually not providing enough information on the pressure at the boundary except in cases such as free-surface flows. For each variable, i.e. velocity and pressure, the boundary Γ is subdivided into Γ_D where Dirichlet boundary conditions apply (such as $u = g\left(\vec{x}, t\right)$), and Γ_N where Neumann boundary conditions apply (such as $\frac{\partial \phi}{\partial n} = 0$ where n denotes the direction normal to the face of the cell where the condition applies).

In practical terms, the most common boundary conditions encountered in flow computations are:

- Inflow (Constant or variable)
- Outflow
- Solid Wall (Fixed or moving)
- Symmetry
- Periodic

4.3.1 Inflow Boundary Condition

When the velocity is specified directly as in the case of an inflow, the Dirichlet boundary condition can be interpreted as follows:

$$\mathbf{u} = \mathbf{u}_{inflow}\left(\mathbf{x}, t\right) \tag{4.33}$$

Where $\mathbf{u}_{inflow}$ is the specified inflow velocity profile.

It has to be noted that the inflow velocity mentioned above is in fact applied to a face and not to the centre of a cell. Thus, by supposing that the inflow velocity is the average velocity between the domain cell and the adjacent ghost cell, the velocity components of the ghost cells can be set as:

$$\mathbf{u}_{GC} = 2 \cdot \mathbf{u}_{inflow} - \mathbf{u}_{DC} \tag{4.34}$$

Where subscript GC and DC denote the ghost cell and the neighbouring domain cell variables respectively as illustrated in figure 4.5.

As far as the pressure is concerned, applying the Neumann condition ($\frac{\partial p}{\partial n} = 0$) leads to:

$$p_{GC} = p_{DC} \tag{4.35}$$

4.3.2 Outflow Boundary Condition

In the case of an outflow, the zero gradient of the velocity in the direction of the flow is used. This translates into:

$$\mathbf{u}_{GC} = \mathbf{u}_{DC} \tag{4.36}$$

Using a reference pressure on the face of the domain cell where the outflow condition applies, and assuming it is the average pressure between the domain cell and the adjacent ghost cell, the ghost cell pressure can be set as:

$$p_{GC} = 2 \cdot p_{ref} - p_{DC} \tag{4.37}$$

Figure 4.6 illustrates the outflow boundary condition.

4.3.3 Solid Wall Boundary Condition

The wall boundary condition, whether the wall is fixed or moving, is in fact the combination of two conditions: namely, the no-slip and no-penetration conditions.

In the more general case of a moving wall, assuming that the velocity at the wall is the average velocity between that in the ghost cell and that in the adjacent domain cell, theses conditions can be interpreted by the following Dirichlet conditions:

$$\mathbf{u}_{GC} = 2 \cdot \mathbf{u}_{wall} - \mathbf{u}_{DC} \tag{4.38}$$

Where the subscript *wall* denotes the variable at the wall, i.e. at the face of the cell lying on the wall (whether the ghost cell or the corresponding domain cell).

In the case of a fixed wall, the above simplifies to:

$$\mathbf{u}_{GC} = -\mathbf{u}_{DC} \tag{4.39}$$

So, applying the Neumann condition for the pressure, the ghost cell pressure is set as:

$$p_{GC} = p_{DC} \tag{4.40}$$

The wall boundary condition is illustrated in figure 4.7.

4.3.4 Symmetry boundary condition

The symmetry boundary condition is in fact the same as a wall boundary condition where slip occurs. Hence, depending on the plane along which the symmetry is set, two of the components of the velocity vector will be set equal in the ghost cell to that in the domain cell.

For example, if the plane of symmetry is the X-Z plane, both u and w components of velocity will be the same in the ghost cell as those in the adjacent domain cell while the v component is set equal to the opposite of that in the domain cell:

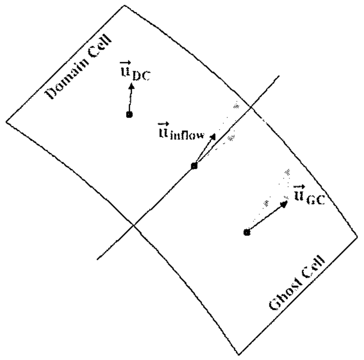

Figure 4.5: Inflow boundary condition

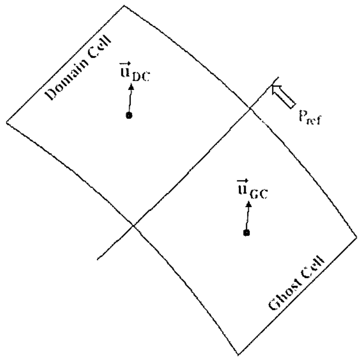

Figure 4.6: Outflow boundary condition

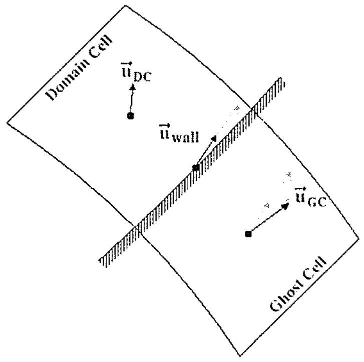

Figure 4.7: Wall boundary condition

$$
\begin{aligned}
u_{GC} &= u_{DC} \\
v_{GC} &= -v_{DC} \\
w_{GC} &= w_{DC}
\end{aligned}
$$

As far as the pressure goes, applying the Neumann condition, the ghost cell pressure is set as:

$$p_{GC} = p_{DC} \tag{4.41}$$

At this stage, it is important to note that, the contravariant components of velocity should be used rather than the cartesian components. For implementation reasons, the symmetry condition is currently restricted to the planes parallel to the (xy), (xz) and (yz) planes.

4.3.5 Periodic boundary condition

The periodic boundary condition consists of setting the variables of a set of ghost cells on one face of the block equal to a similar set of domain cells on another (or even the same) face of the block. Such condition is enforced by means of interfacing as will be described later on in the report. The ghost cells where the periodic condition applies are fed with the value of the variables of the "adjacent" block domain cells.

4.3.6 General Formulation

It thus appears that all the boundary conditions (with the exception of the periodic boundary condition) can be represented using a generic formulation:

$$\phi_{GC} = C_1 + C_2 \cdot \phi_{DC} \tag{4.42}$$

Where ϕ can be the velocity components or the pressure and the constant C_1 and C_2 depend on the condition to be applied. Tables 4.1 and 4.2 summarise the constants used for each boundary condition.

4.3.7 Block Corners and Edges

One aspect of multi-block computation rarely described by other authors but however well known is that of block corners. In the particular case of three-dimensional computations, this extends to the block edges. The reason such corners and edges are of concern is related to the computational cell used in the

Boundary Condition	C_1	C_2
Inflow	$2\mathbf{u}_{inflow}$	-1
Outflow	0	1
Fixed Wall	0	-1
Moving Wall	$2\mathbf{u}_{wall}$	-1
Symmetry (XY plane)	0	1 for u 1 for v -1 for w
Symmetry (XZ plane)	0	1 for u -1 for v 1 for w
Symmetry (YZ plane)	0	-1 for u 1 for v 1 for w

Table 4.1: Ghost cell boundary condition velocity constants

Boundary Condition	C_1	C_2
Inflow	0	1
Outflow	$2p_{ref}$	-1
Fixed Wall	0	1
Moving Wall	0	1
Symmetry	0	1

Table 4.2: Ghost cell boundary condition pressure constants

discretisation scheme and the boundary conditions treatment. In the current implementation, this concerns the ghost cells variables to be set in the corners and edges of each block of the domain. At this point, it is important to note that only the edges of the blocks are of interest since the block corner values are never used in the computational stencil. In the two-dimensional case, the block corners are in fact a special case of block edges. Figure 4.8 illustrates a block edge with the notation adopted for the variables to be set. The subscripts DCE and GCE denote variable in the domain edge (domain cell) and in the block edge (ghost cell).

To illustrate the method used to determine the ghost cell values in the edge of a block, let's consider the case showed in figure 4.9 where the one side of the edge is a solid wall (fixed or moving) and the other an inflow condition.
Using the boundary condition enforcement as described previously, then the velocity in the two ghost cells denoted $GC0$ and $GC1$ can be set as:

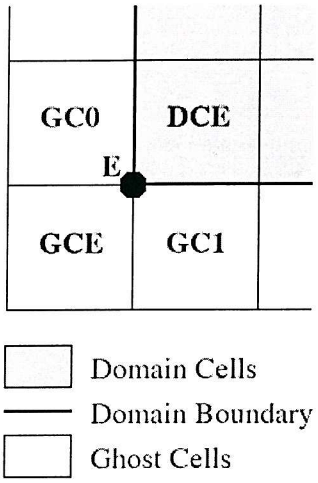

Figure 4.8: Block Edges Layout and Notation

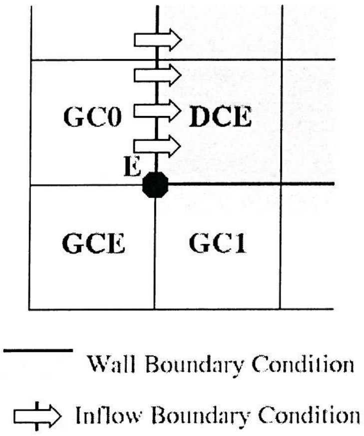

Figure 4.9: Inflow/Solid Wall Block Edge Condition

$$\mathbf{u}_{GC0} = 2\mathbf{u}_{\text{inflow}} - \mathbf{u}_{DCE} \qquad \text{(Inflow)} \tag{4.43}$$

And:

$$\mathbf{u}_{GC1} = 2\mathbf{u}_{\text{solid wall}} - \mathbf{u}_{DCE} \qquad \text{(Solid Wall)} \tag{4.44}$$

Now, the actual edge velocity $\mathbf{u}_E$ is such that:

$$\mathbf{u}_E = \mathbf{u}_{\text{solid wall}} = \frac{1}{4}\left(\mathbf{u}_{GC0} + \mathbf{u}_{DCE} + \mathbf{u}_{GC1} + \mathbf{u}_{GCE}\right) \tag{4.45}$$

It follows that:

$$\mathbf{u}_{GCE} = \mathbf{u}_{GC1} - \mathbf{u}_{GC0} + \mathbf{u}_{DCE} \tag{4.46}$$

If now both conditions were inverted as illustrated by figure 4.10, the following would be obtained:

$$\mathbf{u}_{GCE} = \mathbf{u}_{GC0} - \mathbf{u}_{GC1} + \mathbf{u}_{DCE} \tag{4.47}$$

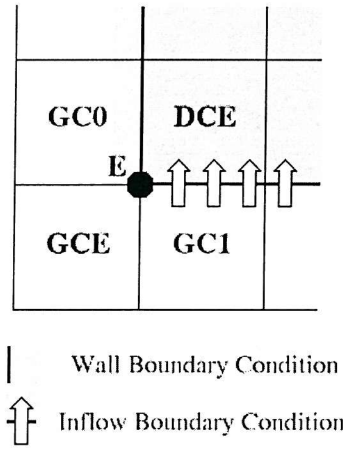

Figure 4.10: Solid Wall/Inflow Block Edge Condition

Following the same procedure as above, it can be shown that all the possible combinations of boundary conditions can be enforced at the block edges using either equation (4.46) or equation (4.47) which will be referred to as type 0 and type 1 respectively.

In a generalised form, the value of the velocity in the edge ghost cell can be set by:

$$\mathbf{u}_{GCE} = C_3 \cdot \mathbf{u}_{GC0} + C_4 \cdot \mathbf{u}_{GC1} + C_5 \cdot \mathbf{u}_{DCE} \tag{4.48}$$

Where C_3, C_4 and C_5 are constants set according to the boundary conditions on each side of the edge. Table 4.3 summarizes the constants used for each case.

For the pressure, a simple extrapolation technique is used based on the value of the pressure in the ghost cells on each side of the edge.

Boundary Condition		Edge Type	C_3	C_4	C_5
Face 0	Face 1				
Inflow	Solid	0	-1	1	1
Solid	Inflow	1	1	-1	1
Inflow	Interface	0/1	0	0	1
Interface	Inflow	0/1	0	0	1
Outflow	Solid	0	0	1	0
Solid	Outflow	1	1	0	0
Outflow	Inflow	0	0	1	0
Inflow	Outflow	1	1	0	0
Outflow	Interface	0	0	1	0
Interface	Outflow	1	1	0	0
Interface	Solid	0	-1	1	1
Solid	Interface	1	1	-1	1
Solid	Solid	0/1	0	0	1
Inflow	Inflow	0/1	0	0	1
Outflow	Outflow	0/1	0	0	1

Table 4.3: Ghost cell boundary condition velocity constants at block edge

4.4 Linear System Iterative Solution

The discretisation of the projection method led to two systems of linear equations to be solved, one for the solution of the Burger equations, the other for the Poisson equation. In both cases, the matrix of coefficients of the unknowns are large and sparse, thus making direct solution rather inefficient. For this reason, iterative method are generally used in computational fluid dynamics. In the present section, an outline of two of those method will be given, namely the Successive Over- Relaxation (SOR) and the Conjugate Gradient (GC) methods. Although both methods are extensively documented in the literature and in textbooks, their implementation in a parallel fashion need further explanation.

4.4.1 Parallel Successive Over-Relaxation

Considering the following system of linear equations:

$$A\mathrm{X} = \mathrm{B} \tag{4.49}$$

Then the i^{th} line can be written as follows:

$$\sum_{j=1}^{n} a_{ij} x_j = b_i \tag{4.50}$$

or:

$$x_i = \left(b_i - \sum_{j=1}^{i-1} a_{ij} x_j - \sum_{j=i+1}^{n} a_{ij} x_j \right) / a_{ii} \tag{4.51}$$

In an iterative method, a solution is guessed and improved by using an appropriate equation. Using the previously calculated values for the right hand side term in equation (4.51), one can thus obtain the left hand side vector. This is called the Jacobi iteration:

$$x_i^{(k+1)} = \left(b_i - \sum_{j=1}^{i-1} a_{ij} x_j^{(k)} - \sum_{j=i+1}^{n} a_{ij} x_j^{(k)} \right) / a_{ii} \tag{4.52}$$

If the computed values are immediately used as they are obtained, then the left hand side can be calculated using the so-called Gauss-Seidel (GS) iteration:

$$x_i^{(k+1)} = \left(b_i - \sum_{j=1}^{i-1} a_{ij} x_j^{(k+1)} - \sum_{j=i+1}^{n} a_{ij} x_j^{(k)} \right) / a_{ii} \tag{4.53}$$

By relaxing the above, the Successive Over-Relaxation (SOR) method is obtained:

$$x_i^{(k+1)} = \omega \left(b_i - \sum_{j=1}^{i-1} a_{ij} x_j^{(k+1)} - \sum_{j=i+1}^{n} a_{ij} x_j^{(k)} \right) / a_{ii} + (1-\omega)\, x_i^{(k)} \tag{4.54}$$

Where ω is the relaxation factor. If $\omega = 1$, the above equation is equivalent to the Gauss-Seidel one. If $\omega > 1$, then the system is over-relaxed. An advantage of the SOR method over the Gauss-Seidel method is that the solution is accelerated and requires far less iterations to reach a converged solution provided the relaxation factor is well chosen. As no real guidance for the relaxation factor can be found in the literature, its choice is often based on trial and error.

Equation (4.54) is equivalent to:

$$\begin{aligned} x_i^{(k+1)} &= x_i^{(k)} - \omega \left[\left(\sum_{j=1}^{i-1} a_{ij} x_j^{(k+1)} + \sum_{j=i}^{n} a_{ij} x_j^{(k)} \right) / a_{ii} - b_i \right] \\ &= x_i^{(k)} - \omega \tilde{\mathcal{R}}_i \end{aligned} \tag{4.55}$$

Where $\tilde{\mathcal{R}}_i$ is the local intermediary residue defined by:

$$\tilde{\mathcal{R}}_i = \left(\sum_{j=1}^{i-1} a_{ij} x_j^{(k+1)} + \sum_{j=i}^{n} a_{ij} x_j^{(k)} \right) / a_{ii} - b_i \tag{4.56}$$

The actual local residue $\mathcal{R}_i$ at an iteration k can be calculated from:

$$\mathcal{R}_i^k = \left(\sum_{j=1}^{n} a_{ij} x_j^{(k)} \right) / a_{ii} - b_i \tag{4.57}$$

As the iterations are performed, the residue $\mathcal{R}_i$ will reduce towards zero. This residue is generally used as a stopping criterion for the iteration.

As seen previously in the discussion on the discretisation of the flow governing equations, the computational stencil is composed of nineteen points or cell, i.e. the current cell and eighteen neighbouring cell. It is thus clear that since values in the ghost cells layer are used, those must be updated at each SOR iteration. The solution thus requires not only the update of the boundary cells to be carried out but also the interface (or overlapping) cells to be updated at every single SOR iteration. Algorithm 4.1 describes the parallel Successive Over-Relaxation method.

Algorithm 4.1: Parallel Successive Over-Relaxation Algorithm

```
For k=1 to k=(max. num. of iteration)
    1. Set overall residue $\mathcal{R} = 0.0$
    2. For i=1 to i=(num. of domain cells)
        • Compute: $\tilde{\mathcal{R}}_i = \left(\sum_{j=1}^{i-1} a_{ij} x_j^{(k+1)} + \sum_{j=i}^{n} a_{ij} x_j^{(k)}\right) / a_{ii} - b_i$
        • Compute: $x_i^{(k+1)} = \omega \left(\tilde{\mathcal{R}}_i\right) + (1 - \omega) x_i^{(k)}$
    3. For i=1 to i=(num. of domain cells)
        (a) Compute: $\mathcal{R}_i^{(k+1)} = \left(\sum_{j=1}^{n} a_{ij} x_j^{(k+1)}\right) / a_{ii} - b_i$
        (b) Compute: $\mathcal{R} = max\left(\left|\mathcal{R}_i^{(k+1)}\right|, \mathcal{R}\right)$
    4. Update X in the ghost cells at boundaries, interface and block edges
    5. If $\mathcal{R} <$ (Min. Residue) Then set flag 'local block convergence' to 'TRUE'
    6. (MPI: Gather) Gather all local convergence flags from all processes
    7. If all processes have converged set flag 'global convergence' to 'TRUE' and exit
```

4.4.2 Parallel Conjugate Gradient

The SOR method although widely used in CFD tends to have a slow convergence rate if the initial guess is innaccurate. On the other hand, if an accurate guess of the solution is available, the SOR method will converge very quickly. In CFD problems, it is rare to have such an accurate initial solution, thus methods with faster convergence rate than that of the SOR method can be very desirable. Among such methods, the conjugate gradient (CG) is one of the simplest to implement. It is based on the minimisation of a function in several directions simultaneaously while searching in one direction only.

The serial CG method is presented in algorithm 4.2 below.

Algorithm 4.2: Conjugate Gradient Algorithm

```
1. For i=1 to i=(num. of domain cells)
    (a) Set initial: $x_i^{(0)}$
    (b) Compute: $r_i^{(0)} = b_i - \sum_{j=1}^{n} a_{ij} x_j^{(0)}$
    (c) Set $d_i^{(0)} = r_i^{(0)}$
2. For k=1 to k=(max. num. of iteration)
    (a) Compute: $\alpha^{(k)} = \sum_{i=1}^{n} r_i^{(k)} r_i^{(k)} / \sum_{i=1}^{n} \left( d_i^{(k)} \sum_{j=1}^{n} a_{ij} d_j^{(k)} \right)$
    (b) For i=1 to i=(num. of domain cells)
        i. Compute: $x_i^{(k+1)} = x_i^{(k)} + \alpha^{(k)} d_i^{(k)}$
        ii. Compute: $r_i^{(k+1)} = r_i^{(k)} - \alpha^{(k)} \sum_{j=1}^{n} a_{ij} d_j^{(k)}$
    (c) Compute: $\beta^{(k)} = \sum_{i=1}^{n} r_i^{(k+1)} r_i^{(k+1)} / \sum_{i=1}^{n} r_i^{(k)} r_i^{(k)}$
    (d) For i=1 to i=(num. of domain cells)
        • Compute: $d_i^{(k+1)} = r_i^{(k)} + \beta^{(k)} d_i^{(k)}$
        • Compute: $\mathcal{R}_i^{(k+1)} = \alpha(k) d_i^{(k+1)}$
        • Compute: $\mathcal{R} = max\left( \left| \mathcal{R}_i^{(k+1)} \right|, \mathcal{R} \right)$
    (e) If $\mathcal{R}$ < (Min. Residue) Then exit
```

In the case of a parallel method, α and β must be computed using the residual values r of the whole solution domain. Also, in the case of α, the search directions $\mathbf{d}$ of the whole solution domain are necessary. The parallel CG must thus include some modification to account for the communication of $\mathbf{r}$, $\mathbf{d}$ and $A\mathbf{d}$ across the various processes.

The parallel CG algorithm is presented below.

Algorithm 4.3: Parallel Conjugate Gradient Algorithm

```
1. For i=1 to i=(num. of domain cells)
    (a) Set initial: $x_i^{(0)}$
    (b) Compute: $r_i^{(0)} = b_i - \sum_{j=1}^{n} a_{ij} x_j^{(0)}$
    (c) Set $d_i^{(0)} = r_i^{(0)}$
2. For k=1 to k=(max. num. of iteration)
    (a) Compute: $\left(\mathbf{r}^{(k)}, \mathbf{r}^{(k)}\right)_{local} = \sum_{i=1}^{n} r_i^{(k)} r_i^{(k)}$
    (b) (MPI: All Reduce) Sum the $\left(\mathbf{r}^{(k)}, \mathbf{r}^{(k)}\right)_{local}$ across all the processes giving $\left(\mathbf{r}^{(k)}, \mathbf{r}^{(k)}\right)$
    (c) Compute: $\left(\mathbf{d}^{(k)}, A\mathbf{d}^{(k)}\right)_{local} = \sum_{i=1}^{n} \left(d_i^{(k)} \sum_{j=1}^{n} a_{ij} d_j^{(k)}\right)$
    (d) (MPI: All Reduce) Sum the $\left(\mathbf{d}^{(k)}, A\mathbf{d}^{(k)}\right)_{local}$ across all the processes giving $\left(\mathbf{d}^{(k)}, A\mathbf{d}^{(k)}\right)$
    (e) Compute: $\alpha^{(k)} = \left(\mathbf{r}^{(k)}, \mathbf{r}^{(k)}\right) / \left(\mathbf{d}^{(k)}, A\mathbf{d}^{(k)}\right)$
    (f) For i=1 to i=(num. of domain cells)
        i. Compute: $x_i^{(k+1)} = x_i^{(k)} + \alpha^{(k)} d_i^{(k)}$
        ii. Compute: $r_i^{(k+1)} = r_i^{(k)} - \alpha^{(k)} \sum_{j=1}^{n} a_{ij} d_j^{(k)}$
    (g) Compute: $\left(\mathbf{r}^{(k+1)}, \mathbf{r}^{(k+1)}\right)_{local} = \sum_{i=1}^{n} r_i^{(k+1)} r_i^{(k+1)}$
    (h) (MPI: All Reduce) Sum the $\left(\mathbf{r}^{(k+1)}, \mathbf{r}^{(k+1)}\right)_{local}$ across all the processes giving $\left(\mathbf{r}^{(k+1)}, \mathbf{r}^{(k+1)}\right)$
    (i) Compute: $\beta^{(k)} = \left(\mathbf{r}^{(k+1)}, \mathbf{r}^{(k+1)}\right) / \left(\mathbf{r}^{(k)}, \mathbf{r}^{(k)}\right)$
    (j) For i=1 to i=(num. of domain cells)
        • Compute: $d_i^{(k+1)} = r_i^{(k)} + \beta^{(k)} d_i^{(k)}$
        • Compute: $\mathcal{R}_i^{(k+1)} = \alpha(k) d_i^{(k+1)}$
        • Compute: $\mathcal{R} = max\left(\left|\mathcal{R}_i^{(k+1)}\right|, \mathcal{R}\right)$
    (k) Update $\mathbf{d}$ in the ghost cells at boundaries, interface and block edges
    (l) If $\mathcal{R} <$ (Min. Residue) Then exit
```

Although the parallel CG method (algorithms 4.3) possesses a convergence rate far greater than that of the parallel SOR (algorithms 4.1), each iteration carried out using this method requires substantially more operations. In the case where an accurate initial guess is known, the SOR method is more efficient than the CG method as the number of iterations to achieve the solution in both cases is similar but the number of operations per iteration is less in the SOR method. On the other hand, if no such initial guess is known, the CG method is more appropriate. When carrying out a numerical solution of a time-dependent problem, as the solution is advanced through time, the results from a previous time step are used as initial guesses. Thus the initial guess is getting more and more accurate. It follows that for the initial steps of the solution, the CG method can provide a more efficient method to solve the large system of equations. As the solution progresses, the initial guess becoming closer and closer to the actual solution, less iterations are required to solve such a system. The SOR method becomes thus more advantageous.

4.5 Overall Flow Solution Procedure

Having derived the various equations to be solved and suitable methods to solve them, the general procedure for the solution of the flow can be summarised in algorithm 4.4. Since the solution is iterative, it is important to determine a stopping criterion for the loop. Generally, a maximum number of iterations (time steps) can be set, but in the case of a steady flow, the solution may converge to the exact solution before reaching the maximum number of iterations. A residue must thus be calculated assessing the difference between the solution at two consecutive time steps. If such a difference is below a certain tolerance level, the solution is assumed steady and thus converged. One way to determine the convergence is by comparing the velocity field between two consecutive time steps.

Algorithm 4.4: Global Flow Solution Algorithm

```
For k=1 to k=(max. num. of iteration)
    1. Solve the Burger equations (Equation (4.25)) using SOR (Algorithm 4.1) or CG (Algorithm 4.3)
    2. Solve the Poisson equation (Equation (4.29)) using SOR (Algorithm 4.1) or CG (Algorithm 4.3)
    3. Solve the projection equations (Equation (4.32))
    4. Update the velocity and pressure in the ghost cells at boundaries, interface and block edges
    5. Compute the local solution residue $\mathcal{R}_{local}$ based on the velocity: $\mathcal{R}_{local} = \frac{\left(\sum_i^n \left[\sum_{j=1}^3 \left|u_{j_i}^{(k+1)} - u_{j_i}^{(k)}\right|\right]\right)}{\left(\sum_i^n \left[\sum_{j=1}^3 \left|u_{j_i}^{(k+1)}\right|\right]\right)}$
    6. Determine the maximum residue across all the processes (MPI: All Reduce) giving $\mathcal{R}$
    7. If $\mathcal{R} <$ (Min. Residue) Then exit
```

4.6 Code Development and Performance

The method presented in this chapter was implemented in a code written over a period of two years during the course of the research. A mixture of the C and Fortran languages was used to take advantage of the data structure capabilities of the first one and the numerical efficiency of the second. The implementation in itself represents around forty thousands lines of codes. The global architecture of the code is based on a communication layer for the data exchange between the various solution processes (i.e. domain blocks) on top of which is the flow solver. Adopting such a strategy implies that different flow solvers could be further implemented using the same communication layer, or additional capabilities for the present solver could be added.

In table 4.5 below, a comparison of the performances of the solution is given for three different mesh sizes, those used in the application presented later in the report (see chapter 7). Regarding the performance of the two different computer node classes (table 4.4) used to process the solution, the same setup will run almost three times faster on the myr-P4 class than on the myr-1024 class as illustrated by the first case presented in table 4.5.

It is also intersting to note that for the last two cases shown in table 4.5, although one has twice the amount of cells of the other, they both take as much time to carry out the iteration. The reason for such a difference resides in the fact that in the first of the two cases, only two nodes were used whereas the second case used four nodes, thus twice as much power.

The average time over $30,000$ iterations shown in the table indicates how long a typical simulation such as those presented in chapter 7 takes to complete.

Node Class	Processors	RAM (Mb)	Network Connection
myr-1024	2x1.0Ghz PIII	1024	Myrinet
myr-P4	2x1.8Ghz P4	2048	

Table 4.4: Computer node class definition

No. of cells	No. of nodes (procs) used	Av. time over 30,000 iter.	Av. time (s) per iter.	Av. time (10^{-6}s) per iter per cell	Node Class
524288	4 (8)	5d 11hr 17min	15.75	30.04	myr-1024
	4 (8)	2d 02hr 38min	6.07	11.58	myr-P4
1048576	2 (4)	5d 22hr 05min	17.05	16.26	myr-P4
2097152	4 (8)	6d 07hr 12min	17.35	8.27	myr-P4

Table 4.5: Performance evaluation of present method

Chapter 5

Fluid Structure Interaction Method

5.1 Forces And Structural Displacement

5.1.1 Forces Solution

The computation of the forces acting on the bodies present in the domain is used to determine the force coefficients. As seen in chapter 3, the forces acting on a body are composed of the contributions of both the pressure acting on the surface of this body and the viscous forces:

$$\mathbf{F} = \mathbf{F_p} + \mathbf{F_v} = -\int_S (p\mathbf{n} + \mu\mathbf{n} \times \omega)\, \mathrm{d}\mathcal{S} \tag{5.1}$$

Using the following non-dimensionalised parameters:

$$p^* = \frac{p}{\rho U_\infty^2} \;\; ; \;\; \omega^* = \frac{U_\infty}{L}\omega \;\; ; \;\; \mathbf{C_F} = \frac{2\mathbf{F}}{\rho U_\infty^2 A} \tag{5.2}$$

where A is a reference area and $\mathbf{C_F}$ is the force coefficient vector, and dropping the superscripts for convenience, equation 5.1 can be re-written as:

$$\mathbf{C_F} = \mathbf{C_{F_p}} + \mathbf{C_{F_v}} = -\frac{2}{A}\int_S \left(p\mathbf{n} + \frac{1}{Re}\mathbf{n} \times \omega\right) \mathrm{d}\mathcal{S} \tag{5.3}$$

In the case of circular cylinders, the reference area A is usually taken as the product of the length L and the diameter D of the cylinder.

Considering now the individual components of the force coefficient vector:

$$C_{F_{x_i}} = C_{F_{p x_i}} + C_{F_{v x_i}} \tag{5.4}$$

Where:

$$C_{F_{p x_i}} = -\frac{2}{A}\int_S p n_{x_i} \mathrm{d}\mathcal{S} \tag{5.5}$$

$$C_{F_{vx_i}} = -\frac{2}{ARe}\int_S \left(n_{x_j}\omega_{x_k} - n_{x_k}\omega_{x_j}\right) \mathrm{d}\mathcal{S} \qquad \text{with } i,j \text{ and } k \text{ cyclic} \tag{5.6}$$

Since the solution domain is represented by a curvilinear mesh, i.e. one that follows the contours of specified boundaries, the objects present in the domain for which force coefficients must be determined are represented by a set of faces. Thus, by approximating the integrals in equations (5.5) and (5.5) as a sum over the faces describing the object, the force coefficients can be calculated from:

$$C_{F_{px_i}} = -\frac{2}{A}\sum_{f=1}^{\substack{num.\\ offaces}} p_f n_{x_{i_f}} \mathcal{S}_f \tag{5.7}$$

And:

$$C_{F_{vx_i}} = -\frac{2}{ARe}\sum_{f=1}^{\substack{num.\\ offaces}} \left(n_{x_{j_f}}\omega_{x_{k_f}} - n_{x_{k_f}}\omega_{x_{j_f}}\right) \mathcal{S}_f \qquad \text{with } i,j \text{ and } k \text{ cyclic} \tag{5.8}$$

Now, in a parallel multiblock solution, the objects may extend over several blocks. The determination of the force coefficient must thus include some inter-process communication to sum the locally calculated coefficients and thus obtain the total force coefficient.

The complete procedure for the determination of the force coefficients acting on a single object is illustrated in algorithm 5.1.

Algorithm 5.1: Force Computation Algorithm (Single Object)

```
1. Initialise the local and global variables: $C_{F_{x_i}} = 0$, $C_{F_{px_i}} = 0$ and $C_{F_{vx_i}} = 0$ for $i = 1,2,3$
2. **For** f=1 **to** f=(num. of faces describing the object)
    (a) Compute: $\mathbf{n}_{x_{i_f}}$ for $i = 1,2,3$
    (b) Compute the face area: $\mathcal{S}_f$
    (c) Compute the vorticity vector at the face: $\omega_{x_{i_f}}$ for $i = 1,2,3$
    (d) Compute the pressure acting on the face: $p_f$
    (e) Compute the local pressure force coefficient: $C_{F_{px_i}} = C_{F_{px_i}} - \frac{2}{A} p_f n_{x_{i_f}} \mathcal{S}_f$ for $i = 1,2,3$
    (f) Compute the local viscous force coefficient: $C_{F_{vx_i}} = C_{F_{vx_i}} - \frac{2}{ARe}\left(n_{x_{j_f}}\omega_{x_{k_f}} - n_{x_{k_f}}\omega_{x_{j_f}}\right)\mathcal{S}_f$
        for $i = 1,2,3$ with $i$,$j$ and $k$ cyclic
    (g) Compute the local force coefficient: $C_{F_{x_i}} = C_{F_{x_i}} + C_{F_{px_i}} + C_{F_{vx_i}}$ for $i = 1,2,3$
    (h) Sum (**Reduce** operation) the force coefficients across all the processes giving the global $C_{F_{x_i}}$,
        $C_{F_{px_i}}$ and $C_{F_{vx_i}}$ for $i = 1,2,3$
```

In the presence of several objects, the above procedure is simply applied to each object present in the domain, an object identifier (integer) being used to distinguish between the various coefficients and inter-process communications.

5.1.2 Structural Displacement Solution

Once the force acting on each object present in the domain is obtained, their displacement can be calculated according to a specific structural model. As discussed in chapter 3, a simple mass-spring-damping system is generally employed to model dynamic cylinders in a flow. The dynamic equilibrium of such a system was given in equation (3.47) and is repeated here, dropping the non-dimensional superscripts for convenience:

$$\frac{\partial^2 \mathbf{x}}{\partial t^2} + \left(\frac{4\pi\zeta}{U}\right)\frac{\partial \mathbf{x}}{\partial t} + \left(\frac{2\pi}{U}\right)^2 \mathbf{x} = \frac{\mathbf{C_F}}{2m} \tag{5.9}$$

Where $\mathbf{x}$ is the non-dimensional displacement vector, t is the non-dimensional time, ζ is the damping ratio, U is the velocity ratio, $\mathbf{C_F}$ is the force coefficient vector and m is the mass ratio.

To solve equation (5.9), the classical fourth order Runge-Kutta method is generally used and given here without proof:

Considering the following equation:

$$m\ddot{x}(t) + b\dot{x}(t) + kx(t) = F(t) \tag{5.10}$$

where $F(t)$ is a function of time, and the initial conditions $x(0)$ and $\dot{x}(0)$ are known.

Then:

$$\ddot{x}(t) = \frac{1}{m}\left[F(t) - b\dot{x}(t) - kx(t)\right] \tag{5.11}$$

Let $x_1(t) = x(t)$ and $x_2(t) = \dot{x}(t)$.

Substituting x_1 and x_2 back into equation (5.11), the following can be defined:

$$\begin{aligned}
\mathcal{F}_1(t, x_1, x_2) &= \dot{x}_1(t) = x_2(t) && (5.12)\\
\mathcal{F}_2(t, x_1, x_2) &= \dot{x}_2(t) = \ddot{x}(t) = \frac{1}{m}\left[F(t) - bx_2(t) - kx_1(t)\right] && (5.13)
\end{aligned}$$

Knowing the initial conditions $x_1(0) = x(0)$ and $x_2(0) = \dot{x}(0)$, it is possible at a time step n to construct the following:

$$\mathcal{X}_{1,1} = \mathcal{F}_1\left(t^{(n)}, x_1^{(n)}, x_2^{(n)}\right) \tag{5.14}$$

$$\mathcal{X}_{2,1} = \mathcal{F}_2\left(t^{(n)}, x_1^{(n)}, x_2^{(n)}\right) \tag{5.15}$$

$$\mathcal{X}_{1,2} = \mathcal{F}_1\left(t^{(n)} + \frac{\Delta t}{2}, x_1^{(n)} + \frac{1}{2}\mathcal{X}_{1,1}, x_2^{(n)} + \frac{1}{2}\mathcal{X}_{2,1}\right) \tag{5.16}$$

$$\mathcal{X}_{2,2} = \mathcal{F}_2\left(t^{(n)} + \frac{\Delta t}{2}, x_1^{(n)} + \frac{1}{2}\mathcal{X}_{1,1}, x_2^{(n)} + \frac{1}{2}\mathcal{X}_{2,1}\right) \tag{5.17}$$

$$\mathcal{X}_{1,3} = \mathcal{F}_1\left(t^{(n)} + \frac{\Delta t}{2}, x_1^{(n)} + \frac{1}{2}\mathcal{X}_{1,2}, x_2^{(n)} + \frac{1}{2}\mathcal{X}_{2,2}\right) \tag{5.18}$$

$$\mathcal{X}_{2,3} = \mathcal{F}_2\left(t^{(n)} + \frac{\Delta t}{2}, x_1^{(n)} + \frac{1}{2}\mathcal{X}_{1,2}, x_2^{(n)} + \frac{1}{2}\mathcal{X}_{2,2}\right) \tag{5.19}$$

$$\mathcal{X}_{1,4} = \mathcal{F}_1\left(t^{(n)} + \frac{\Delta t}{2}, x_1^{(n)} + \frac{1}{2}\mathcal{X}_{1,3}, x_2^{(n)} + \frac{1}{2}\mathcal{X}_{2,3}\right) \tag{5.20}$$

$$\mathcal{X}_{2,4} = \mathcal{F}_2\left(t^{(n)} + \frac{\Delta t}{2}, x_1^{(n)} + \frac{1}{2}\mathcal{X}_{1,3}, x_2^{(n)} + \frac{1}{2}\mathcal{X}_{2,3}\right) \tag{5.21}$$

$$\tag{5.22}$$

i.e:

$$\mathcal{X}_{1,1} = x_2^{(n)} \tag{5.23}$$

$$\mathcal{X}_{2,1} = \frac{1}{m}\left[F^{(n)} - bx_2^{(n)} - kx_1^{(n)}\right] \tag{5.24}$$

$$\mathcal{X}_{1,2} = x_2^{(n)} + \frac{1}{2}\mathcal{X}_{2,1} \tag{5.25}$$

$$\mathcal{X}_{2,2} = \frac{1}{m}\left[F^{(n+\frac{1}{2})} - b\left(x_2^{(n)} + \frac{1}{2}\mathcal{X}_{2,1}\right) - k\left(x_1^{(n)} + \frac{1}{2}\mathcal{X}_{1,1}\right)\right] \tag{5.26}$$

$$\mathcal{X}_{1,3} = x_2^{(n)} + \frac{1}{2}\mathcal{X}_{2,2} \tag{5.27}$$

$$\mathcal{X}_{2,3} = \frac{1}{m}\left[F^{(n+\frac{1}{2})} - b\left(x_2^{(n)} + \frac{1}{2}\mathcal{X}_{2,2}\right) - k\left(x_1^{(n)} + \frac{1}{2}\mathcal{X}_{1,2}\right)\right] \tag{5.28}$$

$$\mathcal{X}_{1,4} = x_2^{(n)} + \mathcal{X}_{2,3} \tag{5.29}$$

$$\mathcal{X}_{2,4} = \frac{1}{m}\left[F^{(n+1)} - b\left(x_2^{(n)} + \mathcal{X}_{2,3}\right) - k\left(x_1^{(n)} + \mathcal{X}_{1,3}\right)\right] \tag{5.30}$$

$$\tag{5.31}$$

And finally, the solution for x and $\dot{x}$ is given by:

$$\begin{aligned} x^{(n+1)} &= x_1^{(n+1)} = x_1^{(n)} + \frac{1}{6}\left(\mathcal{X}_{1,1} + 2\mathcal{X}_{1,2} + 2\mathcal{X}_{1,3} + \mathcal{X}_{1,4}\right) && (5.32) \\ \dot{x}^{(n+1)} &= x_2^{(n+1)} = x_2^{(n)} + \frac{1}{6}\left(\mathcal{X}_{2,1} + 2\mathcal{X}_{2,2} + 2\mathcal{X}_{2,3} + \mathcal{X}_{2,4}\right) && (5.33) \end{aligned}$$

The procedure can thus be summarised as follows in algorithm 5.2:

Algorithm 5.2: Fourth Order Runge-Kutta Algorithm (RK4)

```
1. From the knowledge of $m$, $b$, $k$, $F\left(t^{(n)}\right)$ and $F\left(t^{(n+1)}\right)$, Compute: $\mathcal{X}_{1,1}$, $\mathcal{X}_{2,1}$, $\mathcal{X}_{1,2}$, $\mathcal{X}_{2,2}$, $\mathcal{X}_{1,3}$, $\mathcal{X}_{2,3}$, $\mathcal{X}_{1,4}$ and $\mathcal{X}_{2,4}$
2. Compute: $x^{(n+1)} = x_1^{(n)} + \frac{1}{6}\left(\mathcal{X}_{1,1} + 2\mathcal{X}_{1,2} + 2\mathcal{X}_{1,3} + \mathcal{X}_{1,4}\right)$
   and $\dot{x}^{(n+1)} = x_2^{(n)} + \frac{1}{6}\left(\mathcal{X}_{2,1} + 2\mathcal{X}_{2,2} + 2\mathcal{X}_{2,3} + \mathcal{X}_{2,4}\right)$
```

In the procedure to determine the displacement of a given object, the axes of motion along which the object is allowed to move must be taken into consideration. Seven cases can thus be foreseen:

1. Motion in the X axis only
2. Motion in the Y axis only
3. Motion in the Z axes only
4. Motion in the X and Y axes only
5. Motion in the X and Z axes only
6. Motion in the Y and Z axes only
7. Motion in the X, Y and Z axes

Depending on the case, only certain components of displacement will be updated. The complete procedure to determine the displacement of an object in the solution domain is given in algorithm 5.3.

Algorithm 5.3: Object Structural Displacement Algorithm

```
1. Compute the coefficients: $m = 1.0$, $b = \frac{4\pi\zeta}{U}$ and $k = \left(\frac{2\pi\zeta}{U}\right)^2$
2. For i=1 to i=(num. of dimension)
    • If Motion in the $X_i$ axis is allowed
        (a) Compute $F_{x_i}\left(t^{(n+1)}\right) = \frac{C_{F_{x_i}}^{(n+1)}}{2m}$
        (b) Compute $F_{x_i}\left(t^{(n)}\right) = \frac{C_{F_{x_i}}^{(n)}}{2m}$
        (c) Set $x_i^{(n)} = x_{i_{object}}$ and $\dot{x}_i^{(n)} = \dot{x}_{i_{object}}$
        (d) Solve for $x_i{}^{(n+1)}$ and $\dot{x}_i{}^{(n+1)}$ using the RK4 method (Algorithm 5.2)
        (e) Set $x_{i_{object}}^{(n+1)} = x_i{}^{(n+1)}$ and $\dot{x}_{i_{object}}^{(n+1)} = \dot{x}_i{}^{(n+1)}$
```

5.2 Moving Grid Method

Moving an object or several in the solution domain implies the update of the mesh on which the solution is carried out to account for the displacement of the faces defining the object(s). As discussed in chapter 3, the process of re-meshing a domain, particularly a multi-block domain, can be rather complex if the quality of the grid is to be preserved. Furthermore, the re-meshing procedure can be computationally costly. A hybrid method combining the iterative lineal spring analogy (LSA) method with the algebraic transfinite interpolation (TFI) was shown to be rather attractive as it not only preserves the overall mesh quality but also is computationally efficient.

The general principles behind this method are rather simple. Two steps are taken to update the mesh as was illustrated in figure 3.3:

1. The LSA method is applied to a high level grid composed of the corners of the blocks defining the solution domain. The displacement of the block corners are thus determined.
2. For each block, the TFI method is applied to a lower level mesh, i.e. the actual block mesh, based on the calculated displacement of the block corners. The displacement of all the mesh vertices (except the corners) are thus determined.

In the following sections, the complete method to update the grid will be presented. The three dimensional LSA method will be detailed focusing on the issues raised by a parallel multi-block system. The three-dimensional TFI method will then be described in three steps: the update of the block edges, block faces and block internal vertices.

5.2.1 High Level Grid Motion - The LSA Method

The first step in the update of the mesh describing the solution domain consists of the global deformation of the various blocks composing that domain. This global deformation only affects the corners of the blocks. It is thus important to distinguish between three types of corners:

- Fixed corners, i.e. corners lying on the boundaries of the domain
- Explicitly moving corners, i.e. corners moving according to the motion of part of the domain boundary
- Interface corners, i.e. corners shared by at least two adjacent blocks

In the first two cases, the displacement of the considered corners is set explicitly: either it is nil or it matches the displacement of an object lying on a face connected to that corner.

In the last case, the corners being vertices in the middle of the domain cannot be displaced explicitly. The LSA method is thus applied to this type of corners.

Supposing that at a specific corner requiring to be updated, there are n edges connected and that each of these edges connects the specific corner to another block corner, then the LSA method is interpreted by the following dynamic equilibrium:

$$\sum_{j=1}^{n} \left[k_j \left(\Delta \mathbf{x}_{corner} - \Delta \mathbf{x}_j\right)\right] = 0 \tag{5.34}$$

where $\Delta \mathbf{x}_{corner}$ is the displacement vector of the considered corner, $\Delta \mathbf{x}_j$ corresponds to the displacement vector of the other corner defining edge j, and k_j is the stiffness of edge j defined by:

$$k_j = \frac{1}{l_j} \tag{5.35}$$

with l_j the length of the edge j.

Thus, if all the displacements $\Delta \mathbf{x}_j$ are known, the displacement of the considered corner can be explicitly calculated from:

$$\Delta \mathbf{x}_{corner} = \frac{\sum_{j=1}^{n} \left(k_j \Delta \mathbf{x}_j\right)}{\sum_{j=1}^{n} k_j} \tag{5.36}$$

Separating the known (explicitly set) from the unknown (interface) corner displacements, the following can be written:

$$\left(\sum_{j=1}^{n} k_j\right) \Delta \mathbf{x}_{corner} - \sum_{j_{unknown}} \left(k_j \Delta \mathbf{x}_j\right) = \sum_{j_{known}} \left(k_j \Delta \mathbf{x}_j\right) \tag{5.37}$$

For each moving block corner, equation (5.37) needs to be solved. The complete system thus takes the form of:

$$A \mathbf{\Delta X} = \mathbf{B} \tag{5.38}$$

Where A is the matrix of coefficients to be applied to the unknown displacements, $\mathbf{\Delta X}$ is the vector of the unknown corner displacements and $\mathbf{B}$ is the vector corresponding to the right hand side of equation (5.37).

As seen in chapter (4), such a system of equations can be solved using an iterative method such as the SOR or CG method. Owing to the parallel multi-block aspect of the solution, this could be achieved using two different approaches.

The first approach would consists of solving the complete system on one processor, thus implying that the data related to the high level grid be sent and stored on a single processing unit. The high level grid would then be updated on that processing unit and the updated block corner positions sent to the corresponding block processing units. Although this approach offers the advantage of allowing faster iterative solvers to be used, it results in a rather complex procedure to gather and re-distribute all the data that could affect the computational efficiency.

In the second approach, each block processing unit updates the displacement of the corners of its own block, exchanging information only with the adjacent blocks. The parallel communication layout is thus much simpler than for the first approach. However, this second approach presents the inconvenience of restricting the choice of iterative solver to be used. To avoid the non-matching of the corners displacement, the iterative solver to be employed can only use data from a previous iteration to compute the new displacements. Thus the GS or SOR algorithms are inadequate for such purposes. Furthermore, since the high level mesh is composed of a very small amount of vertices in comparison to the complete mesh, very few iterations will be required to reach a converged solution. The CG method might therefore prove computationally inefficient in comparison to a simpler Jacobi method.

The adopted method, i.e. the second approach, consists therefore in setting the explicitly displaced corners and then solving iteratively equation (5.36), with an update of the displacements of the adjacent block corners at each iteration through an inter-process communication. Algorithm 5.4 describes the complete procedure.

It is important to note that a block corner can only be associated with the motion of a single object on the domain boundary. If several objects were to be associated with that corner, the displacement of the corner could be set by combining the motion of the two objects. However, as will be seen in the presentation of the low-level mesh update, the displacement of the block face vertices is set according to the displacement of the corners. Thus, if an object is present on the face of a block and one of the corners of that face is displaced according to the motion of another object, then the update of the mesh on that face would deform the entire face. The faces defining the object would therefore also be deformed, thus not matching anymore the object surface. As a consequence, only one object per face can be allowed, unless their motion are identical. Furthermore, to avoid the association of more than one object to a single block corner, two objects cannot be placed on block faces sharing a corner.

Algorithm 5.4: High Level Grid Motion Algorithm - LSA Method

```
1. Set $\Delta\mathbf{x}$ for the explicitly displaced corners of the local block, i.e.:
   For each block corner:
     (a) If the corners lying on a fixed domain boundary Then $\Delta\mathbf{x} = \mathbf{0}$
     (b) Else If the corners is associated with the motion of a specified object Then $\Delta\mathbf{x} = \Delta\mathbf{x}_{object}$
2. Set $\Delta\mathbf{x}$ for the other corners using the LSA method, i.e.:
   For each block corner:
    If the corners is an interface corner Then
         For k=1 to k=(max. num. of iteration)
             (a) Compute $\Delta\mathbf{x}_{corner} = \frac{\sum_{j=1}^{n}(k_j \Delta\mathbf{x}_j)}{\sum_{j=1}^{n} k_j}$
             (b) (MPI: Send & Receive) Exchange corner displacement with neighbouring blocks
```

5.2.2 Low Level Grid Motion - The TFI Method

Having displaced the corners of each blocks according to the motion of the object(s) in the domain, the position of the remaining vertices defining each block must be updated. In the case of a multi-block configuration, the update procedure must guarantee the matching of the faces of two adjacent blocks. The transfinite interpolation method was chosen as it satisfies such a necessary condition (see chapter 3).

Three steps are required to carry out the complete update of the block vertices:

- First, the displacements of the vertices on the block edges are determined from the motion of the block corners using a one-dimensional transfinite interpolation (1D-TFI).
- Then, the vertices on the faces of the blocks are displaced using a two-dimensional transfinite interpolation of the displacement of the face edges (2D-TFI).
- Finally, the block interior vertices are updated using a three-dimensional interpolation of the displacement of the block faces.

The TFI method is based on the parametrisation of the mesh vertices coordinates. A simple yet effective parametrisation consists of normalising the coordinates.

A mesh vertex V is defined in the computational space by three indices i, j and k varying from 1 to i_{max}, j_{max} and k_{max} respectively. To parametrise its coordinates, one must consider the length SI, SJ and SK of the mesh curves along the lines of equal i or j or k.

$$SI_{i,j,k} = \begin{cases} 0 & \text{for } i = 1 \\ \sum_{l=2}^{i} \|\mathbf{x}_{i,j,k} - \mathbf{x}_{i-1,j,k}\| & \text{otherwise} \end{cases} \tag{5.39}$$

$$SJ_{i,j,k} = \begin{cases} 0 & \text{for } j = 1 \\ \sum_{l=2}^{j} \|\mathbf{x}_{i,j,k} - \mathbf{x}_{i,j-1,k}\| & \text{otherwise} \end{cases} \tag{5.40}$$

$$SK_{i,j,k} = \begin{cases} 0 & \text{for } k = 1 \\ \sum_{l=2}^{k} \|\mathbf{x}_{i,j,k} - \mathbf{x}_{i,j,k-1}\| & \text{otherwise} \end{cases} \tag{5.41}$$

Where $\mathbf{x}$ are the mesh vertices cartesian coordinates.

The parametrised coordinates ϕ, χ and ψ of a vertex are thus defined by:

$$\phi_{i,j,k} = \begin{cases} 0 & \text{for } i = 1 \\ \frac{SI_{i,j,k}}{SI_{i_{max},j,k}} & \text{otherwise} \end{cases} \tag{5.42}$$

$$\chi_{i,j,k} = \begin{cases} 0 & \text{for } j = 1 \\ \frac{SJ_{i,j,k}}{SJ_{i,j_{max},k}} & \text{otherwise} \end{cases} \tag{5.43}$$

$$\psi_{i,j,k} = \begin{cases} 0 & \text{for } k = 1 \\ \frac{SK_{i,j,k}}{SK_{i,j,k_{max}}} & \text{otherwise} \end{cases} \tag{5.44}$$

Edge Motion - 1D TFI

Using the parametric coordinates, the edges of the block can simply be update according to the type of edge.

For an edge along the i direction, i.e. where (j, k) is one of $(1, 1)$, $(j_{max}, 1)$, (j_{max}, k_{max}) or $(1, k_{max})$:

$$\Delta\mathbf{x}_{i,j,k} = (1 - \phi_{i,j,k})\,\Delta\mathbf{x}_{1,j,k} + \phi_{i,j,k}\Delta\mathbf{x}_{i_{max},j,k} \tag{5.45}$$

For an edge along the j direction, i.e. where (i, k) is one of $(1, 1)$, $(i_{max}, 1)$, (i_{max}, k_{max}) or $(1, k_{max})$:

$$\Delta\mathbf{x}_{i,j,k} = (1 - \chi_{i,j,k})\,\Delta\mathbf{x}_{i,1,k} + \chi_{i,j,k}\Delta\mathbf{x}_{i,j_{max},k} \tag{5.46}$$

Finally, for an edge along the k direction, i.e. where (i, j) is one of $(1, 1)$, $(i_{max}, 1)$, (i_{max}, j_{max}) or $(1, j_{max})$:

$$\Delta\mathbf{x}_{i,j,k} = (1 - \psi_{i,j,k})\,\Delta\mathbf{x}_{i,j,1} + \psi_{i,j,k}\Delta\mathbf{x}_{i,j,k_{max}} \tag{5.47}$$

The update of the vertices lying on a block edge depends only on the displacement of the corners of the block and the parametrised coordinates. Since the corners are displaced identically on an interface between two blocks and since the parametrisation of the coordinates of the vertices lying on the edges is the same for the two adjacent blocks, the edges are exactly matched between two adjacent blocks.

Face Motion - 2D TFI

The displacement of the vertices lying on the faces of the block can then be carried out by interpolating the displacements of the face edges.

For a vertex on a face of constant i, i.e. $i = 1$ or $i = i_{max}$:

$$\begin{aligned}
\Delta\mathbf{x}_{i,j,k} \;=\;& \left(1-\psi_{i,j,k}\right)\Delta\mathbf{x}_{i,j,1} + \psi_{i,j,k}\Delta\mathbf{x}_{i,j,k_{max}} \\
&+ \left(1-\chi_{i,j,k}\right)\Delta\mathbf{x}_{i,1,k} + \chi_{i,j,k}\Delta\mathbf{x}_{i,j_{max},k} \\
&- \left(1-\psi_{i,j,k}\right)\left(1-\chi_{i,j,k}\right)\Delta\mathbf{x}_{i,1,1} - \psi_{i,j,k}\left(1-\chi_{i,j,k}\right)\Delta\mathbf{x}_{i,1,k_{max}} \\
&- \left(1-\psi_{i,j,k}\right)\chi_{i,j,k}\Delta\mathbf{x}_{i,j_{max},1} - \psi_{i,j,k}\chi_{i,j,k}\Delta\mathbf{x}_{i,j_{max},k_{max}}
\end{aligned} \tag{5.48}$$

For a vertex on a face of constant j, i.e. $j = 1$ or $j = j_{max}$:

$$\begin{aligned}
\Delta\mathbf{x}_{i,j,k} \;=\;& \left(1-\psi_{i,j,k}\right)\Delta\mathbf{x}_{i,j,1} + \psi_{i,j,k}\Delta\mathbf{x}_{i,j,k_{max}} \\
&+ \left(1-\phi_{i,j,k}\right)\Delta\mathbf{x}_{1,j,k} + \phi_{i,j,k}\Delta\mathbf{x}_{i_{max},j,k} \\
&- \left(1-\psi_{i,j,k}\right)\left(1-\phi_{i,j,k}\right)\Delta\mathbf{x}_{1,j,1} - \psi_{i,j,k}\left(1-\phi_{i,j,k}\right)\Delta\mathbf{x}_{1,j,k_{max}} \\
&- \left(1-\psi_{i,j,k}\right)\phi_{i,j,k}\Delta\mathbf{x}_{i_{max},j,1} - \psi_{i,j,k}\phi_{i,j,k}\Delta\mathbf{x}_{i_{max},j,k_{max}}
\end{aligned} \tag{5.49}$$

And finally, for a vertex on a face of constant k, i.e. $k = 1$ or $k = k_{max}$:

$$\begin{aligned}
\Delta\mathbf{x}_{i,j,k} \;=\;& \left(1-\chi_{i,j,k}\right)\Delta\mathbf{x}_{i,1,k} + \chi_{i,j,k}\Delta\mathbf{x}_{i,j_{max},k} \\
&+ \left(1-\phi_{i,j,k}\right)\Delta\mathbf{x}_{1,j,k} + \phi_{i,j,k}\Delta\mathbf{x}_{i_{max},j,k} \\
&- \left(1-\chi_{i,j,k}\right)\left(1-\phi_{i,j,k}\right)\Delta\mathbf{x}_{1,1,k} - \chi_{i,j,k}\left(1-\phi_{i,j,k}\right)\Delta\mathbf{x}_{1,j_{max},k} \\
&- \left(1-\chi_{i,j,k}\right)\phi_{i,j,k}\Delta\mathbf{x}_{i_{max},1,k} - \chi_{i,j,k}\phi_{i,j,k}\Delta\mathbf{x}_{i_{max},j_{max},k}
\end{aligned} \tag{5.50}$$

For similar reasons to those explained in the procedure to update the edges, the common face interfacing two adjacent blocks will be updated identically on each blocks, thus guarantying the matching of the face vertices on the two blocks.

Interior Vertex Motion - 3D TFI

Once the edges and faces of a block have been displaced, the remaining interior vertices can be displaced by interpolating the displacement of the vertices on the block faces.

The contribution of the displacement of the vertices on faces of constant i, i.e. $i = 1$ or $i = i_{max}$ is calculated as follows:

$$DI = (1 - \phi_{i,j,k}) * \Delta\mathbf{x}_{1,j,k} + \phi_{i,j,k} * \Delta\mathbf{x}_{i_{max},j,k} \tag{5.51}$$

The contribution of the displacement of the vertices on faces of constant j, i.e. $j = 1$ or $j = j_{max}$ is calculated as follows:

$$DJ = (1 - \chi_{i,j,k}) * \Delta\mathbf{x}_{i,1,k} + \chi_{i,j,k} * \Delta\mathbf{x}_{i,j_{max},k} \tag{5.52}$$

Finally, the contribution of the displacement of the vertices on faces of constant k, i.e. $k = 1$ or $k = k_{max}$ is calculated as follows:

$$DK = (1 - \psi_{i,j,k}) * \Delta\mathbf{x}_{i,j,1} + \psi_{i,j,k} * \Delta\mathbf{x}_{i,j,k_{max}} \tag{5.53}$$

The correction due to the superposition of the contribution of the displacement of vertices on faces of constant i and j can be obtained from:

$$\begin{aligned} DIJ &= (1 - \phi_{i,j,k}) * (1 - \chi_{i,j,k}) * \Delta\mathbf{x}_{1,1,k} + (1 - \phi_{i,j,k}) * (\chi_{i,j,k}) * \Delta\mathbf{x}_{1,j_{max},k} \\ &\quad + (\phi_{i,j,k}) * (1 - \chi_{i,j,k}) * \Delta\mathbf{x}_{i_{max},1,k} + (\phi_{i,j,k}) * (\chi_{i,j,k}) * \Delta\mathbf{x}_{i_{max},j_{max},k} \end{aligned} \tag{5.54}$$

Similarly, the correction due to the superposition of the contribution of the displacement of vertices on faces of constant i and k can be obtained from:

$$\begin{aligned} DIK &= (1 - \phi_{i,j,k}) * (1 - \psi_{i,j,k}) * \Delta\mathbf{x}_{1,j,1} + (1 - \phi_{i,j,k}) * (\psi_{i,j,k}) * \Delta\mathbf{x}_{1,j,k_{max}} \\ &\quad + (\phi_{i,j,k}) * (1 - \psi_{i,j,k}) * \Delta\mathbf{x}_{i_{max},j,1} + (\phi_{i,j,k}) * (\psi_{i,j,k}) * \Delta\mathbf{x}_{i_{max},j,k_{max}} \end{aligned} \tag{5.55}$$

The correction due to the superposition of the contribution of the displacement of vertices on faces of constant j and k can be obtained from:

$$\begin{aligned} DJK &= (1 - \chi_{i,j,k}) * (1 - \psi_{i,j,k}) * \Delta\mathbf{x}_{i,1,1} + (1 - \chi_{i,j,k}) * (\psi_{i,j,k}) * \Delta\mathbf{x}_{i,1,k_{max}} \\ &\quad + (\chi_{i,j,k}) * (1 - \psi_{i,j,k}) * \Delta\mathbf{x}_{i,j_{max},1} + (\chi_{i,j,k}) * (\psi_{i,j,k}) * \Delta\mathbf{x}_{i,j_{max},k_{max}} \end{aligned} \tag{5.56}$$

Similarly, the correction due to the superposition of all the contributions is determined as follows:

$$
\begin{aligned}
DIJK \;=\;& (1-\phi_{i,j,k}) * (1-\chi_{i,j,k}) * (1-\psi_{i,j,k}) * \Delta\mathbf{x}_{1,1,1} \\
&+ (1-\phi_{i,j,k}) * (1-\chi_{i,j,k}) * (\psi_{i,j,k}) * \Delta\mathbf{x}_{1,1,k_{max}} \\
&+ (1-\phi_{i,j,k}) * (\chi_{i,j,k}) * (1-\psi_{i,j,k}) * \Delta\mathbf{x}_{1,j_{max},1} \\
&+ (1-\phi_{i,j,k}) * (\chi_{i,j,k}) * (\psi_{i,j,k}) * \Delta\mathbf{x}_{1,j_{max},k_{max}} \\
&+ (\phi_{i,j,k}) * (1-\chi_{i,j,k}) * (1-\psi_{i,j,k}) * \Delta\mathbf{x}_{i_{max},1,1} \\
&+ (\phi_{i,j,k}) * (1-\chi_{i,j,k}) * (\psi_{i,j,k}) * \Delta\mathbf{x}_{i_{max},1,k_{max}} \\
&+ (\phi_{i,j,k}) * (\chi_{i,j,k}) * (1-\psi_{i,j,k}) * \Delta\mathbf{x}_{i_{max},j_{max},1} \\
&+ (\phi_{i,j,k}) * (\chi_{i,j,k}) * (\psi_{i,j,k}) * \Delta\mathbf{x}_{i_{max},j_{max},k_{max}}
\end{aligned}
\tag{5.57}
$$

Finally, the displacement of an interior vertex can be calculated from:

$$\Delta\mathbf{x}_{i,j,k} = DI + DJ + DK - DIJ - DIK - DJK + DIJK \tag{5.58}$$

The simplified algorithm for the TFI method is presented in the algorithm below (5.5).

Algorithm 5.5: Low Level Grid Motion Algorithm - TFI Method

1. Initialisation
    - (a) Compute the block mesh curve length SI, SJ and SK
    - (b) Compute the parametrised coordinates ϕ, χ and ψ
2. In the main loop:
    - (a) Update the block edges vertices using the 1D-TFI
    - (b) Update the block faces vertices using the 2D-TFI
    - (c) Update the block interior vertices using the 3D-TFI

5.2.3 Overall Solution Method

In a multi-block parallel method, the dynamic mesh issue is not a trivial one. Furthermore, when adopting an overlapping mesh strategy as in the present case, a layer of ghost cells surrounds the blocks. These ghost cells must therefore have a geometry. When lying on the boundary of the domain, a simple mirroring technique is used. However, when lying on an interface between two adjacent blocks, the geometry must be set so as to represent exactly the cells on the adjacent block. It follows that, when dealing with a dynamic mesh, the ghost cells geometry must be updated at the interfaces. Also, as detailed in the flow solution (chapter 4), the solution of the Poisson and Burger equations depends on Laplacians computed from the geometry of the mesh. It is thus necessary to update those Laplacians when updating the dynamic mesh.

Algorithm 5.6 below described in a simplified manner the complete dynamic grid updating procedure.

Algorithm 5.6: Grid Motion Algorithm

```
1. Grid ghost cells initialisation
    (a) Mirror the domain cells for the ghost cells lying on domain boundaries
    (b) Exchange the cell geometry for the ghost cells lying on interfaces
2. Grid Motion Initialisation
    (a) Compute the block mesh curve length $SI$, $SJ$ and $SK$
    (b) Compute the parametrised coordinates $\phi$, $\chi$ and $\psi$
3. In the main loop:
    (a) Compute the block corners displacement using the LSA method
    (b) Update the block edges, faces and interior vertices using the TFI method
    (c) Update the ghost cells geometry at the interfaces
    (d) Update the Burger and Poisson equation Laplacians
```

Figure 5.1 illustrates the motion of a four blocks arrangement around a circular cylinder. As a measure of the preservation of the quality of the grid, the mesh is coloured according to the relative deformation of the cells. The mapping of colours is done by comparing the motion of the cell vertices from their original position with the motion of the cylinder. The blue area denotes cells whose shape virtually did not changed (relative displacement close to 0) while the red area describes the largest shape change (up to 0.8 cylinder diameter). As expected, the shape of the mesh elements close to the cylinder where the original mesh is denser remain similar throughout the motions. On the other hand, those close to the domain boundary where the original mesh is coarser, deform more significantly. It can thus be concluded that the quality of the mesh is preserved by the moving mesh method.

5.3 Solution Procedure

As seen in the previous sections, a complete solution involves quite a number of parts. An initialisation part where the domain is decomposed into blocks, interfaces defined, and a layer of ghost cells created. In the case of a static mesh, the flow solution is then carried out by solving the Burger, Poisson and projection equations. In the more complex case of a dynamic mesh problem, the

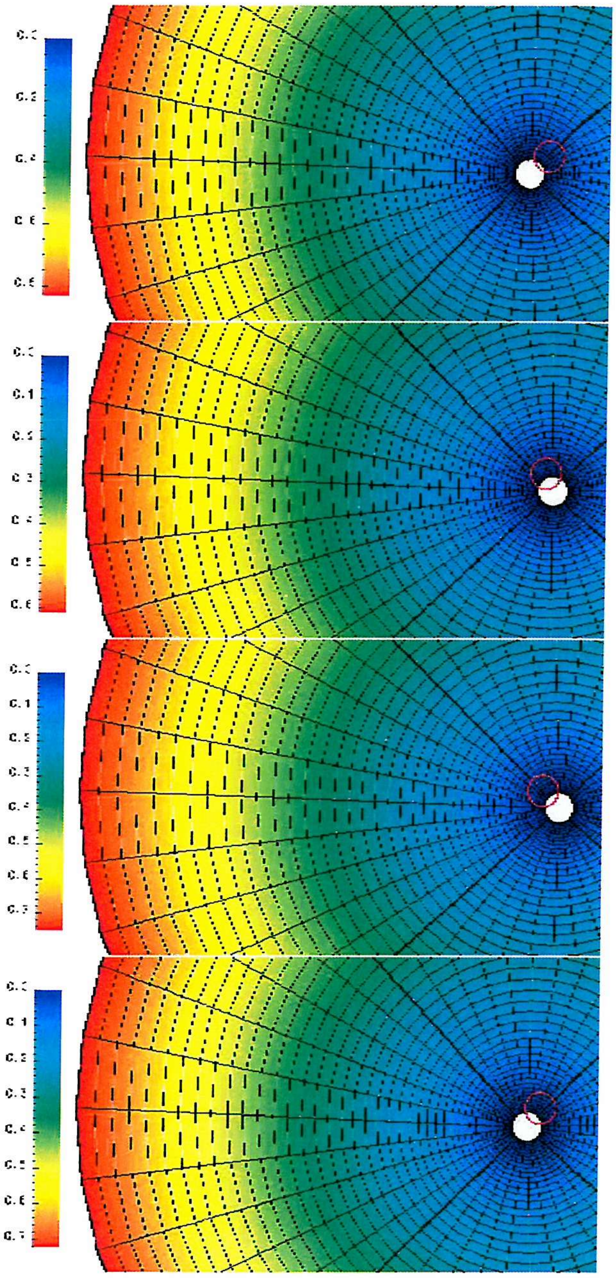

Figure 5.1: Grid Motion - 4 Blocks Arrangement

solution must incorporate the update of the mesh itself, but also the update of the Laplacian used by the Burger and Poisson solvers. In both cases, if a turbulent model is being used, then the turbulent Reynolds number must be computed.

Algorithm 5.7 summarises the complete solution procedure.

Algorithm 5.7: Complete Solution Algorithm

```
1. Read the input files
    (a) Read the general information file
    (b) Read the block information file
    (c) Read the grid files (each proc. reads its own)
2. Initialise the ghost cells
    (a) Initialise the block interface(s)
    (b) Set the boundary constants and variables in the ghost cells
    (c) Determine the ghost cells mesh geometry:
        • At the domain boundary (mirror of domain cells)
        • At the block interface(s) (Geometry exchange with adjacent block(s))
        • At the edges and corners of the block
3. If (Dynamic Mesh) Then Initialise the dynamic mesh parameters $SI$, $SJ$, $SK$, $\phi$, $\chi$ and $\psi$
4. Compute the grid metrics $S_i^j$ and $J$
5. Compute the Burger and Poisson Laplacians
6. While ( not converged ) Or ( iter $<$ max. num. of iteration )
    (a) If (Dynamic Mesh) Then Update block mesh
    (b) If (Turbulent Model) Then Compute turbulent Reynolds number $Re_t$
    (c) Solve the Burger equations
    (d) Solve the Poisson equation
    (e) Solve the Projection equations
    (f) Compute the vorticity
    (g) Compute the forces acting on the object(s) in the domain
    (h) Compute the solution's residual
    (i) Write transient output files
7. Write output files
```

Chapter 6

Validation

6.1 Introduction

Validating a CFD method is not a trivial task. As was demonstrated in the previous chapters, a method to solve numerically a fluid dynamic problem is composed of several parts. Validating the method should thus imply the validation of each individual component of the method.

However, it is quite clear that each component of the method is inherently connected to the other ones. Thus, one cannot validate a single aspect of the method without using other components of the method. There exists however an order or hierarchy in the parts composing the method. Such an order can allow for components to be evaluated individually provided that the previous components in the hierarchy have been validated. The flow solver is at the top of the hierarchy, followed by the structural model and finally the moving grid method.

In the following sections, the validation of the method will be presented following this hierarchy. First, the flow solver will be assessed. Then, the force description model will be investigated and finally the validation of the moving grid method will be carried out.

6.2 Flow Around an Impulsively Started Cylinder

To assess the validity of the flow solver, the problem of an impulsively started cylinder is considered. A cylinder initially at rest is set in motion at a constant velocity and the wake behind the cylinder observed in the initial stages thus enabling the creation, diffusion and convection effects to be evaluated.

In their experiments, Bouard and Coutanceau [8] used a visualisation technique to analyse the results, and in particular, to determine the main geometrical features of the recirculating zone that occurs behind the cylinder. The aim of the present numerical test is to reproduce the experimental setup and compare the data obtained numerically to those of Bouard and Coutanceau. Four different cases were simulated at Reynolds numbers of 60, 200, 550 and 3000.

6.2.1 Problem Description

Initially, the cylinder of diameter $D = 1$ is at rest in a stationary fluid. At $t > 0$, the cylinder is impulsively set in motion at a constant velocity $U_\infty = 1$. The two-dimensional flow development as shown in figure 6.1 is considered where D is the cylinder diameter, θ_s is the angle of separation, L is the length of the vortex and (a, b) are the coordinates of the main vortex centre.

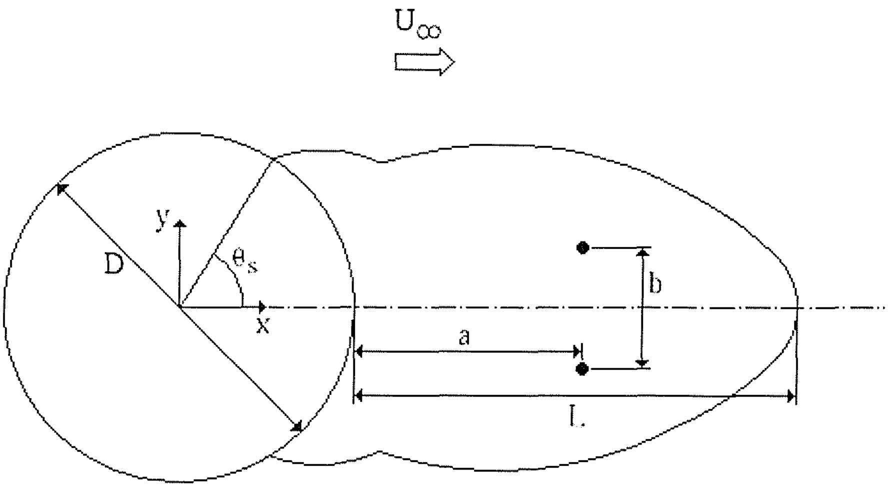

Figure 6.1: Geometrical parameters of the close wake

To carry out the test case, a square domain as shown in figure 6.2 is chosen, the boundaries of which are situated five diameters away from the centre of the cylinder. Since only the initial stages of the development of the flow are considered, such a small extent of the domain is considered sufficient to capture accurately the flow. Also, it is consistent with the general layout adopted by Bouard and Coutanceau where the cylinder of diameter varying between 3 and 15 cm in a tank of dimension 56 × 46 × 100 cm.

In a similar study, Rengel [71] used a single block mesh of identical extension and 180 × 160 elements for the Reynolds number 60 and 200. The volumes close to the cylinder surface in that case were of a size of the order of $0.01D$. However, in the case where the Reynolds number reached 550 and 3000, Rengel experienced oscillations in the solution and reduced the extension of the domain such that the outer boundaries were situated at 4 cylinder diameters from the cylinder centre. This led to a more refined grid and suppressed the numerical oscillations.

The minimum mesh size set on the surface of the cylinder is based on the dimensionless parameter y^+ representing a local Reynolds number in the near-wall region:

$$y^+ = \frac{yu_*}{\nu} \tag{6.1}$$

where y is the distance from the wall surface, $u_* = \sqrt{\frac{\tau_w}{\rho}}$ is the frictional velocity, τ_w is the shear stress at the wall, ρ is the density and ν, the kinematic viscosity.

Using the flat-plate boundary layer theory (Schlichting [74]), the parameter can be approximate by:

$$y^+ = 0.172\frac{y}{L}Re^{0.9} \tag{6.2}$$

where L is the body length and Re, the Reynolds number based on the body length.

For the present numerical solution, the chosen mesh is composed of four blocks, each composed of 512×128 volumes, thus a total of 65536 volumes. Cells on the cylinder surface are thus of a size close to $0.006D$. The same mesh is used for all the Reynolds numbers. Details of the setup including the y^+ value estimated using the above formulation for each Reynolds number are presented in table 6.1.

Reynolds number	y^+	**Grid Sizes**	**Total number of volumes**	**Volume size on cylinder surface**
60	0.04	512×128	65536	$0.006D$
200	0.12			
550	0.30			
3000	1.39			

Table 6.1: Impulsively Started Cylinder - Grid details

On the left, upper and lower boundary, a uniform inflow velocity $U_\infty = 1$ is imposed, while on the right boundary, the outflow condition is enforced.

6.2.2 Numerical Solution

The choice of the time step is based on the Courant-Friedrichs-Lewy (CFL) stability restriction. According to the condition, the distance the fluid trav-

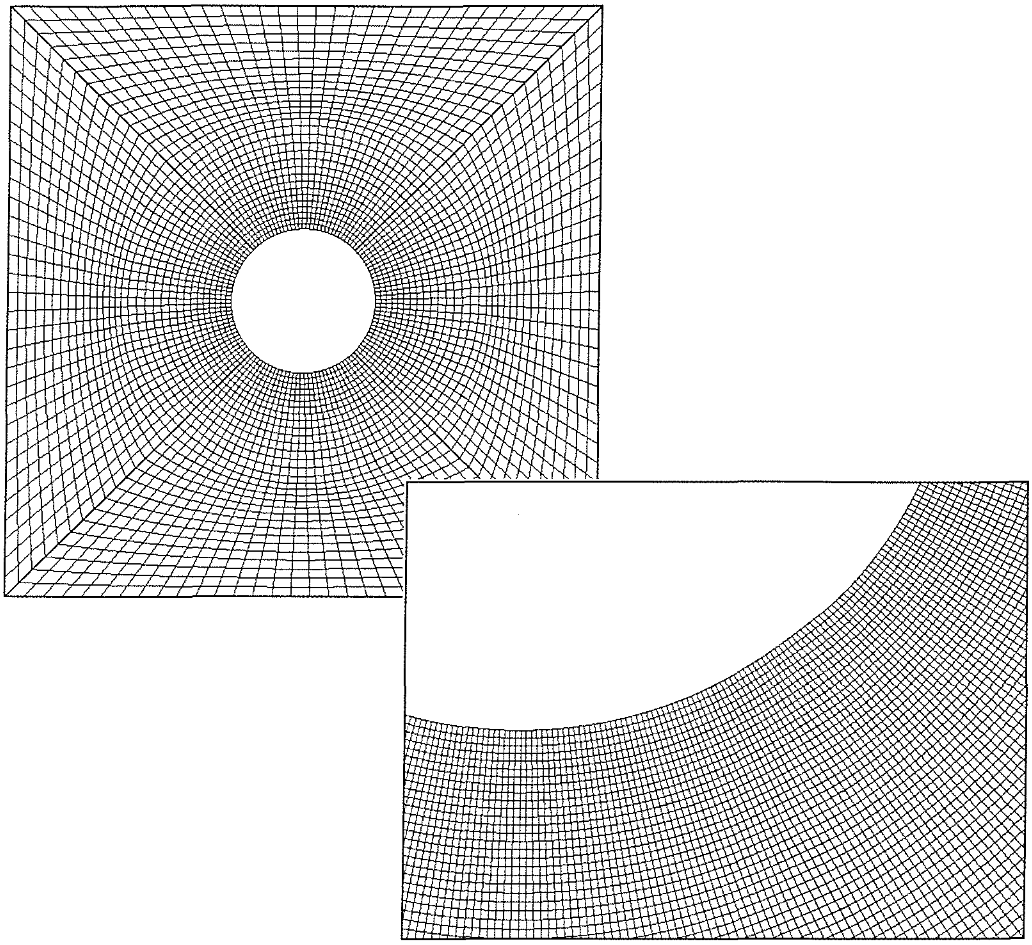

Figure 6.2: 4 Blocks mesh used for the impulsively started cylinder case
Coarse representation where each cell shown contains 4 × 4 volumes (left)
Mesh detail near the cylinder surface (right)

els in one time increment must be less than one space increment, i.e. $(\Delta t < (|u|/\Delta x + |v|/\Delta y)^{-1})$. For the four different Reynolds numbers tested, the numerical solution was carried out up to $t = 3$ with a time step $\Delta t = 5 \times 10^{-4}$ which is much less than the stability criterion ($\approx 3 \times 10^{-3}$).

To compare the results obtained with the current method to the experimental results of Bouard and Coutanceau [8], the motion and global geometry of the main vortex occurring behind the cylinder are tracked with time.

Firstly, the evolution of the streamwise component of velocity in the wake of the cylinder is monitored. Figures 6.3, 6.5, 6.7 and 6.9 show the time evolution of the streamwise component of velocity for the case at $Re = 60$, $Re = 200$, $Re = 550$ and $Re = 3000$.

Such velocity profiles enable the determination of the length of the primary vortex and its evolution with time. In figures 6.4, 6.6, 6.8 and 6.10, this characteristic vortex length is reported along with the time evolution of the coordinates of its core.

The evolution of the streamwise component of velocity and close wake length at the various Reynolds numbers considered compare very weel with the experimental data from Bouard and Coutanceau [8]. Since the vortex main geometrical parameters are well captured by the current method, a visual comparison can be made of the numerically obtained flow streamlines and the visualisation of Bouard and Coutanceau [8] as shown in figures 6.11 and 6.12 for $Re = 550$ and $Re = 3000$. The similarities between the numerical and experimental results are striking. Not only is the primary vortex well captured by the numerical method, but so are the secondary vortices appearing close to the cylinder surface.

Although the cases where the Reynolds number are 550 and 3000 will develop into a flow with three-dimensional components, the early stages of the flow are purely two-dimensional. Thus the two-dimensional numerical solution is perfectly suited to represent these cases. The agreement between the experimental and numerical data found in this case indicates that the present method reproduce accurately the diffusion and convection effects of the flow.

6.3 Flow Around a Fixed Circular Cylinder

There exist a number dynamic phenomena present in the flow around a circular cylinder. Among many, the vortex shedding that occurs for Reynolds numbers above 49 (Roshko [72]) is probably the most dominant characteristic aspect of such flows. The occurrence of the shedding of vortices in the wake of the cylinder is intrinsically linked with a non symmetrical pressure distribution around the cylinder. Furthermore, for low Reynolds numbers, both the shedding of vortices and the pressure distribution are periodic. As a consequence, the forces acting on the cylinder, whether the drag (streamwise) force or the lift (transversal) force, oscillate in a periodic fashion.

In the following section, the study of the flow past a fixed cylinder is undertaken to assess the force model of the method. Firstly, the case of a quasi-steady viscous flow is investigated to test the model in the absence of the vortex shedding. In a second part, the unsteady flow past a fixed circular cylinder is considered, thus including the effect of the vortex shedding.

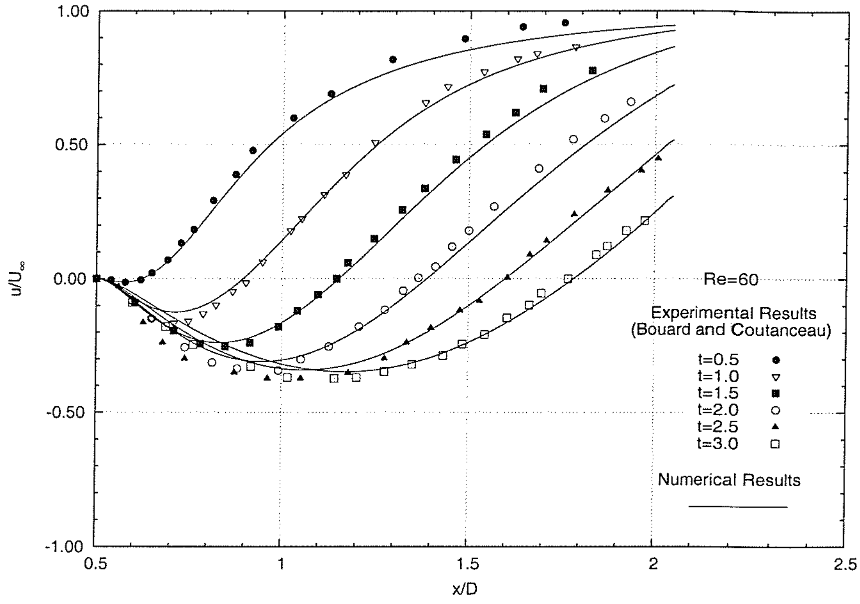

Figure 6.3: Evolution of the streamwise component of velocity on the flow axis for $Re = 60$

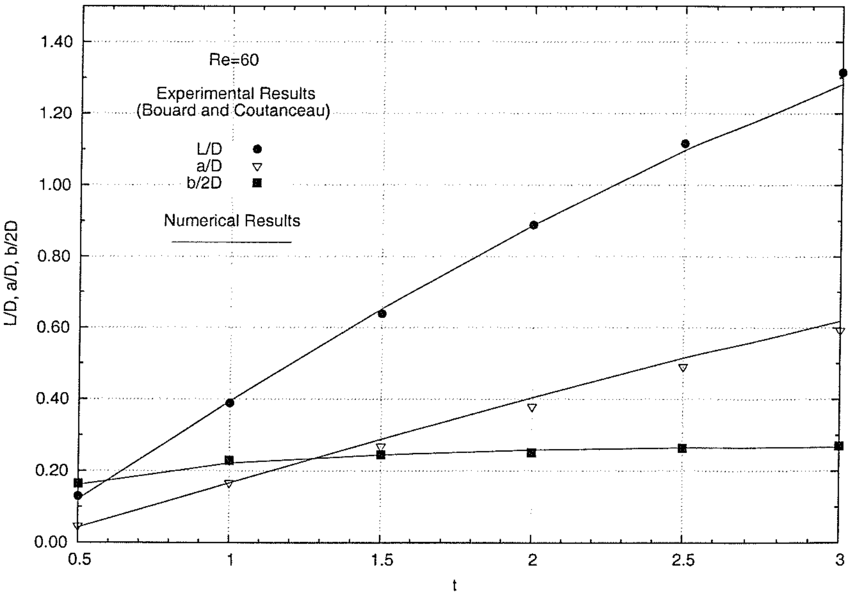

Figure 6.4: Evolution of the closed wake length and coordinates of the main eddy core for $Re = 60$

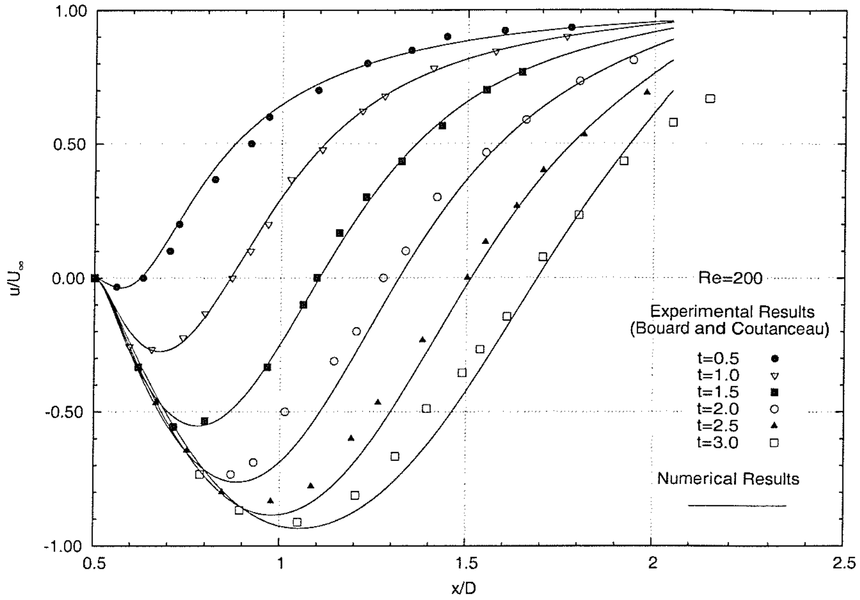

Figure 6.5: Evolution of the streamwise component of velocity on the flow axis for $Re = 200$

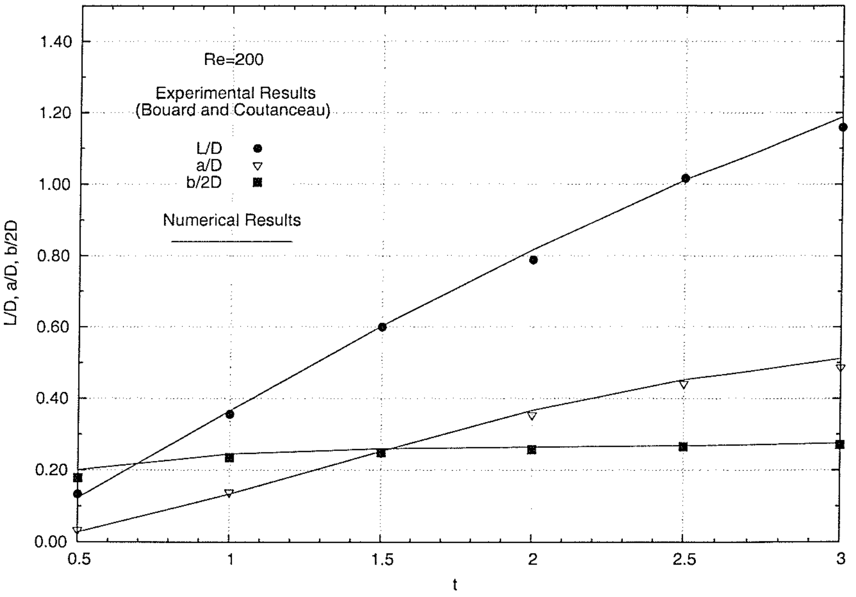

Figure 6.6: Evolution of the closed wake length and coordinates of the main eddy core for $Re = 200$

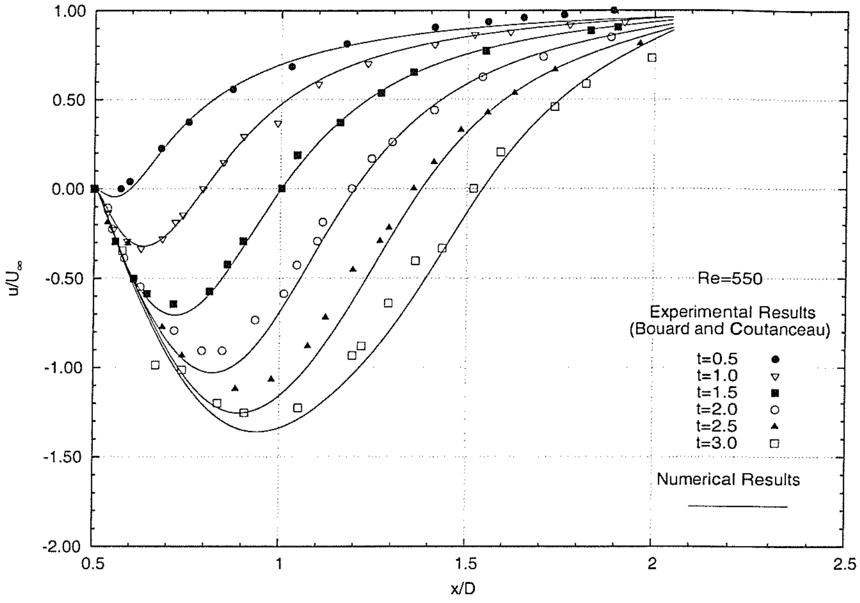

Figure 6.7: Evolution of the streamwise component of velocity on the flow axis for $Re = 550$

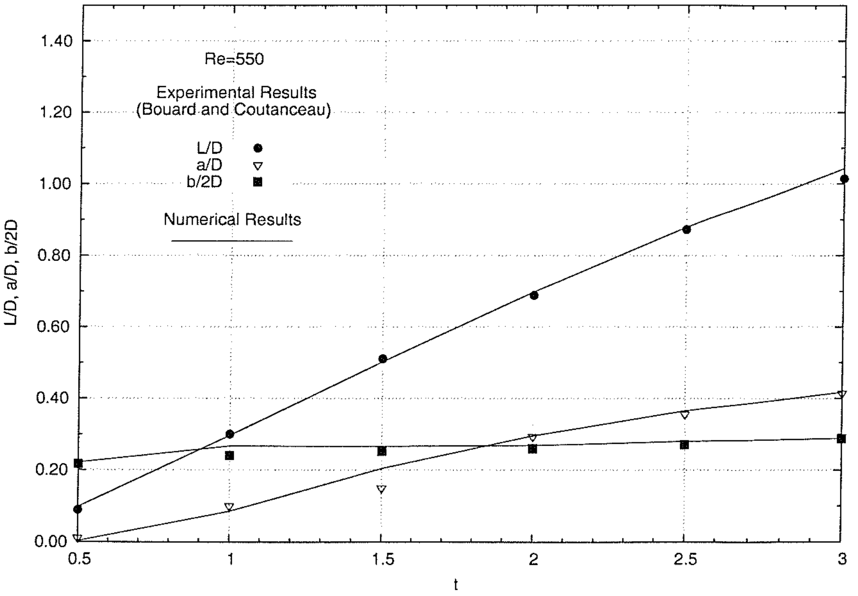

Figure 6.8: Evolution of the closed wake length and coordinates of the main eddy core for $Re = 550$

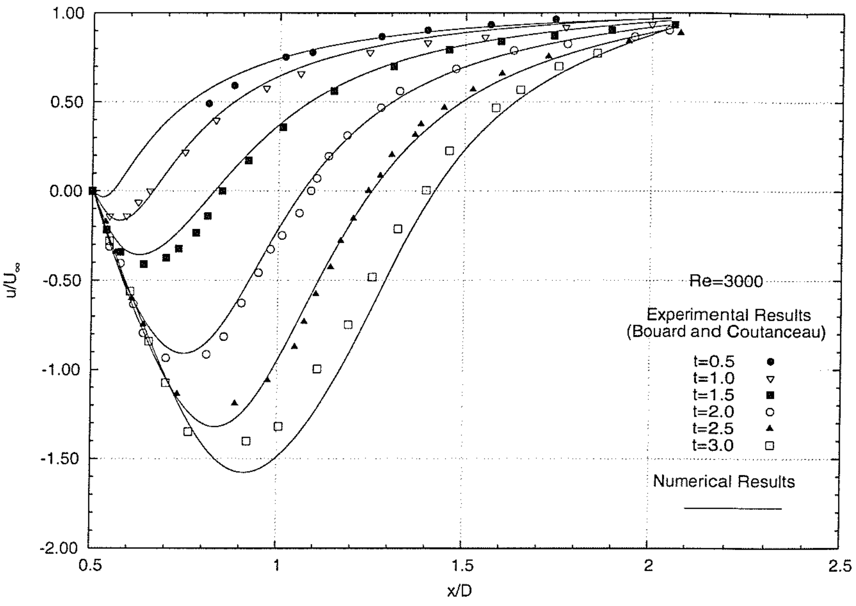

Figure 6.9: Evolution of the streamwise component of velocity on the flow axis for $Re = 3000$

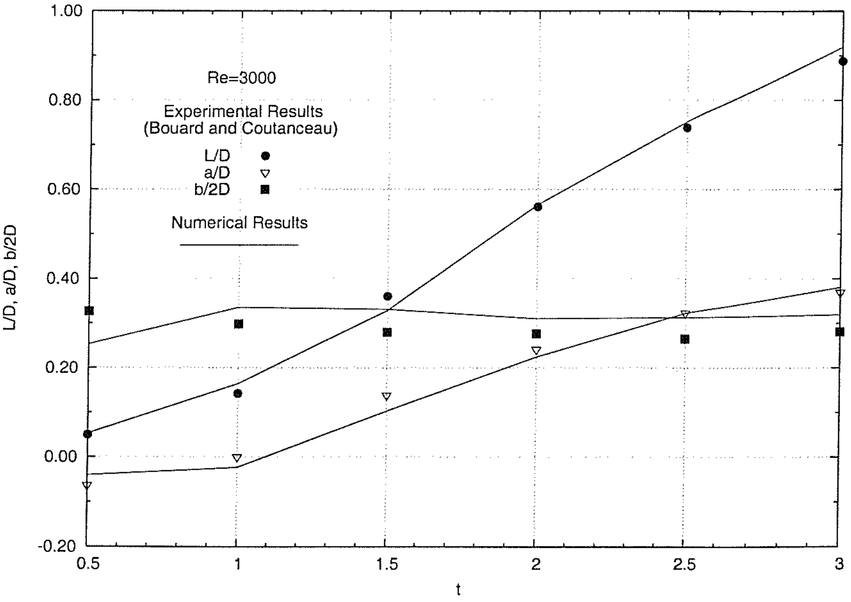

Figure 6.10: Evolution of the closed wake length and coordinates of the main eddy core for $Re = 3000$

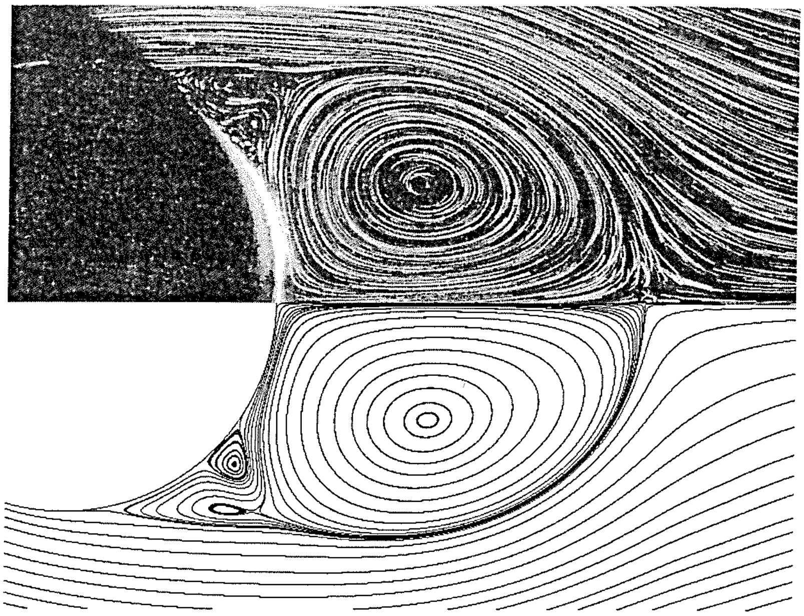

Figure 6.11: Comparison of streamlines obtained experimentally (upper) by Bouard and Coutanceau [8] and numerically (lower) for $Re = 550$ at $t = 2.5$.

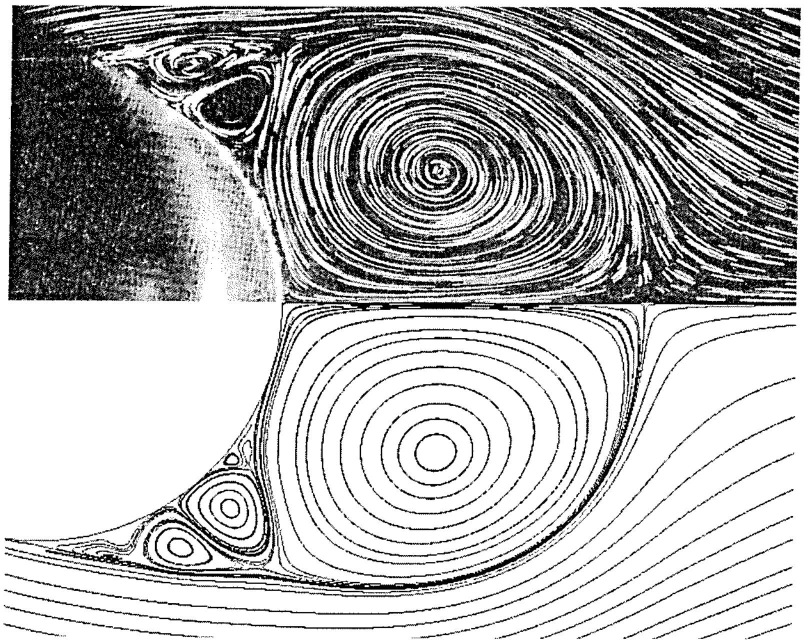

Figure 6.12: Comparison of streamlines obtained experimentally (upper) by Bouard and Coutanceau [8] and numerically (lower) for $Re = 3000$ at $t = 2.5$.

6.3.1 Steady Viscous Flow

In the steady flow past a circular cylinder, at a Reynolds number below 49, two symmetrical vortices are formed in the wake of the cylinder that remain attached to this one. One of the steady flow past a circular cylinder that has been widely reported in the literature is that at a Reynolds number of 40. As for the case of the impulsively started cylinder, the accuracy of the method can be measured through the geometrical characteristics of the wake of the cylinder, i.e. the coordinates of the core of the vortex behind the cylinder, the separation angle and the reattachment length. These characteristics have been previously described in figure 6.1.

Behr *et al.* [6] studied the effects of the location of the lateral boundary on the computation of the flow field at a Reynolds number of 100 and suggested that the external boundary of the domain should be situated at least 8 cylinder diameters away from the cylinder centre. In particular, they found that if the boundary was set closer to the cylinder, the calculated Strouhal number and other quantities could be substantially affected and thus "artificial".

For the numerical solution, an O type grid was chosen, with an outer boundary situated at 15 cylinder diameter from the cylinder centre. The grid is composed of four identical blocks dividing the domain into four quarters. Three degrees of refinement of the mesh were used, namely 64×64, 128×128, and 256×256, thus enabling a grid dependency check to be carried out. The grid is stretched in the radial direction to allow for a greater local refinement close to the cylinder surface. The refinement close to the cylinder surface is critical to obtain an accurate representation of the velocity gradients. Table 6.2 summarises the grid details for the three refinement levels including the y^+ values based on the flat-plate boundary layer theory (Schlichting [74]) and corresponding to the Reynolds numbers studied. Figures 6.13, 6.14 and 6.15 illustrate the three grids, with details being shown close to the cylinder surface.

The boundary conditions comprised a uniform inflow condition on the upstream half of the outer boundary, and an outflow condition on the other half of the outer boundary, i.e. the downstream part.

The time step was chosen so as to satisfy the CFL condition. On the 64×64 and 128×128 grids, a time step of 0.01 was used (stability limit of 0.024 and 0.012 respectively), whereas on the 256×256 grid, a time step of 0.005 was used (stability limit of 0.006). The solution was marched through time until a converged solution was reached with a residue of 10^{-9} as illustrated in figure 6.16 for the solution on the 256×256 grid.

Grid Sizes	**Time Step**	**Total number of volumes**	**Volume size on cylinder surface**	**y^+ Range for** $40 < Re < 1000$
64×64	0.01	4096	$0.0490D$	0.23 to 4.23
128×128	0.01	16384	$0.0245D$	0.12 to 2.11
256×256	0.005	65536	$0.0123D$	0.06 to 1.06

Table 6.2: Grid details

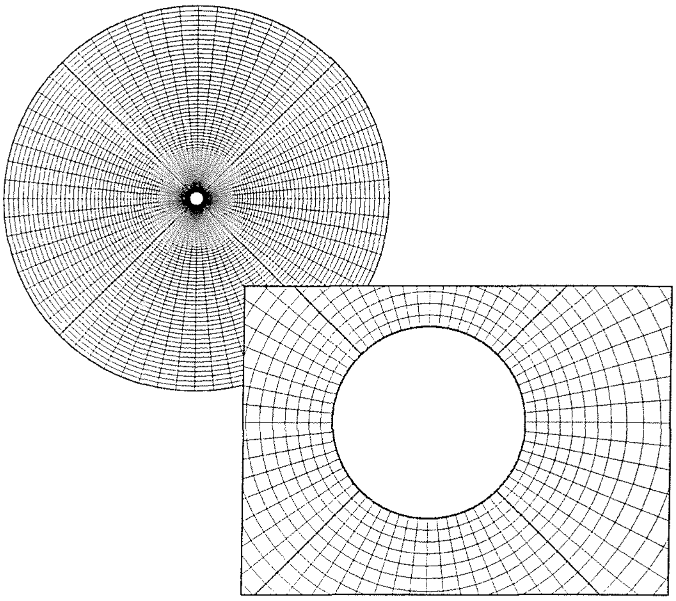

Figure 6.13: Grid 64 × 64 and details near the cylinder surface

As illustrated by figure 6.17, the two symmetrical vortices characteristic of flows at Reynolds below 49 are well reproduced by the present method. The symmetry of the flow is further shown by the distribution of the pressure around the cylinder. The pressure coefficient distribution on the surface of the cylinder is shown on figure 6.18 and exhibit the expected symmetry about the streamwise axis. The results obtained on the 64 × 64, 128 × 128 and 256 × 256 grids compare very well with the numerical results of Rengel [71]. Interestingly, the pressure coefficient at the cylinder stagnation point is greater than 1.0. Such a result is incorrect as the pressure coefficient should be at most equal to 1. However, this error has also been reported by other authors such as Rengel (num. [71]) or Tritton (exp. [84]) and is most likely due to the location of the reference pressure set in the outflow.

Details of the geometrical characteristics of the wake of the cylinder are presented in table 6.3 alongside results found in the literature. It is interesting to note that although the differences between the results obtained for the coarser grid (64 × 64) and the others are noticeable, the 128 × 128 and 256 × 256 grids

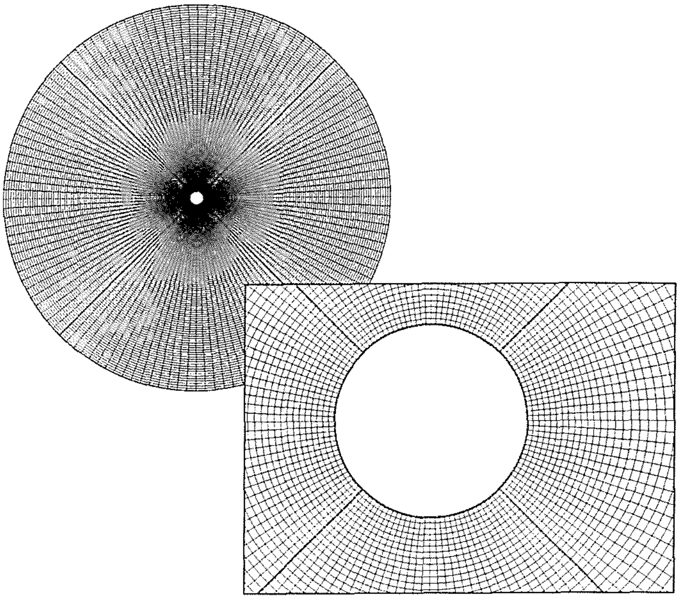

Figure 6.14: Grid 128 × 128 and details near the cylinder surface

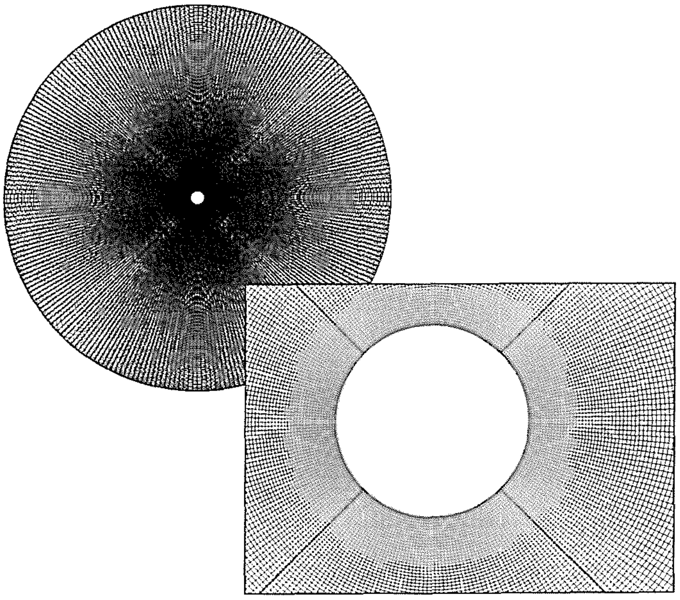

Figure 6.15: Grid 256 × 256 and details near the cylinder surface

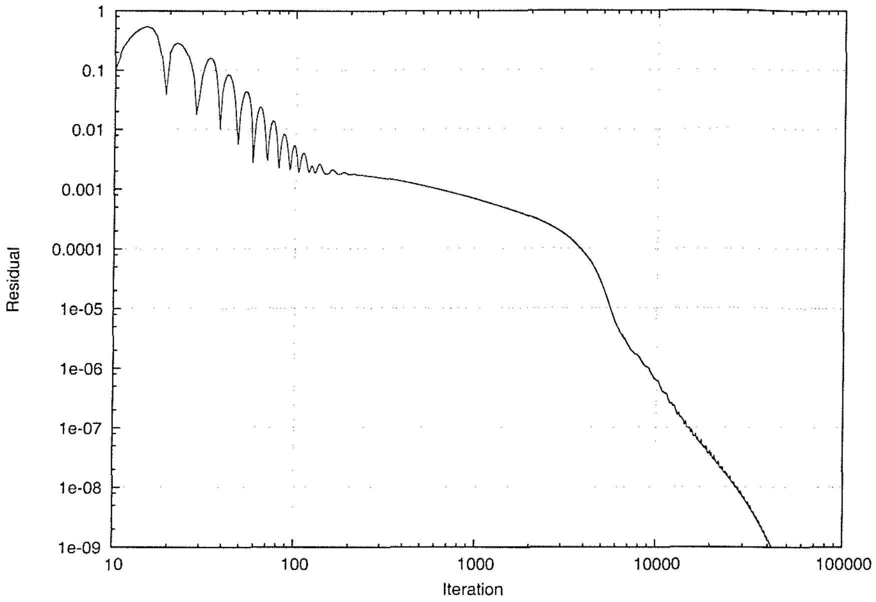

Figure 6.16: Residual history at $Re = 40$ - Grid 256 × 256

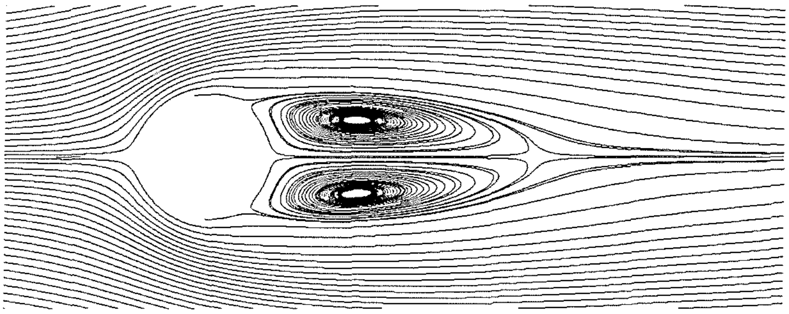

Figure 6.17: Streamlines around a circular cylinder at $Re = 40$ - Grid 128 × 128

resulted in comparable values. One can thus conclude that the results for the two finer grids are converged.

The characteristics of the wake obtained are in very good agreement with those found in the literature As far as the drag coefficient is concerned, the value of 1.55 obtained with the 256 × 256 grid seems slightly lower than the 1.60 found in most published numerical results. This could be due to the domain extension used in these solutions and how the boundary conditions are enforced. However, the drag coefficient compares well with the experimental value from Tritton [84].

The results presented here confirm that the method is able to describe accurately steady flow. Furthermore, the force model produces values in good agreement with those found in the literature

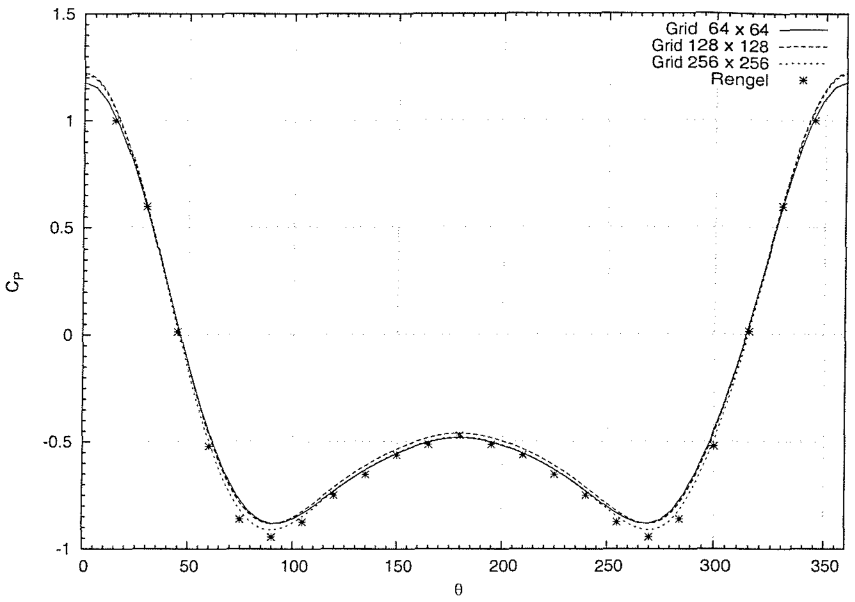

Figure 6.18: Distribution of the pressure coefficient around the cylinder surface at $Re = 40$ (θ is the angle from the point of stagnation on the cylinder)

Reference	C_D	C_v	C_p	L/D	a/D	b/D	θ_S	**Notes**	
Tritton [84]	1.57	–	–	–	–	–	–	Exp.	
Coutanceau & Bouard [7]	–	–	–	2.13	0.76	0.59	53.5	Exp.	
Rengel [71]	1.61	–	–	2.23	0.72	0.58	54.06	FV	180 × 160
Wanderley [88]	1.60	–	–	2.20	0.72	0.60	54.60	FD	100 × 100
	1.61	–	–	2.20	0.71	0.60	54.01		180 × 160
Poncet [69]	1.59	0.55	1.04	–	–	–	–	PM	256 × 256
Present Method	**1.51**	**0.48**	**1.03**	**1.96**	**0.73**	**0.56**	**51.70**	**FV**	**64 × 64**
	1.54	**0.52**	**1.02**	**2.19**	**0.72**	**0.59**	**54.55**		**128 × 128**
	1.55	**0.53**	**1.02**	**2.25**	**0.72**	**0.59**	**54.33**		**256 × 256**

Table 6.3: Summary of results for $Re = 40$.
C_v and C_p are the contribution of the viscous and pressure forces to the drag coefficient.

6.3.2 Unsteady Viscous Flow

Unsteady flows around a circular cylinder have been the focus of numerous studies as reported in chapter 1.1. In particular, the flows for Reynolds numbers varying between 40 and 1000 have been the subject of both experimental and numerical investigations, since both laminar and turbulent regimes are present in this range and plethora of results are available in the literature(Williamson [91, 92], Roshko [72], Zhang *et al.* [101], Dalton [21]). It is thus quite natural to investigate the force model by solving the flow around a circular cylinder at Reynolds numbers varying in this range.

Since most numerical solutions for the considered range have dealt with two-dimensional setup, the validation will be carried out for two-dimensional flows only. Furthermore, the two-dimensional numerical solutions obtained in the context of the validation of the method will provide a base for the comparison with the three-dimensionals solution at the same Reynolds numbers, thus allowing for the assessment of the three-dimensional effects.

Several important parameters are of particular interest when studying the solution of the unsteady flow past a cylinder. The Strouhal number is probably the most important one as it describes the frequency of the shedding of the vortices in the wake of the cylinder. Other parameters closely linked with the Strouhal number include the force coefficients, in particular the average drag coefficient, and the lift coefficient amplitude. One could also consider the various contributions to the force coefficients, i.e. the contribution of the pressure and viscous forces. These quantities will thus be the centre of attention of the validation analysis.

In the present method, the coefficients are explicitly calculated from the pressure and viscous forces contributions, and as the solution is marched through time, the history of the coefficients can easily be recorded. The calculation of the Strouhal number can be more complex. A simple method consists of dividing a known number of periods of the lift coefficient by the time length over which they occur. Such a method, although simple, is however rather inaccurate. A better approach employed here is to use the Fast Fourier transform (FFT) since the coefficients are recorded at regular time steps. Since the Fourier transform method is textbook material, its details will not be presented here.

To carry out the numerical solution for the unsteady flow past a circular cylinder, the two finer grids previously defined are used, namely the 128 × 128 and 256 × 256 grids. A total of 20 simulations are carried out for each case of turbulencemodel used, i.e. using no turbulence model, using the Smagorinsky LES model (LES-S), using the Structure Function LES model (LES-SF) and using the

Selective Structure Function LES model (LES-SSF). Table 6.4 gives a summary of the numerical solution setup.

The time step for both grids was chosen according to the same criteria as for the quasi-steady flow case. However, to account for the increase in the time rate of change of the fluid properties with the increase in the Reynolds number, it was deemed necessary to half the time steps for both grids for the Reynolds number above 400.

Re Range	**Time Step for grid 128 × 128**	**Time Step for grid 256 × 256**	**Turbulence Model**	**Simulation Time**
40-375	0.0100	0.0050	None, LES-S, LES-SF, LES-SSF	300
400-1000	0.0050	0.0025		

Table 6.4: 2D unsteady viscous flow case details

Results for all the cases can be found in tables 6.6, 6.7, 6.8, 6.9 and 6.10.

Figure 6.22 shows for the 256 × 256 grid, the history of the force coefficients along with the power spectrum associated with the lift coefficients to determine the Strouhal number.

Figures 6.23, 6.24 and 6.25 illustrate the streamlines, pressure distribution and vorticity distribution for a complete vortex shedding period for the flow at a Reynolds number of 200 on the 128 × 128 grid.

Table 6.5 presents in a comparative fashion, both the results found in the literature and those obtained in the present investigation.

Three relationships can be used to compare the results obtained using the current method with those available in the literature, namely the Strouhal, drag coefficient and lift coefficient to Reynolds number relationships. In his work, Williamson [92] provided a standard curve from experimental data for the first two relationships that will be used as a basis for comparison. The lift to Reynolds number relationship can be extracted from the literature data although there exists a relative scatter of the data for identical Reynolds numbers as can be seen from table 6.5.

The Strouhal numbers obtained with the current method do agree reasonably well with those found in the literature. This can be further noted on figure 6.19 when comparing the Strouhal-Reynolds number relationship for the various cases with the curve established by Williamson [92]. The results agree very well with

Re	S_t	C_D	C_v	C_p	C_L	Method	Source
100	0.176	1.340	0.355	0.985	0.290	PM	Poncet [69]
100	0.166	1.350	0.350	1.000	–		Henderson [36]
100	0.164	1.330	–	–	0.310		Kravchenko *et al.*[46]
100	0.163	1.330	–	–	0.195	FD	Wanderley *et al.* [88]
100	0.173	1.360	–	–	0.320		Rengel [71]
100	0.168	1.360	–	–	0.340		Herjford [37]
100	**0.166**	**1.332**	**0.314**	**1.018**	**0.331**	**128 × 128 No turb.**	
100	**0.166**	**1.332**	**0.314**	**1.018**	**0.331**	**128 × 128 LES S**	
100	**0.164**	**1.321**	**0.301**	**1.020**	**0.322**	**128 × 128 LES SF**	
100	**0.156**	**1.319**	**0.311**	**1.007**	**0.331**	**128 × 128 LES SSF**	
100	**0.166**	**1.332**	**0.326**	**1.006**	**0.330**	**256 × 256 LES SF**	
200	0.196	1.250	–	–	0.540	FD	Zhang *et al.* [100]
200	0.185	1.310	–	–	0.640	FV	Hoe-Tai *et al.* [39]
200	0.201	1.340	0.245	1.100	0.700	PM	Poncet [69]
200	0.197	1.340	0.250	1.100	–		Henderson [36]
200	0.196	1.180	–	–	0.739	FE	Sphaier *et al.* [78]
200	0.196	1.350	–	–	0.600	FV	Sphaier *et al.* [78]
200	0.192	1.320	–	–	0.534	FD	Wanderley *et al.* [88]
200	0.203	1.350	–	–	0.670		Rengel [71]
200	0.196	1.350	–	–	0.700		Herjford [37]
200	**0.205**	**1.323**	**0.215**	**1.108**	**0.695**	**128 × 128 No turb.**	
200	**0.205**	**1.324**	**0.215**	**1.109**	**0.695**	**128 × 128 LES S**	
200	**0.195**	**1.310**	**0.197**	**1.113**	**0.662**	**128 × 128 LES SF**	
200	**0.195**	**1.324**	**0.215**	**1.109**	**0.696**	**128 × 128 LES SSF**	
200	**0.200**	**1.329**	**0.229**	**1.100Herjford**	**0.679**	**256 × 256 LES SF**	
300	0.211	1.390	0.220	1.170	0.960	PM	Poncet [69]
300	0.210	1.380	0.220	1.160	–		Henderson [36]
300	**0.215**	**1.312**	**0.165**	**1.147**	**0.937**	**128 × 128 No turb.**	
300	**0.205**	**1.319**	**0.165**	**1.153**	**0.936**	**128 × 128 LES S**	
300	**0.205**	**1.337**	**0.148**	**1.190**	**0.878**	**128 × 128 LES SF**	
300	**0.205**	**1.300**	**0.164**	**1.136**	**0.944**	**128 × 128 LES SSF**	
300	**0.210**	**1.357**	**0.182**	**1.174**	**0.908**	**256 × 256 LES SF**	
325	0.206	1.400	–	–	–		Henderson [36]
325	0.210	1.400	–	–	0.950		Mittal *et al.* [61]
325	**0.210**	**1.306**	**0.156**	**1.150**	**0.984**	**128 × 128 No turb.**	
325	**0.215**	**1.313**	**0.156**	**1.157**	**0.983**	**128 × 128 LES S**	
325	**0.215**	**1.341**	**0.139**	**1.202**	**0.918**	**128 × 128 LES SF**	
325	**0.215**	**1.322**	**0.157**	**1.165**	**0.996**	**128 × 128 LES SSF**	
325	**0.215**	**1.362**	**0.174**	**1.188**	**0.950**	**256 × 256 LES SF**	
400	0.223	1.420	0.208	1.212	1.100	PM	Poncet [69]
400	0.220	1.400	0.195	1.205	1.180		Henderson [36]
400	**0.215**	**1.417**	**0.143**	**1.275**	**1.127**	**128 × 128 No turb.**	
400	**0.215**	**1.421**	**0.143**	**1.278**	**1.125**	**128 × 128 LES S**	
400	**0.221**	**1.377**	**0.120**	**1.257**	**1.017**	**128 × 128 LES SF**	
400	**0.225**	**1.345**	**0.137**	**1.208**	**1.127**	**128 × 128 LES SSF**	
400	**0.215**	**1.339**	**0.149**	**1.190**	**1.051**	**256 × 256 LES SF**	

Table 6.5: Comparison of the force coefficients at various Re
The values in bold correspond to the present method.

Re	S_t	C_D	C_v	C_p	C_L	Method	Source
500	0.229	1.440	–	–	1.180	PM	Poncet [69]
500	0.226	1.445	0.172	1.273	1.210		Henderson [36]
500	**0.234**	**1.467**	**0.123**	**1.343**	**1.266**	**128 × 128 No turb.**	
500	**0.234**	**1.467**	**0.123**	**1.344**	**1.264**	**128 × 128 LES S**	
500	**0.225**	**1.410**	**0.100**	**1.310**	**1.113**	**128 × 128 LES SF**	
500	**0.225**	**1.419**	**0.120**	**1.298**	**1.266**	**128 × 128 LES SSF**	
500	**0.234**	**1.354**	**0.128**	**1.226**	**1.149**	**256 × 256 LES SF**	
1000	0.235	1.510	–	–	1.370	FD	Wanderley *et al.* [88]
1000	0.235	1.520	–	–	1.360	FD	Wanderley *et al.* [88]
1000	0.225	1.500	–	–	1.700	FV	Rengel [71]
1000	0.234	1.470	–	–	1.450	FE	Herjford [37]
1000	**0.234**	**1.582**	**0.073**	**1.509**	**1.739**	**128 × 128 No turb.**	
1000	**0.234**	**1.595**	**0.074**	**1.522**	**1.820**	**128 × 128 LES S**	
1000	**0.234**	**1.527**	**0.061**	**1.465**	**1.500**	**128 × 128 LES SF**	
1000	**0.234**	**1.713**	**0.077**	**1.636**	**1.760**	**128 × 128 LES SSF**	
1000	**0.234**	**1.417**	**0.076**	**1.341**	**1.407**	**256 × 256 LES SF**	

Table 6.5: Continued

those of Williamson for Reynolds numbers up to about 250. For higher Reynolds numbers, there exist a relative scatter of the results. This could be due to a resolution issue in the FFT method where the frequency obtained depends highly on the time over which the sampling is taken and the number of periods occurring over that time. The error bars on the figure are an indication of the frequency resolution and thus error on the calculated Strouhal number. However, for each Reynolds number investigated, the Strouhal numbers obtained with the present method fall in the ranges found in the literature (table 6.5).

When comparing the relationship between the drag and lift coefficients and the Reynolds number as shown on figure 6.20 and 6.21, the influence of the turbulence model used for the solution can only be noted for Reynolds number above 250. This can be expected as little to no small scale instabilities are present in the flow for Reynolds number up to about 300.

In the case where no turbulence model is used, or when the Smagorinsky or Selective Structure Function are used, one can observe an over-prediction of both the lift and drag coefficients. Furthermore, the difference between the lift coefficient found numerically and the results found in the literature grows with the Reynolds number.

The Structure Function LES model whether applied using the 128 × 128 or 256 × 256 grid appears to slightly under-predict the drag coefficient for Reynolds number up to about 800. However, this model produces very good results for the lift coefficients. Also, one can note that there are very little differences between the results on the two grids for this turbulence model. Such a finding can be corroborated by those of Breuer [11] who came to the conclusion that, when using LES models, greater refinement did not automatically lead to improvements in the results. The Structure Function LES turbulence model led to a prediction of the force coefficients in better agreement with the data from Williamson [92] than other models, particularly for the 128 × 128 grid at high Reynolds numbers.

This series of tests have revealed that the Structure Function LES turbulence model was better suited to predict the viscous flow around a cylinder in the considered range of Reynolds number. Furthermore, the 128 × 128 grid is sufficiently refined to produce accurate results as far as the lift and drag coefficients are concerned. The 256 × 256 grid did not result in substantially different solutions. However, the added computational cost of such a grid makes it less favoured than the coarser 128 × 128 one for the considered range of Reynolds numbers.

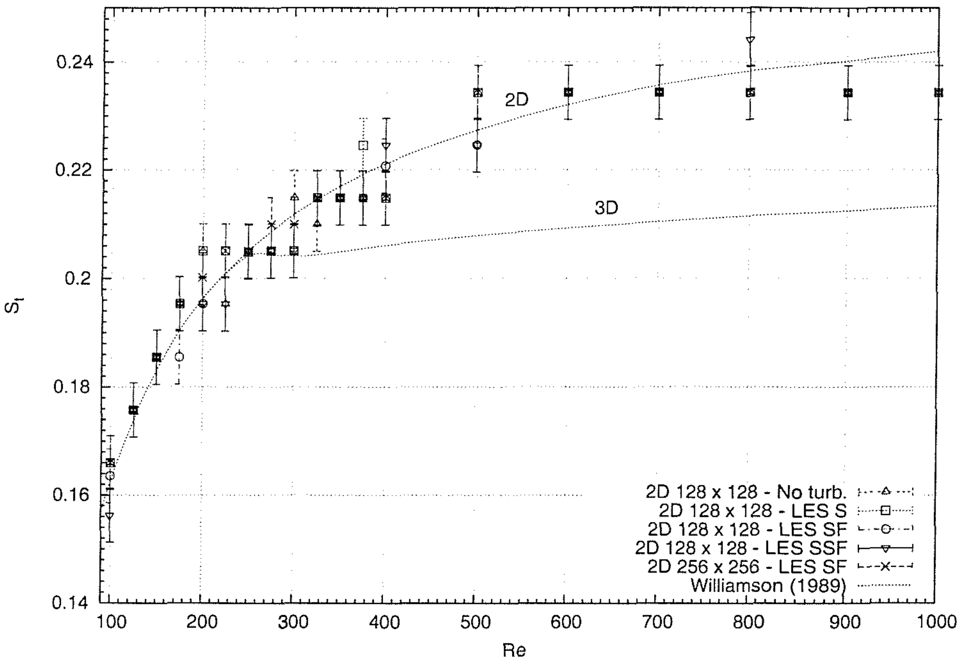

Figure 6.19: Relationship between the Strouhal and Reynolds Numbers

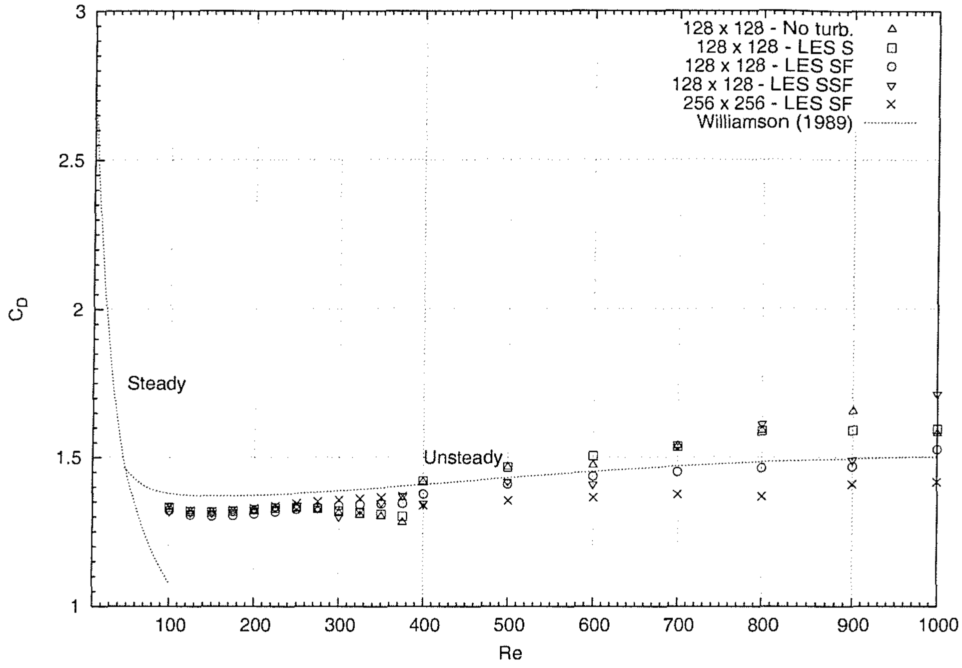

Figure 6.20: Relationship between the drag coefficient and the Reynolds Numbers

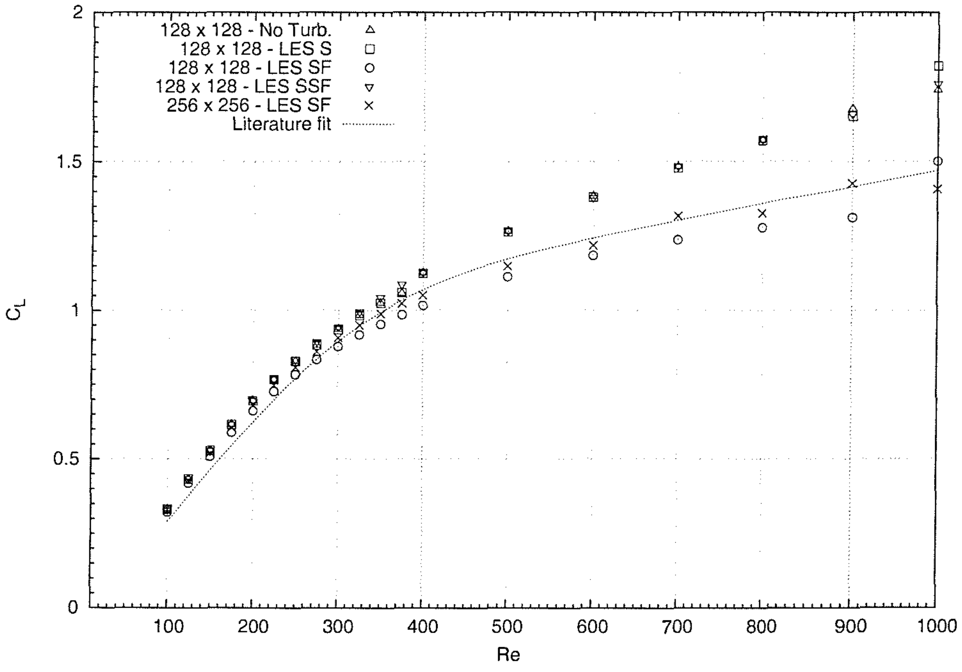

Figure 6.21: Relationship between the lift coefficient and the Reynolds Numbers

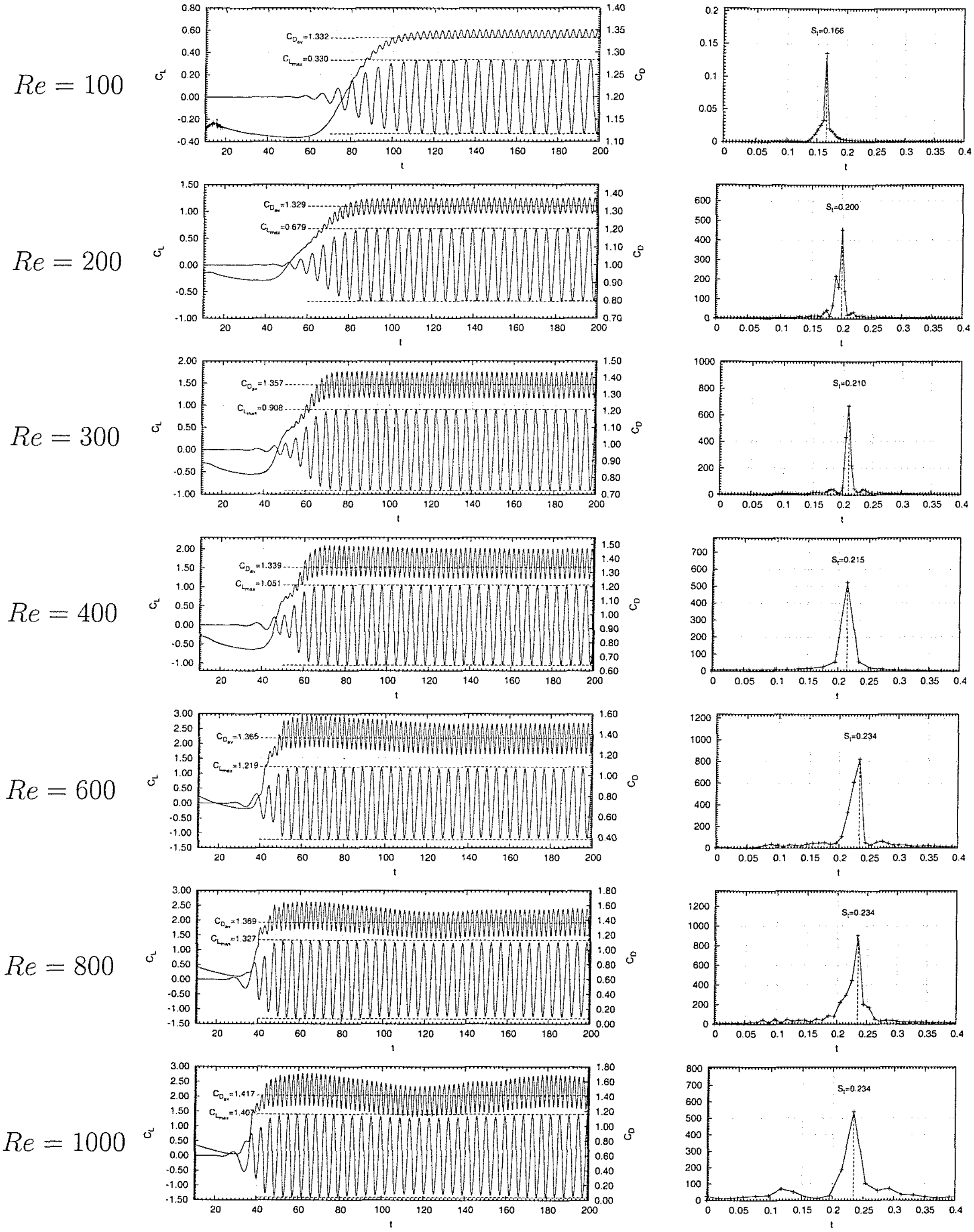

Figure 6.22: Force coefficients history (left) Power Spectrum (right)

Re	St	$\overline{C_D}$	$\overline{C_{D_v}}$	$\overline{C_{D_p}}$	$\widehat{C_L}$	$\widehat{C_{L_v}}$	$\widehat{C_{L_p}}$
40	–	1.535	0.513	1.022	0.000	0.000	0.000
100	0.166	1.332	0.314	1.018	0.331	0.039	0.299
125	0.176	1.318	0.279	1.039	0.433	0.044	0.396
150	0.186	1.315	0.253	1.062	0.528	0.048	0.488
175	0.195	1.318	0.232	1.086	0.616	0.051	0.574
200	0.205	1.323	0.215	1.108	0.695	0.052	0.652
225	0.195	1.328	0.201	1.127	0.767	0.053	0.723
250	0.205	1.329	0.188	1.141	0.828	0.054	0.785
275	0.205	1.322	0.176	1.146	0.882	0.054	0.840
300	0.215	1.312	0.165	1.147	0.937	0.053	0.894
325	0.210	1.306	0.156	1.150	0.984	0.053	0.941
350	0.215	1.302	0.147	1.154	1.025	0.052	0.983
375	0.215	1.281	0.139	1.142	1.057	0.052	1.016
400	0.215	1.417	0.143	1.275	1.127	0.051	1.087
500	0.234	1.467	0.123	1.343	1.266	0.049	1.228
600	0.234	1.473	0.107	1.366	1.383	0.046	1.349
700	0.234	1.539	0.097	1.442	1.482	0.044	1.450
800	0.234	1.590	0.089	1.502	1.571	0.042	1.540
900	0.234	1.655	0.082	1.573	1.676	0.043	1.644
1000	0.234	1.582	0.073	1.509	1.739	0.042	1.708

Table 6.6: Force coefficients for the 2D 128 × 128 grid - No turbulence model

Re	St	$\overline{C_D}$	$\overline{C_{D_v}}$	$\overline{C_{D_p}}$	$\widehat{C_L}$	$\widehat{C_{L_v}}$	$\widehat{C_{L_p}}$
40	–	1.535	0.513	1.022	0.000	0.000	0.000
100	0.166	1.332	0.314	1.018	0.331	0.038	0.298
125	0.176	1.318	0.279	1.040	0.432	0.044	0.396
150	0.186	1.315	0.253	1.063	0.527	0.048	0.488
175	0.195	1.319	0.232	1.087	0.615	0.050	0.574
200	0.205	1.324	0.215	1.109	0.695	0.052	0.652
225	0.205	1.330	0.201	1.129	0.766	0.053	0.723
250	0.205	1.333	0.188	1.144	0.829	0.053	0.785
275	0.205	1.328	0.176	1.152	0.882	0.053	0.839
300	0.205	1.319	0.165	1.153	0.936	0.053	0.893
325	0.215	1.313	0.156	1.157	0.983	0.053	0.941
350	0.215	1.309	0.148	1.162	1.025	0.052	0.983
375	0.225	1.302	0.140	1.162	1.060	0.052	1.019
400	0.215	1.421	0.143	1.278	1.125	0.051	1.085
500	0.234	1.467	0.123	1.344	1.264	0.048	1.227
600	0.234	1.505	0.108	1.396	1.380	0.046	1.346
700	0.234	1.537	0.097	1.440	1.477	0.044	1.445
800	0.234	1.589	0.088	1.501	1.571	0.042	1.540
900	0.234	1.591	0.080	1.511	1.652	0.043	1.623
1000	0.234	1.595	0.074	1.522	1.820	0.043	1.789

Table 6.7: Force coefficients for the 2D 128 × 128 grid - LES S model

Re	St	$\overline{C_D}$	$\overline{C_{D_v}}$	$\overline{C_{D_p}}$	$\widehat{C_L}$	$\widehat{C_{L_v}}$	$\widehat{C_{L_p}}$
40	–	1.537	0.513	1.024	0.000	0.000	0.000
100	0.164	1.321	0.301	1.020	0.322	0.037	0.291
125	0.176	1.306	0.264	1.042	0.419	0.042	0.384
150	0.186	1.302	0.236	1.066	0.508	0.045	0.471
175	0.186	1.304	0.214	1.090	0.589	0.046	0.550
200	0.195	1.310	0.197	1.113	0.662	0.047	0.622
225	0.205	1.317	0.182	1.136	0.726	0.048	0.687
250	0.205	1.325	0.169	1.156	0.783	0.047	0.744
275	0.205	1.331	0.158	1.173	0.834	0.047	0.795
300	0.205	1.337	0.148	1.190	0.878	0.046	0.840
325	0.215	1.341	0.139	1.202	0.918	0.045	0.881
350	0.215	1.345	0.131	1.213	0.954	0.044	0.917
375	0.215	1.345	0.124	1.221	0.985	0.043	0.950
400	0.221	1.377	0.120	1.257	1.017	0.042	0.983
500	0.225	1.410	0.100	1.310	1.113	0.037	1.083
600	0.234	1.437	0.086	1.351	1.185	0.034	1.157
700	0.234	1.452	0.076	1.376	1.237	0.030	1.213
800	0.234	1.465	0.067	1.397	1.279	0.028	1.257
900	0.234	1.469	0.060	1.409	1.312	0.025	1.292
1000	0.234	1.527	0.061	1.465	1.500	0.029	1.477

Table 6.8: Force coefficients for th 2D 128 × 128 grid - LES SF model

Re	St	$\overline{C_D}$	$\overline{C_{D_v}}$	$\overline{C_{D_p}}$	$\widehat{C_L}$	$\widehat{C_{L_v}}$	$\widehat{C_{L_p}}$
40	–	1.537	1.024	0.513	0.000	0.000	0.000
100	0.156	1.319	0.311	1.007	0.331	0.038	0.298
125	0.176	1.313	0.278	1.035	0.433	0.044	0.396
150	0.186	1.312	0.252	1.060	0.528	0.048	0.488
175	0.195	1.317	0.232	1.085	0.616	0.051	0.574
200	0.195	1.324	0.215	1.109	0.696	0.052	0.653
225	0.195	1.330	0.201	1.129	0.769	0.053	0.725
250	0.205	1.337	0.189	1.148	0.835	0.054	0.790
275	0.205	1.328	0.177	1.151	0.894	0.054	0.850
300	0.205	1.300	0.164	1.136	0.944	0.053	0.901
325	0.215	1.322	0.157	1.165	0.996	0.053	0.953
350	0.215	1.349	0.152	1.197	1.044	0.052	1.002
375	0.215	1.371	0.146	1.225	1.088	0.052	1.047
400	0.225	1.345	0.137	1.208	1.127	0.051	1.087
500	0.225	1.419	0.120	1.298	1.266	0.049	1.228
600	0.234	1.410	0.104	1.306	1.378	0.046	1.343
700	0.234	1.536	0.097	1.439	1.483	0.044	1.450
800	0.244	1.613	0.090	1.523	1.575	0.042	1.543
900	0.234	1.491	0.077	1.414	1.659	0.044	1.629
1000	0.234	1.713	0.077	1.636	1.760	0.040	1.731

Table 6.9: Force coefficients for the 2D 128 × 128 grid - LES SSF model

Re	St	$\overline{C_D}$	$\overline{C_{D_v}}$	$\overline{C_{D_p}}$	$\widehat{C_L}$	$\widehat{C_{L_v}}$	$\widehat{C_{L_p}}$
40	–	1.554	0.528	1.026	0.000	0.000	0.000
100	0.166	1.332	0.326	1.006	0.330	0.041	0.294
125	0.176	1.321	0.292	1.029	0.429	0.047	0.387
150	0.186	1.318	0.266	1.052	0.519	0.052	0.475
175	0.195	1.322	0.246	1.076	0.603	0.055	0.556
200	0.200	1.329	0.229	1.100	0.679	0.057	0.630
225	0.205	1.337	0.215	1.122	0.747	0.058	0.698
250	0.205	1.345	0.203	1.142	0.808	0.059	0.757
275	0.210	1.351	0.192	1.159	0.860	0.059	0.810
300	0.210	1.357	0.182	1.174	0.908	0.058	0.858
325	0.215	1.362	0.174	1.188	0.950	0.058	0.901
350	0.215	1.366	0.166	1.200	0.989	0.057	0.940
375	0.215	1.369	0.158	1.211	1.023	0.056	0.975
400	0.215	1.339	0.149	1.190	1.051	0.055	1.004
500	0.234	1.354	0.128	1.226	1.149	0.051	1.106
600	0.234	1.365	0.113	1.253	1.219	0.047	1.179
700	0.234	1.376	0.111	1.265	1.317	0.049	1.276
800	0.234	1.369	0.090	1.279	1.327	0.040	1.293
900	0.234	1.409	0.093	1.316	1.427	0.043	1.390
1000	0.234	1.417	0.076	1.341	1.407	0.035	1.377

Table 6.10: Force coefficients for the 2D 256 × 256 grid - LES SF model

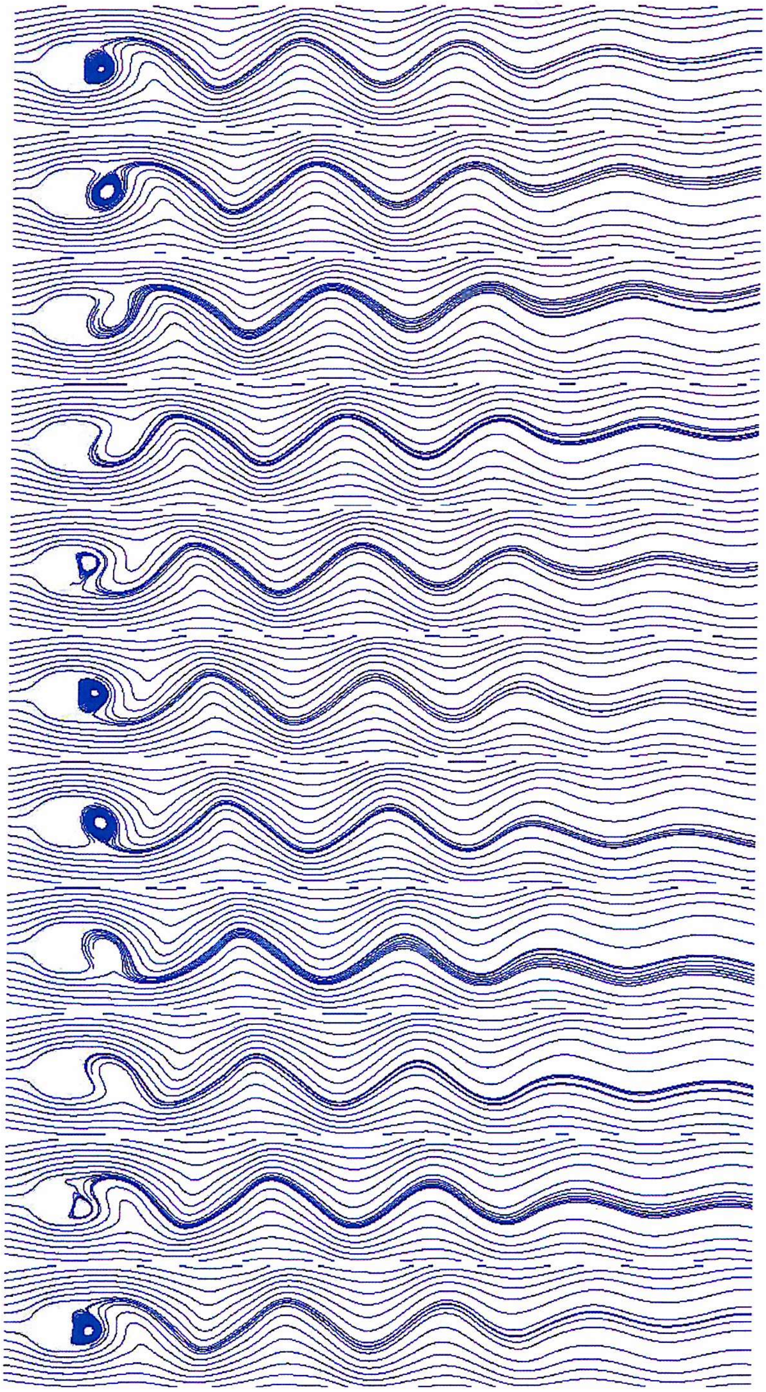

Figure 6.23: Streamlines around a circular cylinder at $Re = 200$ for a complete vortex shedding period

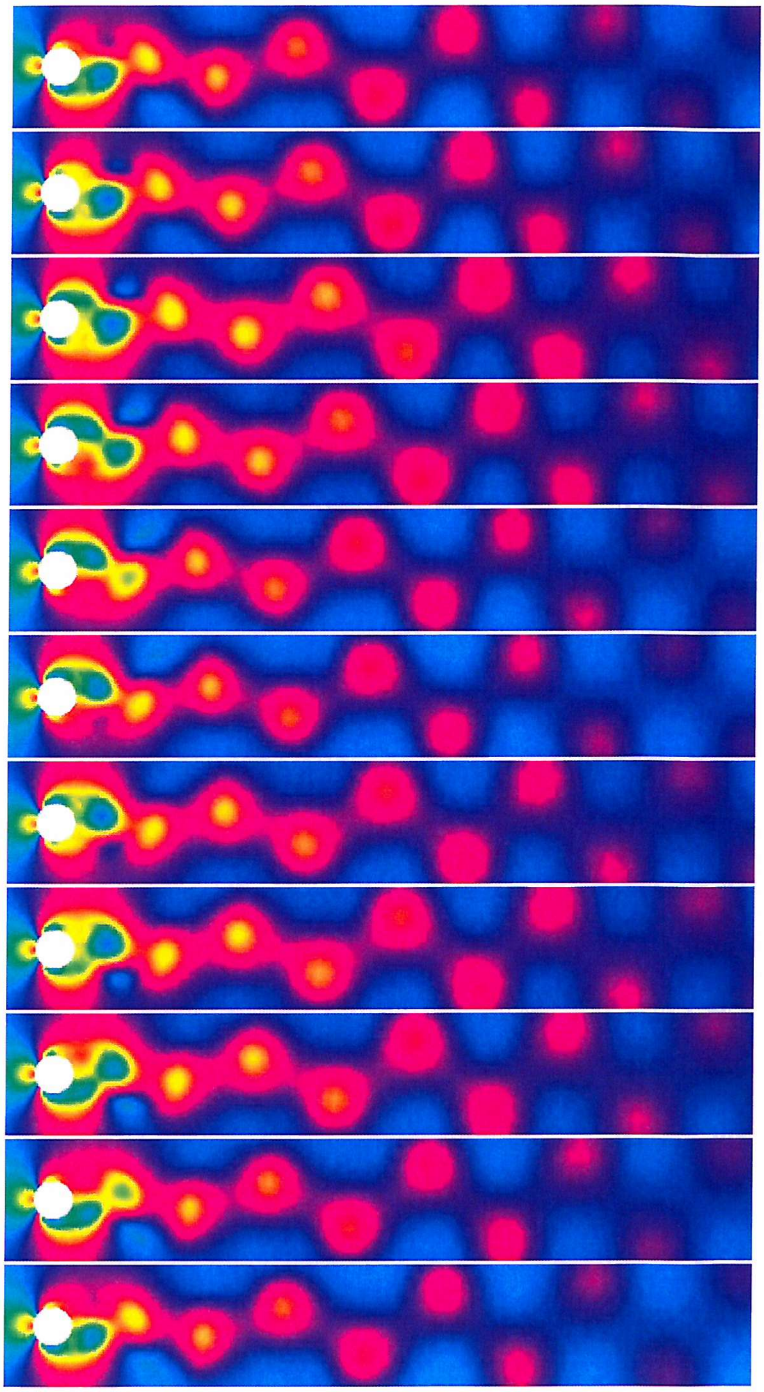

Figure 6.24: Pressure distribution around a circular cylinder at $Re = 200$ for a complete vortex shedding period

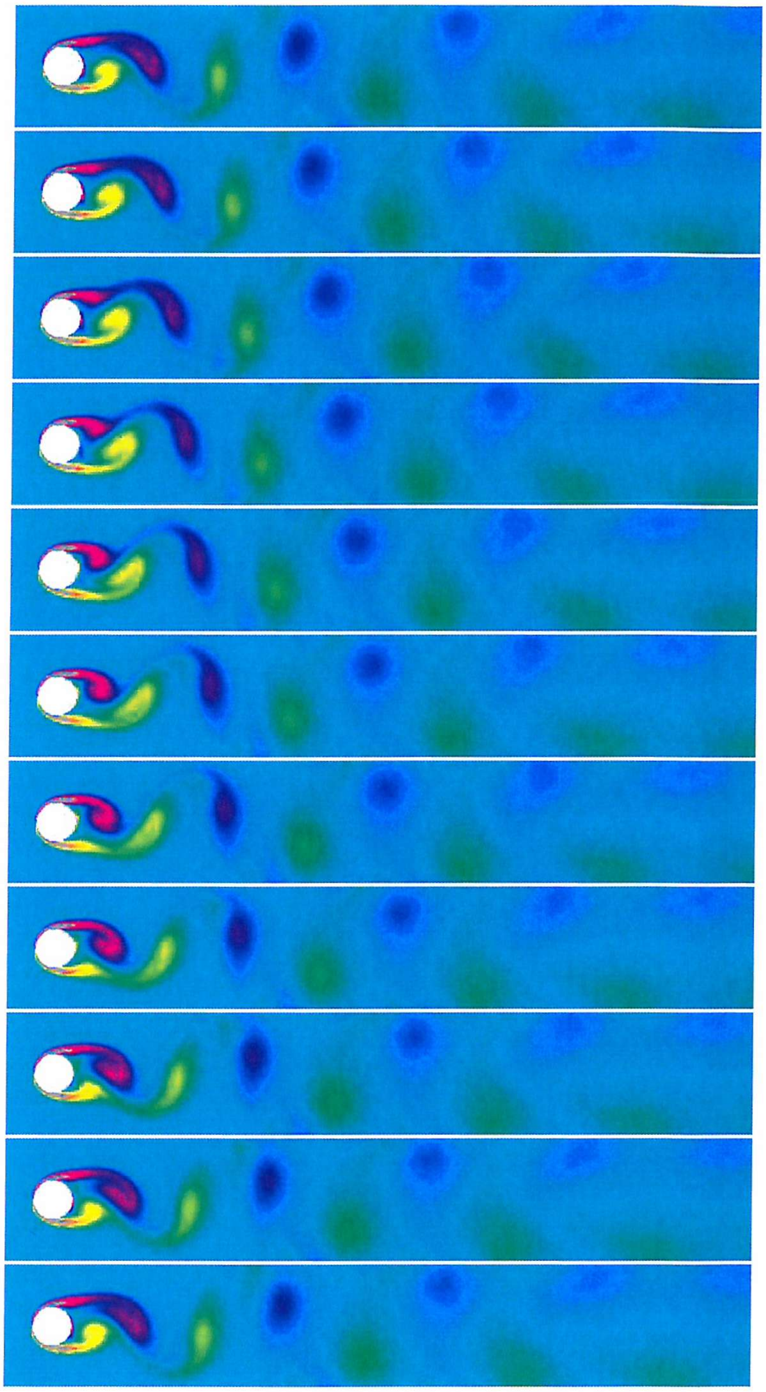

Figure 6.25: Vorticity distribution around a circular cylinder at $Re = 200$ for a complete vortex shedding period

6.4 Flow Around a Freely Oscillating Cylinder

All fluid structure interactions are composed of an excitation on one hand and a response on the other. In the case of a freely oscillating cylinder for example, the excitation corresponds to the forces acting on the cylinder. Such forces are the results of the fluid motion around the cylinder.

Having determined that the flow solver is able to accurately reproduce the diffusion and convection effects of the flow, and furthermore that the force model predicted well the forces acting on the circular cylinder, one can conclude that the fluid excitation aspect of the fluid structure interaction is correctly represented by the present method. Thus the structural response side of the interaction remains to be assessed.

In the present method, the response of the cylinder to the fluid excitation is determined by the solution of a simple mass-spring-damping system and the update of the solution grid (see chapter 5).

To assess the structural response, the problem of the freely oscillating cylinder is considered. The results obtained by Oliveira *et al.* [66] [78] in their numerical experimentation of VIV simulation will be used as a basis for comparison as *their results* are validated against experimental results.

The solution parameters of the original setup are defined in table 6.11 and the non-dimensional ones used in the present solution are given in table 6.12.

Parameter	**Name**	**Value**
Cylinder diameter	D	0.1 m
Reynolds number	Re	275
Inflow velocity	U_∞	0.275 m/s
Mass (2D)	m	13.06 kg/m
Stiffness	k	207.5 N/m^2
Damping	c	1.041 kg/(m.s)
Reduced velocity	U^*	5.5

Table 6.11: Solution parameters

The solution was carried out on the same 128×128 grid as for the two-dimensional flow around a fixed circular cylinder. The time step was set to 0.001 and the simulation time was of 150s.

Results are presented in table 6.4 along with a history of the force coefficients in figure 6.26. Additionally, figure 6.27 displays the trace of the position of the cylin-

UNIVERSITY OF SOUTHAMPTON LIBRARY

Parameter	**Name**	**Value**
Cylinder diameter	D	1.0
Reynolds number	Re	275
Inflow velocity	U_∞	1.0
Mass ratio	m^*	1.306
Damping ratio	ζ	10^{-3}
Reduced velocity	U^*	5.5

Table 6.12: Non-dimensional solution parameters

der and shows the convergence of the motion to the characteristic Lissajous shape.

Although the average drag coefficient found using the present method seems slightly lower than that reported in the literature, the other quantities such as the maximum lift and transversal displacement of the cylinder agree very well with the data from Oliveira *et al.* [66] and Krokstad *et al.* [77] in the "DEEPER" project.

Furthermore, the pattern of vortex shedding seen in figure 6.28 corresponds to a "2S" pattern, i.e. two distinct opposite vortices shed per cycle. This result was also found by Oliveira *et al.* [66] although they reported that a "2P" pattern should be expected, i.e. two pairs of vortex shed per cycle. Oliveira suggested that a reason why the expected pattern of vortex shedding could not be captured may reside in the manner in which the inflow velocity is increased. He subsequently made the hypothesis that three-dimensional effects could play a role in the vortex shedding pattern.

Parameter	**Present Method**	**Oliveira *et al.* [66]**	**DEEPER [77]**
$\mathbf{S_t}$	0.195	–	–
$\mathbf{C_D}$	1.900	2.24	2.24
$\mathbf{C_L}$	0.220	0.24	0.24
x/D	0.595	–	–
y/D	0.609	0.57	0.54

Table 6.13: Comparison of results for the freely oscillating cylinder

As identified by Brika *et al.* [12], the relationship between the relative amplitude of oscillation and reduced velocity is characterised by two branches as illustrated by figure 6.29. The transition between these two branches exhibits an hysteresis loop and each branch is associated with a specific mode of vortex shedding.

Although no results were available for comparison, it was thought that testing

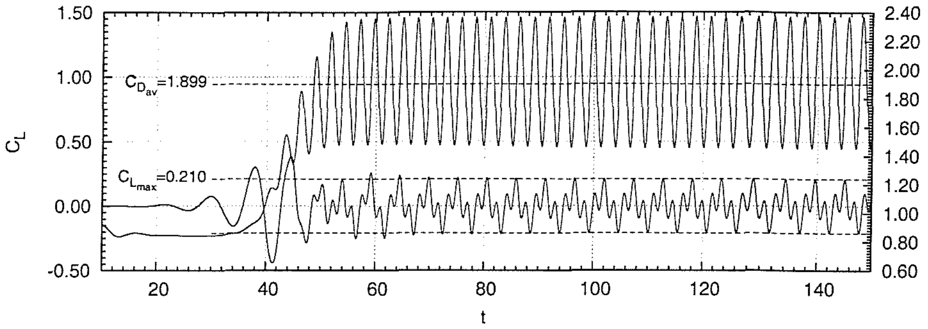

Figure 6.26: Force coefficients history for the freely oscillating cylinder at $Re = 275$, $m^* = 1.306$, $\zeta = 10^{-3}$ and $U^* = 5.5$

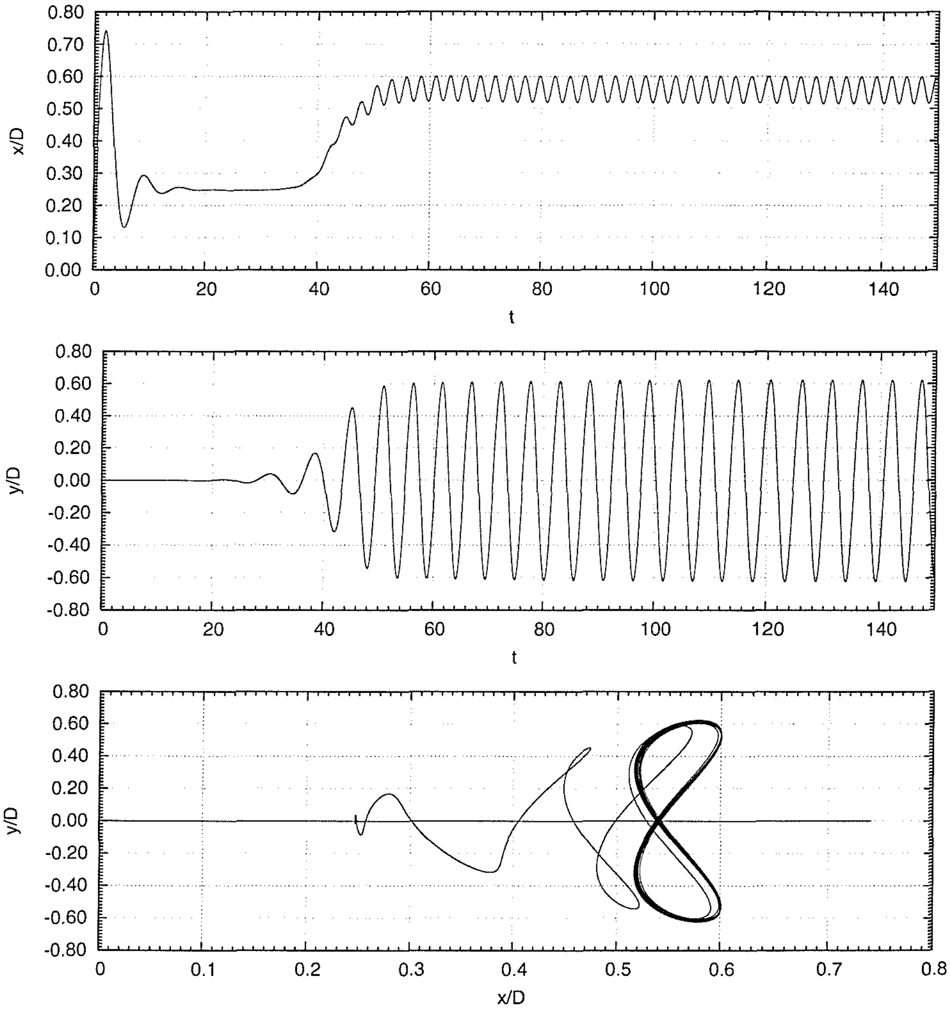

Figure 6.27: Longitudinal (upper) and transversal (middle) displacement history for the freely oscillating cylinder at $Re = 275$, $m^* = 1.306$, $\zeta = 10^{-3}$ and $U^* = 5.5$. The Lower plot is the X-Y phase plot over the complete simulation

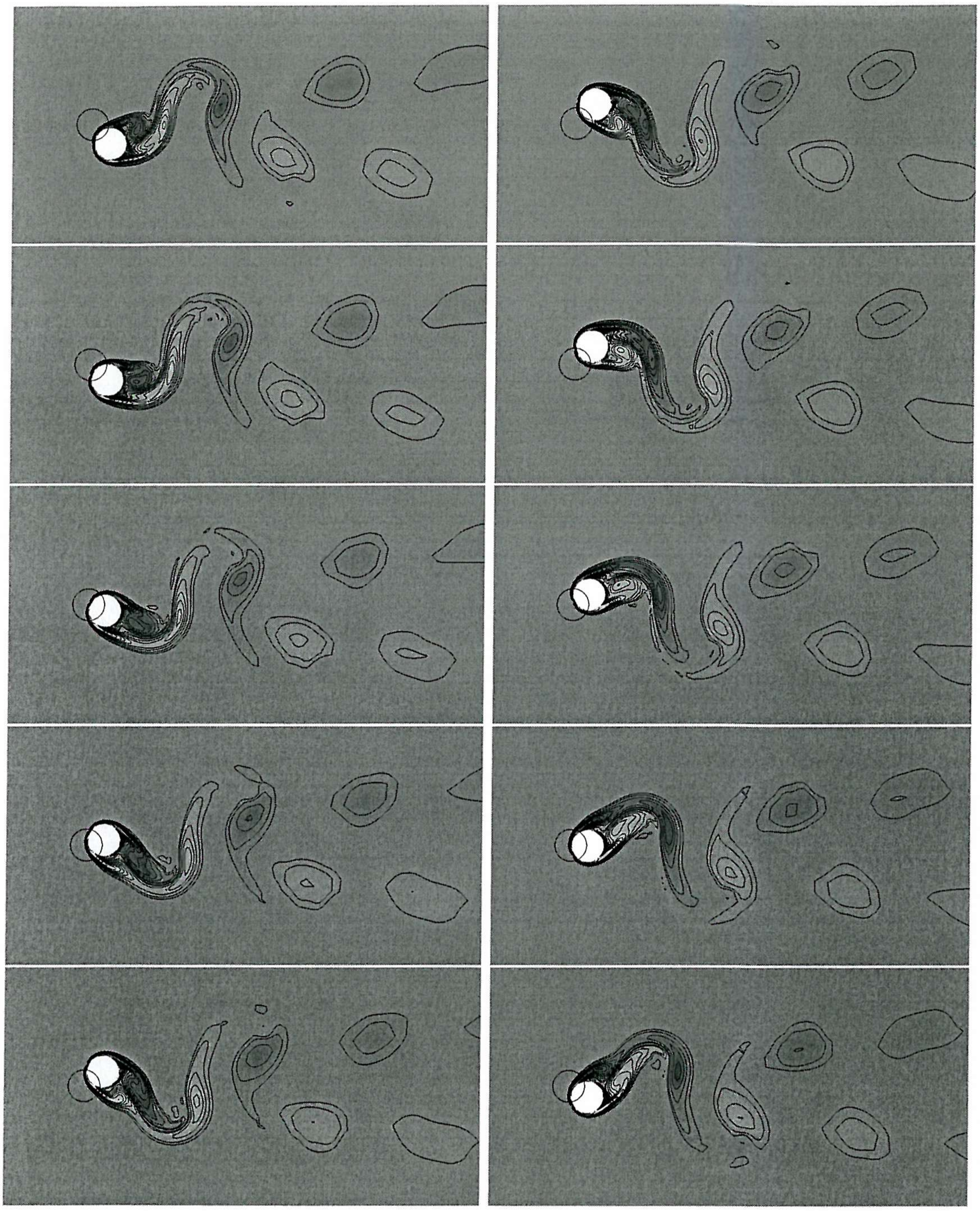

Figure 6.28: Vortex shedding period for the freely oscillating cylinder at $Re = 275$, $m^* = 1.306$, $\zeta = 10^{-3}$ and $U^* = 5.5$
The sequence reads from top to bottom, left column first followed by the right column with a time step between frames of 0.5s. The original position of the cylinder is given by the black circle.

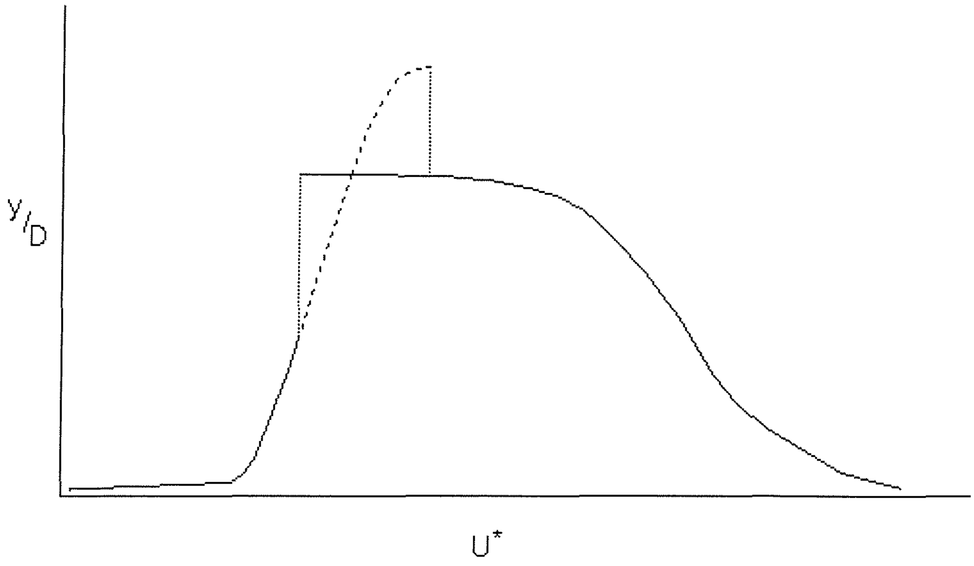

Figure 6.29: Amplitude of vibration versus reduced velocity

the freely oscillating cylinder over a range of reduced velocity may add to the discussion and allow for the relationship between the oscillation amplitude and the reduced velocity to be determined.

Further simulations were thus carried for a reduced velocity varying between 2.5 and 25 with the same Reynolds number, damping ratio and mass ratio.

In figure 6.30 the relative amplitude exhibits the overall expected shape although the hysteresis cannot be seen. Furthermore, figure 6.31 shows the correlation between the relative frequency of oscillation and the reduced velocity.

An interesting issue which was also reported by various authors (Oliveira [66], Pinto *et al.* [68], Sphaier *et al.* [78]) is that over the whole range of tested reduced velocity, only the "2S" mode was shown. In figure 6.32, even though the shedding of vortices at a reduced velocity of 4.52 shows a secondary vortex attached to the primary vortex, the pattern shown is characteristic of the "2S" pattern.

In light of the comparison with the results found in the literature for a two-dimensional freely oscillating cylinder and the characteristic behaviour demonstrated by the additional simulations, the results presented here demonstrated that the moving grid method and the structural model were adequate to simulate the response of objects under fluid excitation.

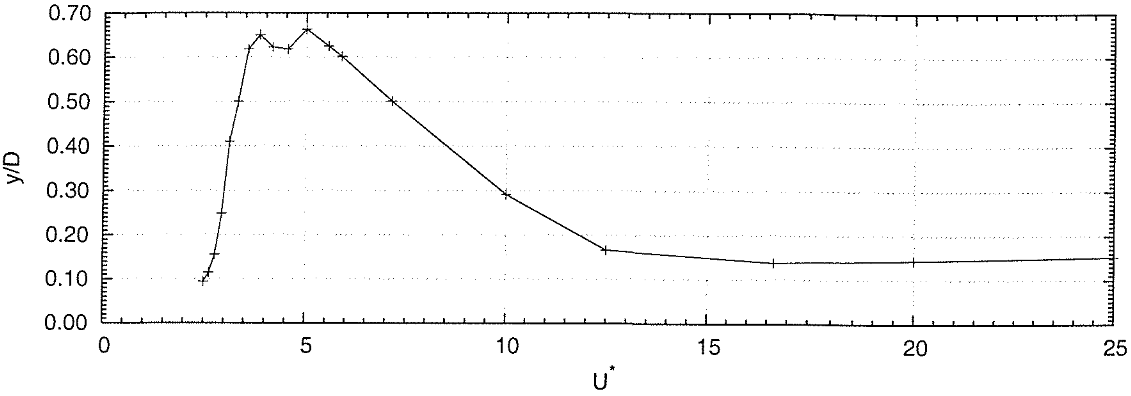

Figure 6.30: Vibration relative amplitude as a function of the reduced velocity for $Re = 275$, $m^* = 1.306$, $\zeta = 10^{-3}$

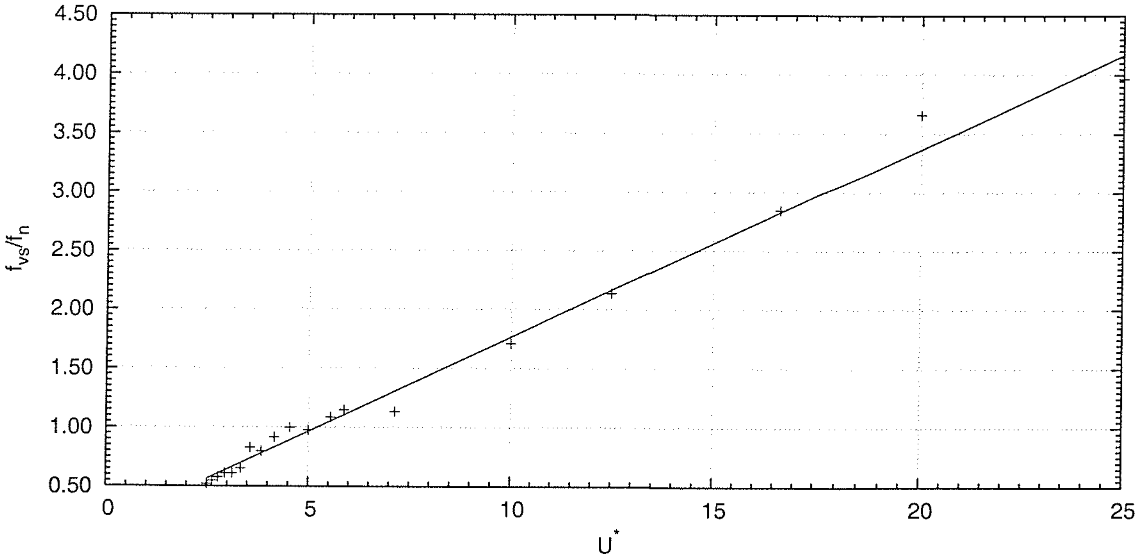

Figure 6.31: Vortex shedding frequency as a function of the reduced velocity for $Re = 275$, $m^* = 1.306$, $\zeta = 10^{-3}$

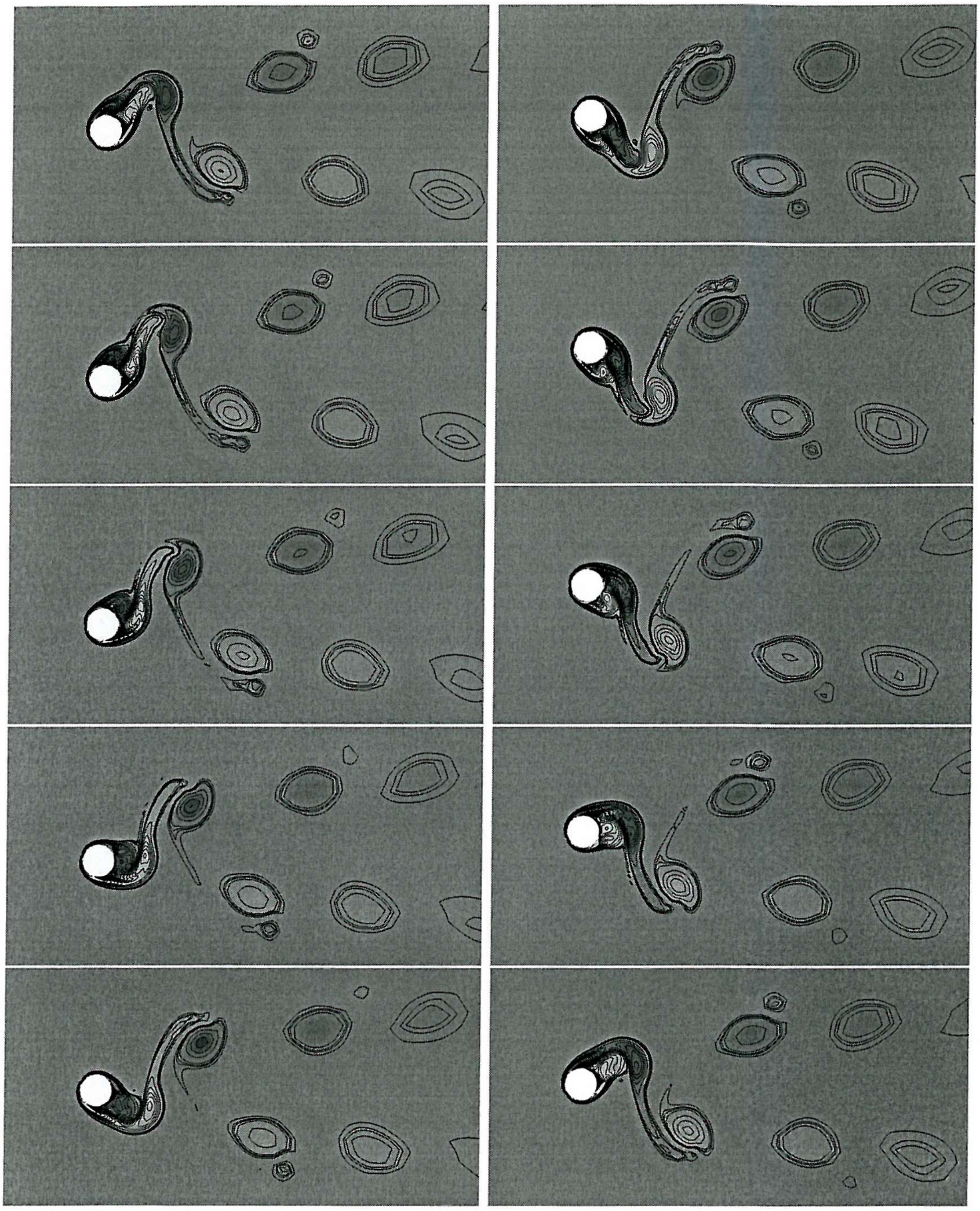

Figure 6.32: Vortex shedding period for the freely oscillating cylinder at $Re = 275$, $m^* = 1.306$, $\zeta = 10^{-3}$ and $U^* = 4.54$
The sequence reads from top to bottom, left column first followed by the right column with a time step between frames of 0.5s. The original position of the cylinder is given by the black circle.

Chapter 7

Three-Dimensional Flow Around a Fixed Circular Cylinder

7.1 Introduction

The study of the three-dimensional flow around a circular cylinder so far has mostly been the focus of experimental investigations only. A review of the current findings was done in chapter 2 and revealed that three-dimensional instabilities occur in the wake of a circular cylinder for Reynolds numbers greater than 180. Furthermore, the two discontinuities found by Williamson [90], [92] in the Strouhal-Reynolds number relationship are associated with two different modes of vortex shedding. The first, named mode A, occurs at a Reynolds number of about 180, whilst the second, mode B, starts occurring between $Re = 230$ and $Re = 260$. These two modes are intrinsically related to the development of three dimensional instabilities. As a consequence, the study of the three-dimensional wake of a circular cylinder implies an investigation into the prediction of these two modes.

As discussed in chapter 2, few numerical solutions have been carried out on such a problem, and have generally focused on a specific Reynolds number or at a specific spanwise length (Thompson *et al.* [83], Zhang *et al.* [101], Kalro *et al.* [42], Lei *et al.* [51]). Since the main focus of the present research is to assess the effect of the spanwise extension of the solution domain on the three-dimensional effects in the wake of a circular cylinder, it is quite natural that most of the investigation will concentrate on that issue. However, a number of issues closely related to the present research need investigation.

In their study of the effect of the spanwise length on the modelling of flow over a circular cylinder, Lei *et al.* [51] concluded that a spanwise length less than two cylinder diameters was insufficient to achieve reliable results. Furthermore, the quasi-periodic beat phenomenon observed experimentally in the lift and drag coefficient history can only be observed for three-dimensional simulations with a spanwise extension greater than twice the cylinder diameter. However, their investigation was carried out for a Reynolds number of 1000. It is thus reasonable to question if for different Reynolds numbers the minimum spanwise length for which reliable prediction can be achieved would be different.

Furthermore, in the same study, the results obtained with a spanwise extension of four cylinder diameters suggested there might be a relationship between this particular spanwise length and the real spanwise wavelength at a Reynolds number of 1000. Since all the numerical solutions encountered in the literature are carried out with periodic boundary conditions on the upper an lower part of the domain, a pseudo periodicity is forced onto the flow. This implies that a reliable solution using the periodic boundary condition can only be achieved if the extension matches an exact number of spanwise wavelengths. It is however difficult, at the present stage of the research into the flow around a circular cylinder to predict accurately such a spanwise wavelength. Could a different boundary condition be enforced on the upper and lower parts of the solution domain that would not incur a pseudo periodicity in the wake? It is also important to be able to distinguish between the effects of the spanwise extension and those of the boundary conditions on the three-dimensional wake.

In the following chapter, these various issues will be addressed. A complete description of the numerical solution setup will be given with details of the spanwise extension of the domain, and the boundary conditions used. Results for the various cases will be presented and analysed. A detailed visualisation of the various cases focusing on the vorticity in the wake of the cylinder will allow for the various vortex shedding modes to be examined. The appearance of the three-dimensional effects in the wake of the cylinder will be shown for the various spanwise extensions and the effect of the extension and boundary condition assessed.

7.2 Numerical Solution Setup

7.2.1 Computational Mesh

As it was shown that the 128×128 grid produced satisfying results in the two-dimensional case, and considering the computational cost of a three-dimensional solution, this grid will be used as a base for the three dimensional solutions.

In [92], Williamson reports that there exists two distinct spanwise wavelength depending on the vortex shedding modes. When mode A occurs, the wavelength is about four cylinder diameters while at mode B, it varies around one cylinder diameter. Clearly, mode A requires a substantially greater spanwise extent of the domain than mode B and if one is to capture it, the solution domain must extend vertically by at least four cylinder diameters.

In the context of the present investigation, three extensions were chosen, namely $\pi/2D$, πD and $2\pi D$. This allows for the cells close to the cylinder surface to have an aspect ratio of 1. Table 7.1 gives the details of the three grids used here and figure 7.1, 7.2 and 7.3 illustrate the solution domain in the three cases. Details of the grid at the cylinder base are shown in figure 7.4. Grid E is composed of four blocks distributed across the perimeter of the cylinder as in the two-dimensional case, whilst grid F was composed of eight blocks, i.e. two layers of the grid blocks used in the grid E. Grid D that was tested at a later stage is composed of eight blocks, in the same configuration as for grid F, but each block of a quarter of the size of those of grid E. The reason for the greater number of blocks in comparison to the grid size for grid D was due to a time constraint and the need to carry out the solution at a faster pace.

Grid	**Spanwise Extension**	**Grid Sizes**	**Total Number of Volumes**	**Volume sizes on Cylinder Surface**
D	$\pi/2D$	$128 \times 128 \times 32$	524288	
E	πD	$128 \times 128 \times 64$	1048576	$0.0490D \times 0.0490D$
F	$2\pi D$	$128 \times 128 \times 128$	2097152	

Table 7.1: 3D Grid details

7.2.2 Boundary Conditions

A substantial difference between the two- and three-dimensional solutions of the flow past a circular cylinder resides in the presence of two extra boundaries, one at each end of the cylinder. As mentioned in the introduction to the chapter, a commonly used boundary condition for these two boundaries is the periodic one. The variables on one of the boundary planes are fed into the other one and vice versa. Such a condition forces a periodicity of the flow and can thus present an inconvenience if the domain spanwise extension does not match a number of spanwise wavelengths. The spanwise wavelength could be increased or decreased depending on whether the extension is slightly less or more than a number of actual periods. Also, by affecting the spanwise wavelength, the three-dimensional instabilities occurring in the wake could be reduced, increased or delayed. Although this type of boundary condition has been employed in most of the three-dimensional solutions of the flow past a circular cylinder, it is believed that an alternative boundary condition could be used that would not affect the

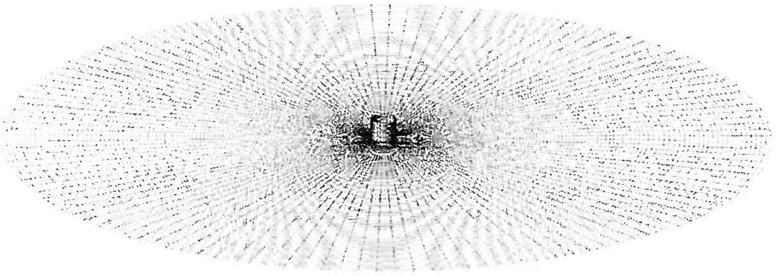

Figure 7.1: Grid D - 128 × 128 × 32

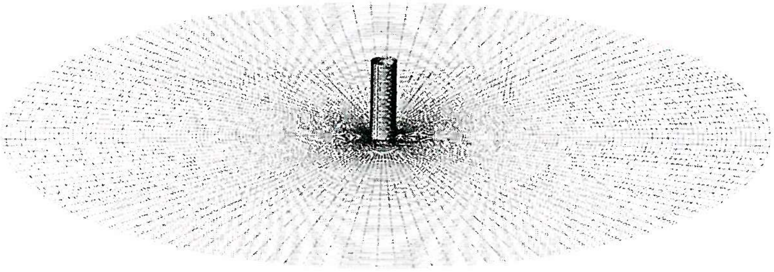

Figure 7.2: Grid E - 128 × 128 × 64

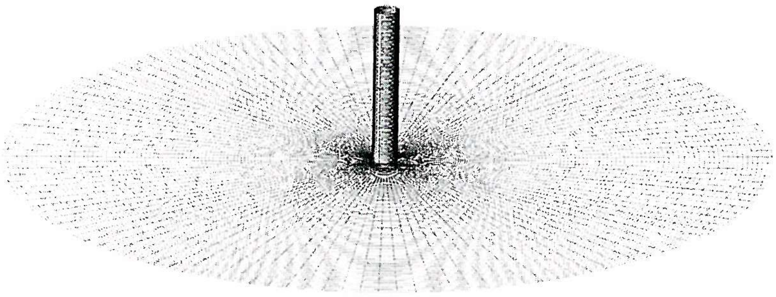

Figure 7.3: Grid F - 128 × 128 × 128

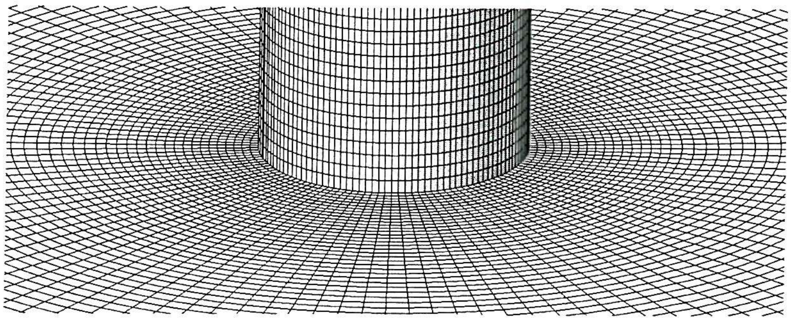

Figure 7.4: Grid details near the cylinder base

spanwise periodicity of the wake as much.

The most obvious approach would be to use an outflow condition on both upper and lower boundaries. However, the imposed constant reference pressure on the boundaries would result in a different distribution of the pressure on the cylinder extremities and thus change the nature of the flow. A symmetric boundary condition was therefore chosen for both upper and lower boundaries that can be assimilated to a slippy wall condition. Although such a boundary condition does not represent the reality of the flow at the boundaries, it does not result in a flow displaying an exact number of periods within the spanwise extension. Quite obviously, such a condition will affect the flow close to the upper and lower boundaries of the domain, but it is believed that it will allow for a better representation of the actual periodicity of the wake.

7.2.3 Numerical Solution

To assess the difference between the two and three-dimensional results, the same cases as for the two-dimensional flows were tested on each of the three grids, D, E and F, using the structure function LES turbulence model. The general details of the cases setup are given in table 7.2.

Re	**Re step**	**Time Step**	**Min. Residue Burger**	**Min. Residue Poisson**	**Turbulence Model**	**Simulation Time**
40	–	0.0100				
125-375	25	0.0100	10^{-7}	10^{-5}	LES-SF	300
400-1000	100	0.0050				

Table 7.2: 3D flow past a circular cylinder - Case details

The solution obtained for the steady flow at $Re = 40$ is used as an initial solution for all the other cases, increasing the Reynolds number progressively until reaching the desired value. The initial solution being converged, very few sub-iterations are required to resolve the pressure field at each time step, thus reducing the overall computation time.

A total number of sixty simulations were thus carried out using the Iridis cluster of the University of Southampton. The processing nodes used were dual 1.8 Ghz Xeon processors nodes with 2 GB of RAM interconnected by a myrinet network. Details of the cluster hardware and software are available on the world wide web at http://www.iss.soton.ac.uk/research/iridis/. Each node carried out the solution of two blocks of the mesh. Thus, the solutions on grid E required two nodes (total of four processors for four grid blocks) while the solution on grid F and D required four nodes (eight processors for eight grid blocks)

7.3 Three-Dimensional Lift, Drag and Strouhal Number

One of the key results in the analysis of the flow past a circular cylinder is the overall force acting on the cylinder. Generally, this force is decomposed in both a streamwise component, i.e. the drag force, and a transversal component, i.e. the lift force. Both drag and lift coefficient are recorded over the duration of the simulation and their behaviour over time can be analysed to reveal characteristic aspects of the flow past a circular cylinder. Among other factors, the Strouhal number can be determined using the lift force coefficient history.

In the present section, the history of the force coefficients for the three grids D, E and F are presented and analysed over the range of Reynolds numbers considered. Key relationships between the lift, drag, Strouhal number and Reynolds number are then deduced and discussed.

As the simulations are carried out using a boundary driven method, the local Reynolds number around the cylinder is progressively accelerated. As a consequence, the flow will always be two-dimensional in the initial stages of the simulations. Whether three-dimensionalities appear in the flow after a certain time is then dependent upon the considered Reynolds number. It is thus expected that the history of the force coefficients will reflect such a transition from two- to three-dimensional flows for Reynolds numbers above approximately 200.

The history of the force coefficients, as presented in figures 7.8, 7.9 and 7.10 for grid D, E and F respectively, revealseveral interesting features.

The first noticeable one is the transition between the purely two-dimensional flow and the three-dimensional flow mentioned above. The regular sinusoidal oscillations with constant amplitudes of both the lift and drag coefficients for the Reynolds number above 300 change to oscillations with more irregular amplitudes when the three-dimensional instabilities appear. These changes in the force coefficient traces bares some consequences on the Strouhal number obtained. For the two dimensional part of the flow, the frequency of oscillations of the lift coefficient, i.e. the frequency of the vortex shedding should match the one found in the two-dimensional simulations whilst the frequency of the oscillation after the wake becomes three-dimensional should be different. In the power spectrum of the lift coefficient (figure 7.8, 7.9 and 7.10), a secondary weaker peak appears and separates from the main one as the Reynolds is increased. Although it is sometimes difficult to see it clearly, this secondary peak occurs in fact at the Strouhal frequency of the two-dimensional part of the flow.

As the spanwise extension is increased from $\pi/2$ for grid D to 2π for grid F, the occurrence of the oscillation of the coefficients is delayed in time. Furthermore, the period over which the flow is two-dimensional increases with the spanwise extension. This difference is particularly noticeable when comparing the traces obtained with grid D with the traces from the other two grids. Interestingly, one could have supposed that the opposite should occur as the shorter spanwise extension would promote two-dimensional flows.

Another interesting feature that appears for Reynolds numbers above 300 is the quasi periodic beat phenomenon. As can be observed in the three figures 7.8, 7.9 and 7.10, the beat is more pronounced as the spanwise extension is decreased. This seems to contradict the findings of Lei *et al.* [51] who could only observe the quasi-periodic beat phenomenon for extensions greater than two cylinder diameters at a Reynolds number of 1000. An explanation may be the coarser grids used in their simulation. Early tests carried out on coarse grids in the present research revealed much more regular behaviour of the force coefficients than for finer grids at Reynolds number of about 1000. It seems thus reasonable to suggest that a coarse grid that can not capture the small scale instabilities, would not be able to predict accurately the forces acting on the cylinder.

The secondary oscillations (quasi-periodic beat) observed in the lift coefficient traces are such that in the case of the lower $\pi/2D$ spanwise extension, the lift reaches both lower and higher values than for the greater extensions. This is particularly evident for Reynolds numbers between 350 and 700. As a consequence, the maximum lift values obtained with grid D are expected to be higher than for the other two grids for this range of Re. For the lower and higher Reynolds numbers, the beat is not so accentuated and matches that observed in the traces obtained with grid E and F in a better fashion.

Some of the findings described above are essential to understand the relationships between the Reynolds number and the Strouhal number, the average drag coefficient and maximum lift coefficient. Tables 7.3, 7.4 and 7.5 give the characteristic force parameters for the three grids. In figure 7.5, a comparison is made between the Strouhal-Reynolds number relationship for the three studied grids and the data obtained experimentally by Williamson [92]. The results show very good agreement with the experimental data. In particular, the transition between the two and three-dimensional part of the curves is well predicted on all three-grids.

Re	St	$\overline{C_D}$	$\overline{C_{D_v}}$	$\overline{C_{D_p}}$	$\widehat{C_L}$	$\widehat{C_{L_v}}$	$\widehat{C_{L_p}}$
100	0.166	1.328	0.309	1.019	0.328	0.038	0.296
125	0.181	1.314	0.273	1.041	0.428	0.043	0.392
150	0.181	1.310	0.246	1.064	0.521	0.047	0.482
175	0.190	1.313	0.225	1.088	0.606	0.049	0.565
200	0.195	1.318	0.207	1.111	0.683	0.050	0.642
225	0.200	1.324	0.193	1.131	0.752	0.051	0.710
250	0.200	1.318	0.179	1.140	0.812	0.051	0.771
275	0.205	1.308	0.166	1.142	0.842	0.049	0.801
300	0.200	1.307	0.156	1.151	0.784	0.044	0.749
325	0.205	1.314	0.147	1.166	0.840	0.044	0.804
350	0.205	1.317	0.139	1.177	0.880	0.044	0.845
375	0.210	1.303	0.131	1.172	0.868	0.041	0.836
400	0.205	1.306	0.125	1.181	0.922	0.041	0.890
500	0.215	1.262	0.102	1.160	1.055	0.039	1.023
600	0.205	1.277	0.087	1.190	1.120	0.036	1.091
700	0.205	1.242	0.075	1.167	1.126	0.032	1.101
800	0.215	1.178	0.064	1.115	0.852	0.025	0.834
900	0.205	1.229	0.059	1.171	1.026	0.024	1.006
1000	0.215	1.155	0.051	1.104	0.651	0.015	0.638

Table 7.3: Force coefficients for grid D

Re	St	$\overline{C_D}$	$\overline{C_{D_v}}$	$\overline{C_{D_p}}$	$\widehat{C_L}$	$\widehat{C_{L_v}}$	$\widehat{C_{L_p}}$
100	0.166	1.331	0.314	1.018	0.331	0.039	0.299
125	0.176	1.318	0.279	1.039	0.433	0.044	0.396
150	0.181	1.315	0.253	1.062	0.528	0.048	0.488
175	0.190	1.318	0.232	1.086	0.616	0.051	0.574
200	0.200	1.323	0.215	1.108	0.696	0.052	0.653
225	0.200	1.328	0.201	1.127	0.767	0.053	0.724
250	0.205	1.328	0.188	1.140	0.830	0.054	0.787
275	0.205	1.309	0.175	1.134	0.885	0.054	0.842
300	0.205	1.302	0.155	1.146	0.850	0.047	0.810
325	0.205	1.302	0.146	1.156	0.839	0.044	0.803
350	0.205	1.292	0.138	1.154	0.819	0.041	0.786
375	0.205	1.264	0.128	1.136	0.845	0.040	0.813
400	0.205	1.264	0.122	1.142	0.795	0.036	0.766
500	0.205	1.256	0.101	1.154	0.830	0.032	0.804
600	0.215	1.211	0.084	1.126	0.781	0.027	0.759
700	0.205	1.213	0.074	1.140	0.851	0.026	0.830
800	0.205	1.177	0.064	1.113	0.890	0.024	0.872
900	0.219	1.195	0.058	1.138	0.826	0.020	0.808
1000	0.215	1.203	0.052	1.151	0.717	0.017	0.703

Table 7.4: Force coefficients for grid E

Re	St	$\overline{C_D}$	$\overline{C_{D_v}}$	$\overline{C_{D_p}}$	$\widehat{C_L}$	$\widehat{C_{L_v}}$	$\widehat{C_{L_p}}$
100	0.161	1.327	0.309	1.019	0.328	0.038	0.296
125	0.176	1.313	0.273	1.040	0.428	0.043	0.392
150	0.186	1.310	0.246	1.064	0.521	0.047	0.482
175	0.190	1.313	0.225	1.088	0.606	0.049	0.565
200	0.195	1.318	0.207	1.111	0.683	0.050	0.642
250	0.205	1.307	0.177	1.130	0.811	0.051	0.769
275	0.200	1.268	0.162	1.106	0.846	0.050	0.805
300	0.205	1.287	0.154	1.132	0.745	0.042	0.709
325	0.205	1.299	0.146	1.153	0.810	0.042	0.776
375	0.205	1.268	0.129	1.139	0.782	0.037	0.752
400	0.205	1.262	0.122	1.140	0.777	0.036	0.748
500	0.205	1.253	0.101	1.151	0.820	0.032	0.793
700	0.205	1.224	0.074	1.150	0.783	0.024	0.765
800	0.205	1.193	0.064	1.129	0.732	0.020	0.716
900	0.205	1.237	0.059	1.178	0.703	0.018	0.690
1000	0.215	1.200	0.052	1.148	0.687	0.016	0.674

Table 7.5: Force coefficients for grid F

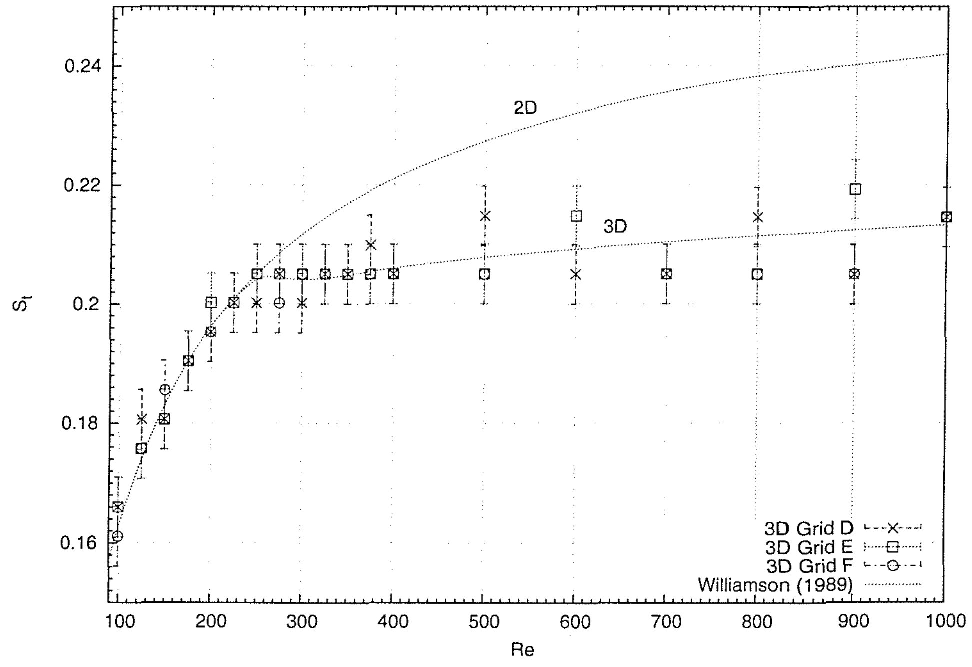

Figure 7.5: Relationship between the Strouhal and Reynolds Numbers

The drag to Reynolds relationship shown in figure 7.6 also exhibits a very good correspondence with the data found in the literature for three-dimensional flows.

It seems thus difficult to assess the difference between the three grids from the Strouhal to Reynolds and Drag Coefficient to Reynolds relationships alone.

The differences between the results obtained at different spanwise extensions starts showing when looking at the lift coefficient relationship with the Reynolds number as illustrated in figure 7.7. Although for Reynolds numbers up to ≈ 350 similar results are found for the three grids, the maximum lift coefficients found for grid D at Reynolds numbers between 350 and 700 are over-predicted and thus a lot closer to the two-dimensional results than the other two grids. This is a consequence of the more accentuated quasi-beating phenomenon observed in the coefficient traces and discussed previously. For Reynolds numbers higher than 700, the lift coefficients obtained with grid D tend to reduce towards those obtained with the other two grids suggesting that the three curves would eventually converge for Reynolds numbers greater than 1000.

Despite the differences in results discussed above, the analysis of the force coefficients is not sufficient to clearly assess the influence of the spanwise extension on the three-dimensional wake behind a circular cylinder. In particular, the quasi-beating phenomenon observed for all three grids suggests that differences in the wake of the cylinder could be observed for the various spanwise extension. It is thus necessary to investigate the vortex shedding using adequate visualisation.

7.4 Vortex Shedding Modes

In the present section, an analysis of a visualisation of the results obtained is carried out. The core part of the analysis will focus on the components of vorticity in the wake of the cylinder. The visualisation was developed using the IBM Data Explorer software (see http://www.opendx.org).

Williamson [90] showed the existence of two modes of vortex shedding in the transition to three-dimensional wake. Furthermore, each of these two modes corresponds to a spanwise instability in the wake and has a distinct geometry (Williamson [92]). In mode A, the streamwise vortices of one sign are in a staggered arrangement from one braid region to the next whilst in mode B, an in-line arrangement of streamwise vortices of the same sign can be seen.

In addition to their specific geometry, both mode A and B exhibit very different spanwise wavelengths. Although a relative scatter of the data can be seen in

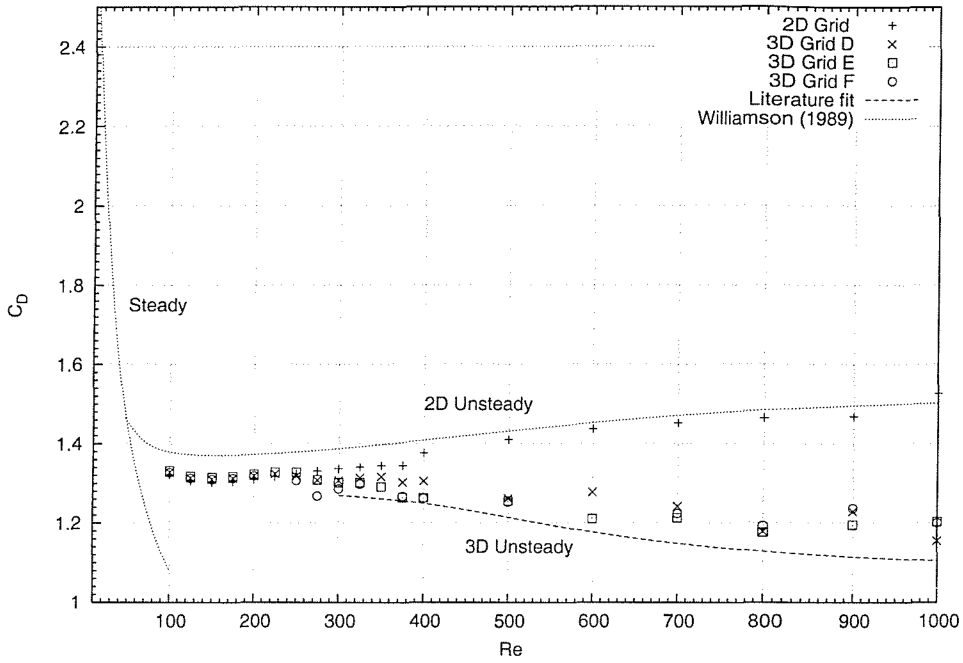

Figure 7.6: Relationship between the drag coefficient and the Reynolds Numbers

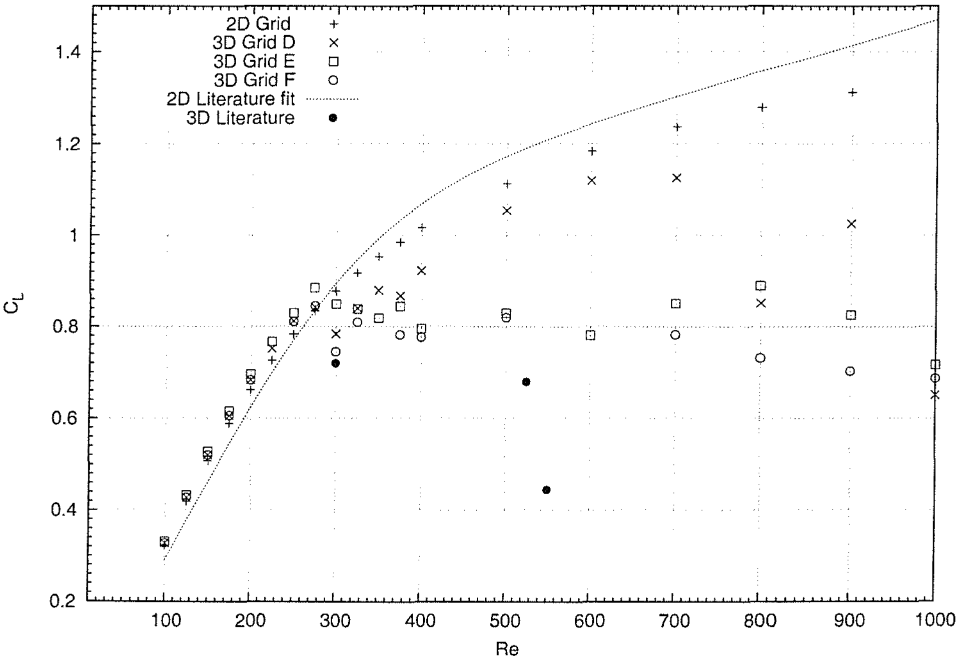

Figure 7.7: Relationship between the lift coefficient and the Reynolds Numbers

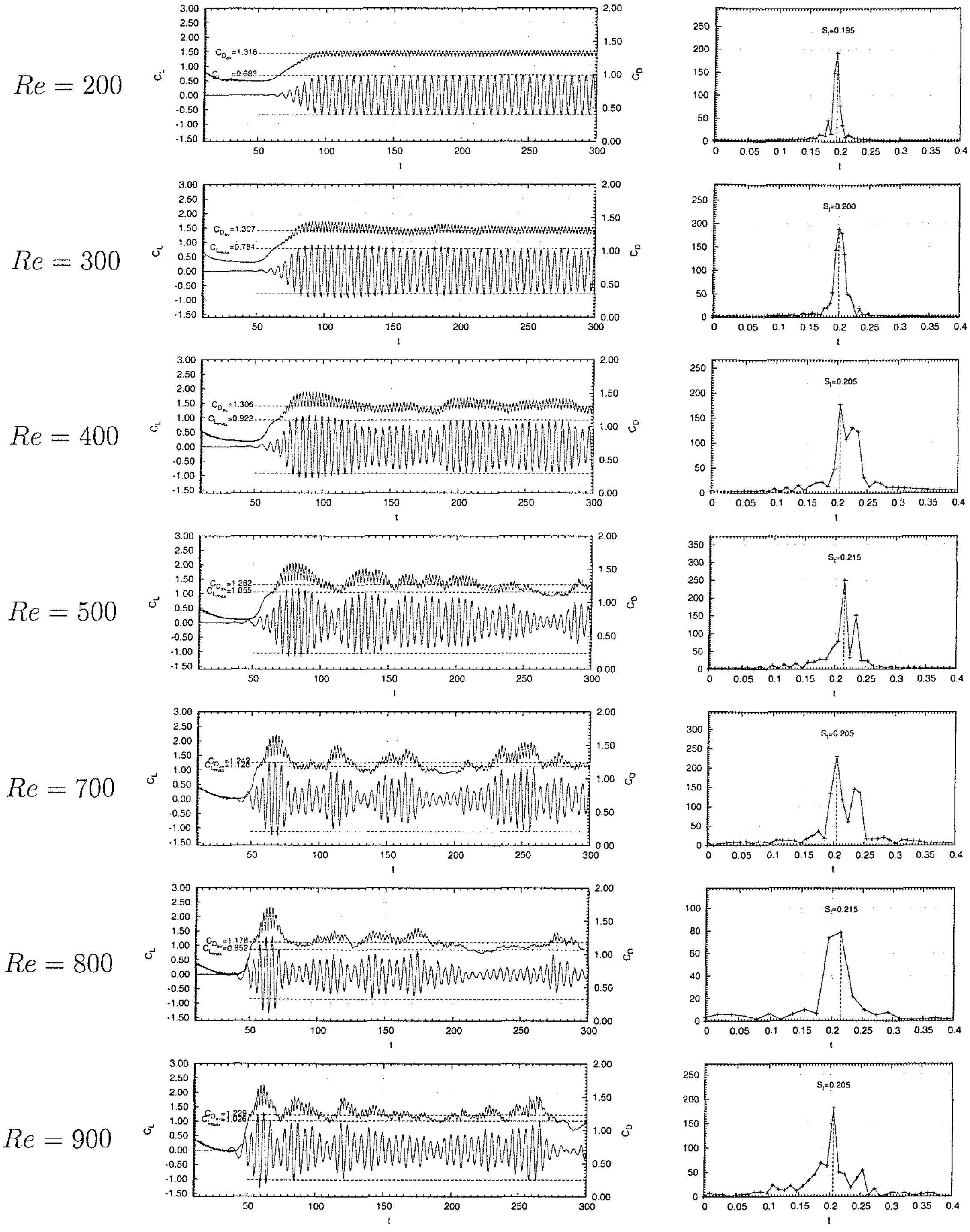

Figure 7.8: Grid D - Force coefficients history (left) and Power Spectrum (right)

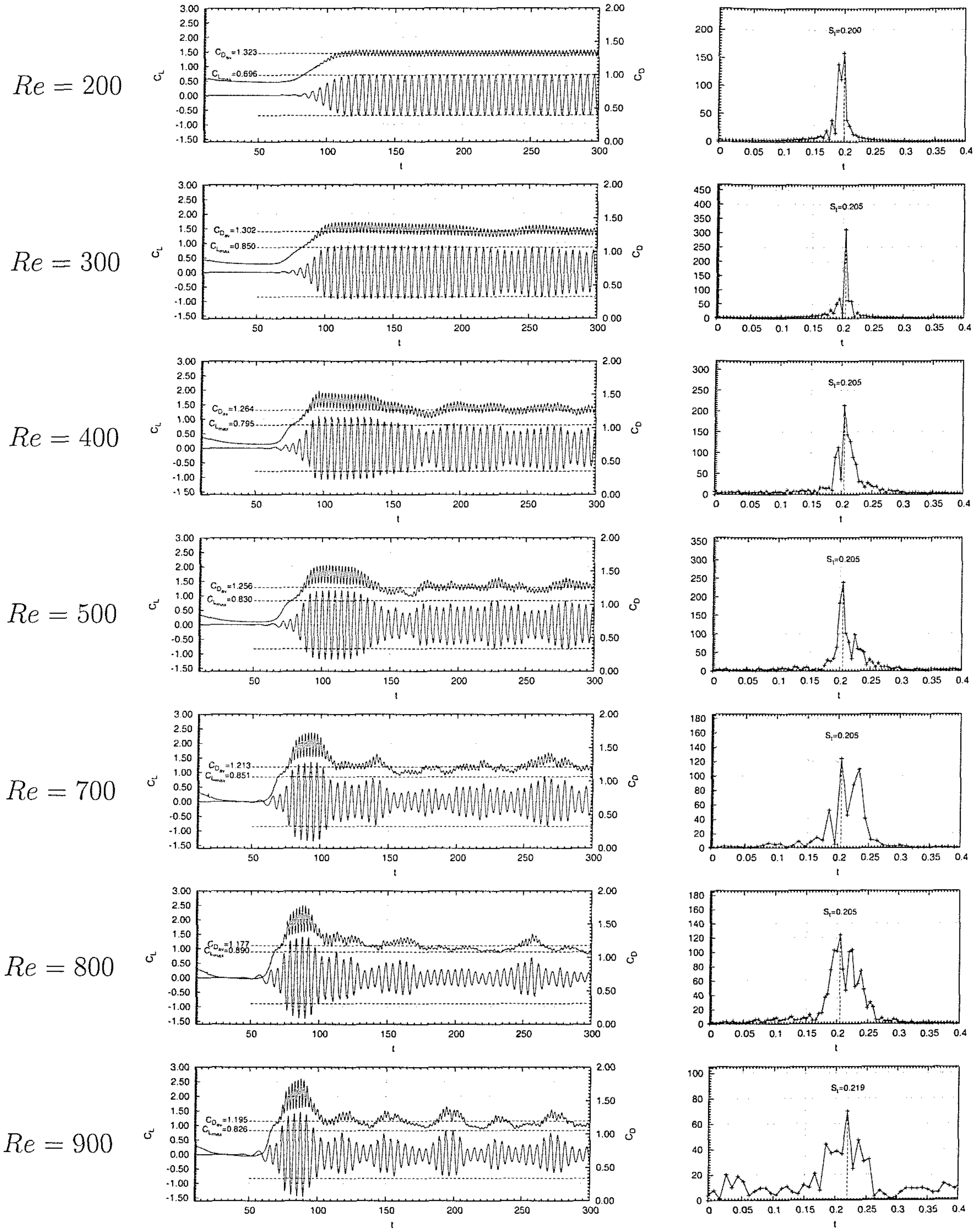

Figure 7.9: Grid E - Force coefficients history (left) and Power Spectrum (right)

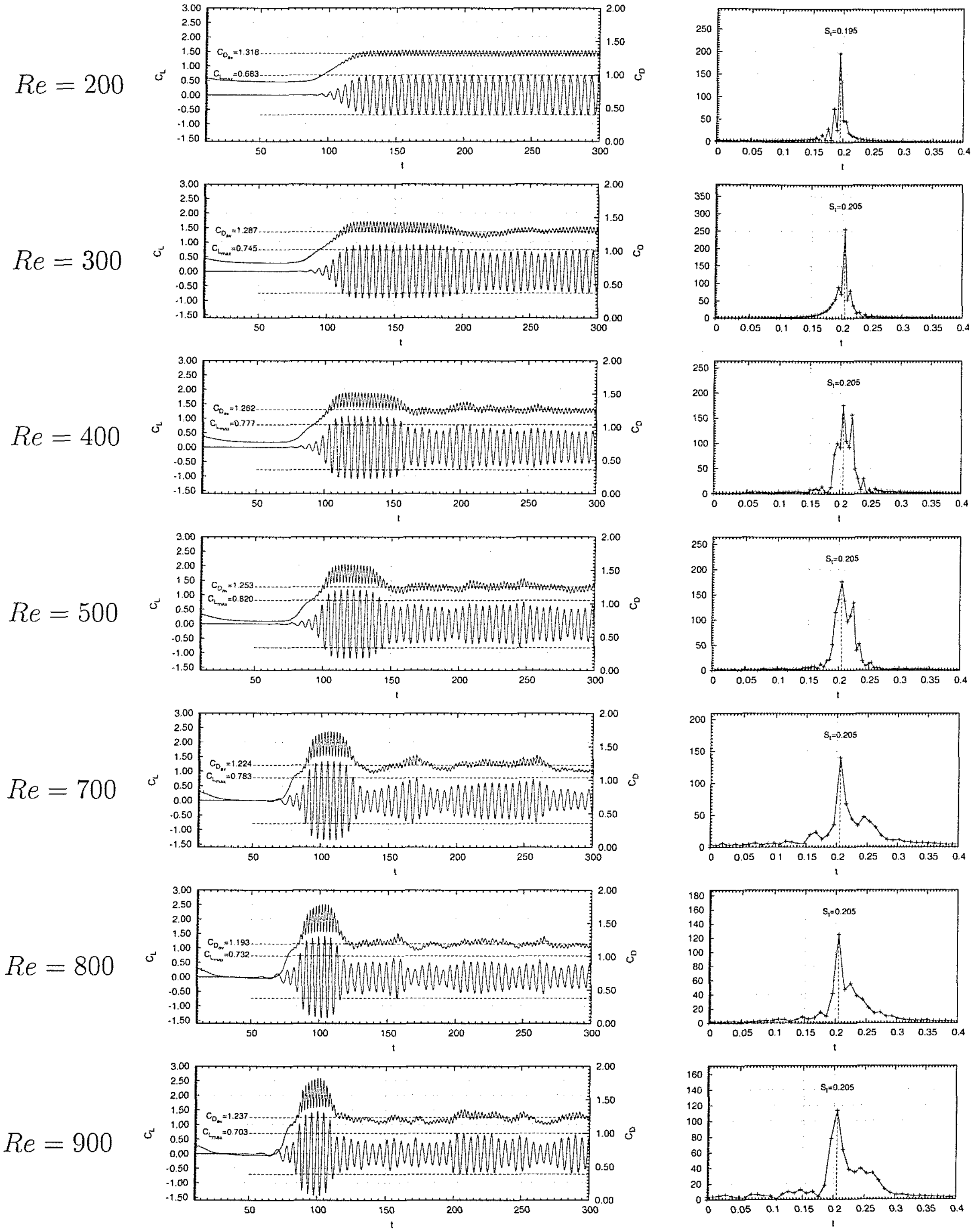

Figure 7.10: Grid F - Force coefficients history (left) and Power Spectrum (right)

the literature, it is usually found that in mode A, the spanwise wavelength is of about $4D$ while it is of about $1D$ for mode B. As a consequence, grid F used in the present research should be adequate to capture mode A as its spanwise extension is $2\pi D$. Grid E of spanwise extension πD might be a bit too short to capture fully the mode and grid D with an extansion of $\pi/2D$ should not allow for mode A to be well predicted. All three grids on the other hand should be able to capture the vortex shedding mode B.

7.4.1 Mode A

In figure 7.11, the influence of the spanwise extension is shown by comparing the streamwise and spanwise components of vorticity at a Reynolds number of 200 on the three grids D, E and F. The dark blue and red surfaces show a particular value of positive and negative streamwise vorticity while the light blue and green surfaces show a particular value of positive and negative spanwise vorticity.

Grid F clearly captures mode A and exhibits a spanwise wavelength of about $4D$. Since this is slightly more than the spanwise extension of grid E, it is understandable that the visualisation shows a partially predicted mode A on grid E. Another interesting comment can be made from this visualisation regarding grid D. Although the spanwise extension of grid D is far too short to capture mode A, its extension is close to half a wavelength, thus explaining the reason for seeing what appears to be half of the spanwise period.

It thus appears that grid D, through the non-periodic spanwise boundary conditions, is capable of capturing half of the spanwise wavelength of the vortex shedding. In figure 7.12, the visualisation of the streamwise and spanwise vorticity for grid D and E at $Re = 225$ supports this argument by showing a complete wavelength period in the case of grid E and an exact half period for grid D.

Although it was not possible to produce a comparative visualisation for grid F owing to the absence of results at this particular Reynolds number, it appears that for $Re = 225$, the spanwise wavelength is closer to πD, thus suggesting that the vortex shedding mode A may have indeed different spanwise wavelengths depending on the Reynolds number. This could explain the relative scatter of data reported by Williamson [92].

The comparison between the experimental visualisation of mode A by Williamson [92] and the present numerical simulation at $Re = 200$ shown in figure 7.13 shows remarkably similar pattern in the vorticity. Furthermore, the wavelength shown in both case is in very good agreement. This confirms that the present method is capable of accurately predicting the vortex shedding mode A provided the grid

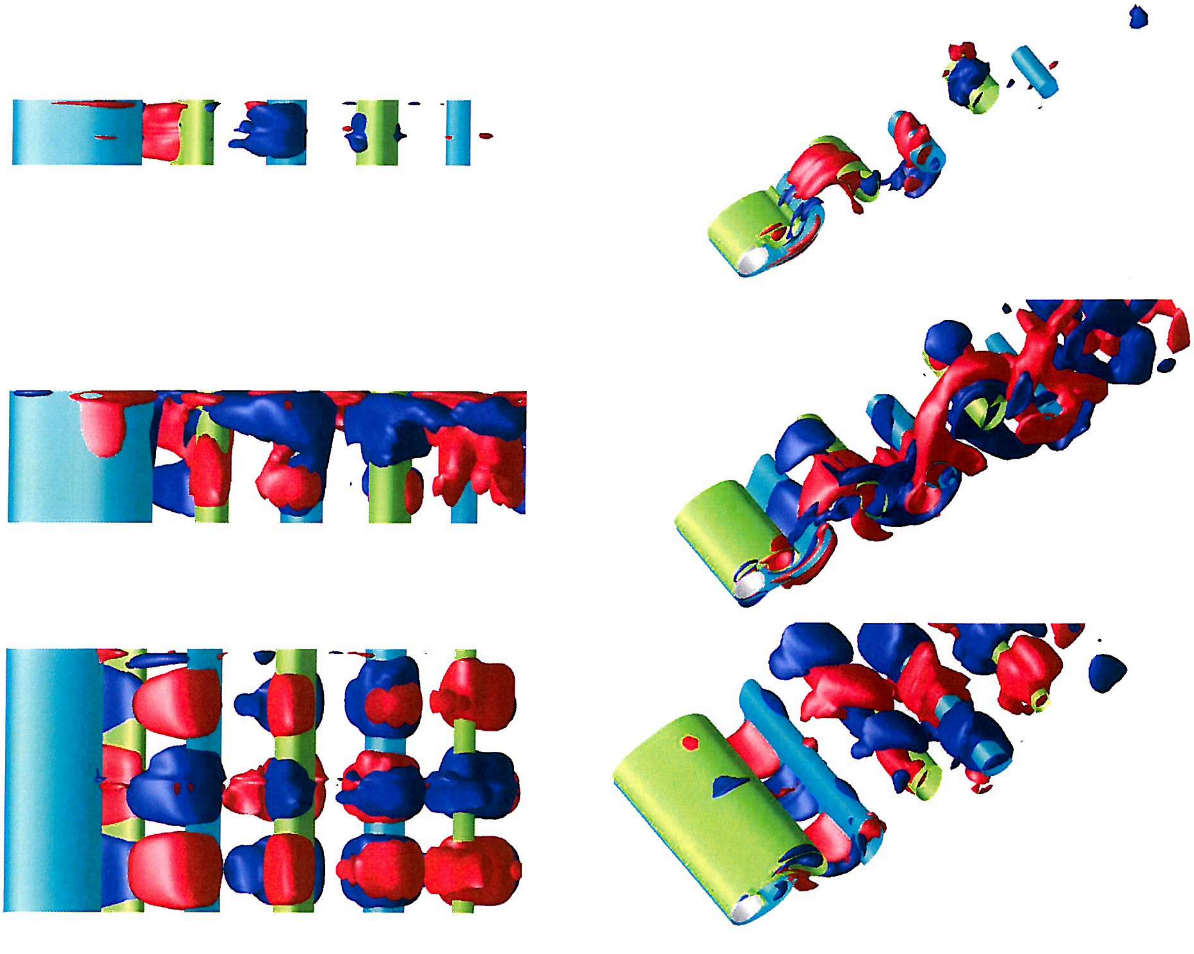

Figure 7.11: Domain spanwise extension influence on Mode A vortex shedding. Comparison of the streamwise and spanwise components of vorticity for grid D (top), grid E (middle) and grid F (bottom) at $Re = 200$.

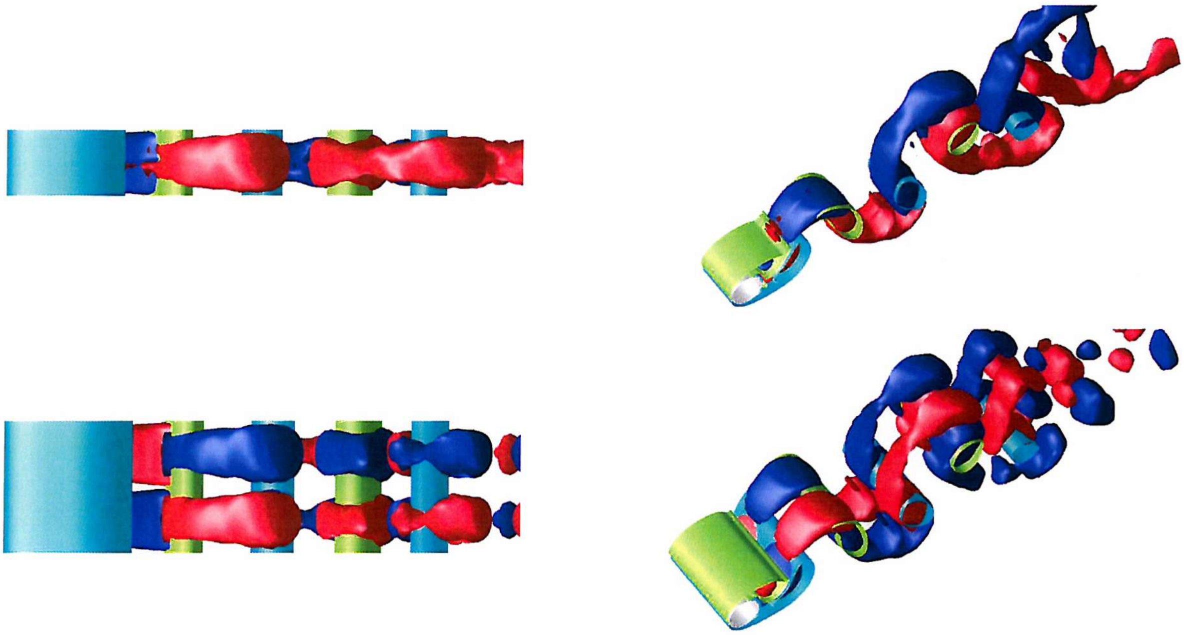

Figure 7.12: Mode A vortex shedding: Comparison of the streamwise and spanwise components of vorticity for Grid D and E at $Re = 225$

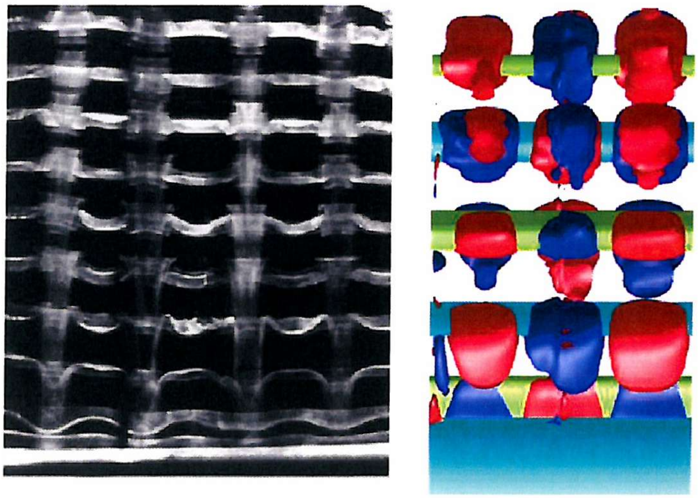

Figure 7.13: Mode A vortex shedding at $Re = 200$
Williamson (exp.)[92](left) and present simulation (right)

possesses sufficient spanwise extension. Although grid E resulted in a good prediction of the wake for $Re = 225$ and grid D could predict half a wavelength, most of mode A occurs at a spanwise extension of about $4D$. It can be concluded that a spanwise extension of at least $2D$ is required to capture half a wavelength at mode A and one of at least $4D$ for the complete wavelength.

7.4.2 Mode B

The transition to the vortex shedding mode B is somewhat difficult to investigate as numerous simulations would be required in the Reynolds number range where it occurs. Since at $Re = 200$ it is clearly established that mode A is occurring, and since the transition occurs approximately between $Re = 230$ and $Re = 260$, a visualisation of the vorticity in the wake of the cylinder for Reynolds numbers between 200 and 300 should give an insight into the transition phase.

A confirmation of this hypothesis is given in figure 7.14 where clear evidences of the occurrence of both mode A and B are provided for $Re = 200$ and $Re = 300$ on grid F. The visualisation at $Re = 250$ shown in this figure is extremely interesting as it exhibits a vortex pattern complying with mode A but with much thiner vortex layers, indicating the transition to mode B. Furthermore, a clear difference with the pure mode A vortex shedding patterns can be seen in the spanwise component of vorticity (light blue and green surfaces).

Further evidence of the transition between the two vortex shedding modes is given in figures 7.15, 7.16 and 7.17 where the components of velocity are shown in the symmetry plane in the wake of the cylinder.

In particular, the transversal component of velocity, U, exhibits a clear wavy pattern at $Re = 250$ that does not show at the lower Reynolds number of 200. At the higher Reynolds number of 300, although there seems to be an oscillation in the spanwise direction of the transversal component of velocity, the pattern exhibited are much more uniform than for $Re = 250$.

Also, in figure 7.17, a clear change of the spanwise component of velocity can be observed. At $Re = 200$, the switching of sign of the velocity is extremely regular and the spanwise velocity component quite strong. At the intermediate $Re = 250$, the spanwise velocity still displays the alternative pattern observed at $Re = 200$ in the far wake of the cylinder, but the close wake seems to be undergoing a transition. At $Re = 300$, the intensity of the spanwise velocity has decreased substantially suggesting that, although three-dimensional instabilities are present in the flow, their spanwise wavelengths are much smaller.

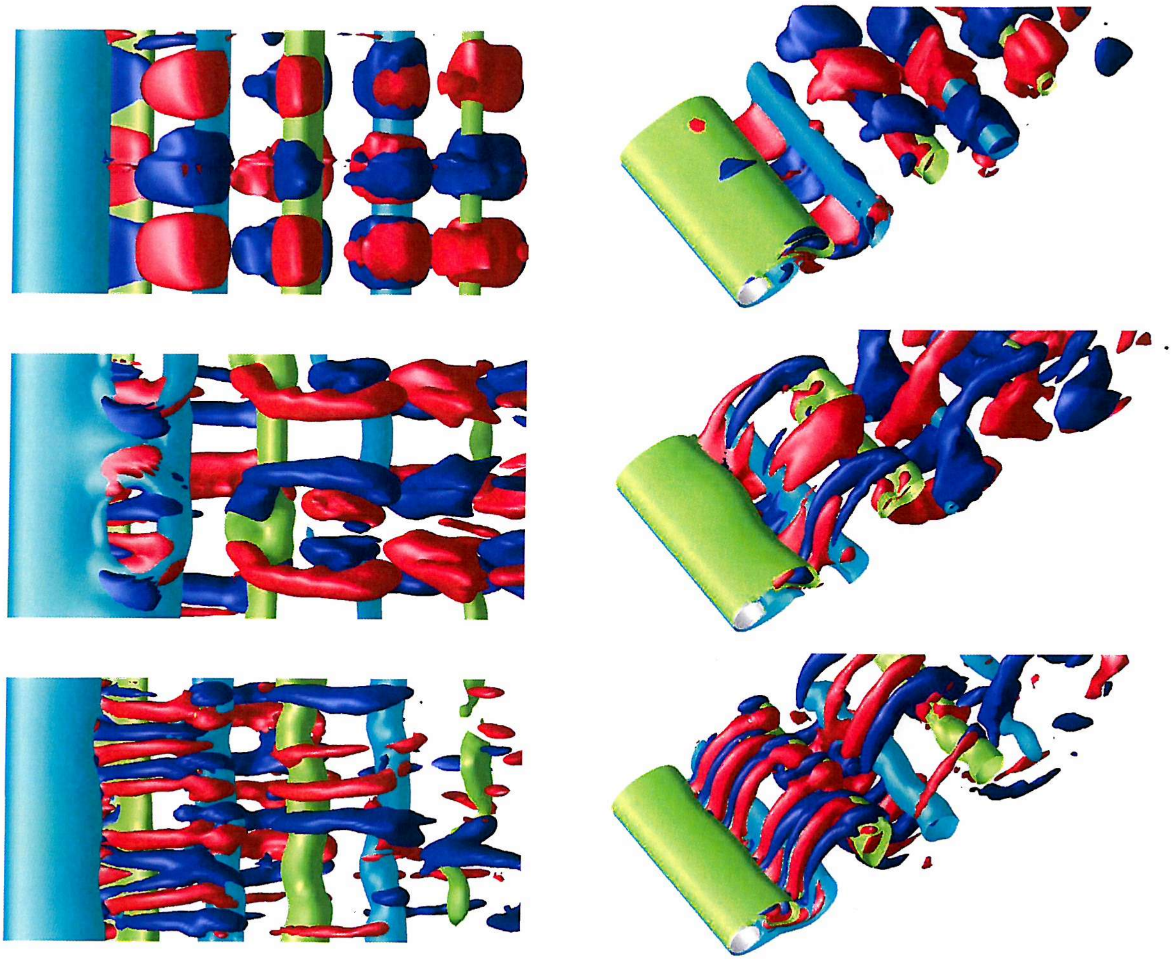

Figure 7.14: Mode A to Mode B Transition - Streamwise and spanwise components of vorticity for grid F - Mode A at $Re = 200$ (top), Transition at $Re = 250$ (middle) and Mode B at $Re = 300$ (bottom)

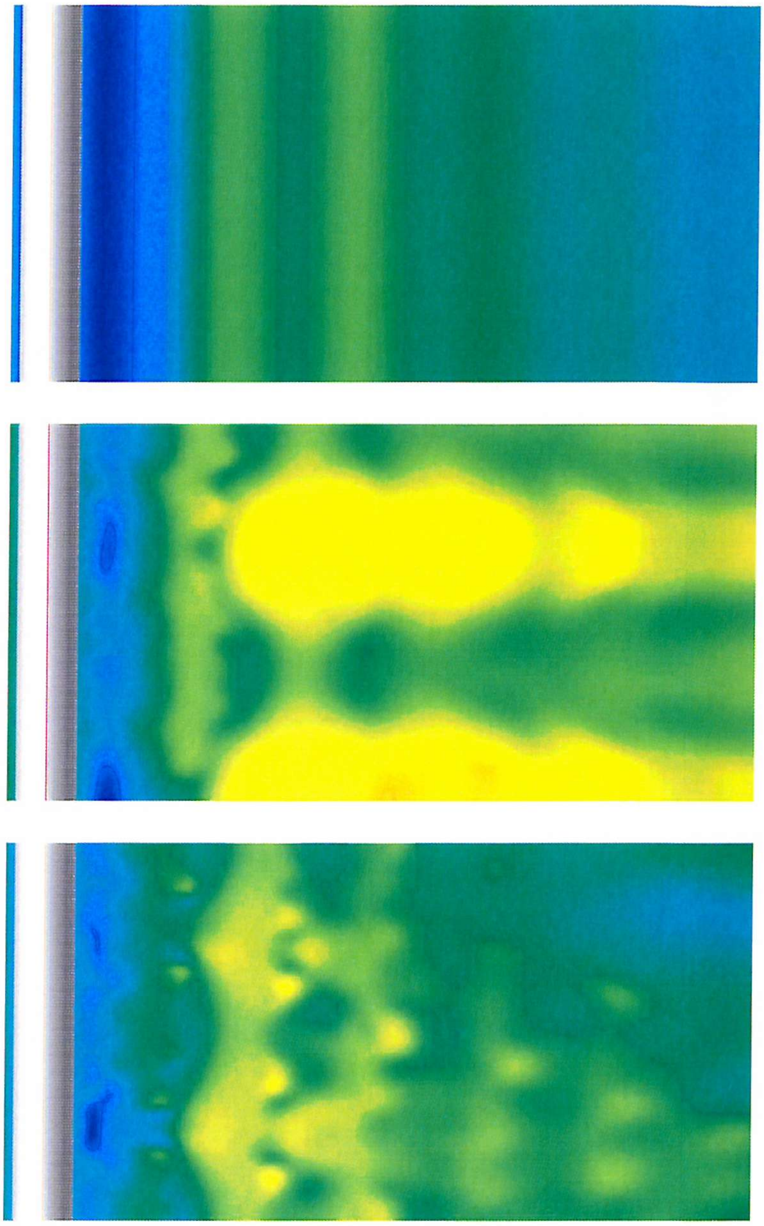

Figure 7.15: Mode A to Mode B Transition - Streamwise components of velocity (U) for grid F - Mode A at $Re = 200$ (top), Transition at $Re = 250$ (middle) and Mode B at $Re = 300$ (bottom)

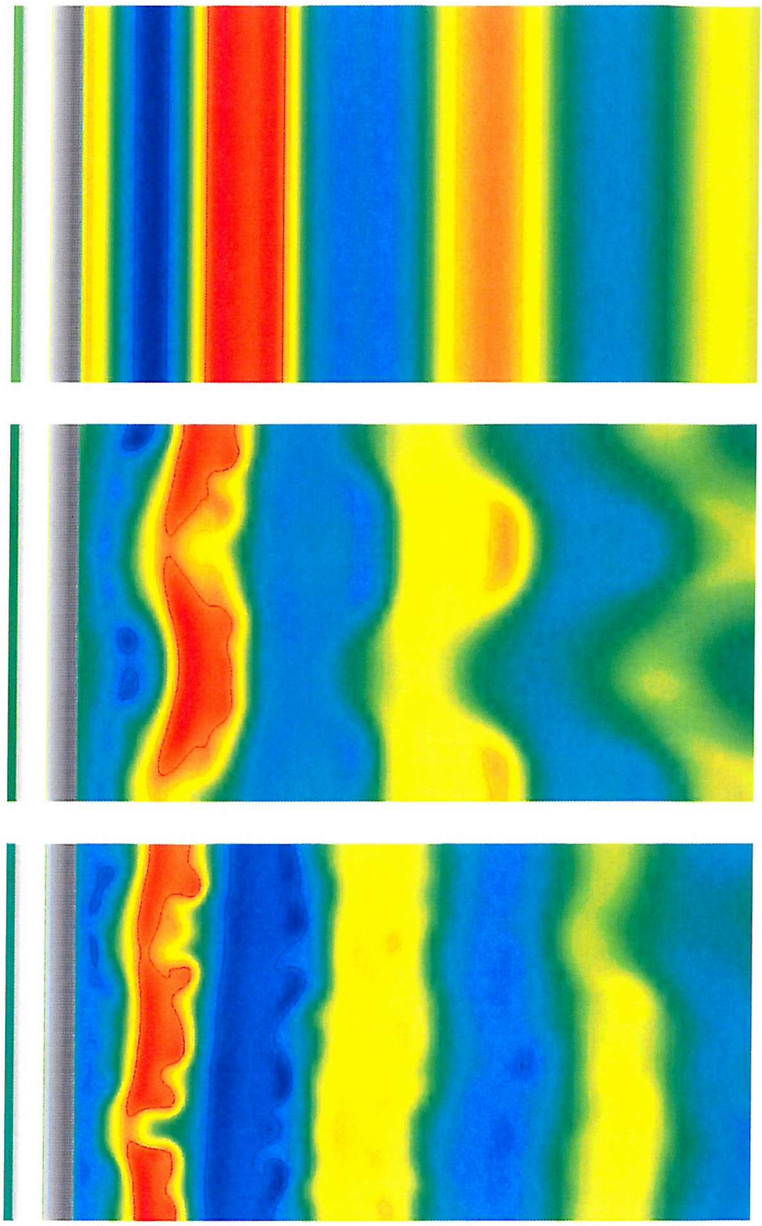

Figure 7.16: Mode A to Mode B Transition - Transversal components of velocity (V) for grid F - Mode A at $Re = 200$ (top), Transition at $Re = 250$ (middle) and Mode B at $Re = 300$ (bottom)

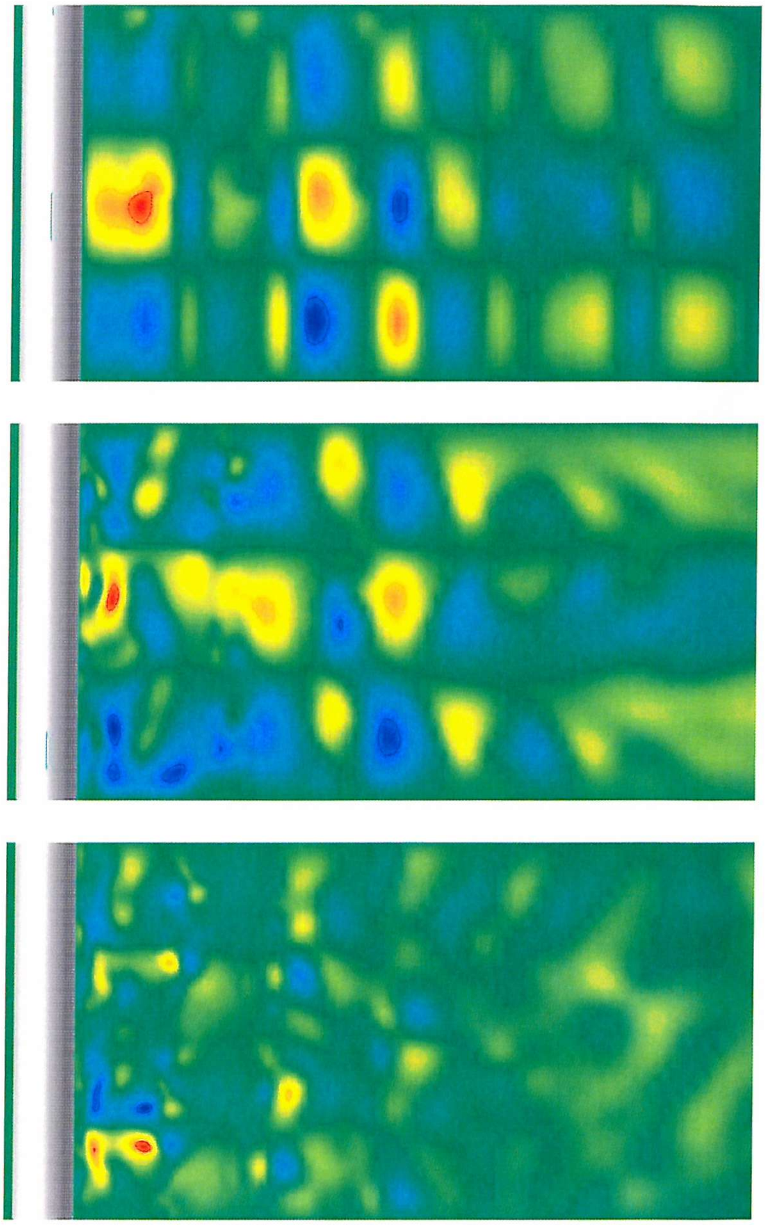

Figure 7.17: Mode A to Mode B Transition - Spanwise components of velocity (W) for grid F - Mode A at $Re = 200$ (top), Transition at $Re = 250$ (middle) and Mode B at $Re = 300$ (bottom)

For Reynolds numbers greater than 300, the shedding of vortices in the wake of the cylinder follows the pattern of mode B. As shown in figure 7.18, the prediction of mode B with grid F compares remarkably well with both experimental (Williamson [92] and numerical (Poncet [69]) results found in the literature.

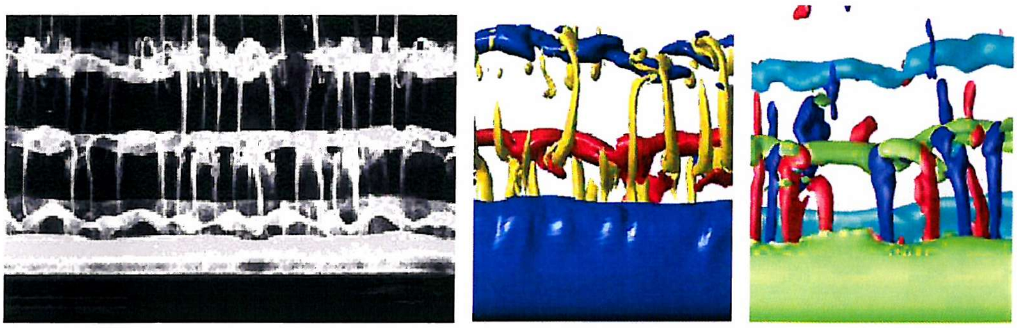

Figure 7.18: Vortex shedding in the wake of a circular cylinder at $Re = 400$. From left to right: Williamson (exp.)[92], Poncet (num.)[69] and present numerical solution

Since the wavelength of mode B is close to $1D$, the three spanwise extensions are sufficient to capture the mode as illustrated by figure 7.19.

Indeed, a visual inspection of figures 7.20, 7.21 and 7.22 reveals that for Reynolds numbers greater than 300, the spanwise wavelength is approximately equal to $1D$ at $Re = 300$, decreasing slightly as the Reynolds number increases to approximately $0.8D$ for $Re = 1000$.

A closer look into the visualisation of the wake vorticity obtained with grid D shows however that two spanwise periods are captured at most Reynolds numbers, thus giving a spanwise wavelength of slightly less than $0.8D$.

7.4.3 Spanwise Wavelength and Extension

Determining the wavelength is rather difficult from the visualisation, particularly at the higher Reynolds number where the wake is more chaotic. However, by looking at the wake close to the cylinder, i.e. at approximately $x/D = 3$, it is possible to estimate the wavelength of the three-dimensional instabilities by averaging a number of periods over the spanwise extension of the cylinder.

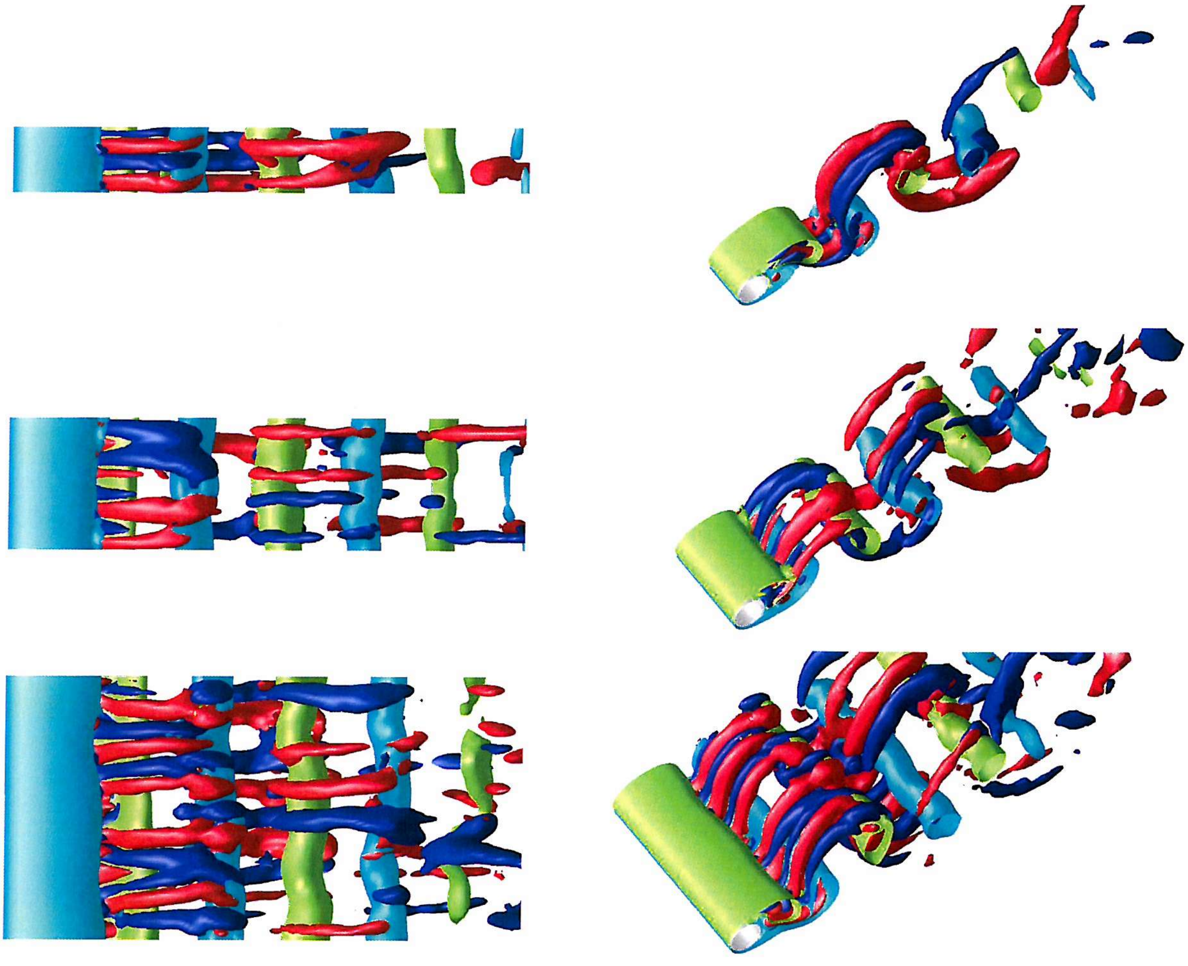

Figure 7.19: Mode B vortex shedding: Comparison of the streamwise and spanwise components of vorticity for grid D (top), grid E (middle) and grid F (bottom) at $Re = 300$

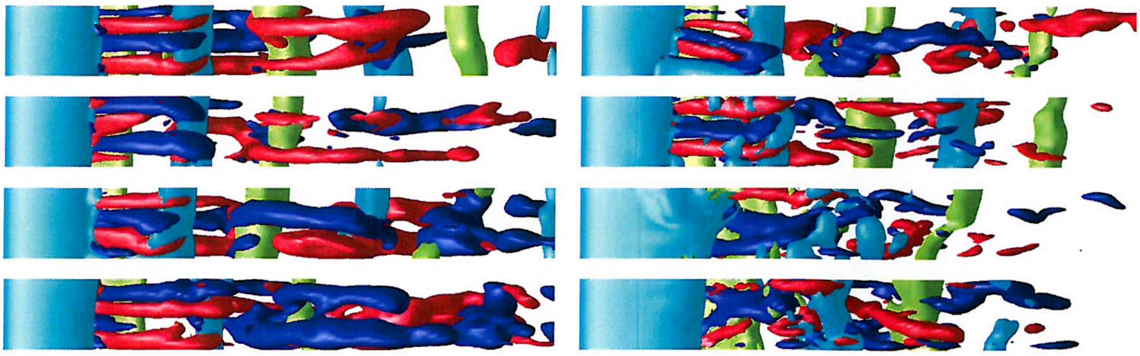

Figure 7.20: Evolution of the spanwise and streamwise vorticity for grid D From top to bottom, left column first followed by the right column: $Re = 300$, 325, 375, 400, 500, 700, 800 and 900.

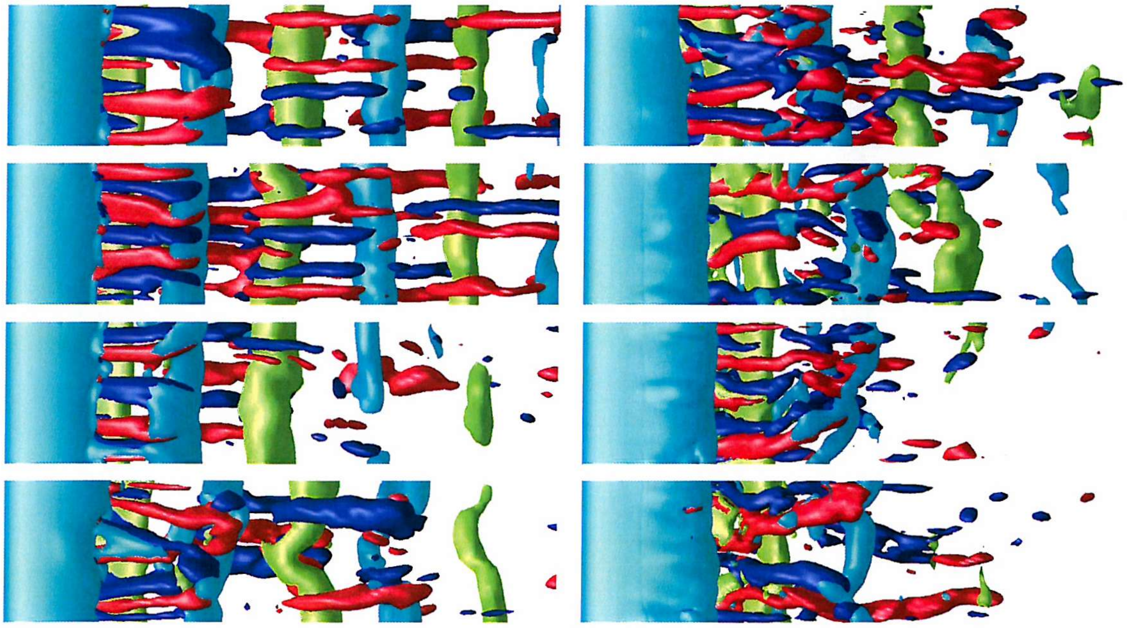

Figure 7.21: Evolution of the spanwise and streamwise vorticity for grid E From top to bottom, left column first followed by the right column: $Re = 300$, 325, 375, 400, 500, 700, 800 and 900.

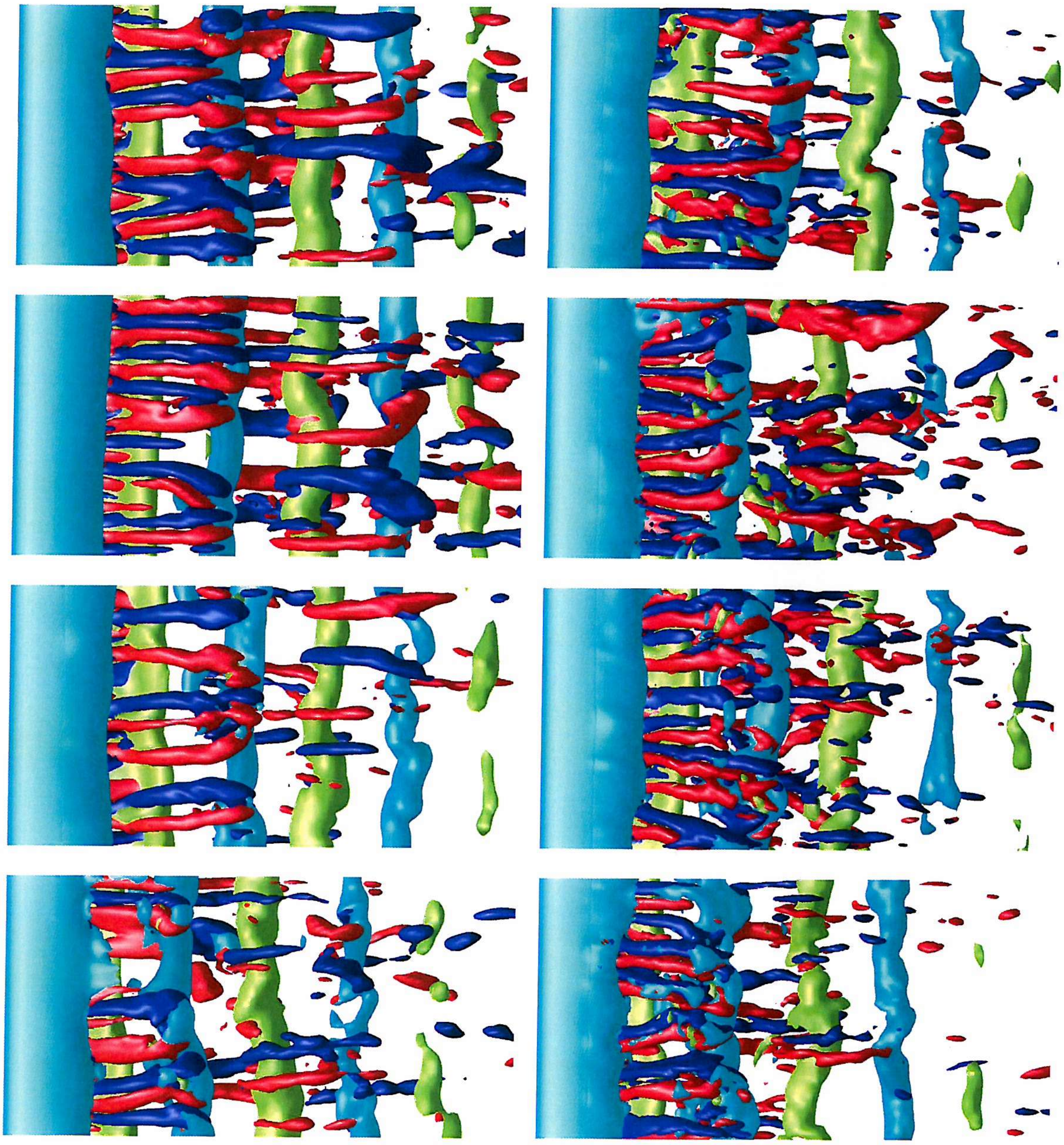

Figure 7.22: Evolution of the spanwise and streamwise vorticity for grid F From top to bottom, left column first followed by the right column: $Re = 300$, 325, 375, 400, 500, 700, 800 and 900.

Although using such a method may appear rather inaccurate considering that very few periods can be observed particularly for the shortest extension (grid D), the resulting estimation agrees rather well with Williamson's measurements [92] as shown in figure 7.23. The separation between the wavelengths at mode A and those at mode B clearly appears and compares well with Williamson's trends.

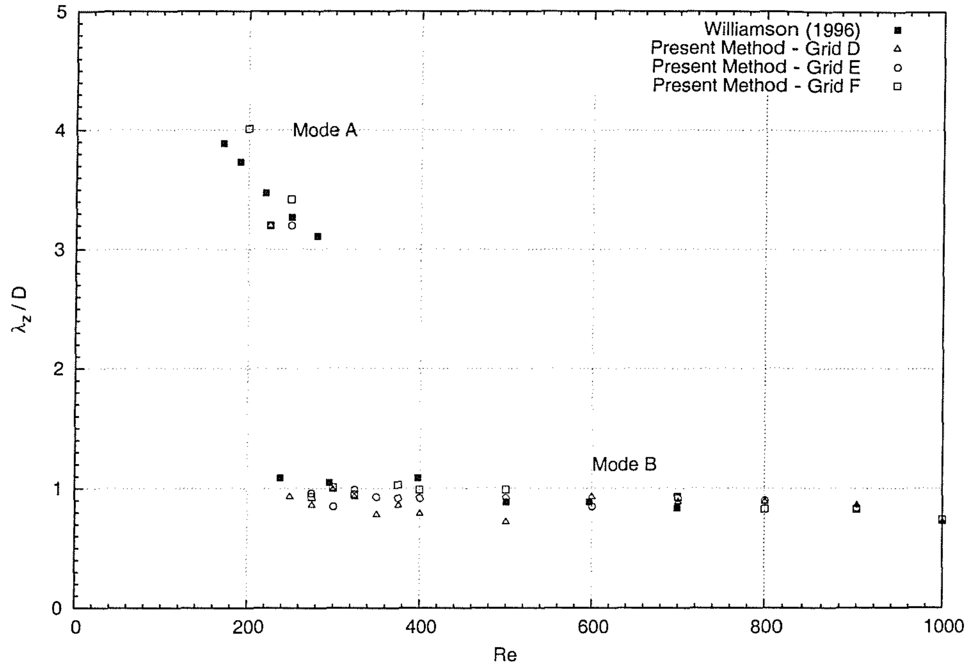

Figure 7.23: Spanwise wavelengths of the three-dimensional instabilities

Furthermore, whilst the wavelengths obtained for grid E and F are similar, those obtained for grid D at a spanwise extension of $\pi/2D$ are slightly shorter for the Reynolds numbers between 250 and 600. Considering that only a single period could be measured from the visualisation of the spanwise vorticity on grid D, the estimation could be rather inaccurate for this particular grid. However, the fact that the wavelength is systematically lower suggests that the spanwise extension and most probably the boundary conditions imposed in that direction affected the three-dimensional instabilities.

7.5 Summary

The investigation of the effects of the spanwise extension on the three-dimensional wake of a circular cylinder revealed several interesting facts.

The analysis of the force coefficients obtained for the three spanwise extensions led to the conclusion that the πD (grid E) and $2\pi D$ (grid F) extensions produced similar results. In the case where the extension was only of $\pi/2D$, both Strouhal number and average drag coefficient were well predicted. However, owing to the more pronounced quasi-periodic beat phenomenon, the lift coefficient amplitude was over-predicted. Nevertheless, the trend observed in the lift coefficient amplitude for that extension suggested that as the Reynolds number is increased, the prediction of the force coefficient for grid D would converge with the other two grids.

The visualisation of the vorticity in the wake of the cylinder confirmed that both grid D and E are not well suited to predict the vortex shedding mode A across the whole range of Reynolds number where it occurs. However, a very interesting result at a Reynolds number of 225 showed that grid D was capable of predicting an exact half wavelength of mode A. Grid F on the other hand allowed for mode A to be fully captured and the transition between mode A and B to be visualised.

For the vortex shedding mode B, it was found that all three extensions and in particular the shortest $\pi/2$ extension produced similar wake vorticity patterns. The agreement between the spanwise and streamwise vorticity observed for the three grids therefore suggests that the extension of grid D is sufficient to predict the flow past a circular cylinder at Reynolds numbers in the mode B range.

Finally, the estimated spanwise wavelength obtained from the visualisation of the three-dimensional instabilities compared very well with experimental data found in the literature for all three spanwise extensions investigated thus confirming that the three-dimensional instabilities are well predicted in all three cases.

In light of these findings, it is possible to conclude that a finite spanwise extension of the cylinder is sufficient to predict the flows past an infinitely long circular cylinder in the considered range of Reynolds numbers. Clear evidences were produced showing that the minimum spanwise extension required for flows at low Reynolds numbers up to about 300 was in the region of four cylinder diameters. For higher Reynolds numbers, a shorter spanwise extension between $\pi/2D$ and πD is sufficient to predict accurately all the characteristic components of the flow, namely the force coefficients, the Strouhal number and also the three-dimensional instabilities and their wavelength. Furthermore, it is reasonable to suggest that such conclusions could extend beyond the range of Reynolds number studied in the present investigation.

Chapter 8

Conclusions

8.1 Summary

The aim of this research was to investigate the three-dimensional wake behind a circular cylinder using numerical tools and determine the influence of the domain spanwise extension on the solution.

The review of the research carried out to date revealed the clear inadequacy of the two-dimensional solutions to describe practical flow problems where a three-dimensional wake occurs. The few three-dimensional numerical solutions reported in the literature predicted a wake in close agreement with the experimental data, capturing the three-dimensional effects. Furthermore, the observation of the vorticity in the wake showed that a spanwise periodicity was occurring thus suggesting that a finite spanwise extension would be sufficient to accurately predict the flow and fluid-structure interaction.

Practical engineering problems often involve long cylinders in a flow. A typical example is that of marine risers subject to current and undergoing vortex-induced vibrations. Determining the minimum spanwise extension of the numerical solution domain required to capture the flow past a circular cylinder thus allows for the problem of the infinitely long cylinder to be reduced to a finite length one. An immediate consequence of significant importance is that the accurate prediction of the vortex-induced vibration of long cables can be obtained from the finite spanwise length domain thus at a reasonable cost.

In this research, a numerical method was presented to solve the incompressible form of the Navier-Stokes equation based on the projection method and the finite volume discretisation. To allow for complex geometries to be solved, a curvilinear coordinates, multi-block approach was adopted that led to a straight forward parallelisation of the solution. In turn, the parallel strategy allows for large or dense computational domains to be solved on computer clusters. Although careful thinking is required to implement such a parallel solution, the method presented here showed a simple and efficient parallelisation. In particular, the development of a general formulation for the enforcement of the boundary conditions allowed for a straight forward implementation. Moreover, such a versatile formulation enables the subsequent addition of new boundary conditions or numerical methods in a very simple manner.

To tackle the fluid-structure interaction, a force model was presented that allows the determination of the forces acting on bodies present in the flow. Furthermore, a structural model combined with a parallel moving mesh procedure was presented that enables the motion of objects present in the domain across several blocks.

The suitability of the solution method for the present research was then demonstrated through the validation of each of its components. The initial stages of the development of the wake behind an impulsively started cylinder were predicted accurately and validated the flow solver. A number of two-dimensional cases of flow past a circular cylinder were then used to demonstrate the validity of the force model and showed a very good agreement with the data found in the literature for the predicted forces acting on the cylinder and the Strouhal number. The structural model and moving mesh method were then assessed on the flow past a freely oscillating cylinder at various reduced velocities, thus showing the ability of the method to accurately predict the flow past moving objects and to handle dynamic objects spread across several domain blocks.

The investigation of the three-dimensional wake of the cylinder was then carried out on three different spanwise extensions of the domain. The numerical results obtained here and validated by the experimental work of Williamson [90, 91, 92] represent a significant contribution to the field of the numerical solution of flows past a circular cylinder. Such a systematic analysis of the influence of the spanwise extension of the solution domain over the considered range of Reynolds numbers has never been reported in the literature.

The study of the behaviour of the forces acting on the cylinder showed a very good agreement with the data found in the literature. In particular, the transition from the two-dimensional to three-dimensional flow clearly appeared and the quasi-periodic beat phenomenon was observed.

However, the differences between the results obtained for the three spanwise extensions could not allow for the clear assessement of the effects of the spanwise extension on the solution. It thus became evident that an appropriate visualisation of the three-dimensional instabilities in the wake of the cylinder was necessary to investigate the effect of the spanwise extension.

The visualisation of the three-dimensional components of the vorticity in the wake of the cylinder provided clear evidences of the different vortex shedding modes. Furthermore, such a visualisation gave an insight into the transition between these modes. The comparison between the wake predicted using the three spanwise extensions revealed clear differences particularly for the vortex shedding mode A and the transition to mode B. Moreover, by determining through the visualisation the wavelengths of the instabilities and comparing the results obtained with the three extensions, it was shown that a finite spanwise extension was sufficient to predict accurately the flow past a circular cylinder.

Indeed, it was found that to correctly reproduce the vortex shedding mode A, a spanwise extension of about four cylinder diameters was sufficient. For the vortex shedding mode B, although the spanwise wavelength was shown to be close to one cylinder diameter, the shorter $\pi/2D$ spanwise extension was not quite sufficient to predict accurately the flow. In particular, owing to a more accentuated quasi-periodic beat phenomenon, the lift coefficient was over-predicted for the Reynolds numbers between 350 and 700.

However, the trends observed in the force coefficients suggest that the results for the three spanwise extensions would eventually converge for Reynolds numbers higher than 1000. Thus, although the $\pi/2D$ spanwise extension was not sufficient in the considered range of Reynolds numbers, it should be for higher Reynolds numbers where the three-dimensional effects are weaker.

It can thus be concluded that the study of the flow past an infinitely long cylinder can be reduced to a finite length one, the length of which is dependent upon the vortex shedding mode. It was shown that the solution of the flow past such a finite length cylinder gives an accurate prediction of the forces acting on the cylinder, the geometry of the wake and the three-dimensional effects, all of which being predicted at a reasonable computational cost. It becomes thus possible to envisage the solution of flows past marine risers undergoing vortex-induced vibrations using a method such as that presented here at a viable cost.

8.2 Further Investigations and Perspectives

The research into the flow past circular cylinders has been for years at the centre of numerous investigations and will still raise considerable interest for the number of phenomenon it encompasses. During the course of the present investigation, several issues were raised that the author believes require further investigation. Also, from the discussion and results presented in this thesis, a few perspectives can be suggested.

An interesting observation that was made when looking into the history of the three-dimensional force coefficients traces was the clear distinction between the two- and three-dimensional phases of the flow. Although the power spectrum revealed a secondary peak in the Strouhal frequencies corresponding to the two dimensional Strouhal number, the use of Fourrier transforms to determine the two dimensional frequency is rather inaccurate. For the Fourrier transforms to produce good results, a large number of periods is desirable which is not the case for the two-dimensional part of the flow. It was also found that the uncertainties existed for the three-dimensional frequencies. It would be interesting to investigate alternative means of measuring the vortex shedding frequencies. Combining the identification of the vortices as they are shed and released in the wake with a proper statistical model could provide a more accurate prediction of the Strouhal frequency.

Furthermore, the same method could be used to determine accurately the three-dimensional instabilities wavelengths. Clearly, the averaging procedure employed in the present work can only be adequate if a large number of periods can be observed in the flow. By identifying the three-dimensional vortices and their shedding, one could, through statistical analysis determine accurately the spanwise wavelengths.

Many engineering flow problems involve oscillating bodies. In particular, the problem of oscillating marine cables or risers has been the centre of attention for quite some time. The method presented here was developed with the capability of dealing with moving bodies and was shown to predict well the flow past an oscillating cylinder. It would thus be very straight forward to extend the present investigation to oscillating cylinders, thus determining the wavelength of the three-dimensional instabilities in the case of oscillating bodies and as a consequence the minimum spanwise extension required. Since the oscillation tend to promote the two-dimensionality of the flow, it is expected that such an extension should be shorter than for the fixed cylinder case.

To solve the problem of flexible marine risers subject to current loading, hybrid methods such as that developped by Dalheim [20] have been employed. In such a method, the fluid forces acting on the cylinder are calculated at various locations along the length of the riser with a two-dimensional CFD method. Using the strip theory, those local forces are combined to obtain the complete fluid loading on the cylinder and furthermore the response of the riser to the excitation. Since the three-dimensional effects are non-negligeable for most practical engineering flows, the use of three-dimensional sections instead of the two-dimensional ones would allow for a better determination of the local forces, and thus improve the overall solution.

Finally, an aspect that was not investigated in the present research concerns the mathematical model representing the flow. More specifically, the assumptions made when dealing with a two-dimensional approximation of the Navier-Stokes equation result in the elimination of a number of factors from the equations. In particular, by assuming that no third dimension exist, the derivatives in that direction are ignored. During the early stages of the development of the present method, tests carried out on a two-dimensional domain, i.e. using a unit thickness of the domain, showed different results than those expected. A carefull inspection revealed that the metrics associated with the third dimension were not all null and thus contributed to the flow. To correctly predict two-dimensional flows, i.e. to match the two-dimensional mathematical model used in the literature, it was necessary to zero those metrics. Investigating the difference in the mathematical models used in both the two- and three-dimensional cases would most certainly provide answers regarding the discrepancies of the results found in the two-dimensional cases.

References

[1] Akay, H. , Ecer, A. , and Fekete, K. , *A semi-explicit parallel solver for viscous incompressible flows*, Computer Methods in Applied Mechanics and Engineering, 151 (1998), pp. 1–12.

[2] Anagnostopoulos, P. , *Numerical investigation of response and wake characteristics of a vortex-excited cylinder in a uniform stream*, Journal of Fluids and Structures, 8 (1994), pp. 367–390.

[3] Anagnostopoulos, P. and Iliadis, G. , *Numerical study of the flow pattern and the in-line response of a flexible cylinder in an oscillating stream*, Journal of Fluids and Structures, 12 (1998), pp. 225–258.

[4] Bearman, P. , *Developments in vortex shedding research*, in WVIVOS - Workshop on Vortex-Induced Vibrations of Offshore Structures, 01, São Paulo, Brazil, 14-16 August 2000.

[5] Bearman, P. , Johannin, L. , and Owen, J. , *Large scale laboratory experiments on vortex-induced vibration*, in Proceedings of the 20th International Conference on Offshore Mechanics and Arctic Engineering, Rio de Janeiro, Brazil, 3-8 June 2001, ASME.

[6] Behr, M. , Hastreiter, D. , Mittal, S. , and Tezduyar, T. , *Incompressible flow past a circular cylinder: dependence of the computed flow field on the location of the lateral boundaries*, Computer Methods in Applied Mechanics and Engineering, 123 (1995), pp. 309–316.

[7] Bouard, R. and Coutanceau, M. , *Experimental determination of the main features of the viscous flow in the wake of a circular cylinder in uniform translation. part 1: Steady flow*, Journal of Fluid Mechanics, 79 (1977), pp. 231–256.

[8] ——, *The early stage of development of the wake behind an impulsively started cylinder for* $40 < re < 10^4$, Journal of Fluid Mechanics, 101 (1980), pp. 583–607.

[9] BOURIS, D. AND BERGELES, G. , *2d les of vortex shedding from a square cylinder*, Journal of Wind Engineering and Industrial Aerodynamics, 80 (1999), pp. 31–46.

[10] BREUER, M. , *Numerical and modeling influences on large eddy simulations for the flow past a circular cylinder*, International Journal of Heat and Fluid Flow, 19 (1998), pp. 512–521.

[11] ——, *A challenging test case for large eddy simulation: High reynolds number circular cylinder flow*, International Journal of Heat and Fluid Flow, 21 (2000), pp. 648–654.

[12] BRIKA, D. AND LANEVILLE, A. , *Vortex-induced vibrations of a long circular cylinder*, Journal of Fluid Mechanics, 250 (1993), pp. 481–508.

[13] CALY, J. , JABARDO, P. , MENEGHINI, J. , PEREIRA, M. , AND FERRARI, J.A., J. , *Three-dimensional vortex shedding from two circular cylinders*, in WVIVOS - Workshop on Vortex-Induced Vibrations of Offshore Structures, 12, São Paulo, Brazil, 14-16 August 2000.

[14] CARRÉ, G. , FOURNIER, L. , AND LANTERI, S. , *Parallel linear multigrid algorithms for the acceleration of compressible flow calculations*, Computer Methods in Applied Mechanics and Engineering, 184 (2000), pp. 427–448.

[15] CHEER, A. , *Unsteady separated wake behind an impulsively started cylinder in slightly viscous fluid*, Journal of Fluid Mechanics, 201 (1980), pp. 485–505.

[16] CHORIN, A. , *Numerical solution of the navier-stokes equations*, Math. Comp., 22 (1968), pp. 745–762.

[17] ——, *Numerical study of slightly viscous flow*, Journal of Fluid Mechanics, 57 (1973), pp. 785–796.

[18] CHRISTIANSEN, J. , *Numerical simulation of hydrodynamics by the method of point vortices*, Journal of Computational Physics, 13 (1973), pp. 367–379.

[19] COOK, H. , BEYNET, P. , AND CORNUT, S. , *The challenge of viv - an operator's view*, in WVIVOS - Workshop on Vortex-Induced Vibrations of Offshore Structures, 13, São Paulo, Brazil, 14-16 August 2000.

[20] DALHEIM, J. , *A new hybrid numerical procedure for prediction of viv of risers in ultra deep waters*, in Proceedings of the 20th International Conference on Offshore Mechanics and Arctic Engineering, Rio de Janeiro, Brazil, 3-8 June 2001, ASME.

[21] Dalton, C. , *Calculation of flow past a circular cylinder using les*, in WVIVOS - Workshop on Vortex-Induced Vibrations of Offshore Structures, 03, São Paulo, Brazil, 14-16 August 2000.

[22] Davis, J. , Hover, F. , Landolt, A. , and Triantafyllou, M. , *Vortex-induced vibrations of rigid and flexible cylinders*, in WVIVOS - Workshop on Vortex-Induced Vibrations of Offshore Structures, 09, São Paulo, Brazil, 14-16 August 2000.

[23] Degand, C. and Farhat, C. , *A three-dimensional torsional spring analogy method for unstructured dynamic meshes*, Computers and Structures, 80 (2002), pp. 305–316.

[24] Deng, G. , Piquet, J. , Queutey, P. , and Visonneau, M. , *Handbook of Computational Fluid Mechanics*, Academic Press, 2000, ch. 2 - Navier-Stokes equations for incompressible flows: finite difference and finite volume methods.

[25] Deschamps, C. , *Transição e Turbulencia - I Escola de Primavera*, Associação Brasileira de Ciências Mecânicas - ABCM, 1998, ch. 3 - Modelos Algêbricos e Differenciais.

[26] di Serafino, D. , *A parallel implementation of a multigrid multiblock euler solver on distributer memory machines*, Parallel Computing, 23 (1997), pp. 2095–2113.

[27] Dubuc, L. , Cantariti, F. , Woodgate, M. , Gribben, B. , Badcock, K. , and Richards, B. , *A grid deformation technique for unsteady flow computations*, International Journal for Numerical Methods in Fluids, 32 (2000), pp. 285–311.

[28] Farhat, C. , Degand, C. , Koobus, B. , and Lesoinne, M. , *Torsional springs for two-dimensional dynamic unstructured fluid meshes*, Computer Methods in Applied Mechanics and Engineering, 163 (1998), pp. 231–215.

[29] Ferziger, J. and Perić, M. , *Computational Methods for Fluid Dynamics*, Springer-Verlag, 2nd ed., 1999.

[30] Fujarra, A. and Pesce, C. , *Some remarks on vortex-induced vibrations of flexible cylinders*, in WVIVOS - Workshop on Vortex-Induced Vibrations of Offshore Structures, 17, São Paulo, Brazil, 14-16 August 2000.

[31] Garbey, M. and Vassilevski, Yu, V. , *A parallel solver for unsteady incompressible 3d navier-stokes equations*, Parallel Computing, 27 (2001), pp. 363–389.

[32] Gatski, T. , *Handbook of Computational Fluid Mechanics*, Academic Press, 2000, ch. 6 - Turbulent Flows: Model Equations and Solution Methodology.

[33] Germano, M. , Piomelli, U. , Moin, P. , and Cabot, W. , *A dynamic subgrid-scale eddy viscosity model*, Physics of Fluid A, 3 (1991), pp. 1760–1765.

[34] Guermond, J.-L. and Quartapelle, L. , *On stability and convergence of projection methods based on pressure poisson equation*, International Journal for Numerical Methods in Fluids, 26 (1998), pp. 1039–1053.

[35] Härtel, C. , *Handbook of Computational Fluid Mechanics*, Academic Press, 2000, ch. 5 - Turbulent Flows: Direct Numerical Simulation and Large Eddy Simulation.

[36] Henderson, R. , *Details of the drag curve near the onset of vortex shedding*, Physics of Fluids, 7 (1995), pp. 2102–2104.

[37] Herjford, K. , *A study of two-dimensional separated flow by a combination of the finite element and Navier-Stokes equations*, PhD thesis, The Norvegian Institute of Technology, Trondheim, Norway, 1995.

[38] Hirsch, C. , *Numerical Computation of Internal and External Flows*, vol. 2: Computational Methods for Inviscid and Viscous Flows, John Wileys & Sons, 1998.

[39] Hoe Tai, C. and Zhao, Y. , *Parallel unsteady incompressible viscous flow computations using an unstructured multigrid method*, Journal of Computational Physics, 192 (2003), pp. 277–311.

[40] Huse, E. , *Flow interference and clashing in deep sea riser arrays*, in WVIVOS - Workshop on Vortex-Induced Vibrations of Offshore Structures, 04, São Paulo, Brazil, 14-16 August 2000.

[41] Jordan, S. and Ragab, S. , *A large-eddy simulation of the near wake of a circular cylinder*, Journal of Fluids Engineering, 120 (1998), pp. 243–252. Transaction of the ASME.

[42] Kalro, V. and Tezduyar, T. , *Parallel 3d computation of unsteady flows around circular cylinders*, Parallel Computing, 23 (1997), pp. 1235–1248.

[43] Khalak, A. and Williamson, C. , *Dynamics of a hydroelastic cylinder with very low mass and damping*, Journal of Fluids and Structures, 10 (1996), pp. 455–472.

[44] KHALAK, A. AND WILLIAMSON, C. , *Motions, forces and mode transitions in vortex-induced vibrations at low mass-damping*, Journal of Fluids and Structures, 13 (1999), pp. 813–851.

[45] KIRIS, C. AND KWAK, D. , *Numerical solution of incompressible navier-stokes equations using a fractional-step approach*, Computers and Fluids, 30 (2001), pp. 829–851.

[46] KRAVCHENKO, A. , MOIN, P. , AND SHARIFF, K. , *B-spline method and zonal grids for simulations of complex turbulent flows*, Journal of Computational Physics, 151 (1999), pp. 757–789.

[47] LANEVILLE, A. AND BRIKA, D. , *The fluid and mechanical coupling between two circular cylinders in tandem arrangement*, Journal of Fluids and Structures, 13 (1999), pp. 967–986.

[48] LANTERI, S. , *Parallel solutions of compressible flows using overlapping and non-overlapping mesh partitionning strategies*, Parallel Computing, 22 (1996), pp. 943–968.

[49] LARSEN, C. , *Empirical viv models*, in WVIVOS - Workshop on Vortex-Induced Vibrations of Offshore Structures, 05, São Paulo, Brazil, 14-16 August 2000.

[50] LARSEN, C. , YTTERVIK, R. , VIKESTAD, K. , AND PASSANO, E. , *Empirical model for analysis of vortex induced vibrations - theoretical background and case studies*, in Proceedings of the 20th International Conference on Offshore Mechanics and Arctic Engineering, Rio de Janeiro, Brazil, 3-8 June 2001, ASME.

[51] LEI, C. , CHENG, L. , AND KAVANAGH, K. , *Spanwise length effects on three-dimensional modelling of flow over a circular cylinder*, Computer Methods in Applied Mechanics and Engineering, 910 (2001), pp. 2909–2923.

[52] LILLY, D. , *A proposed modification of the germano subgrid-scale eddy viscosity model*, Physics of Fluid, A (1992), pp. 633–635.

[53] LIU, F. , CAI, J. , ZHU, Y. , WONG, A. , AND TSAI, H. , *Calculation of wing flutter by a coupled cfd-csd method*, in 38th Aerospace Sciences Meeting & Exhibit, Reno, NV, USA, 10-13 January 2000, AIAA.

[54] LU, X. , DALTON, C. , AND ZHANG, J. , *Application of large eddy simulation to an oscillating flow past a circular cylinder*, Journal of Fluids Engineering, 119 (1997), pp. 519–525. Transaction of the ASME.

[55] LU, X.-Y. AND DALTON, C. , *Calculation of the timing of vortex formation from an oscillating cylinder*, Journal of Fluids and Structures, 10 (1996), pp. 527–541.

[56] MAEDA, H. , *Vortex-induced vibration research in japan*, in WVIVOS - Workshop on Vortex-Induced Vibrations of Offshore Structures, 06, São Paulo, Brazil, 14-16 August 2000.

[57] MAHIR, N. AND ROCKWELL, D. , *Vortex formation from system of two cylinders - part i: Tandem arrangement*, Journal of Fluids and Structures, 10 (1996), pp. 473–489.

[58] ——, *Vortex formation from system of two cylinders - part ii: Side-by-side arrangement*, Journal of Fluids and Structures, 10 (1996), pp. 491–500.

[59] MÉTAIS, O. AND LESIEUR, M. , *Spectral large-eddy simulation of isotropic and stably stratified turbulence*, Journal of Fluid Mechanics, 239 (1992), pp. 157–194.

[60] MILIOU, A. , SHERWIN, S. , AND GRAHAM, J. , *Fluid dynamic loading on curved riser pipes*, in Proceedings of the 20th International Conference on Offshore Mechanics and Arctic Engineering, Rio de Janeiro, Brazil, 3-8 June 2001, ASME.

[61] MITTAL, S. AND KUMAR, V. , *Finite element study of vortex-induced cross-flow and in-line oscillations of a circular cylinder at low reynolds numbers*, International Journal for Numerical Methods in Fluids, 31 (1999), pp. 1087–1120.

[62] ——, *Flow-induced vibrations of a light circular cylinder at reynolds numbers* 10^3 *to* 10^4, Journal of Sound and Vibration, 245 (2001), pp. 923–946.

[63] MOITRA, S. AND GATSKI, T. , *Efficient parallel algorithm for direct numerical simulation of turbulent flows*, tech. rep., NASA Langley Research Center, 1997.

[64] MURAKAMI, S. AND MOCHIDA, A. , *On turbulent vortex shedding flow past 2d square cylinder predicted by cfd*, Journal of Wind Engineering and Industrial Aerodynamics, 54-55 (1995), pp. 191–211.

[65] NOCA, F. , SHIELS, D. , AND JEON, D. , *Measuring instantaneous fluid dynamic forces on bodies, using only velocity fields and their derivatives*, Journal of Fluids and Structures, 11 (1997), pp. 345–350.

[66] OLIVEIRA, M. AND SPHAIER, S. , *Numerical simulation of vortex induced vibrations in three dimensions using a hybrid method*, in Proceedings of the

20th International Conference on Offshore Mechanics and Arctic Engineering, Rio de Janeiro, Brazil, 3-8 June 2001, ASME.

[67] PÉNEAU, F. , BOISSON, H. , AND DJILALI, N. , *Large eddy simulation of the influence of high free-stream turbulence on a spatially evolving boundary layer*, International Journal of Heat and Fluid Flow, 21 (2000), pp. 640–647.

[68] PINTO, M. AND ARANHA, J. , *On the dynamic compression in marine risers*, in WVIVOS - Workshop on Vortex-Induced Vibrations of Offshore Structures, 20, São Paulo, Brazil, 14-16 August 2000.

[69] PONCET, P. , *Méthodes particulaires pour la simulation des sillages tridimensionels*, PhD thesis, Université de Grenoble 1 - Joseph Fourier, Grenoble, France, 2001.

[70] PROTAS, B. , STUCZEK, A. , AND NOWAKOWSKI, A. , *An effective approach to computation of forces in viscous incompressible flows*, Journal of Computational Physics, 159 (2000), pp. 231–245.

[71] RENGEL HERNÁNDEZ, J. , *A projection method for the simulation of unsteady bidimensional incompressible flow*, Master's thesis, Federal University of Rio de Janeiro (UFRJ/COPPE), Ocean Engineering Department, Rio de Janeiro, Brazil, 1999.

[72] ROSHKO, A. , *On the wake and drag of bluff bodies*, J. of Aeronaut. Sci., 22 (1955), p. 124.

[73] SARPKAYA, T. , *Force on a circular cylinder in viscous oscillatory flow at low keulegan-carpenter numbers*, Journal of Fluid Mechanics, 165 (1986).

[74] SCHLICHTING, H. , ed., *Boundary Layer Theory*, McGraw-Hill, 1960.

[75] SCHULZ, K. AND KALLINDERID, Y. , *Unsteady flow structure interaction for incompressible flows using deformable hybrid grids*, Journal of Computational Physics, 143 (1998), pp. 569–597.

[76] SMAGORINSKY., J. , *General circulation experiments with primitive equations. i. the basic experiment*, Monthly Weather Rev., 91 (1963), pp. 99–164.

[77] SOLAAS, F. AND KROKSTAD, J. , *"comparative studies", deeper project report*, tech. rep., Marintek, 1998.

[78] SPHAIER, S. AND OLIVEIRA, M. , *Some numerical experience in vortex-induced vibrations*, in WVIVOS - Workshop on Vortex-Induced Vibrations of Offshore Structures, 24, São Paulo, Brazil, 14-16 August 2000.

[79] Suksangpanomrung, A. , Djilali, N. , and Moinat, P. , *Large-eddy simulation of separated flow over a bluff rectangular plate*, International Journal of Heat and Fluid Flow, 21 (2000), pp. 655–663.

[80] Sun, X. and Dalton, C. , *Application of the les method to the oscillating flow past a circular cylinder*, Journal of Fluids and Structures, 10 (1996), pp. 851–872.

[81] Tannehill, J. , Anderson, D. , and Pletcher, R. , *Computational Fluid Mechanics and Heat Transfer*, Taylor & Francis, 2nd ed., 1997.

[82] Thompson, J. F. , Soni, B. , and Weatherill, N. , eds., *Handbook of Grid Generation*, CRC Press LLc, Boca Raton, FL, 1998.

[83] Thompson, M. , Hourigan, K. , and Sheridan, J. , *Three-dimensional instabilities in the wake of a circular cylinder*, Experimental Thermal and Fluid Science, 12 (1996), pp. 190–196.

[84] Tritton, D. , *Experiments on the flow past a circular cylinder at low reynolds numbers*, Journal of Fluid Mechanics, 6 (1959), pp. 547–567.

[85] Vandiver, J. , *Vortex-induced vibration of flexible risers in steady and unsteady flow*, in WVIVOS - Workshop on Vortex-Induced Vibrations of Offshore Structures, 10, São Paulo, Brazil, 14-16 August 2000.

[86] Vatsa, V. and Wedan, B. , *Parallelization of a multiblock flow code: and engineering implementation*, Computers and Fluids, 28 (1999), pp. 603–614.

[87] Versteeg, H. and Malalasekera, W. , *An Introduction to Computational Fluid Dynamics - The Finite Volume Method*, Longman Scientific & Technical, 1995.

[88] Wanderley, J. and Levi, C. , *Validation of a finite difference method for the simulation of vortex-induced vibration on a circular cylinder*, Ocean Engineering, 29 (2002), pp. 445–460.

[89] Wilcox, D. , *Turbulence-model transition predictions*, AIAA Journal, 13 (1975), pp. 241–243.

[90] Williamson, C. , *The existence of two stages in the transition to three-dimensionality of a cylinder wake*, Physics of Fluids, 31 (1988), pp. 3165–3168.

[91] ——, *Oblique and parallel modes of vortex shedding in the wake of a circular cylinder at low reynolds numbers*, Journal of Fluid Mechanics, 206 (1989), pp. 579–627.

[92] ——, *Vortex dynamics in the cylinder wake*, Annual Review of Fluid Mechanics, 28 (1996), pp. 477–539.

[93] WINKELMANN, R. , HÄUSER, J. , AND WILLIAMS, R. , *Strategies for parallel and numerical scalability of cfd codes*, Computer Methods in Applied Mechanics and Engineering, 174 (1999), pp. 433–456.

[94] WONG, A. , TSAI, H. , CAI, J. , ZHU, Y. , AND LIU, F. , *Unsteady flow calculations with a multi-block moving mesh algorithm*, in 38th Aerospace Sciences Meeting & Exhibit, Reno, NV, USA, 10-13 January 2000, AIAA.

[95] WU, J. , SHERIDAN, J. , WELSH, M. , AND HOURIGAN, K. , *Three-dimensional vortex structures in a cylinder wake*, Journal of Fluid Mechanics, 312 (1996), pp. 201–222.

[96] YAMAMOTO, C. , SALTARA, F. , MARTINS, C. , MENEGHINI, J. , AND FERRARI, J. , *Hydroelastic repsonse of offshore risers using cfd*, in Proceedings of the 20th International Conference on Offshore Mechanics and Arctic Engineering, Rio de Janeiro, Brazil, 3-8 June 2001, ASME.

[97] YANG, Z. AND VOKE, P. , *Large-eddy simulation of separated leading-edge flow in general coordinates*, International Journal for Numerical Methods in Engineering, 49 (2000), pp. 681–696.

[98] YEUNG, R. , SPHAIER, S. , AND VAIDHYANATHAN, M. , *Unsteady flow about bluff cylinders*, International Journal of Offshore and Polar Engineering, 3 (1993), pp. 81–92.

[99] ZDRAVKOVICH, M. , *Different modes of vortex shedding: an overview*, Journal of Fluids and Structures, 10 (1996), pp. 427–437.

[100] ZHANG, J. AND DALTON, C. , *Interaction of a steady approach flow and a circular cylinder undergoing forced oscillation*, Journal of Fluids Engineering, 119 (1997), pp. 808–813. Transaction of the ASME.

[101] ——, *A three-dimensional simulation of a steady approach flow past a circular cylinder at low reynolds number*, International Journal for Numerical Methods in Fluids, 26 (1998), pp. 1003–1022.

[102] ZHENG, X. , LIU, C. , LIU, F. , AND YANG, C. , *Turbulence transition simulation using the k-w model*, International Journal For Numerical Methods in Engineering, 42 (1998), pp. 907–926.

[103] ZHENG, X. AND LIU, F. , *Staggered upwind method for solving navier-stokes and k-w turbulence model equations*, AIAA Journal, 33 (1995), pp. 991–998.

[104] ZHOU, C. , SO, R. , AND LAM, K. , *Vortex-induced vibrations of an elastic circular cylinder*, Journal of Fluids and Structures, 13 (1999), pp. 165–189.

[105] ZHOU, Y. , SO, R. , LIU, M. , AND ZHANG, H. , *Complex turbulent wakes generated by two and three side-by-side cylinders*, International Journal of Heat and Fluid Flow, 21 (2000), pp. 125–133.

Appendix A

Coordinate System

To account for arbitrarily shaped bodies, it is necessary to introduce a general curvilinear coordinates system. Such a system will be effective by transforming the governing equation.

In this section, the relationships used to transform the governing equations between the generalised coordinates system and the physical coordinates system are presented. The geometrical concept and coordinates transformation relationships are essentially based on those presented by Deng *et al.* [24] and are repeated here for convenience.

Let $\mathbf{e}_{x_i}$ be the unit tangent vector in the x_i direction. In a Cartesian system, a line element is thus defined by:

$$\mathrm{d}\mathbf{r} = \mathrm{d}x_i \mathbf{e}_{x_i} \qquad \therefore \qquad \mathbf{r} = \mathbf{0} + x_i \mathbf{e}_{x_i}$$

Where $\mathbf{0}$ corresponds to the origin of the coordinate system.

In a body fitted coordinate system, i.e. curvilinear coordinate system, the line element is defined as:

$$\mathrm{d}\mathbf{r} = \mathrm{d}\xi_j \frac{\partial \mathbf{r}}{\partial \xi_j} = \mathrm{d}\xi_j \mathbf{g}_j$$

The Jacobian of the transformation is:

$$J = \frac{\mathrm{D}\left(x_1, x_2, x_3\right)}{\mathrm{D}\left(\xi_1, \xi_2, \xi_3\right)} = \mathbf{g}_i \cdot \left(\mathbf{g}_j \times \mathbf{g}_k\right) \qquad (i, j, k \ \text{ in cyclic order}) \tag{A.1}$$

$\{\mathbf{g}_i\}$ is the covariant basis of vector tangent to the curves along which ξ_i varies. Let $\{\mathbf{g}^i\}$ be the contravariant basis of vector $\mathbf{g}^i = \mathrm{grad}\xi_i$ normal to the faces $\xi_i = \mathrm{const}$.

The relationship between the covariant and the contravariant vectors is:

$$\frac{\partial \xi_i}{\partial x_k}\frac{\partial x_k}{\partial \xi_j} = \delta_{ij} \quad \text{or} \quad \mathbf{g}^i \cdot \mathbf{g}_j = \delta_{ij} \tag{A.2}$$

$$\therefore \mathbf{g}^i = J^{-1}\mathbf{g}_j \times \mathbf{g}_k \qquad (i, j, k \ \text{ in cyclic order}) \tag{A.3}$$

The Jacobian J can in fact be interpreted as the volume in the physical space $\{x_i\}$ of a unit cube in the computational space $\{\xi_i\}$.

Now, since the area element on a coordinate surface of constant ξ_i is:

$$dA = \|\mathbf{g}_j \times \mathbf{g}_k\| \, \mathrm{d}\xi_j \mathrm{d}\xi_k$$

then the modulus of $\mathbf{S}^i = J\mathbf{g}^i$ is the surface area corresponding to a unit increment $\Delta\xi_j\Delta\xi_k$ (i,j and k cyclic) with its direction orthogonal to the surface $\xi_i = const.$

Thus the flux associated to the vector $\mathbf{V}$ across the surface area of sides $\Delta\xi_j$, $\Delta\xi_k$ (j, k cyclic) is related to the contravariant component $U^i = \mathbf{u} \cdot \mathbf{g}^i$ by:

$$\text{Flux} = JU^i = \mathbf{u} \cdot \mathbf{S}^i \tag{A.4}$$

The oriented area satisfies the so-called first fundamental metric identity:

$$\frac{\partial S^i_j}{\partial \xi_i} = 0 \quad \text{for all j} \tag{A.5}$$

The second fundamental identity also has to be fulfilled when the curvilinear coordinate system $\{\xi_i\}$ moves with time:

$$\frac{\partial J}{\partial t} = J\mathbf{g}^i \cdot \frac{\partial \mathbf{g}^i}{\partial t} = J\mathbf{g}^i \cdot \frac{\partial \mathbf{u_g}}{\partial \xi_i} = \frac{\partial \left(J{U_g}^i\right)}{\partial \xi^i} \tag{A.6}$$

Where $\mathbf{u_g}$ is the velocity of the curvilinear coordinate system, i.e. the grid velocity, whose Cartesian components are:

$$u_{gi} = \left.\frac{\partial x_i}{\partial t}\right|_{\xi=const} \tag{A.7}$$

${U_g}^i$ is the contravariant component of the grid velocity defined by: ${U_g}^i = \mathbf{u_g} \cdot \mathbf{g}^i$.

An important relationship to be used in the chain rule is:

$$\frac{\partial \xi_i}{\partial x_j} = J^{-1}\mathbf{S}^i \cdot \mathbf{e}_{x_j} = J^{-1}S^i_j \tag{A.8}$$

Covariant and contravariant metric tensors:

$$g_{ij} = \mathbf{g}_i \cdot \mathbf{g}_j \quad \text{and} \quad g^{ij} = \mathbf{g}^i \cdot \mathbf{g}^j = g^{-1}\mathbf{S}^i \cdot \mathbf{S}^j \tag{A.9}$$

Where

$$g = \det\left[g_{ij}\right] = J^2 \tag{A.10}$$

Appendix B

Flow Governing Equation in Curvilinear Coordinates Form

B.1 Equations in Cartesian Coordinates System

In the absence of external body forces, the basic governing equation for an incompressible Newtonian fluid are the continuity equation and the momentum equations.

In Cartesian coordinates, these can be written as follows:

Continuity:
$$\frac{\partial u_i}{\partial x_i} = 0 \tag{B.1}$$

Momentum:
$$\frac{\partial u_i}{\partial t} + \frac{\partial (u_i u_j)}{\partial x_j} = -\frac{1}{\rho}\frac{\partial p}{\partial x_i} + \nu \frac{\partial}{\partial x_j}\left(\frac{\partial u_i}{\partial x_j} + \frac{\partial u_j}{\partial x_i}\right) \tag{B.2}$$

Now, to transform these equations to their non-dimensional form, the following relationships are used:

$$x_i^* = \frac{x_i}{L} \; ; \; u_i^* = \frac{u_i}{U_\infty} \; ; \; p^* = \frac{p}{\rho . U_\infty^2} \; ; \; t^* = \frac{t . U_\infty}{L} \; ; \; R_e = \frac{\rho_\infty . U_\infty . L}{\mu_\infty} \tag{B.3}$$

Where the superscript * denotes the non-dimensional quantities.

Substituting for these in the governing equations and dropping the superscript for convenience gives:

Continuity:
$$\frac{\partial u_i}{\partial x_i} = 0 \tag{B.4}$$

Momentum:
$$\frac{\partial u_i}{\partial t}+\frac{\partial\left(u_i u_j\right)}{\partial x_j}=-\frac{\partial p}{\partial x_i}+\frac{1}{Re}\frac{\partial}{\partial x_j}\left(\frac{\partial u_i}{\partial x_j}+\frac{\partial u_j}{\partial x_i}\right) \tag{B.5}$$

B.2 Filtered Equations for LES Model

As seen previously, the filtered equations governing the flow using LES turbulence modelling can be obtained rather easily. The final filtered equations, in their non-dimensional form, are repeated here for convenience:

Continuity:
$$\frac{\partial \overline{u}_i}{\partial x_i}=0 \tag{B.6}$$

Momentum:
$$\frac{\partial \overline{u}_i}{\partial t}+\frac{\partial\left(\overline{u}_i\,\overline{u}_j\right)}{\partial x_j}=-\frac{\partial \overline{p}}{\partial x_i}+\frac{1}{Re}\frac{\partial}{\partial x_j}\left(\frac{\partial \overline{u}_i}{\partial x_j}+\frac{\partial \overline{u}_j}{\partial x_i}\right)+\frac{\partial \tau_{ij}}{\partial x_j}$$

Where:
$$\tau_{ij}-\frac{1}{3}\delta_{ij}\tau_{ll}=\frac{2}{Re_t}\overline{S}_{ij} \tag{B.7}$$

$$\overline{S}_{ij}=\frac{1}{2}\left(\frac{\partial \overline{u}_i}{\partial x_j}+\frac{\partial \overline{u}_j}{\partial x_i}\right) \tag{B.8}$$

and:

$$Re_t=\frac{1}{C_S^2\Delta\left|\overline{S}\right|} \quad \text{with} \quad \left|\overline{S}\right|=\sqrt{2\overline{S}_{ij}\,\overline{S}_{ij}} \tag{B.9}$$

Defining the pseudo-pressure $\overline{q}$ by adding the isotropic part of the turbulence SGS stress tensor to the pressure:

$$\overline{q}=\overline{p}-\frac{1}{3}\tau_{ll} \tag{B.10}$$

The momentum equation can thus be written as follows:

$$\frac{\partial \overline{u}_i}{\partial t}+\frac{\partial\left(\overline{u}_i\,\overline{u}_j\right)}{\partial x_j}=-\frac{\partial \overline{q}}{\partial x_i}+\frac{\partial}{\partial x_j}\left[\left(\frac{1}{Re}+\frac{1}{Re_t}\right)\left(\frac{\partial \overline{u}_i}{\partial x_j}+\frac{\partial \overline{u}_j}{\partial x_i}\right)\right] \tag{B.11}$$

Now, as outlined before, the projection method consists of solving the Burger equations to obtain an intermediary velocity field. A pressure equation is then solved that is used to project the intermediary velocity field onto a zero divergence space.

The set of filtered equations is as follows:

Continuity:
$$\frac{\partial \overline{u}_i}{\partial x_i} = 0 \tag{B.12}$$

Burger:
$$\frac{\partial \overline{u}_i^*}{\partial t} + \frac{\partial \left(\overline{u}_i^* \, \overline{u}_j^*\right)}{\partial x_j} = \frac{\partial}{\partial x_j}\left[\left(\frac{1}{Re} + \frac{1}{Re_t}\right)\left(\frac{\partial \overline{u}_i^*}{\partial x_j} + \frac{\partial \overline{u}_j^*}{\partial x_i}\right)\right] \tag{B.13}$$

Poisson:
$$\frac{\partial^2 \overline{q}}{\partial x_i \partial x_i} = \frac{\partial \overline{u}_j^*}{\partial x_j} \tag{B.14}$$

Projection:
$$\overline{u}_i = \overline{u}_i^* - \frac{\partial \overline{q}}{\partial x_i} \tag{B.15}$$

Where:

$$Re_t = \frac{1}{C_S^2 \Delta \left|\overline{S}\right|} \tag{B.16}$$

$$\left|\overline{S}\right| = \sqrt{2\overline{S}_{ij}\,\overline{S}_{ij}} \tag{B.17}$$

And:

$$\overline{S}_{ij} = \frac{1}{2}\left(\frac{\partial \overline{u}_i}{\partial x_j} + \frac{\partial \overline{u}_j}{\partial x_i}\right) \tag{B.18}$$

B.3 Filtered Equations in Curvilinear Coordinates System

B.3.1 Continuity equation

Using the chain rule, the continuity equation becomes:

$$\frac{\partial \overline{u}_i}{\partial x_i} = 0 \quad \Rightarrow \quad \frac{\partial \xi_j}{\partial x_i}\frac{\partial \overline{u}_i}{\partial \xi_j} = 0$$

Using now equation (A.8) gives the continuity equation in terms of the Cartesian components of velocity:

$$J^{-1} S_i^j \frac{\partial \overline{u}_i}{\partial \xi_j} = 0 \tag{B.19}$$

And, from equation (A.5):

$$J^{-1} \frac{\partial \left(S_i^j \overline{u}_i\right)}{\partial \xi_j} = 0$$

Finally, using equation (A.4), the continuity equation using the contravariant components of velocity can be written as::

$$J^{-1}\frac{\partial\left(J\overline{U}^j\right)}{\partial\xi_j}=0 \tag{B.20}$$

i.e.:

$$\frac{\partial\left(J\overline{U}^j\right)}{\partial\xi_j}=0 \tag{B.21}$$

Where $\overline{U}^j$, the filtered contravariant component of velocity, is defined as: $\overline{U}^j = \overline{u}\cdot\vec{g}^j$.

B.3.2 Burger equations

In the Burger equation (B.13), the time derivative for $x_i =$ const will correspond to a time derivative for $\xi =$ const. Using the chain rule gives:

$$\left.\frac{\partial\overline{u}_i^*}{\partial t}\right|_{x_j=\text{const}} = \left.\frac{\partial\overline{u}_i^*}{\partial t}\right|_{\xi=\text{const}} - \overline{u}_{g_j}^* g_j^k\frac{\partial\overline{u}_i^*}{\partial\xi_k} \tag{B.22}$$

Where: $g_j^k = \vec{g}^k\cdot\vec{e}_{x_j}$.

Thus, multiplying equation (B.13) by the Jacobian of the transformation, J, substituting the above expression for the time derivative and using the chain rule gives:

$$\begin{aligned}
&J\frac{\partial\overline{u}_i^*}{\partial t} - J\overline{u}_{g_j}^* g_j^k\frac{\partial\overline{u}_i^*}{\partial\xi_k} + J\frac{\partial\xi_k}{\partial x_j}\frac{\partial\left(\overline{u}_i^*\overline{u}_j^*\right)}{\partial\xi_k} = \\
&\quad = J\frac{\partial\xi_k}{\partial x_j}\frac{\partial}{\partial\xi_k}\left[\left(\frac{1}{Re}+\frac{1}{Re_t}\right)\left(J^{-1}\frac{\partial\xi_l}{\partial x_j}\frac{\partial\overline{u}_i^*}{\partial\xi_l}+J^{-1}\frac{\partial\xi_l}{\partial x_i}\frac{\partial\overline{u}_j^*}{\partial\xi_l}\right)\right]
\end{aligned}$$

Now, since the second fundamental metric identity (A.6) must be satisfied:

$$\overline{u}_i^*\left(\frac{\partial J}{\partial t} - Jg_i^k\frac{\partial\overline{u}_{g_j}^*}{\partial\xi_k}\right)=0$$

Adding the above to the Burger equation thus gives:

$$\begin{aligned}
&\frac{\partial\left(J\overline{u}_i^*\right)}{\partial t} - Jg_j^k\frac{\partial\left(\overline{u}_{g_j}^*\overline{u}_i^*\right)}{\partial\xi_k} + J\frac{\partial\xi_k}{\partial x_j}\frac{\partial\left(\overline{u}_i^*\overline{u}_j^*\right)}{\partial\xi_k} = \\
&\quad = J\frac{\partial\xi_k}{\partial x_j}\frac{\partial}{\partial\xi_k}\left[\left(\frac{1}{Re}+\frac{1}{Re_t}\right)\left(J^{-1}\frac{\partial\xi_l}{\partial x_j}\frac{\partial\overline{u}_i^*}{\partial\xi_l}+J^{-1}\frac{\partial\xi_l}{\partial x_i}\frac{\partial\overline{u}_j^*}{\partial\xi_l}\right)\right]
\end{aligned}$$

And, from equation (A.8):

$$\begin{aligned}\frac{\partial\left(J\overline{u}_i^*\right)}{\partial t}-S_j^k\frac{\partial\left(\overline{u}_{gj}^*\overline{u}_i^*\right)}{\partial\xi_k}+S_j^k\frac{\partial\left(\overline{u}_i^*\overline{u}_j^*\right)}{\partial\xi_k}&=\\=S_j^k\frac{\partial}{\partial\xi_k}&\left[\left(\frac{1}{Re}+\frac{1}{Re_t}\right)\left(J^{-1}S_j^l\frac{\partial\overline{u}_i^*}{\partial\xi_l}+J^{-1}S_i^l\frac{\partial\overline{u}_j^*}{\partial\xi_l}\right)\right]\end{aligned}$$

Or, since the first fundamental metric identity must be satisfied (eq. (A.5)):

$$\begin{aligned}\frac{\partial\left(J\overline{u}_i^*\right)}{\partial t}+\frac{\partial}{\partial\xi_k}\left[S_j^k\left(\overline{u}_j^*-\overline{u}_{gj}^*\right)\overline{u}_i^*\right]&=\\=\frac{\partial}{\partial\xi_k}&\left[\left(\frac{1}{Re}+\frac{1}{Re_t}\right)\left(J^{-1}S_j^kS_j^l\frac{\partial\overline{u}_i^*}{\partial\xi_l}+J^{-1}S_j^kS_i^l\frac{\partial\overline{u}_j^*}{\partial\xi_l}\right)\right]\end{aligned}\qquad\text{(B.23)}$$

If we now define the contravariant relative velocity component of the fluid with respect to the grid such as:

$$\overline{U}_r^{*k}=S_j^k\left(\overline{u}_j^*-\overline{u}_{gj}^*\right)\qquad\text{(B.24)}$$

Then, equation (B.23) becomes:

$$\begin{aligned}\frac{\partial\left(J\overline{u}_i^*\right)}{\partial t}+\frac{\partial}{\partial\xi_k}\left(\overline{U}_r^{*k}\overline{u}_i^*\right)&=\\\frac{\partial}{\partial\xi_k}\left[\left(\frac{1}{Re}+\frac{1}{Re_t}\right)\left(J^{-1}S_j^kS_j^l\frac{\partial\overline{u}_i^*}{\partial\xi_l}+J^{-1}S_j^kS_i^l\frac{\partial\overline{u}_j^*}{\partial\xi_l}\right)\right]&\end{aligned}\qquad\text{(B.25)}$$

B.3.3 Poisson equation

Using the chain rule, the Poisson equation (B.14) becomes:

$$\frac{\partial\xi_k}{\partial x_i}\frac{\partial}{\partial\xi_k}\left(\frac{\partial\xi_l}{\partial x_i}\frac{\partial\overline{q}}{\partial\xi_l}\right)=\frac{\partial\xi_m}{\partial x_j}\frac{\partial\overline{u}_j^*}{\partial\xi_m}\qquad\text{(B.26)}$$

Using now equation (A.8), the above equation becomes:

$$J^{-1}S_i^k\frac{\partial}{\partial\xi_k}\left(J^{-1}S_i^l\frac{\partial\overline{q}}{\partial\xi_l}\right)=J^{-1}S_j^m\frac{\partial\overline{u}_j^*}{\partial\xi_m}\qquad\text{(B.27)}$$

And, from the first metric identity:

$$J^{-1}\frac{\partial}{\partial\xi_k}\left(J^{-1}S_i^kS_i^l\frac{\partial\overline{q}}{\partial\xi_l}\right)=J^{-1}\frac{\partial\left(S_j^m\overline{u}_j^*\right)}{\partial\xi_m}\qquad\text{(B.28)}$$

Or:

$$\frac{\partial}{\partial \xi_k}\left(J^{-1} S_i^k S_i^l \frac{\partial \overline{q}}{\partial \xi_l}\right) = \frac{\partial\left(S_j^m \overline{u}_j^*\right)}{\partial \xi_m} \tag{B.29}$$

Finally, from the definition of the contravariant components of velocity:

$$\frac{\partial}{\partial \xi_k}\left(J^{-1} S_i^k S_i^l \frac{\partial \overline{q}}{\partial \xi_l}\right) = \frac{\partial\left(J\overline{U}^{*j}\right)}{\partial \xi_m} \tag{B.30}$$

B.3.4 Projection equations

Using the chain rule, the projection equations (eq. (B.15)) become:

$$\overline{u}_i = \overline{u}_i^* - \frac{\partial \xi_j}{\partial x_i}\frac{\partial \overline{q}}{\partial \xi_j} \tag{B.31}$$

Using now equation (A.8), the above equation becomes:

$$\overline{u}_i = \overline{u}_i^* - J^{-1} S_i^j \frac{\partial \overline{q}}{\partial \xi_j} \tag{B.32}$$

B.3.5 Turbulent Stress tensor

Finally, using the chain rule again, equation B.18 becomes:

$$\overline{S}_{ij} = \frac{1}{2}\left(\frac{\partial \xi_k}{\partial x_j}\frac{\partial \overline{u}_i}{\partial \xi_k} + \frac{\partial \xi_l}{\partial x_i}\frac{\partial \overline{u}_j}{\partial \xi_l}\right) \tag{B.33}$$

i.e., with equation (A.8):

$$\overline{S}_{ij} = \frac{J}{2}\left(S_j^k \frac{\partial \overline{u}_i}{\partial \xi_k} + S_i^l \frac{\partial \overline{u}_j}{\partial \xi_l}\right) \tag{B.34}$$

B.4 Summary

The full set of governing equations is the following:

Continuity:
$$\frac{\partial}{\partial \xi_j}\left(J\overline{U}^j\right) = 0$$

Burger:
$$\tfrac{\partial}{\partial t}\left(J\overline{u}_i^*\right) + \tfrac{\partial}{\partial \xi_k}\left(\overline{U_r}^{*k}\overline{u}_i^*\right) =$$
$$\tfrac{\partial}{\partial \xi_k}\left[\left(\tfrac{1}{Re} + \tfrac{1}{Re_t}\right)\left(J^{-1} S_j^k S_j^l \tfrac{\partial \overline{u}_i^*}{\partial \xi_l} + J^{-1} S_j^k S_i^l \tfrac{\partial \overline{u}_j^*}{\partial \xi_l}\right)\right]$$

Poisson: $$\frac{\partial}{\partial \xi_k}\left(J^{-1} S_i^k S_i^l \frac{\partial \overline{q}}{\partial \xi_l}\right) = \frac{\partial}{\partial \xi_m}\left(J\overline{U}^{*j}\right)$$

Projection: $$\overline{u}_i = \overline{u}_i^* - J^{-1} S_i^j \frac{\partial \overline{q}}{\partial \xi_j}$$

Appendix C

Finite Volume Discretisation

C.1 Burger Equation

As established previously (see Appendix B), the Burger equation for incompressible flows in its filtered curvilinear form is:

$$\frac{\partial}{\partial t}\left(J\overline{u}_i^*\right)+\frac{\partial}{\partial \xi_k}\left(\overline{U_r}^{*k}\overline{u}_i^*\right)=\frac{\partial}{\partial \xi_k}\left[\left(\frac{1}{Re}+\frac{1}{Re_t}\right)J^{-1}S_j^k S_j^l\frac{\partial \overline{u}_i^*}{\partial \xi_l}\right] \tag{C.1}$$

The discretisation of the above equation can be achieved by separately discretising the convective term, the diffusive term and the temporal derivative.

<u>Convective term</u>

The convective term of the Burger equation can be expanded as follows:

$$\frac{\partial}{\partial \xi_k}\left(\overline{U_r}^{*k}\overline{u}_i^*\right)=\frac{\partial}{\partial \xi}\left(\overline{U_r}^{*}\overline{u}_i^*\right)+\frac{\partial}{\partial \eta}\left(\overline{V_r}^{*}\overline{u}_i^*\right)+\frac{\partial}{\partial \zeta}\left(\overline{W_r}^{*}\overline{u}_i^*\right) \tag{C.2}$$

Integrating over the control volume gives:

$$\begin{aligned}\oint_{CV}\frac{\partial}{\partial \xi_k}\left(\overline{U_r}^{*k}\overline{u}_i^*\right)dV \;=\;& \oint_{CV}\frac{\partial}{\partial \xi}\left(\overline{U_r}^{*}\overline{u}_i^*\right)dV+\\ & \oint_{CV}\frac{\partial}{\partial \eta}\left(\overline{V_r}^{*}\overline{u}_i^*\right)dV+\\ & \oint_{CV}\frac{\partial}{\partial \zeta}\left(\overline{W_r}^{*}\overline{u}_i^*\right)dV\end{aligned} \tag{C.3}$$

i.e., since $dV = d\xi d\eta d\zeta$:

$$\begin{aligned}
\oint_{CV} \frac{\partial}{\partial \xi}\left(\overline{U_r}^*\overline{u}_i^*\right) d\xi d\eta d\zeta &= \left[\overline{U_r}^*\overline{u}_i^*\right]\Big|_e - \left[\overline{U_r}^*\overline{u}_i^*\right]\Big|_w \\
\oint_{CV} \frac{\partial}{\partial \eta}\left(\overline{V_r}^*\overline{u}_i^*\right) d\xi d\eta d\zeta &= \left[\overline{V_r}^*\overline{u}_i^*\right]\Big|_n - \left[\overline{V_r}^*\overline{u}_i^*\right]\Big|_s \\
\oint_{CV} \frac{\partial}{\partial \zeta}\left(\overline{W_r}^*\overline{u}_i^*\right) d\xi d\eta d\zeta &= \left[\overline{W_r}^*\overline{u}_i^*\right]\Big|_t - \left[\overline{W_r}^*\overline{u}_i^*\right]\Big|_b
\end{aligned} \tag{C.4}$$

where subscripts e, w, n, s, t and b denotes the east, west, north, south, top and bottom faces of the control volume.

Using a simple central difference scheme to evaluate the velocities at a face of a control volume, the following is obtained:

$$\begin{aligned}
\oint_{CV} \frac{\partial}{\partial \xi}\left(\overline{U_r}^*\overline{u}_i^*\right) d\xi d\eta d\zeta &= \frac{1}{2}\,\overline{U_r}^*\Big|_e \left(\overline{u}_{iP}^* + \overline{u}_{iE}^*\right) - \frac{1}{2}\,\overline{U_r}^*\Big|_w \left(\overline{u}_{iP}^* + \overline{u}_{iW}^*\right) \\
\oint_{CV} \frac{\partial}{\partial \eta}\left(\overline{V_r}^*\overline{u}_i^*\right) d\xi d\eta d\zeta &= \frac{1}{2}\,\overline{V_r}^*\Big|_n \left(\overline{u}_{iP}^* + \overline{u}_{iN}^*\right) - \frac{1}{2}\,\overline{V_r}^*\Big|_s \left(\overline{u}_{iP}^* + \overline{u}_{iS}^*\right) \\
\oint_{CV} \frac{\partial}{\partial \zeta}\left(\overline{W_r}^*\overline{u}_i^*\right) d\xi d\eta d\zeta &= \frac{1}{2}\,\overline{W_r}^*\Big|_t \left(\overline{u}_{iP}^* + \overline{u}_{iT}^*\right) - \frac{1}{2}\,\overline{W_r}^*\Big|_b \left(\overline{u}_{iP}^* + \overline{u}_{iB}^*\right)
\end{aligned} \tag{C.5}$$

Also, since $\overline{U_r}^{*k} = S_j^k\left(\overline{u}_j^* - \overline{u_{g_j}}^*\right)$, then:

$$\begin{aligned}
\overline{U_r}^*\Big|_e &= S_j^1\Big|_e \left(\overline{u}_j^* - \overline{u_{g_j}}^*\right)_e \\
&= S_1^1\Big|_e \left(\overline{u}^* - \overline{u_g}^*\right)_e + S_2^1\Big|_e \left(\overline{v}^* - \overline{v_g}^*\right)_e + S_3^1\Big|_e \left(\overline{w}^* - \overline{w_g}^*\right)_e
\end{aligned} \tag{C.6}$$

Using now a simple linear interpolation scheme to obtain the components of velocity at the face of the control volume gives:

$$\begin{aligned}
\overline{U_r}^*\Big|_e = \frac{1}{2}\Big[& S_1^1\Big|_e \left(\overline{u}_P^* + \overline{u}_E^* - \overline{u_g}_P^* - \overline{u_g}_E^*\right) + S_2^1\Big|_e \left(\overline{v}_P^* + \overline{v}_E^* - \overline{v_g}_P^* - \overline{v_g}_E^*\right) + \\
& S_3^1\Big|_e \left(\overline{w}_P^* + \overline{w}_E^* - \overline{w_g}_P^* - \overline{w_g}_E^*\right)\Big]
\end{aligned} \tag{C.7}$$

Similarly:

$$
\begin{aligned}
\overline{U_r}^*\Big|_w &= \frac{1}{2}\left[S_1^1\big|_w\left(\overline{u}_P^* + \overline{u}_W^* - \overline{u_{gP}}^* - \overline{u_{gW}}^*\right) + S_2^1\big|_w\left(\overline{v}_P^* + \overline{v}_W^* - \overline{v_{gP}}^* - \overline{v_{gW}}^*\right) + \right. \\
&\qquad \left. S_3^1\big|_w\left(\overline{w}_P^* + \overline{w}_W^* - \overline{w_{gP}}^* - \overline{w_{gW}}^*\right)\right] \\
\overline{V_r}^*\Big|_n &= \frac{1}{2}\left[S_1^2\big|_n\left(\overline{u}_P^* + \overline{u}_N^* - \overline{u_{gP}}^* - \overline{u_{gN}}^*\right) + S_2^2\big|_n\left(\overline{v}_P^* + \overline{v}_N^* - \overline{v_{gP}}^* - \overline{v_{gN}}^*\right) + \right. \\
&\qquad \left. S_3^2\big|_n\left(\overline{w}_P^* + \overline{w}_N^* - \overline{w_{gP}}^* - \overline{w_{gN}}^*\right)\right] \\
\overline{V_r}^*\Big|_s &= \frac{1}{2}\left[S_1^2\big|_s\left(\overline{u}_P^* + \overline{u}_S^* - \overline{u_{gP}}^* - \overline{u_{gS}}^*\right) + S_2^2\big|_s\left(\overline{v}_P^* + \overline{v}_S^* - \overline{v_{gP}}^* - \overline{v_{gS}}^*\right) + \right. \\
&\qquad \left. S_3^2\big|_s\left(\overline{w}_P^* + \overline{w}_S^* - \overline{w_{gP}}^* - \overline{w_{gS}}^*\right)\right] \\
\overline{W_r}^*\Big|_t &= \frac{1}{2}\left[S_1^3\big|_t\left(\overline{u}_P^* + \overline{u}_T^* - \overline{u_{gP}}^* - \overline{u_{gT}}^*\right) + S_2^3\big|_t\left(\overline{v}_P^* + \overline{v}_T^* - \overline{v_{gP}}^* - \overline{v_{gT}}^*\right) + \right. \\
&\qquad \left. S_3^3\big|_t\left(\overline{w}_P^* + \overline{w}_T^* - \overline{w_{gP}}^* - \overline{w_{gT}}^*\right)\right] \\
\overline{W_r}^*\Big|_b &= \frac{1}{2}\left[S_1^3\big|_b\left(\overline{u}_P^* + \overline{u}_B^* - \overline{u_{gP}}^* - \overline{u_{gB}}^*\right) + S_2^3\big|_b\left(\overline{v}_P^* + \overline{v}_B^* - \overline{v_{gP}}^* - \overline{v_{gB}}^*\right) + \right. \\
&\qquad \left. S_3^3\big|_b\left(\overline{w}_P^* + \overline{w}_B^* - \overline{w_{gP}}^* - \overline{w_{gB}}^*\right)\right] \qquad \text{(C.8)}
\end{aligned}
$$

Diffusive term

The diffusive term of the Burger equation can be expanded as follows:

$$
\begin{aligned}
\frac{\partial}{\partial \xi_k}\left[\left(\frac{1}{Re} + \frac{1}{Re_t}\right) J^{-1} S_j^k S_j^l \frac{\partial \overline{u}_i^*}{\partial \xi_l}\right] &= \frac{\partial}{\partial \xi}\left[\left(\frac{1}{Re} + \frac{1}{Re_t}\right) J^{-1} S_j^1 S_j^l \frac{\partial \overline{u}_i^*}{\partial \xi_l}\right] + \\
&\quad \frac{\partial}{\partial \eta}\left[\left(\frac{1}{Re} + \frac{1}{Re_t}\right) J^{-1} S_j^2 S_j^l \frac{\partial \overline{u}_i^*}{\partial \xi_l}\right] + \\
&\quad \frac{\partial}{\partial \zeta}\left[\left(\frac{1}{Re} + \frac{1}{Re_t}\right) J^{-1} S_j^3 S_j^l \frac{\partial \overline{u}_i^*}{\partial \xi_l}\right] \qquad \text{(C.9)}
\end{aligned}
$$

Considering now the first term on the right hand side, i.e. the first spatial derivative in ξ:

$$
\begin{aligned}
&\tfrac{\partial}{\partial \xi}\left[\left(\tfrac{1}{Re} + \tfrac{1}{Re_t}\right) J^{-1} S_j^1 S_j^l \tfrac{\partial \overline{u}_i^*}{\partial \xi_l}\right] = \\
&= \tfrac{\partial}{\partial \xi}\left[\left(\tfrac{1}{Re} + \tfrac{1}{Re_t}\right) J^{-1}\left[\left(S_1^1 S_1^1 + S_2^1 S_2^1 + S_3^1 S_3^1\right)\tfrac{\partial \overline{u}_i^*}{\partial \xi} + \right.\right. \\
&\left.\left.\left(S_1^1 S_1^2 + S_2^1 S_2^2 + S_3^1 S_3^2\right)\tfrac{\partial \overline{u}_i^*}{\partial \eta} + \left(S_1^1 S_1^3 + S_2^1 S_2^3 + S_3^1 S_3^3\right)\tfrac{\partial \overline{u}_i^*}{\partial \zeta}\right]\right] \qquad \text{(C.10)}
\end{aligned}
$$

Let:

$$\begin{aligned} C_1 &= J^{-1}\left(S_1^1 S_1^1 + S_2^1 S_2^1 + S_3^1 S_3^1\right) \\ C_2 &= J^{-1}\left(S_1^1 S_1^2 + S_2^1 S_2^2 + S_3^1 S_3^2\right) \\ C_3 &= J^{-1}\left(S_1^1 S_1^3 + S_2^1 S_2^3 + S_3^1 S_3^3\right) \end{aligned} \qquad \text{(C.11)}$$

Then:

$$\begin{aligned} &\tfrac{\partial}{\partial \xi}\left[\left(\tfrac{1}{Re}+\tfrac{1}{Re_t}\right) J^{-1} S_j^1 S_j^l \tfrac{\partial \overline{u}_i^*}{\partial \xi_l}\right] = \\ &\quad = \tfrac{\partial}{\partial \xi}\left[\left(\tfrac{1}{Re}+\tfrac{1}{Re_t}\right)\left[C_1 \tfrac{\partial \overline{u}_i^*}{\partial \xi} + C_2 \tfrac{\partial \overline{u}_i^*}{\partial \eta} + C_3 \tfrac{\partial \overline{u}_i^*}{\partial \zeta}\right]\right] \end{aligned} \qquad \text{(C.12)}$$

Integrating over the control volume gives:

$$\begin{aligned} &\oint_{CV} \tfrac{\partial}{\partial \xi}\left[\left(\tfrac{1}{Re}+\tfrac{1}{Re_t}\right) J^{-1} S_j^1 S_j^l \tfrac{\partial \overline{u}_i^*}{\partial \xi_l}\right] dV = \\ &\quad = \oint_{CV} \tfrac{\partial}{\partial \xi}\left[\left(\tfrac{1}{Re}+\tfrac{1}{Re_t}\right)\left[C_1 \tfrac{\partial \overline{u}_i^*}{\partial \xi} + C_2 \tfrac{\partial \overline{u}_i^*}{\partial \eta} + C_3 \tfrac{\partial \overline{u}_i^*}{\partial \zeta}\right]\right] d\xi d\eta d\zeta \end{aligned} \qquad \text{(C.13)}$$

i.e.:

$$\begin{aligned} \oint_{CV} \frac{\partial}{\partial \xi}\left[\left(\frac{1}{Re}+\frac{1}{Re_t}\right) J^{-1} S_j^1 S_j^l \frac{\partial \overline{u}_i^*}{\partial \xi_l}\right] dV &= \left[\left(\frac{1}{Re}+\frac{1}{Re_t}\right)\left[C_1 \frac{\partial \overline{u}_i^*}{\partial \xi} + C_2 \frac{\partial \overline{u}_i^*}{\partial \eta} + C_3 \frac{\partial \overline{u}_i^*}{\partial \zeta}\right]\right]\Bigg|_e - \\ &\quad \left[\left(\frac{1}{Re}+\frac{1}{Re_t}\right)\left[C_1 \frac{\partial \overline{u}_i^*}{\partial \xi} + C_2 \frac{\partial \overline{u}_i^*}{\partial \eta} + C_3 \frac{\partial \overline{u}_i^*}{\partial \zeta}\right]\right]\Bigg|_w \end{aligned}$$

$$\text{(C.14)}$$

i.e.:

$$\begin{aligned} &\oint_{CV} \tfrac{\partial}{\partial \xi}\left[\left(\tfrac{1}{Re}+\tfrac{1}{Re_t}\right) J^{-1} S_j^1 S_j^l \tfrac{\partial \overline{u}_i^*}{\partial \xi_l}\right] dV = \\ &\quad = \left(\tfrac{1}{Re}+\tfrac{1}{Re_t}\right)\Big|_e \left[C_1\big|_e \tfrac{\partial \overline{u}_i^*}{\partial \xi}\Big|_e + C_2\big|_e \tfrac{\partial \overline{u}_i^*}{\partial \eta}\Big|_e + C_3\big|_e \tfrac{\partial \overline{u}_i^*}{\partial \zeta}\Big|_e\right] - \\ &\quad\ \left(\tfrac{1}{Re}+\tfrac{1}{Re_t}\right)\Big|_w \left[C_1\big|_w \tfrac{\partial \overline{u}_i^*}{\partial \xi}\Big|_w + C_2\big|_w \tfrac{\partial \overline{u}_i^*}{\partial \eta}\Big|_w + C_3\big|_w \tfrac{\partial \overline{u}_i^*}{\partial \zeta}\Big|_w\right] \end{aligned}$$

$$\text{(C.15)}$$

Now, using once more a simple interpolation scheme for the face derivatives:

$$
\begin{aligned}
\left.\frac{\partial \overline{u}_i^*}{\partial \xi}\right|_e &= \overline{u}_{iE}^* - \overline{u}_{iP}^* \\
\left.\frac{\partial \overline{u}_i^*}{\partial \eta}\right|_e &= \frac{1}{4}\left(\overline{u}_{iN}^* + \overline{u}_{iNE}^* - \overline{u}_{iS}^* - \overline{u}_{iSE}^*\right) \\
\left.\frac{\partial \overline{u}_i^*}{\partial \zeta}\right|_e &= \frac{1}{4}\left(\overline{u}_{iT}^* + \overline{u}_{iTE}^* - \overline{u}_{iB}^* - \overline{u}_{iBE}^*\right) \\
\left.\frac{\partial \overline{u}_i^*}{\partial \xi}\right|_w &= \overline{u}_{iP}^* - \overline{u}_{iW}^* \\
\left.\frac{\partial \overline{u}_i^*}{\partial \eta}\right|_w &= \frac{1}{4}\left(\overline{u}_{iN}^* + \overline{u}_{iNW}^* - \overline{u}_{iS}^* - \overline{u}_{iSW}^*\right) \\
\left.\frac{\partial \overline{u}_i^*}{\partial \zeta}\right|_w &= \frac{1}{4}\left(\overline{u}_{iT}^* + \overline{u}_{iTW}^* - \overline{u}_{iB}^* - \overline{u}_{iBW}^*\right)
\end{aligned}
\tag{C.16}
$$

Thus:

$$
\begin{aligned}
&\oint_{CV} \tfrac{\partial}{\partial \xi}\left[\left(\tfrac{1}{Re} + \tfrac{1}{Re_t}\right) J^{-1} S_j^1 S_j^l \tfrac{\partial \overline{u}_i^*}{\partial \xi_l}\right] dV = \\
&= \left.\left(\tfrac{1}{Re} + \tfrac{1}{Re_t}\right)\right|_e \left[C_{1e}\left(\overline{u}_{iE}^* - \overline{u}_{iP}^*\right) + \tfrac{1}{4} C_{2e}\left(\overline{u}_{iN}^* + \overline{u}_{iNE}^* - \overline{u}_{iS}^* - \overline{u}_{iSE}^*\right)\right. \\
&\qquad \left. + \tfrac{1}{4} C_{3e}\left(\overline{u}_{iT}^* + \overline{u}_{iTE}^* - \overline{u}_{iB}^* - \overline{u}_{iBE}^*\right)\right] \\
&\quad - \left.\left(\tfrac{1}{Re} + \tfrac{1}{Re_t}\right)\right|_w \left[C_{1w}\left(\overline{u}_{iP}^* - \overline{u}_{iW}^*\right) + \tfrac{1}{4} C_{2w}\left(\overline{u}_{iN}^* + \overline{u}_{iNW}^* - \overline{u}_{iS}^* - \overline{u}_{iSW}^*\right)\right. \\
&\qquad \left. + \tfrac{1}{4} C_{3w}\left(\overline{u}_{iT}^* + \overline{u}_{iTW}^* - \overline{u}_{iB}^* - \overline{u}_{iBW}^*\right)\right]
\end{aligned}
\tag{C.17}
$$

Similarly, using:

$$
\begin{aligned}
C_4 &= J^{-1}\left(S_1^2 S_1^2 + S_2^2 S_2^2 + S_3^2 S_3^2\right) \\
C_5 &= J^{-1}\left(S_1^2 S_1^3 + S_2^2 S_2^3 + S_3^2 S_3^3\right) \\
C_6 &= J^{-1}\left(S_1^3 S_1^3 + S_2^3 S_2^3 + S_3^3 S_3^3\right)
\end{aligned}
\tag{C.18}
$$

It can be shown that the second term of the diffusive term can be expanded as folows:

$$\begin{aligned}
&\oint_{CV} \frac{\partial}{\partial \eta} \left[\left(\frac{1}{Re} + \frac{1}{Re_t} \right) J^{-1} S_j^2 S_j^l \frac{\partial \overline{u}_i^*}{\partial \xi_l} \right] dV = \\
&= \left(\frac{1}{Re} + \frac{1}{Re_t} \right) \bigg|_n \left[C_{4n} \left(\overline{u}_{iN}^* - \overline{u}_{iP}^* \right) + \frac{1}{4} C_{2n} \left(\overline{u}_{iNE}^* + \overline{u}_{iE}^* - \overline{u}_{iNW}^* - \overline{u}_{iW}^* \right) \right. \\
&\qquad\qquad \left. + \frac{1}{4} C_{5n} \left(\overline{u}_{iTN}^* + \overline{u}_{iT}^* - \overline{u}_{iBN}^* - \overline{u}_{iB}^* \right) \right] \\
&\quad - \left(\frac{1}{Re} + \frac{1}{Re_t} \right) \bigg|_s \left[C_{4s} \left(\overline{u}_{iP}^* - \overline{u}_{iS}^* \right) + \frac{1}{4} C_{2s} \left(\overline{u}_{iSE}^* + \overline{u}_{iE}^* - \overline{u}_{iSW}^* - \overline{u}_{iW}^* \right) \right. \\
&\qquad\qquad \left. + \frac{1}{4} C_{5s} \left(\overline{u}_{iTS}^* + \overline{u}_{iT}^* - \overline{u}_{iBS}^* - \overline{u}_{iB}^* \right) \right]
\end{aligned} \tag{C.19}$$

And the third term gives:

$$\begin{aligned}
&\oint_{CV} \frac{\partial}{\partial \zeta} \left[\left(\frac{1}{Re} + \frac{1}{Re_t} \right) J^{-1} S_j^3 S_j^l \frac{\partial \overline{u}_i^*}{\partial \xi_l} \right] dV = \\
&= \left(\frac{1}{Re} + \frac{1}{Re_t} \right) \bigg|_t \left[C_{6t} \left(\overline{u}_{iT}^* - \overline{u}_{iP}^* \right) + \frac{1}{4} C_{3t} \left(\overline{u}_{iTE}^* + \overline{u}_{iE}^* - \overline{u}_{iTW}^* - \overline{u}_{iW}^* \right) \right. \\
&\qquad\qquad \left. + \frac{1}{4} C_{5t} \left(\overline{u}_{iTN}^* + \overline{u}_{iN}^* - \overline{u}_{iTS}^* - \overline{u}_{iS}^* \right) \right] \\
&\quad - \left(\frac{1}{Re} + \frac{1}{Re_t} \right) \bigg|_s \left[C_{6b} \left(\overline{u}_{iP}^* - \overline{u}_{iB}^* \right) + \frac{1}{4} C_{3b} \left(\overline{u}_{iBE}^* + \overline{u}_{iE}^* - \overline{u}_{iBW}^* - \overline{u}_{iW}^* \right) \right. \\
&\qquad\qquad \left. + \frac{1}{4} C_{5b} \left(\overline{u}_{iBN}^* + \overline{u}_{iN}^* - \overline{u}_{iBS}^* - \overline{u}_{iS}^* \right) \right]
\end{aligned} \tag{C.20}$$

Gathering all the terms and grouping them adequately, we can define:

$$
\begin{aligned}
\mathcal{L}_{BW} &= \frac{1}{4}\left(C_{3w}+C_{3b}\right)\\
\mathcal{L}_{SW} &= \frac{1}{4}\left(C_{2w}+C_{2s}\right)\\
\mathcal{L}_{W} &= C_{1w}-\frac{1}{4}\left(C_{2n}-C_{2s}+C_{3t}-C_{3b}\right)\\
\mathcal{L}_{NW} &= -\frac{1}{4}\left(C_{2w}+C_{2n}\right)\\
\mathcal{L}_{TW} &= -\frac{1}{4}\left(C_{3w}+C_{3t}\right)\\
\mathcal{L}_{BS} &= \frac{1}{4}\left(C_{5sw}+C_{5b}\right)\\
\mathcal{L}_{B} &= C_{6b}-\frac{1}{4}\left(C_{3e}-C_{3w}+C_{5n}-C_{5s}\right)\\
\mathcal{L}_{BN} &= -\frac{1}{4}\left(C_{5n}+C_{5b}\right)\\
\mathcal{L}_{S} &= C_{4s}-\frac{1}{4}\left(C_{2e}-C_{2w}+C_{5t}-C_{5b}\right)\\
\mathcal{L}_{P} &= -\left(C_{1e}+C_{1w}+C_{4n}+C_{4s}+C_{6t}+C_{6b}\right)\\
\mathcal{L}_{N} &= C_{4n}+\frac{1}{4}\left(C_{2e}-C_{2w}+C_{5t}-C_{5b}\right)\\
\mathcal{L}_{TS} &= -\frac{1}{4}\left(C_{5s}+C_{5t}\right)\\
\mathcal{L}_{T} &= C_{6t}+\frac{1}{4}\left(C_{3e}-C_{3w}+C_{5n}-C_{5s}\right)\\
\mathcal{L}_{TN} &= \frac{1}{4}\left(C_{5n}+C_{5ts}\right)\\
\mathcal{L}_{BE} &= -\frac{1}{4}\left(C_{3e}+C_{3b}\right)\\
\mathcal{L}_{SE} &= -\frac{1}{4}\left(C_{2e}+C_{2s}\right)\\
\mathcal{L}_{E} &= C_{1e}+\frac{1}{4}\left(C_{2n}-C_{2s}+C_{3t}-C_{3b}\right)\\
\mathcal{L}_{NE} &= \frac{1}{4}\left(C_{2e}+C_{2n}\right)\\
\mathcal{L}_{TE} &= \frac{1}{4}\left(C_{3e}+C_{3t}\right)
\end{aligned}
\tag{C.21}
$$

Hence the diffusive term of the Burger equation is discretised as:

$$
\oint_{CV}\frac{\partial}{\partial\xi_k}\left[\left(\frac{1}{Re}+\frac{1}{Re_t}\right)J^{-1}S_j^kS_j^l\frac{\partial\overline{u}_i^*}{\partial\xi_l}\right]dV=\left(\frac{1}{Re}+\frac{1}{Re_t}\right)\sum_j\mathcal{L}_j\overline{u}_{ij}^* \tag{C.22}
$$

Where j is one of BW, SW, W, NW, TW, BS, B, BN, S, P, N, TS, T, TN, BE, SE, E, NE and TE.

Temporal Derivative Term

Using the previously described discretisation, and integrating the time derivative over the same control volume as for the convective and diffusive term, the following can be written:

$$\oint_{CV} \frac{\partial}{\partial t} (J\overline{u}_i^*) = \mathcal{D}_i - \mathcal{C}_i \tag{C.23}$$

Where $\mathcal{D}_i$ and $\mathcal{C}_i$ are the diffusive and convective terms respectively.

Using a Crank-Nicholson scheme for the diffusive term and an Adams-Bashford scheme for the convective term, it follows:

$$\frac{(J\overline{u}_i^*)^{(n+1)} - (J\overline{u}_i^*)^{(n)}}{\Delta t} = \frac{1}{2}\left(\mathcal{D}_i^{(n)} + \mathcal{D}_i^{(n+1)}\right) - \frac{1}{2}\left(3\mathcal{C}_i^{(n)} - \mathcal{C}_i^{(n-1)}\right) \tag{C.24}$$

Where superscripts $n-1$, n and $n+1$ denote the previous, current and next time step values.

Thus:

$$\frac{2}{\Delta t} (J\overline{u}_i^*)^{(n+1)} - \mathcal{D}_i^{(n+1)} = \frac{2}{\Delta t} (J\overline{u}_i^*)^{(n)} + \mathcal{D}_i^{(n)} - 3\mathcal{C}_i^{(n)} + \mathcal{C}_i^{(n-1)} \tag{C.25}$$

Or:

$$\sum_j \mathcal{T}_j \left(\overline{u}_{ij}^*\right)^{(n+1)} = \frac{2}{\Delta t} (J\overline{u}_i^*)^{(n)} + \mathcal{D}_i^{(n)} - 3\mathcal{C}_i^{(n)} + \mathcal{C}_i^{(n-1)} \tag{C.26}$$

Where j is one of BW, SW, W, NW, TW, BS, B, BN, S, P, N, TS, T, TN, BE, SE, E, NE and TE and:

$$\mathcal{T}_j = \delta_P^j \frac{2}{\Delta t} J - \left(\frac{1}{Re} + \frac{1}{Re_t}\right) \mathcal{L}_j \tag{C.27}$$

Where $\delta_P^j = 1$ if $j = P$ and 0 otherwise.

C.2 Poisson Equation

The discretisation of the Poisson equation takes a very similar form to that of the diffusive term of the Burger equation.

$$\frac{\partial}{\partial \xi_k}\left(J^{-1}S_i^k S_i^l \frac{\partial \overline{q}}{\partial \xi_l}\right) = \frac{\partial}{\partial \xi_m}\left(J\overline{U}^{*j}\right) \tag{C.28}$$

Integrating over a control volume gives:

$$\oint_{CV} \frac{\partial}{\partial \xi_k}\left(J^{-1}S_i^k S_i^l \frac{\partial \overline{q}}{\partial \xi_l}\right) dV = \oint_{CV} \frac{\partial}{\partial \xi_m}\left(J\overline{U}^{*j}\right) dV \tag{C.29}$$

i.e., using the same Laplacian as for the diffusive term of the Burger equation:

$$\sum_j \mathcal{L}_j \overline{u}^{*j} = \oint_{CV}\left[\frac{\partial}{\partial\xi}\left(J\overline{U}^*\right) + \frac{\partial}{\partial\eta}\left(J\overline{V}^*\right) + \frac{\partial}{\partial\zeta}\left(J\overline{W}^*\right)\right] d\xi d\eta d\zeta \tag{C.30}$$

Thus:

$$\sum_j \mathcal{L}_j \overline{u}^{*j} = \left(J\overline{U}^*\right)\Big|_e - \left(J\overline{U}^*\right)\Big|_w + \left(J\overline{V}^*\right)\Big|_n - \left(J\overline{V}^*\right)\Big|_s + \left(J\overline{W}^*\right)\Big|_t - \left(J\overline{W}^*\right)\Big|_b \tag{C.31}$$

Where, since $\overline{U}^{*m} = S_j^m \overline{u}_j^*$, then:

$$\overline{U}^*\Big|_e = \left(S_1^1 \overline{u}^* + S_2^1 \overline{v}^* + S_3^1 \overline{w}^*\right)\Big|_e \tag{C.32}$$

That is, using a simple linear interpolation scheme for the face variables:

$$\overline{U}^*\Big|_e = \frac{1}{2}\left[S_1^1\big|_e (\overline{u}_P^* + \overline{u}_E^*) + S_2^1\big|_e (\overline{v}_P^* + \overline{v}_E^*) + S_3^1\big|_e (\overline{w}_P^* + \overline{w}_E^*)\right] \tag{C.33}$$

Similarly:

$$\begin{aligned}
\overline{U}^*\Big|_w &= \frac{1}{2}\left[S_1^1\big|_w (\overline{u}_P^* + \overline{u}_W^*) + S_2^1\big|_w (\overline{v}_P^* + \overline{v}_W^*) + S_3^1\big|_w (\overline{w}_P^* + \overline{w}_W^*)\right] \\
\overline{V}^*\Big|_n &= \frac{1}{2}\left[S_1^2\big|_n (\overline{u}_P^* + \overline{u}_N^*) + S_2^2\big|_n (\overline{v}_P^* + \overline{v}_N^*) + S_3^2\big|_n (\overline{w}_P^* + \overline{w}_N^*)\right] \\
\overline{V}^*\Big|_s &= \frac{1}{2}\left[S_1^2\big|_s (\overline{u}_P^* + \overline{u}_S^*) + S_2^2\big|_s (\overline{v}_P^* + \overline{v}_S^*) + S_3^2\big|_s (\overline{w}_P^* + \overline{w}_S^*)\right] \\
\overline{W}^*\Big|_t &= \frac{1}{2}\left[S_1^3\big|_t (\overline{u}_P^* + \overline{u}_T^*) + S_2^3\big|_t (\overline{v}_P^* + \overline{v}_T^*) + S_3^3\big|_t (\overline{w}_P^* + \overline{w}_T^*)\right] \\
\overline{W}^*\Big|_b &= \frac{1}{2}\left[S_1^3\big|_b (\overline{u}_P^* + \overline{u}_B^*) + S_2^3\big|_b (\overline{v}_P^* + \overline{v}_B^*) + S_3^3\big|_b (\overline{w}_P^* + \overline{w}_B^*)\right]
\end{aligned} \tag{C.34}$$

C.3 Projection Equation

The discretisation of the Projection equation can be carried out rather simply.

From the projection equation:

$$\overline{u}_i = \overline{u}_i^* - J^{-1} S_i^j \frac{\partial \overline{q}}{\partial \xi_j} \tag{C.35}$$

Integrating over a control volume:

$$\oint_{CV} \overline{u}_i dV = \oint_{CV} \overline{u}_i^* dV - \oint_{CV} J^{-1} S_i^j \frac{\partial \overline{q}}{\partial \xi_j} dV \tag{C.36}$$

i.e.:

$$\oint_{CV} \overline{u}_i dV = \oint_{CV} \overline{u}_i^* dV - \oint_{CV} J^{-1} \left(S_i^1 \frac{\partial \overline{q}}{\partial \xi} + S_i^2 \frac{\partial \overline{q}}{\partial \eta} + S_i^3 \frac{\partial \overline{q}}{\partial \zeta} \right) d\xi d\eta d\zeta \tag{C.37}$$

Furthermore:

$$\overline{u}_i = \overline{u}_i^* - J^{-1} \left[S_i^1 \left(\overline{q}|_e - \overline{q}|_w \right) + S_i^2 \left(\overline{q}|_n - \overline{q}|_s \right) + S_i^3 \left(\overline{q}|_t - \overline{q}|_b \right) \right] \tag{C.38}$$

Using again a simple linear interpolation scheme for the face variables gives:

$$\overline{u}_i = \overline{u}_i^* - \frac{1}{2} J^{-1} \left[S_i^1 \left(\overline{q}_E - \overline{q}_W \right) + S_i^2 \left(\overline{q}_N - \overline{q}_S \right) + S_i^3 \left(\overline{q}_T - \overline{q}_B \right) \right] \tag{C.39}$$

The three velocity components are thus computed from:

$$\begin{aligned}
\overline{u} &= \overline{u}^* - \frac{1}{2} J^{-1} \left[S_1^1 \left(\overline{q}_E - \overline{q}_W \right) + S_1^2 \left(\overline{q}_N - \overline{q}_S \right) + S_1^3 \left(\overline{q}_T - \overline{q}_B \right) \right] \\
\overline{v} &= \overline{v}^* - \frac{1}{2} J^{-1} \left[S_2^1 \left(\overline{q}_E - \overline{q}_W \right) + S_2^2 \left(\overline{q}_N - \overline{q}_S \right) + S_2^3 \left(\overline{q}_T - \overline{q}_B \right) \right] \\
\overline{w} &= \overline{w}^* - \frac{1}{2} J^{-1} \left[S_3^1 \left(\overline{q}_E - \overline{q}_W \right) + S_3^2 \left(\overline{q}_N - \overline{q}_S \right) + S_3^3 \left(\overline{q}_T - \overline{q}_B \right) \right] \qquad \text{(C.40)}
\end{aligned}$$

C.4 Vorticity Equation

The vorticity equation is:

$$\overrightarrow{\omega} = \overrightarrow{\nabla} \times \overrightarrow{u} = \begin{vmatrix} \overrightarrow{i} & \overrightarrow{j} & \overrightarrow{k} \\ \frac{\partial}{\partial x} & \frac{\partial}{\partial y} & \frac{\partial}{\partial z} \\ u & v & w \end{vmatrix} = \overrightarrow{i} \left(\frac{\partial w}{\partial y} - \frac{\partial v}{\partial z} \right) + \overrightarrow{j} \left(\frac{\partial u}{\partial z} - \frac{\partial w}{\partial x} \right) + \overrightarrow{k} \left(\frac{\partial v}{\partial x} - \frac{\partial u}{\partial y} \right) \tag{C.41}$$

Or:

$$\omega_i = \frac{\partial u_k}{\partial x_j} - \frac{\partial u_j}{\partial x_k} \qquad \text{with } i,\ j \text{ and } k \text{ cyclic} \tag{C.42}$$

Using the chain rule:

$$\omega_i = \frac{\partial \xi_l}{\partial x_j}\frac{\partial u_k}{\partial \xi_l} - \frac{\partial \xi_m}{\partial x_k}\frac{\partial u_j}{\partial \xi_m} = J^{-1}\left[\frac{\partial\left(S_j^l u_k\right)}{\partial \xi_l} - \frac{\partial\left(S_k^m u_j\right)}{\partial \xi_m}\right] \tag{C.43}$$

Hence:

$$\begin{aligned}
\omega_\xi &= J^{-1}\left[\frac{\partial}{\partial \xi}\left(S_2^1 w - S_3^1 v\right) + \frac{\partial}{\partial \eta}\left(S_2^2 w - S_3^2 v\right) + \frac{\partial}{\partial \zeta}\left(S_2^3 w - S_3^3 v\right)\right] \\
\omega_\eta &= J^{-1}\left[\frac{\partial}{\partial \xi}\left(S_3^1 u - S_1^1 w\right) + \frac{\partial}{\partial \eta}\left(S_3^2 u - S_1^2 w\right) + \frac{\partial}{\partial \zeta}\left(S_3^3 u - S_1^3 w\right)\right] \\
\omega_\zeta &= J^{-1}\left[\frac{\partial}{\partial \xi}\left(S_1^1 v - S_2^1 u\right) + \frac{\partial}{\partial \eta}\left(S_1^2 v - S_2^2 u\right) + \frac{\partial}{\partial \zeta}\left(S_1^3 v - S_2^3 u\right)\right]
\end{aligned} \tag{C.44}$$

Integrating over a control volume gives:

$$\begin{aligned}
\oint_{CV} \omega_\xi dV &= J^{-1}\left[\left(S_2^1 w - S_3^1 v\right)\Big|_e - \left(S_2^1 w - S_3^1 v\right)\Big|_w + \left(S_2^2 w - S_3^2 v\right)\Big|_n - \left(S_2^2 w - S_3^2 v\right)\Big|_s\right. \\
&\quad \left. + \left(S_2^3 w - S_3^3 v\right)\Big|_t - \left(S_2^3 w - S_3^3 v\right)\Big|_b\right] \\
\oint_{CV} \omega_\eta dv &= J^{-1}\left[\left(S_3^1 u - S_1^1 w\right)\Big|_e - \left(S_3^1 u - S_1^1 w\right)\Big|_w + \left(S_3^2 u - S_1^2 w\right)\Big|_n - \left(S_3^2 u - S_1^2 w\right)\Big|_s\right. \\
&\quad \left. + \left(S_3^3 u - S_1^3 w\right)\Big|_t - \left(S_3^3 u - S_1^3 w\right)\Big|_b\right] \\
\oint_{CV} \omega_\zeta dV &= J^{-1}\left[\left(S_1^1 v - S_2^1 u\right)\Big|_e - \left(S_1^1 v - S_2^1 u\right)\Big|_w + \left(S_1^2 v - S_2^2 u\right)\Big|_n - \left(S_1^2 v - S_2^2 u\right)\Big|_s\right. \\
&\quad \left. + \left(S_1^3 v - S_2^3 u\right)\Big|_t - \left(S_1^3 v - S_2^3 u\right)\Big|_b\right]
\end{aligned} \tag{C.45}$$

I.e.:

$$
\begin{aligned}
\oint_{CV} \omega_\xi = \frac{1}{2} J^{-1} [\quad & S^1_2|_e\, w|_e - S^1_3|_e\, v|_e - S^1_2|_w\, w|_w + S^1_3|_w\, v|_w \\
& + S^2_2|_n\, w|_n - S^2_3|_n\, v|_n - S^2_2|_s\, w|_s + S^2_3|_s\, v|_s \\
& + S^3_2|_t\, w|_t - S^3_3|_t\, v|_t - S^3_2|_b\, w|_b + S^3_3|_b\, v|_b \quad] \\
\oint_{CV} \omega_\eta = \frac{1}{2} J^{-1} [\quad & S^1_3|_e\, u|_e - S^1_1|_e\, w|_e - S^1_3|_w\, u|_w + S^1_1|_w\, w|_w \\
& + S^2_3|_n\, u|_n - S^2_1|_n\, w|_n - S^2_3|_s\, u|_s + S^2_1|_s\, w|_s \\
& + S^3_3|_t\, u|_t - S^3_1|_t\, w|_t - S^3_3|_b\, u|_b + S^3_1|_b\, w|_b \quad] \\
\oint_{CV} \omega_\zeta = \frac{1}{2} J^{-1} [\quad & S^1_1|_e\, v|_e - S^1_2|_e\, u|_e - S^1_1|_w\, v|_w + S^1_2|_w\, u|_w \\
& + S^2_1|_n\, v|_n - S^2_2|_n\, u|_n - S^2_1|_s\, v|_s + S^2_2|_s\, u|_s \\
& + S^3_1|_t\, v|_t - S^3_2|_t\, u|_t - S^3_1|_b\, v|_b + S^3_2|_b\, u|_b \quad]
\end{aligned}
\tag{C.46}
$$

As previously, the face variables are simply computed from the linear interpolation between the cell-centered variables.

C.5 Turbulence Models

Smagorinsky Model

The Smagorinsky turbulence model is described by the following expression for the turbulent Reynolds number:

$$
\frac{1}{Re_t} = C_S^2 \Delta \left|\overline{S}\right| \tag{C.47}
$$

Where:

$$
\left|\overline{S}\right| = \sqrt{2\overline{S}_{ij}\overline{S}_{ij}} \tag{C.48}
$$

The discretisation of the Smagorinsky turbulence model thus essentially resides in the discretisation of the rate of strain tensor given by:

$$
\overline{S}_{ij} = \frac{1}{2}\left(\frac{\partial \overline{u}_i^*}{\partial x_j} + \frac{\partial \overline{u}_j^*}{\partial x_i}\right) \tag{C.49}
$$

Now, the above equation can be transformed into its curvilinear form using the chain rule, giving:

$$
\overline{S}_{ij} = \frac{1}{2}\left(\frac{\partial \xi_k}{\partial x_j}\frac{\partial \overline{u}_i^*}{\partial \xi_k} + \frac{\partial \xi_l}{\partial x_i}\frac{\partial \overline{u}_j^*}{\partial \xi_l}\right) \tag{C.50}
$$

I.e., using the first fundamental metric identity:

$$\begin{aligned}\overline{S}_{ij} &= \frac{1}{2}\left(J^{-1}S_j^k\frac{\partial\overline{u}_i^*}{\partial\xi_k} + J^{-1}S_i^l\frac{\partial\overline{u}_j^*}{\partial\xi_l}\right)\\ &= \frac{1}{2J}\left(\frac{\partial\left(S_j^k\overline{u}_i^*\right)}{\partial\xi_k} + \frac{\partial\left(S_i^l\overline{u}_j^*\right)}{\partial\xi_l}\right) \qquad \text{(C.51)}\end{aligned}$$

Now, since:

$$\overline{S}_{ij} = \overline{S}_{11} + \overline{S}_{12} + \overline{S}_{13} + \overline{S}_{21} + \overline{S}_{22} + \overline{S}_{23} + \overline{S}_{31} + \overline{S}_{32} + \overline{S}_{33} \qquad \text{(C.52)}$$

And:

$$\begin{aligned}\overline{S}_{12} &= \overline{S}_{21}\\ \overline{S}_{13} &= \overline{S}_{31}\\ \overline{S}_{23} &= \overline{S}_{32} \qquad \text{(C.53)}\end{aligned}$$

Then:

$$\overline{S}_{ij} = \overline{S}_{11} + \overline{S}_{22} + \overline{S}_{33} + 2\left(\overline{S}_{12} + \overline{S}_{13} + \overline{S}_{23}\right) \qquad \text{(C.54)}$$

Where:

$$\begin{aligned}\overline{S}_{11} &= \frac{1}{2J}\left(\frac{\partial}{\partial\xi_k}\left(S_1^k\overline{u}^*\right) + \frac{\partial}{\partial\xi_l}\left(S_1^l\overline{u}^*\right)\right)\\ &= \frac{1}{J}\left[\frac{\partial}{\partial\xi}\left(S_1^1\overline{u}^*\right) + \frac{\partial}{\partial\eta}\left(S_1^2\overline{u}^*\right) + \frac{\partial}{\partial\zeta}\left(S_1^3\overline{u}^*\right)\right] \qquad \text{(C.55)}\end{aligned}$$

Similarly:

$$\begin{aligned}\overline{S}_{22} &= \frac{1}{J}\left[\frac{\partial}{\partial\xi}\left(S_2^1\overline{v}^*\right) + \frac{\partial}{\partial\eta}\left(S_2^2\overline{v}^*\right) + \frac{\partial}{\partial\zeta}\left(S_2^3\overline{v}^*\right)\right]\\ \overline{S}_{33} &= \frac{1}{J}\left[\frac{\partial}{\partial\xi}\left(S_3^1\overline{w}^*\right) + \frac{\partial}{\partial\eta}\left(S_3^2\overline{w}^*\right) + \frac{\partial}{\partial\zeta}\left(S_3^3\overline{w}^*\right)\right]\\ \overline{S}_{12} &= \frac{1}{2J}\left[\frac{\partial}{\partial\xi}\left(S_2^1\overline{u}^* + S_1^1\overline{v}^*\right) + \frac{\partial}{\partial\eta}\left(S_2^2\overline{u}^* + S_1^2\overline{v}^*\right) + \frac{\partial}{\partial\zeta}\left(S_2^3\overline{u}^* + S_1^3\overline{v}^*\right)\right]\\ \overline{S}_{13} &= \frac{1}{2J}\left[\frac{\partial}{\partial\xi}\left(S_3^1\overline{u}^* + S_1^1\overline{w}^*\right) + \frac{\partial}{\partial\eta}\left(S_3^2\overline{u}^* + S_1^2\overline{w}^*\right) + \frac{\partial}{\partial\zeta}\left(S_3^3\overline{u}^* + S_1^3\overline{w}^*\right)\right]\\ \overline{S}_{23} &= \frac{1}{2J}\left[\frac{\partial}{\partial\xi}\left(S_3^1\overline{v}^* + S_2^1\overline{w}^*\right) + \frac{\partial}{\partial\eta}\left(S_3^2\overline{v}^* + S_2^2\overline{w}^*\right) + \frac{\partial}{\partial\zeta}\left(S_3^3\overline{v}^* + S_2^3\overline{w}^*\right)\right]\end{aligned}$$

(C.56)

Integrating over a control volume gives:

$$\begin{aligned}
\oint_{CV} \overline{S}_{11} d\xi d\eta d\zeta = \overline{S}_{11} &= \frac{1}{J}\left[S^1_1\big|_e \overline{u}^*\big|_e - S^1_1\big|_w \overline{u}^*\big|_w + S^2_1\big|_n \overline{u}^*\big|_n\right. \\
&\quad \left. - S^2_1\big|_s \overline{u}^*\big|_s + S^3_1\big|_t \overline{u}^*\big|_t - S^3_1\big|_b \overline{u}^*\big|_b\right] \\
\oint_{CV} \overline{S}_{22} d\xi d\eta d\zeta = \overline{S}_{22} &= \frac{1}{J}\left[S^1_2\big|_e \overline{v}^*\big|_e - S^1_2\big|_w \overline{v}^*\big|_w + S^2_2\big|_n \overline{v}^*\big|_n\right. \\
&\quad \left. - S^2_2\big|_s \overline{v}^*\big|_s + S^3_2\big|_t \overline{v}^*\big|_t - S^3_2\big|_b \overline{v}^*\big|_b\right] \\
\oint_{CV} \overline{S}_{33} d\xi d\eta d\zeta = \overline{S}_{33} &= \frac{1}{J}\left[S^1_3\big|_e \overline{w}^*\big|_e - S^1_3\big|_w \overline{w}^*\big|_w + S^2_3\big|_n \overline{w}^*\big|_n\right. \\
&\quad \left. - S^2_3\big|_s \overline{w}^*\big|_s + S^3_3\big|_t \overline{w}^*\big|_t - S^3_3\big|_b \overline{w}^*\big|_b\right]
\end{aligned}$$

$$\begin{aligned}
\oint_{CV} \overline{S}_{12} d\xi d\eta d\zeta = \overline{S}_{12} &= \frac{1}{2J}\left[S^1_2\big|_e \overline{u}^*\big|_e + S^1_1\big|_e \overline{v}^*\big|_e - S^1_2\big|_w \overline{u}^*\big|_w - S^1_1\big|_w \overline{v}^*\big|_w\right. \\
&\quad + S^2_2\big|_n \overline{u}^*\big|_n + S^2_1\big|_n \overline{v}^*\big|_n - S^2_2\big|_s \overline{u}^*\big|_s - S^2_1\big|_s \overline{v}^*\big|_s \\
&\quad \left. + S^3_2\big|_t \overline{u}^*\big|_t + S^3_1\big|_t \overline{v}^*\big|_t - S^3_2\big|_b \overline{u}^*\big|_b - S^3_1\big|_b \overline{v}^*\big|_b\right] \\
\oint_{CV} \overline{S}_{13} d\xi d\eta d\zeta = \overline{S}_{13} &= \frac{1}{2J}\left[S^1_3\big|_e \overline{u}^*\big|_e + S^1_1\big|_e \overline{w}^*\big|_e - S^1_3\big|_w \overline{u}^*\big|_w - S^1_1\big|_w \overline{w}^*\big|_w\right. \\
&\quad + S^2_3\big|_n \overline{u}^*\big|_n + S^2_1\big|_n \overline{w}^*\big|_n - S^2_3\big|_s \overline{u}^*\big|_s - S^2_1\big|_s \overline{w}^*\big|_s \\
&\quad \left. + S^3_3\big|_t \overline{u}^*\big|_t + S^3_1\big|_t \overline{w}^*\big|_t - S^3_3\big|_b \overline{u}^*\big|_b - S^3_1\big|_b \overline{w}^*\big|_b\right] \\
\oint_{CV} \overline{S}_{23} d\xi d\eta d\zeta = \overline{S}_{23} &= \frac{1}{2J}\left[S^1_3\big|_e \overline{v}^*\big|_e + S^1_2\big|_e \overline{w}^*\big|_e - S^1_3\big|_w \overline{v}^*\big|_w - S^1_2\big|_w \overline{w}^*\big|_w\right. \\
&\quad + S^2_3\big|_n \overline{v}^*\big|_n + S^2_2\big|_n \overline{w}^*\big|_n - S^2_3\big|_s \overline{v}^*\big|_s - S^2_2\big|_s \overline{w}^*\big|_s \\
&\quad \left. + S^3_3\big|_t \overline{v}^*\big|_t + S^3_2\big|_t \overline{w}^*\big|_t - S^3_3\big|_b \overline{v}^*\big|_b - S^3_2\big|_b \overline{w}^*\big|_b\right]
\end{aligned} \tag{C.57}$$

Again, the face variables can be computed using a simple linear interpolation between the appropriate cell-centred values.

Structure Function Model

In the case of the Structure Function model, the turbulent Reynolds number is obtained from:

$$\frac{1}{Re_t} = 0.063\Delta\sqrt{\overline{F}_2\left(\overrightarrow{x}, \Delta, t\right)} \tag{C.58}$$

It follows that the discretisation of the structure function model consists mainly of the discretisation of the structure function itself, i.e.:

$$\overline{F}_2\left(\overrightarrow{x},\Delta,t\right) = \langle\left\|\overrightarrow{\overline{u}^*}\left(\mathbf{x}+\mathbf{r},t\right) - \overrightarrow{\overline{u}^*}\left(\mathbf{x},t\right)\right\|^2\rangle_{\|\overrightarrow{r}\|=\Delta} \qquad \text{(C.59)}$$

Considering the six direct neighbouring volume to our control volume, the above can be written as:

$$\begin{aligned}\overline{F}_2 = \frac{1}{6}(\quad & \left\|\overrightarrow{\overline{u}^*}_E - \overrightarrow{\overline{u}^*}_P\right\|^2 + \left\|\overrightarrow{\overline{u}^*}_W - \overrightarrow{\overline{u}^*}_P\right\|^2 + \left\|\overrightarrow{\overline{u}^*}_N - \overrightarrow{\overline{u}^*}_P\right\|^2 \\ & + \left\|\overrightarrow{\overline{u}^*}_S - \overrightarrow{\overline{u}^*}_P\right\|^2 + \left\|\overrightarrow{\overline{u}^*}_T - \overrightarrow{\overline{u}^*}_P\right\|^2 + \left\|\overrightarrow{\overline{u}^*}_B - \overrightarrow{\overline{u}^*}_P\right\|^2\Big)\end{aligned} \qquad \text{(C.60)}$$

I.e.:

$$\begin{aligned}\overline{F}_2 = \frac{1}{6}[\quad & (\overline{u}^*_E - \overline{u}^*_P)^2 + (\overline{v}^*_E - \overline{v}^*_P)^2 + (\overline{w}^*_E - \overline{w}^*_P)^2 \\ & (\overline{u}^*_W - \overline{u}^*_P)^2 + (\overline{v}^*_W - \overline{v}^*_P)^2 + (\overline{w}^*_W - \overline{w}^*_P)^2 \\ & (\overline{u}^*_N - \overline{u}^*_P)^2 + (\overline{v}^*_N - \overline{v}^*_P)^2 + (\overline{w}^*_N - \overline{w}^*_P)^2 \\ & (\overline{u}^*_S - \overline{u}^*_P)^2 + (\overline{v}^*_S - \overline{v}^*_P)^2 + (\overline{w}^*_S - \overline{w}^*_P)^2 \\ & (\overline{u}^*_T - \overline{u}^*_P)^2 + (\overline{v}^*_T - \overline{v}^*_P)^2 + (\overline{w}^*_T - \overline{w}^*_P)^2 \\ & (\overline{u}^*_B - \overline{u}^*_P)^2 + (\overline{v}^*_B - \overline{v}^*_P)^2 + (\overline{w}^*_B - \overline{w}^*_P)^2]\end{aligned} \qquad \text{(C.61)}$$

Selective Structure Function Model

The Selective Structure Function model is very similar to the Structure function and only differs the latter by a switch function ζ based on the three dimensionality of the flow:

$$\frac{1}{Re_t} = 0.098\zeta\Delta\sqrt{\overline{F}_2\left(\overrightarrow{x},\Delta,t\right)} \qquad \text{(C.62)}$$

Where:

$$\zeta = \begin{cases} 0 & \text{for } \beta < 20^o \\ e^{-(d\beta/3)^2} & \text{for } 20^o \geq \beta \geq 10^o \text{ and } \mathrm{d}\beta = |\beta - 20| \\ 1 & \text{for } \beta > 20^o \end{cases} \qquad \text{(C.63)}$$

The angle β represent the angle between the local vorticity and the average neighbouring vorticity. It is evaluated as follows:

$$\beta = acos\left(\frac{\overrightarrow{\omega}_P \cdot \overrightarrow{\omega}_{av}}{\|\overrightarrow{\omega}_P\| \cdot \|\overrightarrow{\omega}_{av}\|}\right) \qquad \text{(C.64)}$$

Where:

$$\overrightarrow{\omega}_{av} = \frac{1}{6}\left(\overrightarrow{\omega_E} + \overrightarrow{\omega_W} + \overrightarrow{\omega_N} + \overrightarrow{\omega_S} + \overrightarrow{\omega_T} + \overrightarrow{\omega_B}\right) \qquad \text{(C.65)}$$

And:

$$\overrightarrow{\omega}_P \cdot \overrightarrow{\omega}_{av} = \omega_{\xi_P}\omega_{\xi_{av}} + \omega_{\eta_P}\omega_{\eta_{av}} + \omega_{\zeta_P}\omega_{\zeta_{av}} \tag{C.66}$$

$$\|\overrightarrow{\omega}_P\| \cdot \|\overrightarrow{\omega}_{av}\| = \sqrt{\left(\omega_{\xi_P}^2 + \omega_{\eta_P}^2 + \omega_{\zeta_P}^2\right)\left(\omega_{\xi_{av}}^2 + \omega_{\eta_{av}}^2 + \omega_{\zeta_{av}}^2\right)} \tag{C.67}$$

C.6 Metrics

The metrics required for the discretisation are as follow:

Since:

$$\overrightarrow{S}^i = \left\{ \begin{array}{c} y_{\xi_j} z_{\xi_k} - y_{\xi_k} z_{\xi_j} \\ x_{\xi_k} z_{\xi_j} - x_{\xi_j} z_{\xi_k} \\ x_{\xi_j} y_{\xi_k} - x_{\xi_k} y_{\xi_j} \end{array} \right\} \quad \text{with } i,\ j \text{ and } k \text{ cyclic} \tag{C.68}$$

In 3D, this implies 9 coefficients to be defined as:

$$\begin{aligned}
S_1^1 &= y_\eta z_\zeta - y_\zeta z_\eta \\
S_1^2 &= y_\zeta z_\xi - y_\xi z_\zeta \\
S_1^3 &= y_\xi z_\eta - y_\eta z_\xi \\
S_2^1 &= x_\zeta z_\eta - x_\eta z_\zeta \\
S_2^2 &= x_\xi z_\zeta - x_\zeta z_\xi \\
S_2^3 &= x_\eta z_\xi - x_\xi z_\eta \\
S_3^1 &= x_\eta y_\zeta - x_\zeta y_\eta \\
S_3^2 &= x_\zeta y_\xi - x_\xi y_\zeta \\
S_3^3 &= x_\xi y_\eta - x_\eta y_\xi
\end{aligned} \tag{C.69}$$

The Jacobian of the transformation between cartesian and curvilinear space can be calculated from:

$$J = x_\xi \left(y_\eta z_\zeta - y_\zeta z_\eta\right) + x_\eta \left(y_\zeta z_\xi - y_\xi z_\zeta\right) + x_\zeta \left(y_\xi z_\eta - y_\eta z_\xi\right) \tag{C.70}$$